



Universiteit
Leiden

The Netherlands

Nuclear quantum effects in solid water: new insights from computational modeling

Rasti, S.

Citation

Rasti, S. (2022, October 25). *Nuclear quantum effects in solid water: new insights from computational modeling*. Retrieved from <https://hdl.handle.net/1887/3484763>

Version: Publisher's Version

License: [Licence agreement concerning inclusion of doctoral thesis in the Institutional Repository of the University of Leiden](#)

Downloaded from: <https://hdl.handle.net/1887/3484763>

Note: To cite this publication please use the final published version (if applicable).

Nuclear Quantum Effects in Solid Water –
New Insights from Computational Modeling

Proefschrift

ter verkrijging van
de graad van Doctor aan de Universiteit Leiden,
op gezag van rector magnificus prof.dr.ir. H. Bijl,
volgens besluit van het college voor promoties
te verdedigen op dinsdag 25 oktober 2022
klokke 16:15 uur

door

Soroush Rasti
geboren te Iran
in 1991

Promotor: Prof. dr. G. J. Kroes

Co-promotor: Dr. J. Meyer

Promotiecommissie

Prof. dr. M. Ubbink

Prof. dr. M. T. M. Koper

Prof. dr. H. Jónsson University of Iceland

Prof. dr. H. M. Cuppen Radboud Universiteit Nijmegen

Dr. A. L. M. Lamberts

The research described in this thesis has been performed at the Theoretical Chemistry group of the Leiden Institute of Chemistry (Einsteinweg 55, 2333 CC, Leiden). This work has been supported by the Netherlands Organisation for Scientific Research (NWO) via Vidi grant no. 723.014.009.

Dedicated to my lovely wife Maryam, for all of her love and support.

Contents

1	Introduction	1
1.1	Hydrogen Bond Network in Ice	1
1.2	Modeling Ice Properties	4
1.3	Aims and Scope of this Thesis	6
1.4	Main Results	8
1.5	Outlook	10
1.6	References	12
2	Theory and Methods	15
2.1	Born-Oppenheimer Approximation	16
2.2	Density Functional Theory	17
2.2.1	Exchange-Correlation Functionals	18
2.2.2	Van der Waals Interactions	21
2.2.3	Computational Aspects	24
2.3	Force Field Methods for Modeling Ice	26
2.3.1	Fixed-Charge Pair Potentials	28
2.3.2	AMOEBA	33
2.3.3	SCME	38
2.3.4	MB-pol	42
2.4	Phonons	47
2.4.1	Harmonic Approximation	47
2.4.2	Lattice Dynamics	48

2.4.3	Vibrational Free Energy	50
2.4.4	Quasi-Harmonic Approximation	51
2.4.5	Computational Aspects	53
2.5	References	57
3	Importance of Zero-point Energy for Crystalline Ice Phases	61
3.1	Introduction	62
3.2	Methodology	65
3.2.1	Total energy calculations	65
3.2.2	Inclusion of Zero-Point Energy Effects	67
3.2.3	Determination of Phase-Transition Pressures	68
3.3	Results and Discussions	69
3.3.1	Equilibrium Structures	69
3.3.2	Cohesive Energies	70
3.3.3	Phase Transition Pressures	75
3.3.4	Analysis of Zero-Point Energy Effects	77
3.4	Conclusion	80
3.A	Appendix	82
3.A.1	Data for Equilibrium Ice Structures	82
3.5	References	86
4	Calorimetric Signature of Deuterated Ice II	89
4.1	Introduction	90
4.2	Methods	93
4.2.1	Experimental Methods	93
4.2.2	Computational Details	94
4.3	Results and Discussion	95
4.3.1	Experiments	95
4.3.2	Calculations	97
4.4	Conclusions	101
4.A	Appendix	104

4.5	References	106
5	Transferable Potential Function for Flexible H₂O	109
5.1	Introduction	111
5.2	Flexible SCME Model	114
5.3	The Dipole and Quadrupole Moment Surfaces	119
5.3.1	Ab initio QMS Calculations and Fit	121
5.4	Forces	125
5.5	Flexible Model Fit	127
5.6	Model Validation	130
5.7	Discussion and Conclusions	137
5.A	Appendix	145
5.A.1	Analytical Forces	145
5.A.2	Deviation of M-site Models	155
5.A.3	Energy-Volume Curves for Ice Ih	155
5.8	References	158
6	Volume Isotope Effect of Ice Ih	163
6.1	Introduction	164
6.2	Methods	166
6.3	Results and Discussion	168
6.4	Conclusion and Outlook	175
6.A	Appendix	176
6.A.1	Comparison to Previous DFT Calculations	176
6.A.2	Convergence Tests for the VIE Calculations	177
6.A.3	Zero-point Pressures from Experimental Data	178
6.5	References	182
	Samenvatting	185
	Curriculum Vitae	189

List of Publications	191
Afterword	193

CHAPTER 1

Introduction

Solid water, commonly referred to as ice, is ubiquitous throughout the universe as a material with many unique properties. Ice plays an important role for cloud formation on earth and helping life survive on this planet. Arctic ice regulates its temperature by reflecting sunlight, and ice glaciers are an important reservoir of fresh water. Without ice, no aquatic plants and animals would survive throughout the winter months [1, 2]. Furthermore, ice under extreme conditions has received special attention in astronomy and planetary science. When searching for life on other planets, detecting ice is commonly considered to be a prerequisite. Consequently, studying ice is important for interdisciplinary research, and has been an active field in the physical sciences for many years. Since ice restructures in different phases under different temperature and pressure conditions, thermodynamic properties and their roots in chemical bonding are an interesting subject of study in the physical sciences [3].

1.1 Hydrogen Bond Network in Ice

Chemical bonding in ice is surprisingly complex despite the simple chemical formula of water (H_2O). A water molecule consists of one oxygen atom covalently bound to two hydrogen atoms forming a bond angle of 104.5° . Since electrons are not equally

shared in these bonds, the O and the H atoms are left with slight negative and positive charges, respectively. The resulting electrostatic interaction between hydrogen and oxygen atoms of different water molecules are the most obvious cause for the existence of hydrogen bonds (HBs). In addition, HBs also share some characteristics of covalent bonding such as being directional and only involving a limited number of interaction partners. Each water molecule can form HBs with up to four other molecules: two through its hydrogen atoms and two through the two lone electron pairs of its oxygen atom [4]. In other words, each water molecule donates and accepts two HBs. The strength of HBs largely depends on the relative orientation of the contributing water molecules. Consequently, hydrogen bonds are typically 10-100 times weaker than covalent bonds but can be about ten times stronger than van der Waals (vdW) interactions [5]. HBs are thus capable of storing a lot of energy, which results in an unusual high heat capacity. This property of ice makes the climate more moderate in many parts of this planet, resulting in more stable conditions for life on earth [6, 7].

In the most common phase of ice on earth, ice Ih, the hydrogen bond network results in bond angles which come very close to the 109.5° found as vertex-center-vertex angle in an ideal tetrahedron. Despite the energy cost to deform the bond angle of a water molecule in gas phase (see above), the tetrahedral bond angle is favourable for the stability of ice Ih. It also implies a rather “open structure” consisting of non-planar hexagonal rings, with the oxygen atoms forming a honeycomb structure that becomes “visible” when cutting ice Ih in the basal plane. Inside those rings there is almost sufficient space for an additional H_2O molecule. This results in the density of ice Ih being 8.3% lower than the density of liquid water – and thus the famous and tremendously important property of the former floating on the latter.

While the oxygen atoms form a periodic lattice, this does not hold for the hydrogen atoms. According to the ice rules [8], each hydrogen atom is always found between precisely two oxygen atoms. In 1935 Pauling showed that these ice rules result in $(\frac{3}{2})^N$ possible configurations for N HBs. Assuming equal likelihood for all of these configurations and thus quasi-random placement of the hydrogen atom yields a very

simple estimate for the so-called residual entropy ($S_0 = Nk_B \ln(\frac{3}{2})$), which was shown to be surprisingly accurate by the experiments of Giauque and Stout in 1936. Other experiments [11, 12] suggested the existence of a hydrogen-ordered version of ice Ih, which is depicted as ice XI in Fig. 1.1. This figure also shows seven hydrogen-disordered ice phases. They can transform to hydrogen-ordered phases when being cooled to lower temperatures or by changing the pressure.

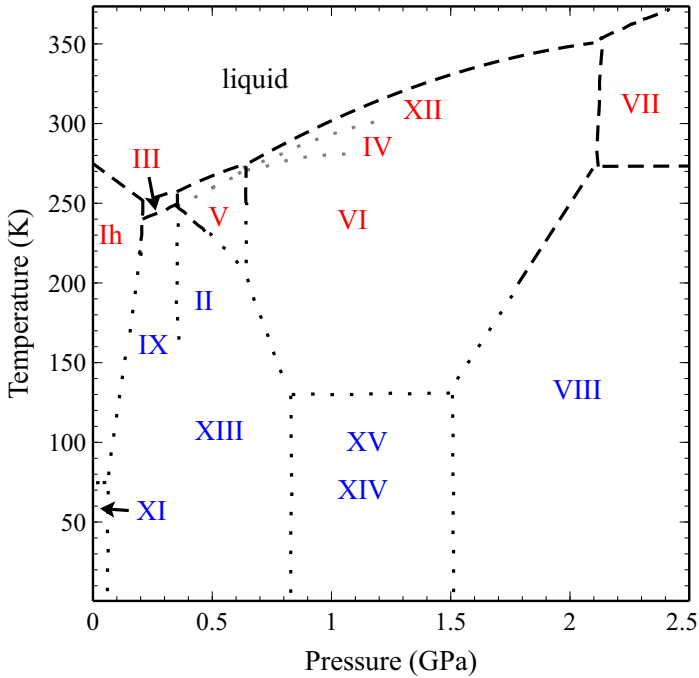


Figure 1.1: Phase diagram of water and ice as function of pressure and temperature Salzmann [13]. Hydrogen-disordered and hydrogen-ordered ice phases are indicated by red and blue labels, respectively. Measured (extrapolated) phase boundaries are shown by black dashed (dotted) lines. Gray dotted lines show phase boundaries for metastable phases, e.g. IV and XII.

1.2 Modeling Ice Properties

For a long time, experimental techniques have been the only way to obtain scientific insights about structural and thermodynamic properties of ice. X-ray or neutron scattering experiments for example have provided significant insights to understand how the water molecules are arranged in different ice phases and thus allowed to unravel the importance of hydrogen bond networks. Remarkably, it was Pauling’s theoretical work that proposed for the first time that four water molecules are connected in a tetrahedral arrangement in ice Ih [7, 9]. This structural model was confirmed by a neutron diffraction scattering experiment afterwards [14]. Nowadays, the knowledge obtained from computational modeling and experiments is considered complementary to each other. Ideally, calculations allow to quantitatively understand measurements and thus provide insights as well as stimulate new experiments. The improvement of computational facilities and algorithms used for computational modeling during the last decades has increased the scope for the latter, which allows to address questions like the structure of ice under extreme conditions. For instance, studying the enormous geophysical pressure produced by planetary cores demands considerable efforts in real experiments, while calculations can easily take a pV -term into account in a thermodynamic context [15, 16].

For any atomistic computational modeling, an interaction potential is mandatory to calculate properties of ice. In the simplest case, such a potential only depends on the nuclear coordinates and relies on empirically motivated and parametrized expressions for different contributions to the bonding. Interatomic pair potentials with fixed atomic charges are the prime example of this approach [17–19]. More accurate models have been developed by accounting for (atomic or molecular) polarizability [20–22], which is particularly relevant for long-range electrostatic interactions that play an important role in ice. In so-called first-principles approaches, electrons are explicitly included in the description of the inter- and intramolecular interactions of water molecules. The electron structure thereby implicitly mitigates all different kind of (molecular) many-body effects among the nuclei. For extended systems like ice, density functional

theory (DFT) is often the only viable computational option to model sufficiently large unit cells. Although DFT is in principle exact, any practical calculation requires an approximation for the so-called exchange-correlation (xc) functional. In the context of hydrogen bond networks, accurate accounting for long-ranged van der Waals (vdW) interactions in the context of DFT requires special attention.

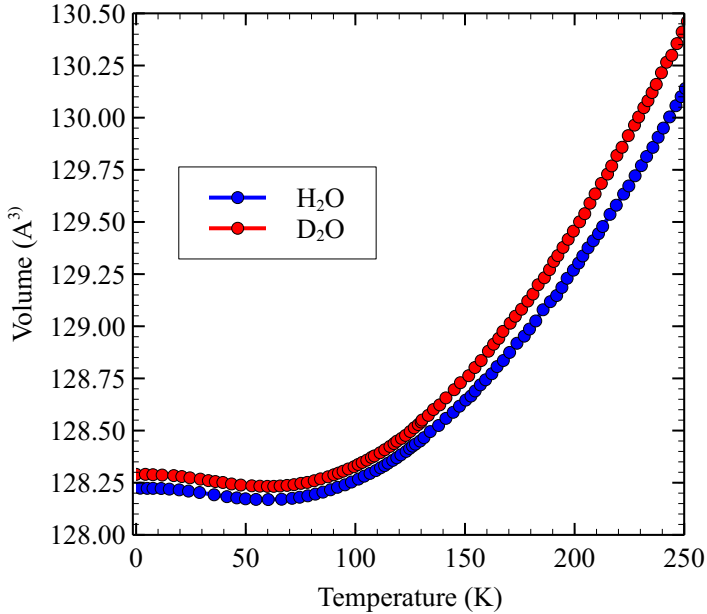


Figure 1.2: Measured unit cell volume of ice Ih comprised of H₂O (blue) and D₂O (red) molecules as a function of temperature based on high-precision neutron scattering experiments [23].

Apart from the interaction potential, modeling ice can also be challenged by having to take nuclear quantum effects (NQE) into account [24–30]. NQEs result from the fact that in particular the hydrogen atoms behave more like quantum mechanical rather than classical particles. Likewise, vibrational modes are better described by quantum mechanical rather than classical (harmonic) oscillators, which immediately gives rise to zero-point energy (ZPE). Without NQEs, ice would have considerable smaller heat

capacity. It would thus take much less energy to melt ice [31] – with obvious consequences for everyday life. Figure 1.2 depicts two other (subtle) manifestations of NQEs in ice: negative thermal expansion (NTE) and the volume isotope effect (VIE). Normal materials expand their volume upon increasing the temperature. Ice Ih on the other hand is anomalous in this respect and keeps shrinking for (increasing) temperatures between 0 to 50 K (for both H_2O and D_2O isotopologues), which is referred to as NTE. Most materials show a normal VIE, which means substitution with heavier isotopes results in a smaller volume at temperatures approaching the absolute zero. Handwavingly, in a classical picture, this can be rationalized by the smaller vibrational amplitude ascribed to a heavier nucleus experiencing the same chemical interaction potential at the same temperature. For instance, the lattice vector of ^{22}Ne is by 0.6 % smaller than ^{20}Ne at 0 K [32]. Quite the opposite, although Ne and H_2O have the very similar masses, the volume of H_2O isotopologue of ice Ih is 0.1 % smaller than D_2O (see Fig. 1.2) [24, 33, 34]. As seen in Fig. 1.2, this difference persists and even increases further up to the boiling point [35, 36]. The fact that ice features this anomalous VIE illustrates that the aforementioned rationalization is too simple and demands more elaborate computational modeling.

1.3 Aims and Scope of this Thesis

The following questions are being addressed in this thesis:

1. How important is the contribution of zero-point energy to thermodynamical properties of ice phases?
2. How accurately do available interaction potentials allow to model (small) difference in H_2O and D_2O ices related to nuclear quantum effects?
3. Do interaction potentials need to be improved when nuclear quantum effects in ice are taken into account?

Chapter 2 It summarizes the theoretical background of the methods used in this thesis. Starting from the Born-Oppenheimer approximation, interaction potentials used for modeling ice in the following are grouped into two categories: DFT and force fields. In the DFT section, a brief description of xc functionals is given, including special attention to vdW corrections because of their important role in modeling hydrogen-bond networks in ice. The force field section describes a set of particular interaction potentials ranging from simple fixed-charge pair potentials to accounting for many-body contributions by including polarizability at atomic sites and for entire H_2O molecules as well as additional short-range effects. This chapter concludes with a concise description of phonons and their relevance for thermodynamic properties in the harmonic and quasi-harmonic approximation (QHA).

Chapter 3 To set the stage for subsequent chapters, the importance of zero-point energy is quantified for crystalline ice phases using several commonly used fixed-charge pair potentials in comparison to several state-of-the-art exchange-correlation functionals within DFT.

Chapter 4 Calorimetric experiments for the ice II to ice Ic phase transition have revealed a surprising isotope effect. The concomitant transition enthalpy is endothermic for H_2O and exothermic for D_2O , albeit with only a small difference of about 180 J mol^{-1} . Such a sign change upon isotope substitution is unprecedented in ice research, and I have accepted the challenge to rationalise this finding by computational modeling.

Chapter 5 The original single center multipole expansion (SCME) model [37, 38], a physically motivated force-field including molecular polarizability (up to the quadrupole-quadrupole level), does not allow to describe intramolecular vibrations. Shifts of the latter due to the interaction with other water molecules cannot be accounted for, making it impossible to properly describe zero-point energy-related effects. Motivated by the results of Chapter 3, SCME is extended to “self-consistently” include ZPE in the parametrization procedure.

Chapter 6 The anomalous volume isotope and non-thermal expansion effects are investigated by making use of the extended SCME model from the previous chapter and compared to other force field and density-functional theory-based results. Both of these nuclear quantum effects are very challenging for computational modeling: the former could so far be obtained when using particular exchange-correlation functionals [39].

1.4 Main Results

The main scientific results of Chapters 3 to 6 are summarized here:

Chapter 3 : Importance of ZPE for crystalline ice phases

A systematic comparison for seven hydrogen-ordered crystalline ice phases (Ih, IX, II, XIII, XIV, XV, VIII) between many commonly-used fixed-charge pair potentials and density functional theory based on various exchange-correlation functionals is presented. The latter includes some recently developed meta-GGA functionals and accounting for vdW interactions. Starting from space-group-constrained relaxed structures for all ice phases, highly-accurate phonon calculations within the QHA are carried out. The resulting zero-point energies have a much stronger effect on the cohesive energies and equilibrium volumes for the force fields than for DFT and result in better agreement with experimental data for the former. When including ZPE the force fields yield equilibrium volumes and cohesive energies that are in better agreement with experimental data than most density functionals. This is further analyzed in detail by i) a decomposition of the cohesive energies into intramolecular deformation, electrostatic and vdW contributions and ii) a comparison of O–H-stretching-mode shifts due to volume changes to available experimental data from Raman spectroscopy.

Chapter 4 : Calorimetric Signature of Deuterated Ice II

The transition enthalpy of ice II to ice Ic are measured by calorimetry as $+40 \text{ J mol}^{-1}$ for H_2O and -140 J mol^{-1} for D_2O , resulting in an isotope effect of about 180 J mol^{-1} . A hierarchy of theoretical expressions for the transition enthalpy is used to account

for more and more (subtle) contributions. Apart from zero-point energy, also the usually neglected configurational entropy is ultimately taken into account because ice II is a hydrogen-order and ice Ic is a hydrogen-disordered phase. The expressions are evaluated computationally using two force fields, q-TIP4P/F and MB-pol, that are known to perform well for calculating the cohesive energy and vibrational properties of different ice phases. To that end, highly-accurate phonon calculations in the QHA are carried out. Considering the fact that the measured transition enthalpies are one to two order of magnitude smaller than what is commonly considered as chemical accuracy (4 kJ mol^{-1}) in computational modeling, it is not surprising that the sign change cannot be reproduced. However, both force fields yield the isotope effect due to (dominantly) the zero-point energy differences between the H_2O and corresponding D_2O ice phases in reasonable agreement with the measurements: q-TIP4P/F is able to account for about 3/4 of the isotope effect, while MB-pol only catches about 1/3.

Chapter 5 : Transferable Potential Function for Flexible H_2O

The single center multipole expansion (SCME) model [37, 38] is extended towards flexible water molecules, resulting in a new model called SCME/f. To that end, the coordinate dependence of the quadrupole moment tensor of a single H_2O molecule needs to be fitted to high-level quantum-chemistry calculations for small water cluster. Other parameters from the original SCME formulation are readjusted as well to incorporate ZPE corrections for lattice energies of ice Ih – enabling a proper incorporation of experimental data. This requires to carry out computationally demanding phonon calculations within the quasi-harmonic approximation “on-the-fly” for the reparametrization candidates in an iterative procedure. The resulting best fit is a significant improvement over the original SCME potential function – as evidenced also by comparing the energetics of “rigid” water cluster structures. Finally, the importance of accurately describing the variation of the quadrupole moment tensor with molecular structure is analyzed by comparison to simpler models.

Chapter 6 : Volume Isotope Effect of Ice Ih

This chapter demonstrates that a polarizable force field is able to model the anomalous

VIE of ice Ih, which has hitherto been deemed impossible. The state-of-the-art MB-pol force field also describes the NTE more accurately than most DFT-based approaches. In the subsequent analysis, the short-range three-body contributions (involving three water molecules) as described by MB-pol are found to play a very important role for the proper description of the VIE, whereas they are of minor importance e.g. for the cohesive energy. This could be a reason for why the SCME/f model performs slightly worse. Furthermore, a phonon mode decomposition of the so-called zero-point pressure (P_{ZP}) illustrates that the librational and stretching are the most important phonon modes responsible for the anomalous VIE, which could be verified by future experiments.

1.5 Outlook

In all chapters included in this thesis NQEs have been explicitly included in the computational modeling of different ice phases. Obviously, measurements always implicitly include these effects. Whalley has already estimated and emphasized in his pioneering work in the 1950s that they can have a very sizeable influence on “intermolecular forces” [40, 41]. Parameters for many interaction potentials have been obtained by fitting “extrapolated” experimental data with ZPE contributions semi-empirically removed. However, the ZPE given by the semi-empirical correction and directly obtained from the interaction potential “a posteriori” do then not necessarily agree. Fitting to the “raw” data requires to calculate ZPEs during the parametrisation procedure and thus comes with a significantly higher computational effort. In Chapter 5 it is demonstrated this is possible nowadays, resulting in an improved SCME model. Therefore, the same strategy could also be applied to other interaction potentials for water in the future.

Apart from using NQEs to systematically improve the quality of the interaction potentials, the accuracy of the quasi-harmonic approximation employed in this work also deserves further attention. This holds in particular for Chapter 4, where very small energy scales (J mol^{-1}) are relevant for the transition enthalpy of ice II to ice Ic.

Path-integral molecular dynamics (PIMD) allows to include anharmonic effects in the modeling of NQEs. Although PIMD comes at much higher computational cost than the quasi-harmonic approximation, it would be very interesting to carry out PIMD simulations for the same interaction potentials and investigate whether this could yield better agreement with the absolute transition enthalpies reported in Chapter 4 – ideally reproducing the water-isotopologue-related sign change.

In both Chapter 3 and Chapter 6 the experiments by Minceva-Sukarova *et al.* [42] are being invoked. The authors of that study have measured Raman spectra of different ice phases as a function of temperature and pressure. Since the latter is related to expansion and compression of the unit cell volume of an ice crystal, it can be compared to the corresponding predictions vibrational frequency shifts (and concomitant changes of the phonon density of state) obtained from calculations with different interactions potentials. These frequency shifts are crucial in the context of ZPE and the VIE as detailed in Chapter 3 and Chapter 6, respectively. The aforementioned experiments only report results for stretching modes of different water isotopologues. It would be very important to also have experimental data for the other modes (translation, librational and bending) in the future, because this is the only way to verify whether interaction potentials for water can predict NQEs (like the VIE and NTE in particular) accurately and for the right reason – and thus provide fundamentally important insights about the latter.

Ultimately, intriguing vibrational properties of ice (Ih) do not stop in the bulk, but have also been observed for ice surfaces. For example, low-energy electron diffraction and helium scattering experiments have suggested largely enhanced vibrational amplitudes related to water molecules at the surface [43–45] and dispersionless surface phonon bands [45]. It remains to be seen whether future work that builds on the calculations carried out in this thesis might elucidate those enigmatic vibrational features of ice surfaces.

1.6 References

1. G. A. Jeffrey, G. A. Jeffrey, *An introduction to hydrogen bonding* (Oxford university press New York, 1997), vol. 12.
2. G. Gilli, P. Gilli, *The nature of the hydrogen bond: outline of a comprehensive hydrogen bond theory* (Oxford University Press, 2009), vol. 23.
3. A. Leadbetter, M. Blackman, *Proceedings of the Royal Society of London. Series A. Mathematical and Physical Sciences* **287**, 403–425 (1965).
4. E. R. Pounder, *The physics of ice* (Elsevier, 2013).
5. P. Ball, *A biography of water* (Phoenix, 2000).
6. N. H. Fletcher, *cpi* (2009).
7. V. F. Petrenko, R. W. Whitworth, *Physics of ice* (Oxford University Press, 1999).
8. V. F. Petrenko, R. W. Whitworth, *Physics of ice* (OUP Oxford, 1999).
9. L. Pauling, *J. Am. Chem. Soc.* **57**, 2680–2684 (1935).
10. W. Giaque, J. Stout, *Journal of the American Chemical Society* **58**, 1144–1150 (1936).
11. Y Tajima, T Matsuo, H Suga, *Nature* **299**, 810–812 (1982).
12. R. Howe, R. Whitworth, *The Journal of chemical physics* **90**, 4450–4453 (1989).
13. C. G. Salzmann, *J. Chem. Phys* **150**, 060901 (2019).
14. S. Peterson, H. A. Levy, *Acta Crystallographica* **10**, 70–76 (1957).
15. D Alfe, M. Gillan, G. Price, *Nature* **405**, 172–175 (2000).
16. M. Gillan, D Alfe, J Brodholt, L Vočadlo, G. Price, *Reports on progress in physics* **69**, 2365 (2006).
17. H. J. Berendsen, J. P. Postma, W. F. van Gunsteren, J. Hermans, in *Intermolecular forces* (Springer, 1981), pp. 331–342.
18. W. L. Jorgensen, J. Chandrasekhar, J. D. Madura, R. W. Impey, M. L. Klein, *J. Chem. Phys* **79**, 926–935 (1983).
19. C. Vega, J. L. Abascal, *Physical Chemistry Chemical Physics* **13**, 19663–19688 (2011).
20. J. Applequist, J. R. Carl, K.-K. Fung, *J. Am. Chem. Soc.* **94**, 2952–2960 (1972).
21. B. T. Thole, *Chemical Physics* **59**, 341–350 (1981).
22. P. E. Lopes, B. Roux, A. D. MacKerell, *Theoretical Chemistry Accounts* **124**, 11–28 (2009).
23. A. D. Fortes, *Acta Cryst. B* **74**, 196–216 (2018).
24. C. P. Herrero, R. Ramírez, *J. Chem. Phys.* **134**, 094510 (2011).
25. S. Habershon, T. E. Markland, D. E. Manolopoulos, *J. Chem. Phys* **131**, 024501 (2009).
26. A. Soper, C. Benmore, *Phys. Rev. Lett.* **101**, 065502 (2008).
27. R Ramírez, C. Herrero, *J. Chem. Phys* **133**, 144511 (2010).
28. J. A. Morrone, R. Car, *Phys. Rev. Lett.* **101**, 017801 (2008).

-
29. X.-Z. Li, B. Walker, A. Michaelides, *Proceedings of the National Academy of Sciences* **108**, 6369–6373 (2011).
 30. A. Zeidler, P. S. Salmon, H. E. Fischer, J. C. Neufeind, J. M. Simonson, *et al.*, *Phys. Rev. Lett.* **107**, 145501 (2011).
 31. C Vega, M. M. Conde, C. McBride, J. L. F. Abascal, E. G. Noya, *et al.*, *The Journal of chemical physics* **132**, 046101 (2010).
 32. D. Batchelder, D. Losee, R. Simmons, *Phys. Rev.* **173**, 873 (1968).
 33. K. Röttger, A. Endriss, J. Ihringer, S. Doyle, W. F. Kuhs, *Acta Cryst. B* **50**, 644–648 (1994).
 34. A. D. Fortes, I. G. Wood, J. P. Brodholt, L. Vočadlo, *J. Chem. Phys.* **119**, 4567–4572 (2003).
 35. G. S. Kell, *J. Phys. Chem. Ref. Data* **6**, 1109–1131 (1977).
 36. G. Kell, *J. Chem. Engin. Data* **12**, 66–69 (1967).
 37. E. Batista, *Development of a New Water-Water Interaction Potential and Applications to Molecular Processes in Ice* (University of Washington, 1999).
 38. K. T. Wikfeldt, E. R. Batista, F. D. Vila, H. Jónsson, *Phys. Chem. Chem. Phys.* **15**, 16542 (2013).
 39. B. Pamuk, J. M. Soler, R. Ramírez, C. P. Herrero, P. W. Stephens, *et al.*, *Phys. Rev. Lett.* **108**, 193003 (2012).
 40. E. Whalley, *Trans. Faraday Soc.* **53**, 1578 (1957).
 41. E. Whalley, *"Trans. Faraday Soc."* **54**, 1613 (1958).
 42. B. Minceva-Sukarova, W. F. Sherman, G. R. Wilkinson, *J. Phys. C: Solid State Phys.* **17**, 5833–5850 (1984).
 43. N Materer, U Starke, A Barbieri, M Van Hove, G. Somorjai, *et al.*, *The Journal of Physical Chemistry* **99**, 6267–6269 (1995).
 44. N Materer, U Starke, A Barbieri, M. Van Hove, G. Somorjai, *et al.*, *Surface science* **381**, 190–210 (1997).
 45. J Braun, A Glebov, A. Graham, A Menzel, J. Toennies, *Physical review letters* **80**, 2638 (1998).

CHAPTER 2

Theory and Methods

Atomistic modelling of water in its condensed form can be done at very different levels of theory. Here, those which are relevant to this thesis are briefly described, including some numerical and computational details where appropriate. First, the stage is set in Section 2.1 by the Born-Oppenheimer approximation, which is most fundamental for the description of interactions and dynamics at the atomic scale. After that, Section 2.2 introduces density functional theory (DFT) as one of the most popular and successful first-principles methods for inter- and intramolecular interactions between individual water molecules. Given the importance of van-der-Waals interactions for the latter, this chapter also pays special attention on how these interactions can be accounted for in the context of DFT. Coarse-graining away the electronic structure, force fields are another commonly-used approach for modelling water-water interactions as presented in Section 2.3. Those which are used in this thesis can be grouped into two categories, fixed-charged and polarizable force fields of different complexity. Since the main goal of this thesis is studying properties of crystalline forms of water ice which are heavily affected by the lattice vibrations of the latter, this chapter ends with concise descriptions of phonons in Section 2.4. In particular, their relation to the Helmholtz free energy is described and the so-called quasi-harmonic approximation is presented in order to account for thermal expansion.

2.1 Born-Oppenheimer Approximation

The description of a chemical system from first principles starts from the quantum mechanical many-body problem that is given in its time-independent form by the electron-nuclear Schrödinger equation

$$\hat{H}\Psi = E\Psi \quad . \quad (2.1)$$

E is the ground state (total) energy of the system (at zero temperature), Ψ is the electron-nuclear wave function that describes the spatial coordinates $\{\mathbf{R}_A\}_{A=1}^M$ of M nuclei and the spatial and spin coordinates $\{\mathbf{r}_i, \sigma_i\}_{i=1}^N$ of N electrons. The Hamilton operator is given by

$$\hat{H} = -\sum_{i=1}^N \frac{\nabla_i^2}{2} - \sum_{A=1}^M \frac{\nabla_A^2}{2M_A} + \sum_{i=1}^N \sum_{j>i}^N \frac{1}{|\mathbf{r}_i - \mathbf{r}_j|} + \sum_{A=1}^M \sum_{B>A}^M \frac{Z_A Z_B}{|\mathbf{R}_A - \mathbf{R}_B|} - \sum_{i=1}^N \sum_{A=1}^M \frac{Z_A}{|\mathbf{r}_i - \mathbf{R}_A|} \quad (2.2)$$

in Hartree atomic units. M_A and Z_A are the mass and charge of a nucleus A , respectively, ∇_A (∇_i) denotes the Laplacian operator with respect to nuclear (electronic) coordinates. The first and third term are the kinetic energy of and Coulomb repulsion between the electrons, and the second and fourth term describe the same for the nuclei. The last term accounts for the Coulomb attraction between electrons and nuclei.

Exact analytical solutions of Eq. (2.2) are possible only for very few chemically relevant systems. Also numerically it is enormously difficult to calculate the full electron-nuclear wave function. Instead, electrons and nuclei are usually decoupled from each other according to the Born-Oppenheimer approximation [1], which is based on the large mass difference between the former: even for the lightest atom M_A is already about 2000 times larger than the electron mass. The electronic part of \hat{H} is given by

$$\hat{H}_{\text{elec}} = -\sum_{i=1}^N \frac{\nabla_i^2}{2} + \sum_{i=1}^N \sum_{j>i}^N \frac{1}{|\mathbf{r}_i - \mathbf{r}_j|} - \sum_{i=1}^N \sum_{A=1}^M \frac{Z_A}{|\mathbf{r}_i - \mathbf{R}_A|} \quad , \quad (2.3)$$

which yields an electronic Schrödinger equation analogous to Eq. (2.2)

$$\hat{H}_{\text{elec}}\Psi_{\text{elec}} = E_{\text{elec}}\Psi_{\text{elec}} \quad (2.4)$$

with energy E_{elec} for the electronic ground state. This equation is easier to solve than Eq. (2.2), but still approximations are needed for chemically interesting systems. One of the most popular approximations is described in Section 2.2.

The Born-Oppenheimer approximation allows to express the total (potential) energy of a chemical system for a set of nuclear positions $(\{\mathbf{R}_A\}_{A=1}^M)$ as

$$E_{\text{total}} = E_{\text{elec}} + \sum_{A=1}^M \sum_{B>A}^M \frac{Z_A Z_B}{|\mathbf{R}_A - \mathbf{R}_B|} \quad . \quad (2.5)$$

The real-valued function $E_{\text{total}}(\{\mathbf{R}_A\}_{A=1}^M)$ of $3M$ variables constitutes the system's potential energy surface (PES). Instead of solving Eq. (2.4), a PES can also be constructed (semi-)empirically based on physical-chemical properties of the system and thus without explicitly accounting for the electrons – which is commonly referred to as a force field. There are many such force fields for water, and those which are relevant in the context of this thesis are described in Section 2.3.

2.2 Density Functional Theory

One of the most popular and successful approaches for solving the electronic Schrödinger equation (Eq. (2.4)) is density functional theory. According to the Hohenberg-Kohm theorem it is fundamentally possible to write E_{elec} as a functional of the electron density $n(\mathbf{r})$ [2]. Unfortunately, a universal (Hohenberg-Kohn) density functional is not known. However, Kohn and Sham have suggested to use an auxiliary system of non-interacting electrons as a starting point for to approximate this functional. This system has a well-defined kinetic energy

$$T_s(\{\phi_i\}) = \int d\mathbf{r} \tau_s(\mathbf{r}) = -\frac{1}{2} \sum_i \int d\mathbf{r} \phi_i^*(\mathbf{r}) \nabla^2 \phi_i(\mathbf{r}) \quad , \quad (2.6)$$

where ϕ_i are the single-particle (so-called Kohn-Sham) orbitals and $\tau_s(\mathbf{r})$ is the concomitant kinetic energy density. The Kohn-Sham orbitals yield the electron density ¹

¹The sums in Eqs. (2.6) and (2.7) extend over an appropriate amount of orbitals depending on the treatment of electron spin.

as

$$n(\mathbf{r}) = \sum_i |\phi_i|^2 \quad . \quad (2.7)$$

T_s constitutes a large contribution to E_{elec} , and the same holds for the classical electrostatic repulsion

$$E_{\text{Hartree}}[n(\mathbf{r})] = \int d\mathbf{r} \int d\mathbf{r}' \frac{n(\mathbf{r}) n(\mathbf{r}')}{|\mathbf{r} - \mathbf{r}'|} \quad (2.8)$$

and electron-nuclear attraction

$$E_{\text{ext}}[n(\mathbf{r})] = - \sum_{A=1}^M \int d\mathbf{r} \frac{n(\mathbf{r}) Z_A}{|\mathbf{r} - \mathbf{R}_A|} \quad (2.9)$$

energies. This results in the decomposition

$$E_{\text{elec}}[n] = T_s\{\phi_i\} + E_{\text{Hartree}}[n(\mathbf{r})] + E_{\text{ext}}[n(\mathbf{r})] + E_{\text{xc}}[n(\mathbf{r})] \quad , \quad (2.10)$$

which is employed by the vast majority of practical DFT calculations nowadays. The so-called exchange-correlation functional $E_{\text{xc}}[n(\mathbf{r})]$ is supposed to capture all the quantum-mechanical contributions of the actual system of interacting electrons that are missed by the other terms. Again, the exchange-correlation functional is not known exactly, but since it is a much smaller contribution to E_{elec} than the Hohenberg-Kohn functional, much simpler approximations can thus yield very accurate results. Minimizing Eq. (2.10) with respect to the electron density yields the Kohn-Sham equations, which are Schrödinger-like equations for the Kohn-Sham orbitals. This equations need to be solved self-consistently due to the relation between the latter and the electron density given by Eq. (2.7).

2.2.1 Exchange-Correlation Functionals

Nowadays there are many different exchange-correlation functionals available. They are usually categorized according to their complexity by the scheme originally suggest by John Perdew [3]. This Jacob’s ladder (see Fig. 2.1) is comprised of several rungs starting from the Hartree approximation, i.e., only accounting for exchange (“earth”) and ascending to the exact exchange-correlation functional (“heaven”). The simplest and therefore most common approximations for E_{xc} (first three rungs) are used in

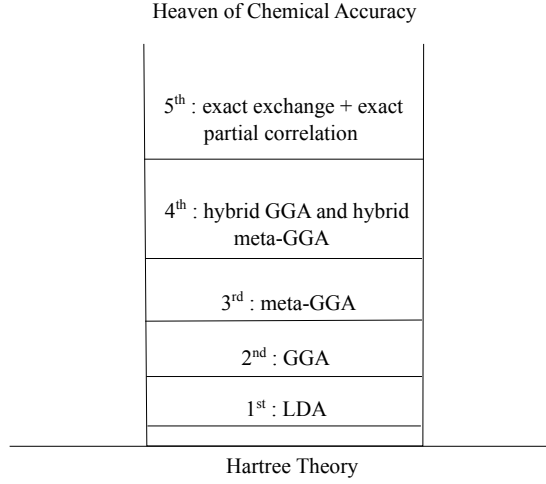


Figure 2.1: Jacob’s ladder for categorizing different approximations for E_{xc} according to Perdew *et al.* [3]

the scope of this thesis (see Chapter 3 in particular) and therefore described in the following subsections.

2.2.1.1 Local Density Approximation

In the local density approximation (LDFA) for E_{xc} the electron density at each point (\mathbf{r}) is taken to define a homogenous electron gas (HEG), so that the corresponding exchange-correlation functional is obtained as the superposition

$$E_{xc}^{LDA}[n] = \int d\mathbf{r} n(\mathbf{r}) (\epsilon_x^{\text{HEG}}[n(\mathbf{r})] + \epsilon_c^{\text{HEG}}[n(\mathbf{r})]) \quad . \quad (2.11)$$

The exchange energy density of the HEG is known analytically

$$\epsilon_x^{\text{HEG}}[n] = -\frac{3}{4} \sqrt[3]{\frac{3n(\mathbf{r})}{\pi}} \quad . \quad (2.12)$$

For the correlation energy density of the HEG $\epsilon_c^{\text{HEG}}[n]$ accurate Quantum Monte Carlo energy are available for a large range of electron densities [4, 5]. Historically, these results have been interpolated differently by, e.g. Vosko-Wilk-Nusair (VWN) [6], Perdew and Zunger (PZ) [7] as well as Perdew and Wang (PW) [8], which has led to numeri-

cally (but not conceptually) different LDAs. The differences are very small so that one usually still refers to “the LDA”.

In general, for inhomogeneous systems, the LDA underestimates the correlation and overestimates the exchange energy so that the total balance, $E_{\text{xc}}^{\text{LDA}}$, benefits from error cancellation. Since LDA satisfies several so-called sum rules [9, 10], this error cancellation is not accidental but systematical. Still, the cohesive energies of ice and water clusters are overestimated by more than 50 % [11–13]. In addition, the LDA completely misses long-range van der Waals interactions due to its strictly local dependence on the electron density.

2.2.1.2 Generalized Gradient Approximation

Generalized gradient approximations (GGAs) for the exchange-correlation energy are based on the general form

$$E_{\text{xc}}^{\text{GGA}}[n] = \int d\mathbf{r} n(\mathbf{r}) \epsilon_{\text{xc}}^{\text{HEG}}[n(\mathbf{r})] F_{\text{xc}}^{\text{GGA}}[n(\mathbf{r}), \nabla n(\mathbf{r})] \quad . \quad (2.13)$$

In the spirit of a Taylor expansion the so-called gradient enhancement factor $F_{\text{xc}}^{\text{GGA}}$ depends not only on the density but also on its gradient at a point \mathbf{r} , which is why GGAs are also called semi-local functionals. There is no unique way how to construct $F_{\text{xc}}^{\text{GGA}}$, which has resulted in a variety of different GGA functionals. Some examples are the GGAs developed by Lee, Yang and Parr (LYP) [14], Perdew and Wang (PW91) [15] and Perdew, Burke and Ernzerhof (PBE) [16]. In general, they are more accurate for chemical systems because the density varies strongly when covalent bonds are formed, and they come at essentially the same computational cost as the LDA.

2.2.1.3 Meta-generalized Gradient Approximation

Meta-generalized gradient approximations (MGGAs) for E_{xc} sit on the third rung of Jacob’s ladder. This class of exchange-correlation functionals take the second derivative of the electron density ($\nabla^2 n(\mathbf{r})$) and/or the kinetic energy density (see Eq. (2.6)) into account. Previous studies indicate that meta-GGAs such as TPSS [17] and SCAN [18] can improve the accuracy for numerous systems, including (small) water clusters and

ice [19–22] The computational cost for meta-GGAs is slightly higher than for GGAs, which is mainly because it is more difficult to achieve self-consistency when solving the Kohn-Sham equations.

2.2.2 Van der Waals Interactions

Van der Waals (vdW) interactions can appear (with different meaning) in the context of electrostatic, induction, and dispersion interactions. In the following, the focus is on the latter, i.e. the attractive interaction caused by fluctuating dipoles which are constituted by the correlated motion of electrons in individual atoms. This kind of interaction primarily contributes at the long range and therefore none of the exchange correlation functionals described in the previous section can properly account for them. Nowadays there are many different approaches available that can account for van der Waals interactions in DFT calculations [23–26]. Those which have been employed in this thesis are described very briefly in the following subsections.

2.2.2.1 C_6 Correction and Many-Body Dispersion

Dispersion interactions were introduced by London [27] as so-called London forces. Using the second-order quantum mechanical perturbation theory, the concomitant energy can be expanded as

$$E_{\text{vdW}}^{AB} = - \sum_{n \geq 6}^{\infty} \frac{C_n^{AB}}{R_{AB}^n} \quad , \quad (2.14)$$

where C_n^{AB} are dispersion coefficients for the interaction between a pair of atoms A and B at distance R_{AB} from each other. Focusing on the first non-zero term, an accurate determination of the C_6^{AB} coefficient becomes the primary target for all DFT-based vdW methods described in the remainder of this section. It is calculated according to the Casimir-Polder equation [28]

$$C_6^{AB} = \frac{3}{\pi} \int_0^{\infty} d\omega \alpha_A(i\omega) \alpha_B(i\omega) \quad , \quad (2.15)$$

where $\alpha_{A,B}$ are the dipole polarizabilities of the respective atoms due to an external electric field. Accurate calculations of $\alpha(i\omega)$ are challenging because a large amount of

accurately described electronically excited states are required. Dipole polarizabilities can also be obtained experimentally in the condensed or gas phase from measurements of the dielectric function [29], Rayleigh scattering [30] and molecular beam [31] experiments.

C_6 correction schemes, which are also commonly referred to as DFT+vdW or DFT-D schemes, add an additional term to the total energy of a DFT calculation that is of the form

$$E_{\text{vdW}} = - \sum_A \sum_{B>A} f_{\text{damp}}(R_{AB}) \frac{C_6^{AB}}{R_{AB}^6} . \quad (2.16)$$

Maintaining the short range interaction between two atoms A and B at the DFT level, the damping function $f_{\text{damp}}(R_{AB})$ smoothly switches off the dispersion interactions at small distances. Obviously, Eq. (2.16) can be easily evaluated after the actual DFT calculation and therefore comes at hardly any additional computational cost on top of the former.

In this thesis, the so-called TS correction scheme suggested by Tkatchenko and Scheffler [32] is used. It is based on accurate TD-DFT calculations of C_6 coefficients for the vdW interactions between individual atoms, $C_{6,0}$, by Chu and Dalgarno [33]. To account for changes for atoms in molecules (or in a solid), these coefficients are rescaled to

$$C_{6,\text{eff}}^{AA} = v_{AA}[n] C_{6,0}^{AA} . \quad (2.17)$$

Here the scaling factor $v_{AA}[n]$ describes the change of atomic volume based on Hirshfeld partitioning [34] of the electron density n that is obtained from the DFT calculation for the “non-free” atoms A . The corresponding C_6 coefficients for heteronuclear pairs of atoms are obtained from

$$C_{6,\text{eff}}^{AB} = \frac{2 C_{6,\text{eff}}^{AA} C_{6,\text{eff}}^{BB}}{\frac{\alpha_{0,B}}{\alpha_{0,A}} C_{6,\text{eff}}^{AA} + \frac{\alpha_{0,A}}{\alpha_{0,B}} C_{6,\text{eff}}^{BB}} , \quad (2.18)$$

where the (static dipole) polarizabilities of the free atoms α_0 are also taken from the work of Chu and Dalgarno [33]. $f_{\text{damp}}(R_{AB})$ is chosen as a Fermi-type damping function with parameters that are optimized to the S22 database from Jurečka *et al.* [35].

The TS scheme provides a surprisingly accurate description of van der Waals interactions in the DFT context in particular for molecular systems. However, it struggles with accounting for (long-range) screening in the condensed phase, which has been addressed by an extension to the TS scheme Tkatchenko *et al.* [36]. This so-called many-body dispersion scheme (MBD) replaces Eq. (2.16) by a quantum mechanical many-body expression for a system of coupled dipole oscillators with frequency-dependent polarizabilities $\alpha(i\omega)$, which for the “non-free” atoms are again obtained from Hirshfeld partitioning. MBD still comes at moderate computational costs compared to the underlying DFT calculation and therefore can easily be applied to condensed phases of water.

2.2.2.2 van der Waals Density Functionals

Van der Waals density functionals (vdW-DFs)² add a long-range contribution typically to semi-local exchange-correlation functionals

$$E_{xc}[n] = E_x^{\text{GGA}}[n] + E_c^0[n] + E_c^{\text{lr}}[n] \quad . \quad (2.19)$$

Usually, the exchange energy is taken from a particular GGA [38, 39], and the short-range correlation energy E_c^0 is treated at the LDA level [26]. The simplest expression for the long-range correlation energy is

$$E_c^{\text{lr}} = \frac{1}{2} \int d\mathbf{r} \int d\mathbf{r}' n(\mathbf{r}) \Phi(\mathbf{r}, \mathbf{r}') n(\mathbf{r}') \quad . \quad (2.20)$$

$\Phi(\mathbf{r}, \mathbf{r}')$ is the non-local kernel, for which different expressions have been suggested [38, 40, 41] and some of them been applied to water [42] and ice [43] systems.

From a computational point of view, the straightforward numerical implementation of Eq. (2.20) by evaluating the six dimensional integral is computationally expensive. However, many DFT codes employ the technique suggested by Román-Pérez and Soler [44]. This technique significantly reduces the computational effort and thus enables self-consistent calculations which come at almost the same cost as calculations with GGA functionals.

²Acknowledging the work of two pioneers in their development, they also referred to as Langreth-Lunqvist functionals. [37–39]

2.2.3 Computational Aspects

In principal, all-electron calculations for condensed phases of water can nowadays be carried out very accurately and computationally conveniently based by using numerical atom-centered basis sets. However, in practice, not all exchange-correlation functionals have been available in the code implementing the latter, which is why it was necessary to resort to plane-waves basis sets for some of the DFT calculations in this thesis.

2.2.3.1 Numerical Atom-Centered Basis Sets

One type of basis sets employed in this thesis are all-electron numerical atom-centered orbitals (NAO) as implemented in the FHI-AIMS code [45], which can be written as

$$\psi_i(\mathbf{r}) = \psi_i(r, \theta, \varphi) = \frac{u_i(r)}{r} Y_{l_i m_i}(\theta, \varphi) \quad . \quad (2.21)$$

Here $Y_{l(i), m(i)}$ is a spherical harmonic function with (atomic angular momentum indexes) l and m that implicitly depend on the basis function index i . $u_i(r)$ is obtained as numerical solution of Schrödinger-like radial equation

$$\left[-\frac{1}{2} \frac{d^2}{dr^2} + \frac{l_i(l_i + 1)}{r^2} + v_i(r) + v_{\text{cut}}(r) \right] u_i(r) = \epsilon_i u_i(r) \quad (2.22)$$

for a particular (radial) potential $v_i(r)$ and a reasonably chosen confining potential $v_{\text{cut}}(r)$. $v_i(r)$ determines the shape of the concomitant basis function. To construct the minimal basis set it is taken from a DFT calculation for the free neutral (and non-spin-polarized) atom of a given chemical element using the exchange-correlation functional selected for the target system. This way, core electrons are described very accurately and efficiently because their orbitals hardly change due the formation of chemical bonds. Additional basis functions are added by using $v_i(r)$ from free hydrogen-like atoms or ions, analogous to polarization functions in Gaussian basis sets. In FHI-AIMS these basis functions are ranked and grouped into tiers for each element based on how much they reduce the total energy for dimers at different bond distances covering the binding curve for that element [45]. $v_{\text{cut}}(r)$ is a steeply increasing potential that ensures $u_i(r)$ quickly goes to zero beyond a certain distance, which is usually chosen

to be between 4 to 5 Å for light elements. This allows to minimize the computational effort for numerical operations involving the basis functions (e.g. integrations), ideally resulting in linear scaling of the latter with respect to the amount of atoms. Predefined choices for basis set tiers and parameters determining the numerical accuracy of the basis set representation (including $v_{\text{cut}}(r)$) are available in FHI-AIMS in form of the so-called *light*, *tight* and *very tight* settings [45]. In this thesis, adequate settings have been selected based on thorough convergence tests.

2.2.3.2 Plane-Wave Basis Sets

According to Bloch’s theorem electronic states $\phi_{n,\mathbf{k}}(\mathbf{r})$ in a crystalline solid with band index n at point \mathbf{k} in the first Brillouin zone can be described exactly by the Fourier expansion

$$\phi_{n,\mathbf{k}}(\mathbf{r}) = \sum_{\mathbf{G}} C_{n,\mathbf{G}+\mathbf{k}} \exp(i(\mathbf{G} + \mathbf{k})\mathbf{r}) \quad . \quad (2.23)$$

The discrete set of plane wave vectors \mathbf{G} are given by the reciprocal lattice of the crystal. For numerical applications of Eq. (2.23) in a computer code, the plane-wave expansion needs to be cut off to keep the amount of basis set coefficients $C_{n,\mathbf{G}+\mathbf{k}}$ finite. In practice, this is achieved by choosing a cut-off energy E_{cut} such that

$$\frac{1}{2}|\mathbf{G} + \mathbf{k}|^2 \leq E_{\text{cut}} \quad . \quad (2.24)$$

Obviously, the choice of the cut-off energy determines the numerical accuracy of a plane-wave DFT calculation. Core electrons require very large values for E_{cut} because they are strongly localised at a particular nucleus and cause the radial parts of the corresponding valence electrons to oscillate in this core region in order to maintain orthogonality. Since the computational effort increases significantly with increasing E_{cut} , practical plane-wave calculations freeze the core electrons into the nuclei to avoid the two aforementioned problems. Each chemical element is thus represented by a so-called pseudopotential.

In this thesis, the VASP code is used for all plane-wave DFT calculations, which also provides a set pre-constructed pseudopotentials. The latter and concomitant E_{cut} have

been chosen carefully based on convergence tests and comparison with FHI-AIMS for each system under investigation.

2.2.3.3 Reciprocal Space Sampling

For a crystalline solid many quantities, like e.g. the electron density, are obtained by integration over the first Brillouin zone. Since the electronic wave-functions for different \mathbf{k} -points are very similar³, it is possible to approximate the integrals by a summation over a discrete set of \mathbf{k} -points. Throughout this thesis, uniform \mathbf{k} -point grids as suggested by Monkhorst and Pack [46] are used, and convergence of the results with respect to the grid density has been carefully checked.

This method generates a uniform \mathbf{k} points mesh along three lattice vectors in reciprocal space. It is worth noting that an inadequate \mathbf{k} point sampling can lead to inaccurate results. Nevertheless, setting a denser set of \mathbf{k} points can solve this problem. Therefore, it is crucial to check the number of \mathbf{k} points for having accurate and converged results.

2.3 Force Field Methods for Modeling Ice

The potential energy surface that the nuclei experience after the electronic problem has been solved separately according to the Born-Oppenheimer approximation (see Section 2.1) can be describe by a so-called force field model, which is given by a particular (often physically motivated) functional form together with a set of parameters. The construction of such force fields for modelling water in both the liquid and solid phase has a long history. As a result, there are now several tens of such water models available, many of which have been demonstrated to provide an accurate description of many physical properties of water and ice. [49, 57–59].

Figure 2.2 provides an overview of the particular force fields used in this thesis, grouped according to their complexity. The simplest ones, i.e., the SPC/E [60] and TIPnP

³See Eq. (2.23), but this also hold for an appropriate expansion of Bloch states in atom-centered basis sets.

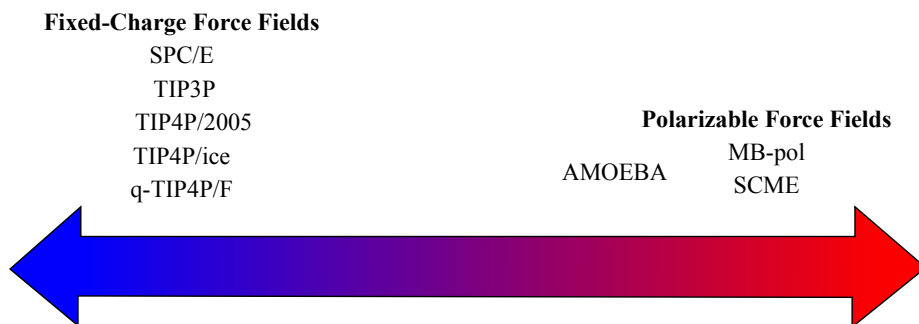


Figure 2.2: Spectrum of the complexity of water force fields. The force fields used in this thesis are SPC/E [47], TIP3P [48], TIP4P/2005 [49], TIP4P/ice [50], and q-TIP4P/F [51], AMOEBA [52, 53], MB-pol [54, 55], and SCME [56].

families of potentials [48], at the left side of this spectrum use fixed point charges for modelling electrostatic and Lennard-Jones potentials (for approximating van der Waals interactions, the latter of which have been discussed earlier in Section 2.2.2 in the context of DFT). The resulting electrostatic and vdW pair potentials are parametrized to reproduce the properties of liquid water or ice. Consequently, the so obtained empirical parameters of these two-body interactions also need to approximately account for any interactions involving three or more water molecules that are not included systematically. The majority of these force fields treat a single water molecule as a rigid monomer – assuming that the energy cost to deform individual water molecules is much larger than intermolecular interactions. SPC/fw [61] and q-TIP4P/F [51] are two examples where flexibility has been added. The explicit expressions and parameters of all the fixed-charged pair potentials used in this thesis are summarized in Section 2.3.1.

Force fields towards the right of Fig. 2.2 all explicitly include (higher) electrostatic multipole moments as well as polarization effects. The latter implicitly accounts for many-body interactions in the electrostatics. Both provide a well-defined classical limit for the interaction between water molecules at large distances, which is relevant

for modelling many delicate properties of water and ice correctly [52, 54, 55, 62, 63]. The common approach for including polarization effects is the Appliquès polarizable point dipole model [64]. This approach is further extended by Thole [65] to address the polarization catastrophe. Some of known Thole-type polarization force fields are TTM3-F [66], TTM4-F [62], AMOEBA [52, 53], SCME [56] and MB-pol [54, 55], the last three of which are being employed in this thesis. Other examples for polarizable force fields are DPP2 [67], CC-pol [68, 69] and WHBB [70]. They have not been considered here because they cannot be used for large systems as they are primarily targeted for water in the gas-phase [71] or because they are rigid water models (DPP2 and CC-pol). In its original formulation, the latter also partially holds for SCME [56], but lifting this limitation completely is part of this thesis (see Chapter 5). The main difference between AMOEBA, SCME and MB-pol is how the quantum mechanical many-body contributions to dispersion and repulsion between water molecules at the short range are being accounted for. As described in Section 2.3.2, AMOEBA is empirically parametrized similar to fixed-charge force fields, but it includes atomic multipole moments (up to quadrupoles) and polarizabilities (up to dipoles). In contrast, both SCME and MB-pol rely on highly accurate *ab initio* quantum chemistry calculations. The main difference is that SCME primarily tries to capture as much as possible by including high-order molecular electrostatic contributions (up to permanent molecular hexadecapoles and induced quadrupoles), which leads to a still fairly small amount of parameters (see Section 2.3.3). On the other hand, MB-pol utilizes a rather complex mathematical construct to fit the contributions to the intermolecular interactions at short distances involving (up to) three water molecules directly to quantum chemical data (see Section 2.3.4).

2.3.1 Fixed-Charge Pair Potentials

The first fixed-charge water model was proposed by Bernal and Fowler [72] in 1933. Nowadays there are now several tens of these models available, among which the extended single charge model (SPC/E [47]) and some of the members of the family of transferable intermolecular potential (TIP) models are employed in this thesis. These

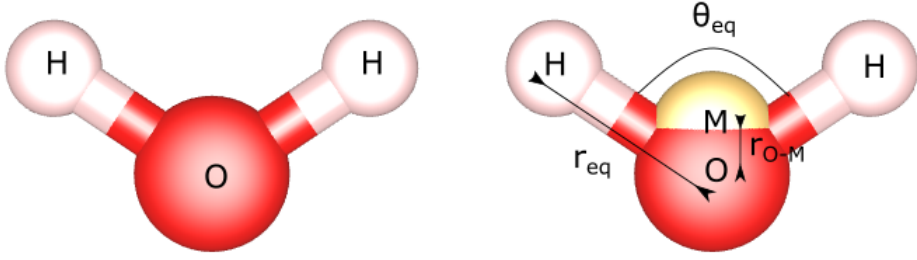


Figure 2.3: Three-site (left) and four-site (right) geometries of fixed-charge water force field. The oxygen atom is shown in red, hydrogen in white, and the virtual site in yellow. r_{eq} represents the equilibrium bond distance between oxygen and hydrogen, θ_{eq} is the equilibrium H–O–H bond angle, and $r_{\text{O-M}}$ shows the distance between oxygen and virtual site in case of four-site force fields.

models are either based on three (TIP3P [48]) or four (TIP4P/2005 [49]) atomic sites per water molecule as show in Fig. 2.3. They have been modified specifically for ice (TIP4P/ice [50]) or to effectively account for quantum effects while introducing molecular flexibility (q-TIP4P/F [51]).

All of these force fields models describe the total energy based on four energy terms:

$$E_{\text{total}} = \underbrace{E_{\text{elec}} + E_{\text{vdW}}}_{\text{intermolecular}} + \underbrace{E_{\text{bond}} + E_{\text{angle}}}_{\text{intramolecular}} \quad (2.25)$$

Here, the electrostatic (E_{elec}) and van der Waals (E_{vdW}) contributions constitute the intermolecular, and the O–H bond stretching (E_{bond}) and H–O–H angle bending (E_{angle}) constitute the intramolecular contributions.

The electrostatic interactions are described by pairwise Coulomb potentials between the sites i and j that carry the electric charges q_i and q_j :

$$E_{\text{elec}} = \frac{1}{4\pi\epsilon_0} \sum_i \sum_{j>i} \frac{q_i q_j}{|\mathbf{r}_i - \mathbf{r}_j|} \quad \text{if } |\mathbf{r}_i - \mathbf{r}_j| < r_{\text{c,elec}} \quad (2.26)$$

ϵ_0 is the electric constant. In the simplest case, to decrease computational cost, only interactions between sites at distances $|\mathbf{r}_i - \mathbf{r}_j|$ smaller than the the cut-off radius

Table 2.1: Electrostatic and Lennard-Jones parameters for SPC/E, TIP3P, TIP4P/2005, TIP4P/ice, and q-TIP4P/F force fields. Maintaining charge neutrality for each water molecule, the oxygen and hydrogen partial charges for the three-site models is $+q$ and $-q/2$, respectively. In four-site models (TIP4P/2005, TIP4P/ice, and q-TIP4P/F), $+q$ is located at the virtual site (see Fig. 2.3). The Lennard-Jones potentials only act between oxygen atoms and thus only $\epsilon_{\text{O-O}}$ and $\sigma_{\text{O-O}}$ in Eq. (2.27) are non-zero. The only exception to that is TIP3P, which is why the corresponding parameters are listed separately in Table 2.2.

	$q(e)$	$\epsilon_{\text{O-O}}(\text{kcal mol}^{-1})$	$\sigma_{\text{O-O}}(\text{\AA})$
SPC/E	0.8200	0.1553	3.1660
TIP3P	0.8300	[see Table 2.2]	
TIP4P/2005	1.1128	0.1852	3.1589
TIP4P/ice	1.1794	0.2108	3.1668
q-TIP4P/F	1.1128	0.1852	3.1589

Table 2.2: Lennard-Jones parameters for the intermolecular interactions between O–O, O–H and H–H pairs in the TIP3P model.

	O–O	O–H	H–H
ϵ (kcal mol $^{-1}$)	0.1521	0.0836	0.0460
σ (Å)	3.1507	1.7753	0.4000

$r_{\text{c,elec}}$ are taken into account. Contributions from sites beyond the latter can be efficiently accounted for by reciprocal space techniques like for example Ewald summation [73].

E_{vdW} accounts for Pauli repulsion at small and van der Waals attraction at large distances (see Section 2.2.2 for a discussion of the latter in the DFT context). It is given by:

$$E_{\text{vdW}} = \sum_i \sum_{j>i} 4\epsilon_{ij} \left[\left(\frac{\sigma}{\mathbf{r}_i - \mathbf{r}_j} \right)^{12} - \left(\frac{\sigma}{\mathbf{r}_i - \mathbf{r}_j} \right)^6 \right] \quad \text{if } |\mathbf{r}_i - \mathbf{r}_j| < r_{\text{c,vdW}} \quad (2.27)$$

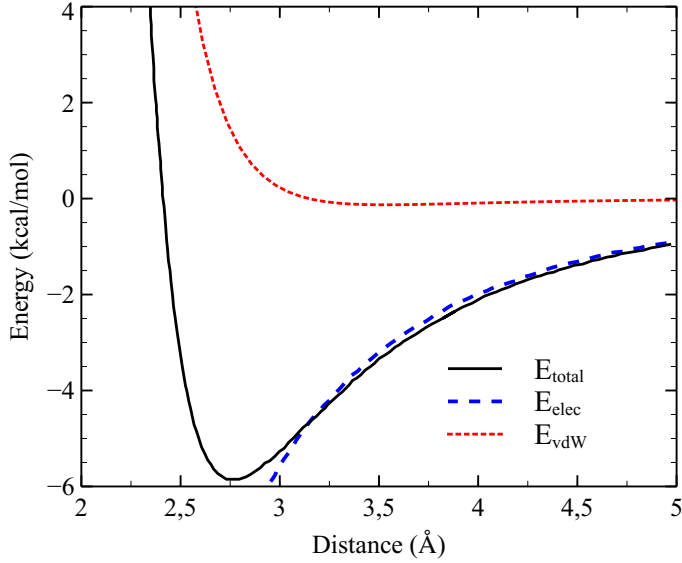


Figure 2.4: SPC/E electrostatic, van der Waals and total energy without intramolecular contribution in kcal mol^{-1} unit when two single water molecules oriented on their hydrogen-bond network.

Here $\sqrt[6]{2}\sigma$ is the equilibrium distance that yields $-\epsilon_{ij}$, i.e. the depth of the potential well. Again, for computational convenience, pairs at distances larger than the cut-off distance $r_{c,\text{vdW}}$ are usually neglected. Unlike for the Coulomb potential, the use of reciprocal space techniques is usually not necessary due the much faster decay of this 6-12 Lennard-Jones potential as a function of distance. The relevance of E_{vdW} for the bonding in different ice phases is analyzed in Chapter 3.

Table 2.1 compiles the parameters related to intermolecular interactions (q , ϵ , and σ) as introduced in Eqs. (2.26) and (2.27) above for each force field. **SPC/E** force field is a result of the re-parametrization of the original SPC [74] potential. Fig. 2.4 shows the SPC/E electrostatic energy (Eq. (2.26)), Lennard-Jones energy (Eq. (2.27)), and total energy without intra-molecular contribution when two single molecule are interacting on their hydrogen-bond side. **TIP3P** is very similar to the SPC/E model but with some minor modifications. One of the main changes is adding additional Lennard-Jones

Table 2.3: Geometry parameters for five fixed-charge water models used in this work. The r_{eq} , θ_{eq} , $r_{\text{O-M}}$ are illustrated in Fig. 2.3.

Water models	$r_{\text{eq}}(\text{\AA})$	$r_{\text{O-M}}(\text{\AA})$	$\theta_{\text{eq}}(\text{degree})$
SPC/E	1.000	n/a	109.5
TIP3P	0.957	n/a	104.5
TIP4P/2005	0.957	0.155	104.5
TIP4P/ice	0.957	0.158	104.5
q – TIP4P/F	0.942	0.155	107.4

parameters for the interactions between hydrogen-hydrogen and oxygen-hydrogen pairs, which are compiled in Table 2.2. In the four-site models **TIP4P/2005**, **TIP4P/ice**, **q-TIP4P/F**, the negative charge of the oxygen atom is located on an additional virtual site on the bisector of the H–O–H angle. Figure 2.3 illustrates this construction, and the model-specific distances from the oxygen atom $r_{\text{O-M}}$ are listed in Table 2.3. This way, the (continuous) electron density as obtained by a quantum mechanical description is mimicked better than with a three-site model. As evidenced by Table 2.1, the parameters related to intermolecular interactions are the same for TIP4P/2005 and q-TIP4P/F. They were obtained in a way to reproduce the phase-diagram of water and ice [49, 51]. TIP4P/ice results from a subsequent reparametrization to better match thermodynamic properties of ice. For example, TIP4P/ice can accurately describe the melting temperature of ice [50].

Intramolecular energy contributions in Eq. (2.25) have not been included in the original **SPC/E**, **TIP3P**, **TIP4P/2005**, **TIP4P/ice** models, i.e. they all describe rigid water molecules. In order to account for intramolecular vibrations, in this thesis I have adapted the common approach to add flexibility by employing simple harmonic potentials. Bond stretching is described by the harmonic potential

$$E_{\text{bond}} = \sum_i K_r [(r_{i,1} - r_{\text{eq}})^2 + (r_{i,2} - r_{\text{eq}})^2] \quad (2.28)$$

where $r_{i,1}$ and $r_{i,2}$ are the two O–H bond lengths of a single water molecule and r_{eq} is the model-specific equilibrium bond distance provided in Table 2.3. The same bond

force constant $K_r = 450.372 \text{ kcal mol}^{-1} \text{ \AA}^{-2}$ obtained from the measured Raman spectrum of liquid water [75] is employed for all of the aforementioned models. Equivalently, bending is described by

$$E_{\text{angle}} = \sum_i K_{\theta} (\theta_i - \theta_{\text{eq}})^2 \quad (2.29)$$

where θ_i is the H–O–H angle of each water molecule and θ_{eq} is the model-specific equilibrium bond angle given in Table 2.3. Again, the same bending force constant $K_{\theta} = 55 \text{ kcal mol}^{-1} \text{ rad}^{-2}$ obtained from experimental data is used for all the models mentioned above.

q-TIP4P/F is a flexible water model “by design” [51]. The bond stretching is accounted for based on a Morse potential

$$E_{\text{bond}} = \sum_i E_{\text{Morse}}(r_{i,1}) + E_{\text{Morse}}(r_{i,2}) \quad (2.30)$$

which is approximated according to

$$E_{\text{Morse}}(r) \approx D_r \left[\alpha_r^2 (r - r_{\text{eq}})^2 - \alpha_r^3 (r - r_{\text{eq}})^3 + \frac{7}{12} \alpha_r^4 (r - r_{\text{eq}})^4 \right] \quad (2.31)$$

Thanks to this anharmonic potential, q-TIP4P/F is able to capture the anharmonic and anticorrelation effects between the O–H bond and the hydrogen bonding. [51] The bending contribution to the intramolecular interactions is a harmonic potential like in Eq. (2.29) above. The corresponding parameters, $D_r = 116.09 \text{ kcal mol}^{-1}$ and $\alpha_r = 2.287 \text{ \AA}^{-1}$ as well as $K_{\theta} = 43.925 \text{ kcal mol}^{-1} \text{ rad}^{-2}$, respectively, are optimized such that path integral molecular dynamics simulations yield best possible agreement with the experimental absorption spectrum, diffusion constant, and vibrational properties of liquid water [51].

In this thesis, all of the fixed-charge pair potentials described in this section are employed via the LAMMPS MD package [76].

2.3.2 AMOEBA

Ren and Ponder [52] have developed the so-called *Atomic Multipole Optimized Energies for Biomolecular Applications* (AMOEBA), which includes polarization effects as well

Table 2.4: Parameters for the electrostatic interactions in the AMOEBA model. For the dipole and quadrupole moments of oxygen atoms, the H–O–H bisector is chosen as z -axis and the x -axis is in the plane defined by the H_2O molecule. For hydrogen, the z -axis is aligned along the O–H bond direction, and the x -axis lies in the molecular plane pointing towards the other H atom. In both cases, the y -axis is added such that right-handed coordinate systems are completed. Only non-zero components in these reference frames of both multipole moments are listed here.

	O	H
charge	$q_{\text{O}} = -0.426\,16\,e$	$q_{\text{H}} = +0.213\,08\,e$
dipole moment	$\mu_{\text{O},z} = +0.062\,51\,e\,a_0$	$\mu_{\text{H},x} = -0.101\,17\,e\,a_0$ $\mu_{\text{H},y} = -0.271\,71\,e\,a_0$
quadrupole moment	$\Theta_{\text{O},xx} = +0.175\,76\,e\,a_0^2$ $\Theta_{\text{O},yy} = -0.231\,60\,e\,a_0^2$ $\Theta_{\text{O},zz} = +0.055\,84\,e\,a_0^2$	$\Theta_{\text{H},xx} = +0.122\,83\,e\,a_0^2$ $\Theta_{\text{H},yy} = +0.089\,50\,e\,a_0^2$ $\Theta_{\text{H},zz} = -0.212\,33\,e\,a_0^2$ $\Theta_{\text{H},xy} = -0.069\,89\,e\,a_0^2$
polarizability	$\alpha_{\text{O}} = +0.920\,\text{\AA}^3$ $= +6.209 \cdot 4\pi\epsilon_0 a_0^3$	$\alpha_{\text{H}} = +0.539\,\text{\AA}^3$ $= +3.637 \cdot 4\pi\epsilon_0 a_0^3$

as intramolecular flexibility. In this thesis, the most recent parameterization for water given in 2014 by Laury *et al.* [77] (AMOEBA14) is used. The total energy expression of AMOEBA consists of the following terms:

$$E_{\text{total}} = \underbrace{E_{\text{elec}}^{\text{perm}} + E_{\text{elec}}^{\text{ind}} + E_{\text{vdW}}}_{\text{intermolecular}} + \underbrace{E_{\text{bond}} + E_{\text{angle}} + E_{\text{UB}}}_{\text{intramolecular}} \quad (2.32)$$

In contrast to the fixed-charge models described in the previous section, the electrostatic contribution takes both permanent ($E_{\text{elec}}^{\text{perm}}$) and induced ($E_{\text{elec}}^{\text{ind}}$) atomic multipole moments into account. The permanent electrostatic moments include monopoles, dipoles, and quadrupoles obtained from high-level electronic structure calculations for the hydrogen and oxygen atomic sites (see Table 2.4) enumerated by i , which are written conveniently in poly-tensorial notation $M_i = [q_i, \mu_{i,x}, \mu_{i,y}, \mu_{i,z}, \Theta_{i,xx}, \Theta_{i,xy}, \dots, \Theta_{i,zz}]^T$.

This allows to write

$$\begin{aligned}
 E_{\text{elec}}^{\text{perm}} = & \sum_{\substack{i,j \\ j>i}} q_i [T^{ij}, T_x^{ij}, T_y^{ij}, T_z^{ij}, T_{xx}^{ij}, T_{xy}^{ij}, \dots, T_{zz}^{ij}] M_j \\
 & + \sum_{\substack{i,j \\ j>i}} \sum_{\alpha} \mu_{i,\alpha} [T_{\alpha}^{ij}, T_{\alpha x}^{ij}, T_{\alpha y}^{ij}, T_{\alpha z}^{ij}, T_{\alpha xx}^{ij}, T_{\alpha xy}^{ij}, \dots, T_{\alpha zz}^{ij}] M_j \\
 & + \sum_{\substack{i,j \\ j>i}} \sum_{\alpha,\beta} \Theta_{i,\alpha\beta} [T_{\alpha\beta}^{ij}, T_{\alpha\beta x}^{ij}, T_{\alpha\beta y}^{ij}, T_{\alpha\beta z}^{ij}, T_{\alpha\beta xx}^{ij}, T_{\alpha\beta xy}^{ij}, \dots, T_{\alpha\beta zz}^{ij}] M_j,
 \end{aligned} \tag{2.33}$$

where the left parts of the “scalar-products” with M_j are the multipole interaction tensor elements in Stone’s [78] notation

$$T = \frac{1}{R} \tag{2.34}$$

$$T_{\alpha} = -\frac{R_{\alpha}}{R^3} \tag{2.35}$$

$$T_{\alpha\beta} = \frac{1}{R^5} [3R_{\alpha}R_{\beta} - R^2\delta_{\alpha\beta}] \tag{2.36}$$

$$T_{\alpha\beta\gamma} = \frac{1}{R^7} [15R_{\alpha}R_{\beta}R_{\gamma} - 3R^2(R_{\alpha}\delta_{\beta\gamma} + R_{\beta}\delta_{\alpha\gamma} + R_{\gamma}\delta_{\alpha\beta})] \tag{2.37}$$

$$T_{\alpha\beta\gamma\delta} = \frac{1}{R^9} [105R_{\alpha}R_{\beta}R_{\gamma}R_{\delta} \tag{2.38}$$

$$\begin{aligned}
 & - 15R^2(R_{\alpha}R_{\beta}\delta_{\gamma\delta} + R_{\alpha}R_{\gamma}\delta_{\beta\delta} + R_{\alpha}R_{\delta}\delta_{\beta\gamma} + R_{\beta}R_{\gamma}\delta_{\alpha\delta} + R_{\gamma}R_{\delta}\delta_{\alpha\beta}) \\
 & + 3R^4(\delta_{\alpha\beta}\delta_{\gamma\delta} + \delta_{\alpha\gamma}\delta_{\beta\delta} + \delta_{\alpha\delta}\delta_{\beta\gamma})]
 \end{aligned}$$

Here R denotes the distances between two sites and the site indicators i and j have been omitted for brevity.

Since AMOEBA includes polarizabilities of hydrogen and oxygen atoms as given in Table 2.4, a smeared charge distribution

$$\rho = \frac{3a}{4\pi} \exp(-au^3) \tag{2.39}$$

with dimensionless width parameter $a = 0.39$ is used in practice, where $u = R_{ij}(\alpha_i\alpha_j)^{-\frac{1}{6}}$.

This has originally been suggested by Thole [65, 79] in order to avoid a polarization catastrophe at short-distances. Consequently, the multipole interaction tensor elements T_{\dots} need to be replaced by their damped counterparts T_{\dots}^{D} , which include additional weights for the individual terms resulting from Eq. (2.39) but are otherwise of equivalent form [52].

Table 2.5: Parameters for the intermolecular vdW interactions between O–O, O–H and H–H pairs in the AMOEBA model.

	O–O	O–H	H–H
ϵ (kcal mol ⁻¹)	0.1512	0.0263	0.0105
R^0 (Å)	3.5791	3.2001	2.1176

Induced dipoles are calculated via the product of the polarizabilities and the electric field $\mathbf{F}^i = (F_x^i, F_y^i, F_z^i)$ at atomic site i

$$\begin{aligned} \mu_{i,\alpha}^{\text{ind}} = \alpha_i F_\alpha^i = \alpha_i \sum_{\{j\}} [T_\alpha^{ij}, T_{\alpha x}^{ij}, T_{\alpha y}^{ij}, T_{\alpha z}^{ij}, T_{\alpha xx}^{ij}, T_{\alpha xy}^{ij}, \dots, T_{\alpha zz}^{ij}] M_j \\ + \sum_{\{j'\}} [T_{\alpha x}^{ij'}, T_{\alpha y}^{ij'}, T_{\alpha z}^{ij'}] \cdot [\mu_{j',x}^{\text{ind}}, \mu_{j',y}^{\text{ind}}, \mu_{j',z}^{\text{ind}}]^T \end{aligned} \quad (2.40)$$

\mathbf{F}^i has two contributions. The first one results from the permanent multipole moments of all the water molecules surrounding the molecule containing the atomic site i (summation over $\{j\}$). The second one is from the induced dipoles of all other atomic sites except site i (summation over $\{j'\}$) Equation (2.40) is solved iteratively to yield a self-consistent solution for all the $\mu_{i,\alpha}^{\text{ind}}$ [52]. Substituting $\mu_{i,\alpha} + \mu_{i,\alpha}^{\text{ind}}$ for $\mu_{i,\alpha}$ in Eq. (2.33) yields additional terms which define the induced electrostatic energy contribution $E_{\text{elec}}^{\text{ind}}$.

Also in contrast to the fixed-charge models, the van der Waals intermolecular interactions (E_{vdw}) are based on the buffered 14-7 potential originally suggested by [80]. Dudek and Ponder [81] showed that when combined with quadrupole moments, this potential allows to better reproduce reference energetics obtained from *ab initio* calculations – in particular in the repulsive regime when two interacting sites approach each other. In the AMOEBA14 parametrization the buffered 14-7 potential is given by

$$E_{\text{vdw}}^{ij} = \epsilon_{ij} \left(\frac{1.07}{\rho_{ij} + 0.07} \right)^7 \left(\frac{1.12}{\rho_{ij}^7 + 0.12} - 2 \right) \quad , \quad (2.41)$$

where ϵ_{ij} is the minimum energy at distance R_{ij}^0 for the interacting sites i and j . $\rho_{ij} = \frac{R_{ij}}{R_{ij}^0}$ describes the rescaled distance between this pair. Like in TIP3P (see Section 2.3.1)

all oxygen and hydrogen atomic sites contribute, and the parameters are tabulated in Table 2.5.

The intramolecular interactions in Eq. (2.32) consist of bonding ($E_{\text{bond}} = \sum_{i,o} E_{\text{bond}}^{i,o}$), H–O–H bending ($E_{\text{angle}} = \sum_i E_{\text{angle}}^i$), and the Urey-Bradley ($E_{\text{UB}} = \sum_i E_{\text{UB}}^i$) contributions.

E_{bond} is based on an anharmonic potential, which includes deviations of the O–H bond length r from its equilibrium value $r_0 = 0.9565 \text{ \AA}$ up to fourth order

$$E_{\text{bond}}^{i,o} = K_{\text{r}}(r_{i,o} - r_0)^2 [1 - 2.55(r_{i,o} - r_0) - 3.793125(r_{i,o} - r_0)^2] \quad (2.42)$$

where $K_{\text{r}} = 556.82 \text{ kcal mol}^{-1} \text{ \AA}^{-2}$ is the stretching force constant i enumerates the water molecules and $o = 1, 2$ the O–H bonds in each molecule.

E_{angle} is described by

$$E_{\text{angle}}^i = K_{\theta} (\theta_i - \theta_0)^2 \eta(\theta_i, \theta_0) \quad (2.43)$$

where $K_{\theta} = 48.98 \text{ kcal mol}^{-1} \text{ rad}^{-2}$ is the bending force constant and

$$\begin{aligned} \eta(\theta, \theta_0) = & 1 - 0.014(\theta - \theta_0) + 5.6 \cdot 10^{-5}(\theta - \theta_0)^2 \\ & + 7.0 \cdot 10^{-7}(\theta - \theta_0)^3 + 2.2 \cdot 10^{-8}(\theta - \theta_0)^4 \end{aligned} \quad (2.44)$$

accounts for anharmonicity up to second order deviations from the equilibrium bond angle $\theta_0 = 107.91^\circ$.

E_{UB} is based on the simple harmonic expression

$$E_{\text{UB}}^i = K_l (l_i - l_0)^2 \quad (2.45)$$

where l_0 is the ideal length of virtual bond between the two hydrogens inside a single water molecule and $K_l = -7.6 \text{ kcal mol}^{-1} \text{ \AA}^{-2}$ is the force constant associated with this virtual bond.

The implementation of AMOEBA14 available in the TINKER package [53, 82] is used in this thesis.

Table 2.6: Parameters for the electrostatic interactions in the SCME model. The multipole moments are with respect to the center of mass of a H₂O molecule. The H–O–H bisector is chosen as the negative z -axis and the x -axis is in the plane defined by the H₂O molecule. The y -axis is added such that right-handed coordinate system is completed. Only non-zero components in this reference frames are listed here.

dipole moment ($e a_0$)		
$\mu_z = -0.729\,81$		
quadrupole moment ($e a_0^2$)		
$\Theta_{xx} = +1.955\,32$	$\Theta_{yy} = -1.858\,67$	$\Theta_{zz} = -0.096\,65$
octupole moment ($e a_0^3$)		
$\Omega_{xxy} = -3.271\,90$	$\Omega_{yyz} = +1.366\,06$	$\Omega_{zzz} = +1.905\,85$
hexadecapole moment ($e a_0^4$)		
$\Phi_{xxxx} = -0.949\,03$	$\Phi_{xxyy} = -3.384\,90$	$\Phi_{xxzz} = +4.333\,93$
$\Phi_{yyyy} = +4.098\,35$	$\Phi_{yyzz} = -0.713\,45$	$\Phi_{zzzz} = -3.620\,48$

2.3.3 SCME

The *Single Center Multipole Expansion* (SCME) is a water model that in its original formulation by Wikfeldt *et al.* [56] is based on rigid water molecules. Chapter 5 of this thesis describes an extension that adds flexibility and thus intramolecular energy contributions. Unlike AMOEBA, SCME employs permanent molecular multipole moments which are defined with respect to the center of mass of a H₂O molecule up to and including hexadecapoles. Like in AMOEBA, polarizability is accounted for, but also including induced molecular quadrupoles instead of only atomic dipoles. The total energy used by SCME

$$E_{\text{total}} = \underbrace{E_{\text{elec}}^{\text{perm+ind}} + E_{\text{disp}} + E_{\text{rep}}}_{\text{intermolecular}} \quad (2.46)$$

consists of permanent and induced electrostatic ($E_{\text{elec}}^{\text{perm+ind}}$), dispersion (E_{disp}) as well as short-range repulsion (E_{rep}) contributions.

Table 2.7: Same as Table 2.6, but for polarizabilities.

dipole–dipole polarizability ($4\pi\epsilon_0 a_0^3$)		
$\alpha_{xx} = +10.31146$	$\alpha_{yy} = +9.54890$	$\alpha_{zz} = +9.90656$
dipole–quadrupole polarizability ($4\pi\epsilon_0 a_0^4$)		
$A_{x,xz} = -8.42037$	$A_{y,yz} = -1.33400$	$A_{z,xx} = -2.91254$
$A_{z,yy} = +4.72407$	$A_{z,zz} = -1.81153$	
quadrupole–quadrupole polarizability ($4\pi\epsilon_0 a_0^5$)		
$C_{xx,xx} = +12.11907$	$C_{xx,yy} = -6.95326$	$C_{xx,zz} = -5.16582$
$C_{xy,xy} = +7.86225$	$C_{xz,xz} = +11.98862$	$C_{yy,yy} = +11.24741$
$C_{yy,zz} = -4.29415$	$C_{yz,yz} = -6.77226$	$C_{zz,zz} = +9.45997$

The electrostatic energy component is given by

$$E_{\text{elec}}^{\text{perm+ind}} = -\frac{1}{2} \sum_i \left(\mu_{\alpha}^i \tilde{F}_{\alpha}^i + \frac{1}{3} \Theta_{\alpha\beta}^i \tilde{F}_{\alpha\beta}^i + \frac{1}{15} \Omega_{\alpha\beta\gamma}^i \tilde{F}_{\alpha\beta\gamma}^i + \frac{1}{105} \Phi_{\alpha\beta\gamma\delta}^i \tilde{F}_{\alpha\beta\gamma\delta}^i \right), \quad (2.47)$$

where the prefactor of $\frac{1}{2}$ avoids double counting. For the remainder of this section, the Einstein convention is being employed, i.e. doubly occurring Cartesian components (x , y , z), which are denoted by Greek letters, are being summed over. The summation over different water molecules on the other hand is written out explicitly. Dipole, quadrupole, octopole and hexadecapole moments of a particular water molecule i are denoted by μ^i , Θ^i , Ω^i and Φ^i , respectively. The dipoles and quadrupoles are based on measured values [83, 84], whereas the higher multipoles have been obtained from quantum chemical calculations at the MP2 level [85]. They are all defined with respect to the center of mass of a H_2O molecule and compiled in Table 2.6. \tilde{F}_{α}^i is the α -component of the electric field, caused by all the other molecules except for molecule i and scaled by a switching function f^{sw} that depends on the center-of-mass distance r_{ij}^{com} between molecules i and j :

$$\tilde{F}_{\alpha}^i = \sum_{\substack{j \\ j \neq i}} f^{\text{sw}}(r_{ij}^{\text{com}}) F_{\alpha}^{ij} \quad (2.48)$$

F_{α}^{ij} is the multipole expansion of the electric field caused by water molecule j at the

center of mass of molecule i

$$F_{\alpha}^{ij} = T_{\alpha\beta}^{ij} \left(\mu_{\beta}^j + \Delta\mu_{\beta}^j \right) - \frac{1}{3} T_{\alpha\beta\gamma}^{ij} \left(\Theta_{\beta\gamma}^j + \Delta\Theta_{\beta\gamma}^j \right) + \frac{1}{15} T_{\alpha\beta\gamma\delta}^{ij} \Omega_{\beta\gamma\delta}^j - \frac{1}{105} T_{\alpha\beta\gamma\delta\epsilon}^{ij} \Phi_{\beta\gamma\delta\epsilon}^j, \quad (2.49)$$

where again Stone's T notation is used for the multipole interaction tensors as in the previous Section 2.3.2 (see Eqs. (2.34) to (2.38))⁴. The derivatives of this multipole expansion (with respect to Cartesian directions) are denoted by adding additional (Greek) indices, i.e. n additional indices for the n -th derivative:

$$F_{\alpha\dots\delta}^{ij} = \frac{\partial}{\partial r_{\beta}} \dots \frac{\partial}{\partial r_{\delta}} F_{\alpha}^{ij} \quad (2.50)$$

These derivatives also define $\tilde{F}_{\alpha\dots\delta}^i$ by substituting F_{α}^{ij} in Eq. (2.48) accordingly. The induced dipole ($\Delta\mu_{\alpha}^i$) and quadrupole ($\Delta\Theta_{\alpha\beta}^i$) moments of water molecule i are obtained self-consistently from

$$\Delta\mu_{\alpha}^i = \alpha_{\alpha\beta}^i \tilde{F}_{\beta}^i + \frac{1}{3} A_{\alpha,\beta\gamma}^i \tilde{F}_{\beta\gamma}^i \quad (2.51)$$

$$\Delta\Theta_{\alpha\beta}^i = A_{\gamma,\alpha\beta}^i \tilde{F}_{\gamma}^i + C_{\gamma\delta,\alpha\beta}^i \tilde{F}_{\gamma\delta}^i. \quad (2.52)$$

Here $\alpha_{\alpha\beta}^i$, $A_{\alpha,\beta\gamma}^i$ and $C_{\alpha\beta,\gamma\delta}^i$ are the corresponding dipole-dipole, dipole-quadrupole and quadrupole-quadrupole polarizabilities, respectively. Again, the values compiled in Table 2.7 are based on experiments ($\alpha_{\alpha\beta}$) and quantum chemical calculations ($A_{\alpha,\beta\gamma}$ and $C_{\alpha\beta,\gamma\delta}$) [56]. Equations (2.51) and (2.52) together with Eqs. (2.48) and (2.49) (and their multi-subscripts counterparts) are solved iteratively until all components of the electric field and its gradients as well as the induced multipole moments are converged up to certain threshold.⁵ f^{sw} smoothly switches off any electrostatic interactions at short ($r_{ij}^{\text{com}} < 5 \text{ \AA}$) and long ($r_{ij}^{\text{com}} > 11 \text{ \AA}$) distances.⁶ The overlap of electron densities associated with different water molecules at short distances leads to strong repulsion due to quantum mechanical effects (Pauli repulsion), which is captured by the E_{rep} term in Eq. (2.46) (*vide infra*). Like for the simplest water force fields described in Section 2.3.1, the long-range cut-off included in f^{sw} is an approximation that makes

⁴ $T_{\alpha\beta\gamma\delta\epsilon} = \nabla_{\epsilon} T_{\alpha\beta\gamma\delta}$

⁵ 10^{-7} a.u. in the original work of Wikfeldt *et al.* [56].

⁶See Wikfeldt *et al.* [56] for details on the definition of f^{sw} .

Table 2.8: Parameters for the dispersion and repulsion interactions in the SCME model. All values are giving in atomic units matching to Eqs. (2.53) to (2.57)

damping		
$\tau_d = 2.32837906$		
dispersion		
$C_6 = 46.44309964$	$C_8 = 1141.70326668$	$C_{10} = 33441.11892923$
repulsion		
$A = 1857.45898793$	$C = 1.68708507 \cdot 10^6$	
$b = 1.44350000$	$c = 1.83402715$	$d = 0.35278471$
$a_0 = +1.02508535 \cdot 10^{-1}$	$a_1 = -1.72461186 \cdot 10^{-4}$	$a_2 = +1.02195556 \cdot 10^{-7}$
$a_3 = -2.60877107 \cdot 10^{-11}$	$a_4 = +3.06054306 \cdot 10^{-15}$	$a_5 = -1.32901339 \cdot 10^{-19}$

the evaluation of the SCME computationally convenient, in particular when dealing with infinitely extended (bulk) ice structures.

The dispersion and repulsion energies are obtained by only considering the oxygen-oxygen distances r_{ij}^{OO} between different water molecules. The dispersion energy is given by

$$E_{\text{disp}} = - \sum_{\substack{i,j \\ j>i}} \left[f_6^{\text{TT}}(r_{ij}^{\text{OO}}) \frac{C_6}{(r_{ij}^{\text{OO}})^6} + f_8^{\text{TT}}(r_{ij}^{\text{OO}}) \frac{C_8}{(r_{ij}^{\text{OO}})^8} + f_{10}^{\text{TT}}(r_{ij}^{\text{OO}}) \frac{C_{10}}{(r_{ij}^{\text{OO}})^{10}} \right] , \quad (2.53)$$

with coefficients C_n ($n \in \{6, 8, 10\}$) compiled in Table 2.8 and the Tang-Toennies [86] damping function

$$f_{2n}^{\text{TT}}(r_{ij}^{\text{OO}}) = 1 - \exp(-\tau_d r_{ij}^{\text{OO}}) \sum_{k=0}^{2n} \frac{(\tau_d r_{ij}^{\text{OO}})^k}{k!} , \quad (2.54)$$

The damping factor τ_d is physically motivated by the inverse decay length of the charge density in a water monomer (see Table 2.8).

The original formulation of SCME [56] employs a modified Born-Mayer potential for

the repulsion energy

$$E_{\text{rep}} = A \sum_{\substack{i,j \\ j>i}} [1 + B(\rho_j) + B(\rho_i)] (r_{ij}^{\text{OO}})^{-b} \exp(-c \cdot r_{ij}^{\text{OO}}) \quad , \quad (2.55)$$

where

$$B(\rho_i) = \begin{cases} 0 & \text{if } \rho_i \leq 1600 \\ \sum_{n=0}^5 a_n \rho_i^n & \text{if } 1600 < \rho_i < 8000 \\ 0.0875 & \text{if } 8000 \leq \rho_i \quad . \end{cases} \quad (2.56)$$

ρ_i is the superposition of the electron densities of all water molecules surrounding a given molecule i

$$\rho_i = \sum_{\substack{j \\ j \neq i}} \exp(-d \cdot r_{ij}^{\text{OO}}) \frac{C}{(r_{ij}^{\text{OO}})^3} \quad (2.57)$$

The eleven parameters A , C , a_n ($n = 0, 1, \dots, 5$), b , c and d compiled in Table 2.8 have been obtained by Wikfeldt *et al.* [56] via fitting to quantum chemical calculations for small water clusters (consisting of up to six H_2O molecules, at the MP2 level). Finally, in the extension of SCME for flexible water molecules that is presented in Chapter 5 of this thesis, the Born-Mayer term needed to be substituted by a different expression.

2.3.4 MB-pol

The MB-pol potential has been developed by Paesani and coworkers [54, 55, 87]. Compared to the AMOEBA and SCME models described in the two previous subsections, MB-pol relies on a much larger number of parameters, which are consequently obtained by fitting to accurate quantum chemical calculations at the CCSD(T) level [88, 89]. Therefore, in the interest of conciseness and unlike in the previous sections, not all analytical expressions are provided here. Instead, only the essential concepts are explained and compared to AMOEBA and SCME wherever relevant.

Like all water force fields described in the preceding sections, MB-pol is based on the notion that interactions between water molecules can be separated into different contributions of varying relevance at different separation distances [78]. The electron

densities of individual molecules hardly overlap in the long-range part, which is therefore dominated by dispersion and electrostatic interactions. MB-pol (only) considers pair-wise contributions to the dispersion interactions – analogous to the fixed-charge force fields, AMOEBA and SCME. For the electrostatic interactions, MB-pol employs a Thole-type model (TTM) [65], which is based on (smeared) atomic charges and includes polarization and thus many-body effects at the long range similar to AMOEBA but rather different from SCME. Building on earlier work resulting in the so-called HBB2-pol force field [88, 89], MB-pol explicitly accounts for quantum mechanical many-body effects involving up to three water molecules at the short range. This is a unique feature compared to all other force fields considered so far. Going beyond three-body terms has not been found to be necessary for achieving chemical accuracy [90–93]. Since no “simple” analytical form is known for the concomitant short-range two- and three-body potentials, these are heavily parametrised based on a large dataset generated by the aforementioned quantum chemical calculations.

Consequently, the total energy of the MB-pol model

$$E_{\text{total}} = \underbrace{E_{\text{elec}} + E_{\text{short}}^{2\text{B}} + E_{\text{short}}^{3\text{B}}}_{\text{intermolecular} + \text{intramolecular}} + \underbrace{E_{\text{disp}}}_{\text{intermolecular}} + \underbrace{E^{1\text{B}}}_{\text{intramolecular}} \quad (2.58)$$

is decomposed into permanent and induced electrostatic (E_{elec}), dispersion (E_{disp}), short-range two-body ($E_{\text{short}}^{2\text{B}}$) and three-body ($E_{\text{short}}^{3\text{B}}$) intermolecular contributions.

The intramolecular contribution that accounts for the flexibility of a single water molecule (one-body term $E^{1\text{B}}$) is taken “as is” from Partridge and Schwenke [94].

The electrostatic energy in MB-pol is based on the so-called TTM4-F model as originally constructed by Burnham *et al.* [62], Burnham *et al.* [95], and Burnham and Xantheas [96]. This bares similarities to the AMOEBA model presented in 2.3.2, i.e., it accounts for permanent and induced electrostatic intermolecular interactions

$$E_{\text{elec}} = E_{\text{TTM4-F}} = E_{\text{TTM4-F}}^{\text{perm}} + E_{\text{TTM4-F}}^{\text{ind}} \quad , \quad (2.59)$$

with smeared charges and induced dipoles located on the H and shifted slightly away from O *atomic sites* of a H₂O molecule. Only charge-charge, charge-dipole and dipole-

dipole interactions (the latter also intramolecular) are included in Eq. (2.59), i.e., unlike in SCME (higher order) molecular multipole moments are not considered explicitly. The dependence of the atomic charges on the geometry of a single water molecule is obtained from the dipole moment surface (DMS) by Partridge and Schwenke [94]. Babin *et al.* [54] use the same values for the polarizabilities and charge (Thole) smearing parameters as given by Burnham *et al.* [62], except for a reduced dipole-dipole interaction related smearing width.⁷

The expression for the dispersion energy

$$E_{\text{disp}} = \sum_{a>b} V_{6,8}(\mathbf{x}_a, \mathbf{x}_b) = - \sum_{a>b} \sum_{\substack{i \in a \\ j \in b}} \left[f_6^{\text{TT}}(\delta_6^{ij} r_{ij}) \frac{C_6^{ij}}{r_{ij}^6} + f_8^{\text{TT}}(\delta_8^{ij} r_{ij}) \frac{C_8^{ij}}{r_{ij}^8} \right] \quad (2.60)$$

is similar to SCME. \mathbf{x}_a and \mathbf{x}_b denote all the atomic positions belonging to water molecules a and b . $V_{6,8}$ obviously contributes to two-body interactions at the long range as it includes summation over all atomic sites i and j in two different H_2O molecules a and b , respectively, with concomitant distances r_{ij} only considered up to r_{ij}^{-8} . f_6^{TT} is the Tang-Toennies damping function already given by Eq. (2.54). The parameters $\delta_{6,8}^{\text{HH}}$, $\delta_{6,8}^{\text{OH}}$, $\delta_{6,8}^{\text{OO}}$ and $C_{6,8}^{\text{HH}}$, $C_{6,8}^{\text{OH}}$, $C_{6,8}^{\text{OO}}$ for Eq. (2.60) are obtained from fitting to the results from the aforementioned quantum chemical calculations.

The short-range two-body energy contribution

$$E_{\text{short}}^{2\text{B}} = \sum_{a>b} V_{\text{short}}^{2\text{B}}(\mathbf{x}_a, \mathbf{x}_b) \quad (2.61)$$

is based on the short-range two-body potential

$$V_{\text{short}}^{2\text{B}}(\mathbf{x}_a, \mathbf{x}_b) = s^{2\text{B}}(r_{\text{O}_a\text{O}_b}) V_{\text{poly}}^{2\text{B}}(\xi_1^{2\text{B}}, \dots, \xi_{31}^{2\text{B}}) \quad , \quad (2.62)$$

which involves all the atomic positions \mathbf{x}_a and \mathbf{x}_b of two different water molecules plus two oxygen lone-pair sites each. These two additional sites L_1 and L_2 are schematically depicted for one water molecule in Fig. 2.5. Babin *et al.* [54] have represented $V_{\text{poly}}^{2\text{B}}(\xi_1^{2\text{B}}, \dots, \xi_{31}^{2\text{B}})$ by permutationally invariant polynomials up to fourth degree in the variables $\xi_i^{2\text{B}}$, which are based on the six intramolecular distances ($\xi_i^{2\text{B}} = \exp(-k_i^{2\text{B}} d_i)$,

⁷It has been set identical to its intermolecular counterpart.

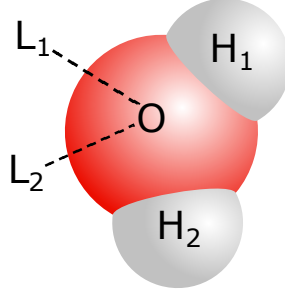


Figure 2.5: Oxygen lone-pair sites L_1 and L_2 used in the short-range two-body potential V_{short}^{2B} (see Eq. (2.62)).

$i = 1, \dots, 6$), nine intermolecular Coulomb-like terms ($\xi_i^{2B} = \exp(-k_i^{2B} d_i)/d_i$, $i = 7, \dots, 15$) and the sixteen intermolecular distances involving the aforementioned oxygen lone-pair sites ($\xi_i^{2B} = \exp(-k_i^{2B} d_i)$, $i = 16, \dots, 31$). Here d_i denote actual distances between sites and k_i^{2B} ($i = 1, \dots, 31$) are fit parameters, which are obtained from the aforementioned quantum chemical calculations after (long-range) two-body contributions resulting from E_{elec} and E_{disp} have been subtracted. s^{2B} smoothly switches on V_{short}^{2B} in a range $5.5 \text{ \AA} < r_{O_a O_b} < 7.5 \text{ \AA}$ based on the distance $r_{O_a O_b}$ between the two oxygen atoms of the molecules a and b .

The short-range three-body energy contribution

$$E_{3B}^{\text{short}} = \sum_{a>b>c} V_{\text{short}}^{3B}(\mathbf{x}_a, \mathbf{x}_b, \mathbf{x}_c) \quad (2.63)$$

is based on the short-range three-body potential

$$V_{\text{short}}^{3B}(\mathbf{x}_a, \mathbf{x}_b, \mathbf{x}_c) = [s^{3B}(t_{ab})s^{3B}(t_{ac}) + s^{3B}(t_{ab})s^{3B}(t_{bc}) + s^{3B}(t_{ac})s^{3B}(t_{bc})] V_{\text{poly}}^{3B}(\xi_1^{3B}, \dots, \xi_{36}^{3B}), \quad (2.64)$$

involving the atomic positions of three different water molecules ($\mathbf{x}_a, \mathbf{x}_b, \mathbf{x}_c$). Babin *et al.* [55] have constructed V_{poly}^{3B} in similar to V_{poly}^{2B} by using permutationally invariant polynomials up to fourth degree in the variables ξ_i^{3B} . All monomials contributing to V_{poly}^{3B} are based on the 9 intramolecular distances ($\xi_i^{3B} = \exp(-k_i^{3B} d_i)$, $i = 1, \dots, 9$

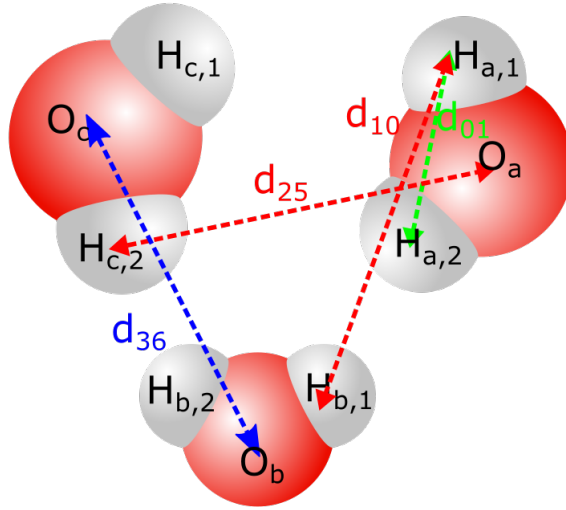


Figure 2.6: Schematic representation of four particular distances d_{10} , d_{25} (both red), d_{36} (blue), and d_{01} (green) between atoms of the three depicted H_2O molecules a , b and c . The corresponding variables $\xi_i^{3\text{B}} = \exp(-k_i^{3\text{B}} d_i)$, $i \in \{1, 10, 25, 36\}$ yield monomials that contribute to $V_{\text{poly}}^{3\text{B}}$ (see Eq. (2.64)), i.e., $V_{\text{poly}}^{3\text{B}} = \dots + \xi_{10}\xi_{25} + \xi_{10}\xi_{25}\xi_{36} + \xi_{10}\xi_{25}\xi_{36}\xi_{01} + \dots$

– 3 pairs each per H_2O) and the 27 intermolecular distances ($\xi_i^{3\text{B}} = \exp(-k_i^{3\text{B}}d_i)$, $i = 10, \dots, 36$ – 3 pairs of molecules with 9 distance pairs each). This is further illustrated in Fig. 2.6. $k_i^{3\text{B}}$ ($i = 1, \dots, 36$) are fit parameters, which are obtained from the aforementioned quantum chemical calculations after (long-range) three-body contributions resulting from $E_{\text{TTM4-F}}^{\text{ind}}$ (see Eq. (2.59)) has been subtracted. $s^{3\text{B}}(t_{ab}) = s^{3\text{B}}(t_{ab}(r_{\text{O}_a\text{O}_b}))$ smoothly deactivates $V_{\text{short}}^{3\text{B}}$ for oxygen-oxygen distances $r_{\text{O}_a\text{O}_b} > 4.5 \text{ \AA}$ between the two H_2O molecules a and b .

Throughout this thesis, the original parameterisation and implementation of MB-pol developed by the Paesani group [54, 55, 87] is used.

2.4 Phonons

This section first introduces the harmonic approximation for the total energy of a crystalline solid. Solving the lattice dynamical equations then yields uncoupled vibrational modes (phonons) characterised by frequencies and displacement eigenvectors as a function of phonon wave vector. The (harmonic) phonon system is then conveniently characterised by its density of states and subject to statistical treatment in the canonical ensemble to describe non-zero temperatures. Afterwards, the quasi-harmonic approximation is introduced in order to account for thermal expansion. The section concludes with computational aspects focussing on the finite-displacement technique that is used throughout in this thesis.

2.4.1 Harmonic Approximation

Not considering any defects, the total internal energy E of a perfect crystal with equilibrium lattice vectors $\mathbf{R}^{\text{eq}} = (\mathbf{a}^{\text{eq}}, \mathbf{b}^{\text{eq}}, \mathbf{c}^{\text{eq}})^{\text{T}}$ ⁸ can be expanded around the equilibrium positions of the atoms. Terminating this expansion after the second order is called the

⁸i.e., those which yield the lowest total energy of the crystal for atoms in their equilibrium positions

harmonic approximation

$$\begin{aligned}
 E^{\text{harm}}(\mathbf{u}; \mathbf{R}^{\text{eq}}) &= E_0(\mathbf{R}^{\text{eq}}) + E_1(\mathbf{u}; \mathbf{R}^{\text{eq}}) + E_2(\mathbf{u}; \mathbf{R}^{\text{eq}}) \\
 &= E(\mathbf{u} = \mathbf{0}; \mathbf{R}^{\text{eq}}) + \sum_{n,i,\alpha} \underbrace{\left. \frac{\partial E}{\partial u_{n,i,\alpha}} \right|_{\mathbf{u}=\mathbf{0}}}_{=-F_{n,i,\alpha}(\mathbf{u}=\mathbf{0}; \mathbf{R}^{\text{eq}})=0} u_{n,i,\alpha} \\
 &\quad + \frac{1}{2} \sum_{n,i,\alpha} \sum_{n',i',\alpha'} \left. \frac{\partial^2 E}{\partial u_{n,i,\alpha} \partial u_{n',i',\alpha'}} \right|_{\mathbf{u}=\mathbf{0}} u_{n,i,\alpha} u_{n',i',\alpha'} \\
 &= E^{\text{eq}} + \frac{1}{2} \sum_{n,i,\alpha} \sum_{n',i',\alpha'} \Phi_{n,i,\alpha}^{n',i',\alpha'}(\mathbf{u} = \mathbf{0}; \mathbf{R}^{\text{eq}}) u_{n,i,\alpha} u_{n',i',\alpha'} \quad .
 \end{aligned} \tag{2.65}$$

Here the summations extend over the infinitely many unit cells of the crystal (n'), the N_{cell} atoms within a unit cell ($i' = 1, \dots, N_{\text{cell}}$) and their Cartesian coordinates ($\alpha' = 1, 2, 3$). $u_{n,i,\alpha}$ denotes the displacement along Cartesian direction α of atom i in a replica n . When no atoms are displaced ($\mathbf{u} = \mathbf{0}$), only the zeroth order term E_0 contributes and thus defines the (constant) equilibrium energy $E^{\text{eq}} = E(\mathbf{u} = \mathbf{0}; \mathbf{R}^{\text{eq}})$ of the crystal. In the following, E^{eq} is chosen as energy zero such that it does not need to be explicitly denoted. The first order term E_1 vanishes because all force components $F_{n,i,\alpha}(\mathbf{u} = \mathbf{0}; \mathbf{R}^{\text{eq}})$ acting on atom i in a cell n vanish by definition when the atoms are sitting at their equilibrium positions. This only leaves the second order (or so-called harmonic) term E_2 , which is fully defined by the force constants $\Phi_{n,i,\alpha}^{n',i',\alpha'}(\mathbf{u} = \mathbf{0}; \mathbf{R}^{\text{eq}})$ of the material. The equilibrium lattice vectors are explicitly denoted in Eq. (2.65) in preparation of the so-called quasi-harmonic approximation, which is introduced below in Section 2.4.4.

2.4.2 Lattice Dynamics

According to Eq. (2.65), the forces in the harmonic approximation are given by

$$F_{n,i,\alpha}^{\text{harm}} = - \frac{\partial E^{\text{harm}}}{\partial u_{n,i,\alpha}} = - \sum_{n',i',\alpha'} \Phi_{n,i,\alpha}^{n',i',\alpha'} u_{n',i',\alpha'} \quad , \tag{2.66}$$

resulting in the following Newtonian equations of motion

$$- \sum_{n',i',\alpha'} \Phi_{n,i,\alpha}^{n',i',\alpha'} u_{n',i',\alpha'} = M_i \frac{\partial^2 u_{n,i,\alpha}}{\partial t^2} \tag{2.67}$$

for each atom with mass M_i in the crystal. In principal, the force constant matrix $\Phi_{n,i,\alpha}^{n',i',\alpha'}$ couples the motion of all atoms in the crystal, with the strength of the couplings typically decreasing with increasing distance from a reference atom. Equation (2.67) can be solved by the following plane-wave-like ansatz for the displacement patterns

$$u_{n,i,\alpha}(\mathbf{q}, t) = \frac{A}{\sqrt{M_i}} \tilde{u}_{i,\alpha}(\mathbf{q}) \exp(i(\mathbf{q} \cdot \mathbf{R}_n - \omega(\mathbf{q})t)) \quad , \quad (2.68)$$

where the linear combination of lattice vectors $\mathbf{R}_n = n_a(n)\mathbf{a}^{\text{eq}} + n_b(n)\mathbf{b}^{\text{eq}} + n_c(n)\mathbf{c}^{\text{eq}}$ describes the offset of replica cell n from the (reference) unit cell. The wave vector \mathbf{q} characterizes the periodicity of such a displacement pattern with (angular) frequency $\omega(\mathbf{q})$. All possible displacement patterns can be described by wave vectors that are contained in the (first) Brillouin zone of the crystal (Wigner-Seitz cell of the reciprocal lattice). The unit vector $\tilde{u}_{i,\alpha}(\mathbf{q})$ describes the displacements of each atom in a unit cell and A is the amplitude of the resulting displacement pattern. Substitution of this ansatz into Eq. (2.67)

$$\omega^2 \tilde{u}_{i,\alpha}(\mathbf{q}) = \sum_{i',\alpha'} \sum_n \frac{1}{\sqrt{M_i M_{i'}}} \Phi_{n,i,\alpha}^{n',i',\alpha'} \tilde{u}_{i',\alpha'}(\mathbf{q}) \exp(i\mathbf{q} \cdot \mathbf{R}_n) \quad (2.69)$$

then allows to determine the frequencies $\omega(\mathbf{q})$ and directions of atomic displacements $\tilde{u}_{i,\alpha}(\mathbf{q})$ that are described by Eq. (2.68). Introducing the so-called dynamical matrix

$$D_{i,\alpha}^{i',\alpha'}(\mathbf{q}) = \sum_n \frac{1}{\sqrt{M_i M_{i'}}} \Phi_{n,i,\alpha}^{n',i',\alpha'} \exp(i\mathbf{q} \cdot \mathbf{R}_n) \quad , \quad (2.70)$$

Eq. (2.69) constitutes an eigenvalue problem for this $3j \times 3j$ dimensional matrix

$$\omega^2 \tilde{u}_{i,\alpha}(\mathbf{q}) = \sum_{i',\alpha'} D_{i,\alpha}^{i',\alpha'}(\mathbf{q}) \tilde{u}_{i',\alpha'}(\mathbf{q}) \quad . \quad (2.71)$$

Since $D(\mathbf{q})$ is Hermitian it can be diagonalized and the $3N_{\text{cell}}$ different eigenvectors and concomitant eigenvalues provide solutions for the displacements $\nu_b(\mathbf{q})$ and their concomitant frequencies $\omega_b(\mathbf{q})$, respectively, where $b = 1, \dots, 3N_{\text{cell}}$. Each solution it describes is a particular phonon state. At each \mathbf{q} -point these states are enumerated by the band index b , and the total amount of bands is determined by the amount of atoms in the primitive unit cell. In practice, solutions for a discrete set of \mathbf{q} -points sampling the Brillouin zone are being calculated.

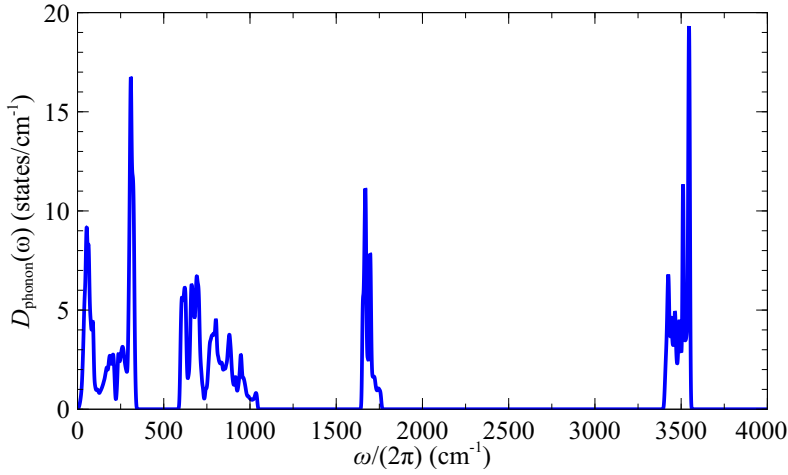


Figure 2.7: Phonon DOS of ice-Ih calculated with the q-TIP4P/F model. Five different sets of phonon modes are clearly separated by their respective frequency ranges, namely hydrogen-bond bending (0 to 150 cm⁻¹), hydrogen-bond stretching (150 to 500 cm⁻¹), librational (500 to 1500 cm⁻¹), H–O–H bending (1500 to 2000 cm⁻¹), and O–H stretching (2000 to 4000 cm⁻¹).

It is convenient to characterize the phonon spectrum by the amount of states per frequency and unit cell, which is expressed by the phonon density of states (DOS)

$$D_{\text{phonon}}(\omega) = \frac{V}{(2\pi)^3} \sum_b \int_{\text{BZ}} d\mathbf{q} \delta(\omega - \omega_b(\mathbf{q})) \quad . \quad (2.72)$$

V is the volume of the unit cell and the integration extends over the (first) Brillouin zone (BZ). Figure 2.7 shows D_{phonon} for the most common crystalline ice phase (ice Ih) as calculated with a particular fixed-charged force field (see Section 2.3.1).

2.4.3 Vibrational Free Energy

The canonical partition function of the phonon system Z_{phonon} at temperature T is obtained by summing over all phonon states, which are enumerated by their phonon wavevectors (\mathbf{q} in the first Brillouin zone), band indexes (b) and the amount of vibrational quanta (m) that are “stored” in each state. According to the harmonic ap-

proximation there is no coupling between the different phonon modes. Consequently, the vibrational partition function factorizes into the contribution of individual phonon (harmonic) oscillators

$$Z_{\text{phonon}}(T) = \prod_{\mathbf{q},b} \sum_{m=0}^{\infty} \exp\left(-\frac{\hbar\omega_b(\mathbf{q})(m + \frac{1}{2})}{k_B T}\right) = \prod_{\mathbf{q},b} \frac{\exp(-\frac{\hbar\omega_b(\mathbf{q})}{2k_B T})}{1 - \exp(-\frac{\hbar\omega_b(\mathbf{q})}{k_B T})} \quad , \quad (2.73)$$

where k_B is the Boltzmann constant. This yields the phonon contribution to the Helmholtz free energy

$$\begin{aligned} F_{\text{phonon}}(T) &= -k_B T \ln(Z_{\text{phonon}}) \\ &= \underbrace{\frac{1}{2} \sum_{\mathbf{q},b} \hbar\omega_b(\mathbf{q})}_{\text{ZPE}} + k_B T \sum_{\mathbf{q},b} \ln \left[1 - \exp\left(\frac{-\hbar\omega_b(\mathbf{q})}{k_B T}\right) \right] \end{aligned} \quad (2.74)$$

The first term is the zero-point energy (ZPE), which will be the focus of Chapters 3 and 6. The partition function also yields the vibrational entropy of the phonon system

$$S_{\text{phonon}}(T) = \frac{1}{T} \sum_{\mathbf{q},b} \frac{\hbar\omega_b(\mathbf{q})}{\exp\left(\frac{-\hbar\omega_b(\mathbf{q})}{k_B T}\right) - 1} - k_B \sum_{\mathbf{q},b} \ln \left[1 - \exp\left(\frac{-\hbar\omega_b(\mathbf{q})}{k_B T}\right) \right] \quad . \quad (2.75)$$

The internal energy of the phonon system at finite temperature thus becomes

$$\begin{aligned} F_{\text{vib}}(T) &= F_{\text{phonon}}(T) + T S_{\text{phonon}}(T) \\ &= \frac{1}{2} \sum_{\mathbf{q},b} \hbar\omega_b(\mathbf{q}) + \sum_{\mathbf{q},b} \frac{\hbar\omega_b(\mathbf{q})}{\exp\left(\frac{-\hbar\omega_b(\mathbf{q})}{k_B T}\right) - 1} \quad , \end{aligned} \quad (2.76)$$

which at $T = 0$ K is equal to the ZPE introduced in Eq. (2.74).

2.4.4 Quasi-Harmonic Approximation

Thermal expansion is not described by the harmonic approximation, which can be rationalized by the fact that the expectation value for the position of each phonon oscillator is zero. That means that even at higher temperatures the vibrational free energy given by Eq. (2.74) still describes a crystal where the atoms are (on average) at the same equilibrium positions as for zero temperature. Substituting the equilibrium

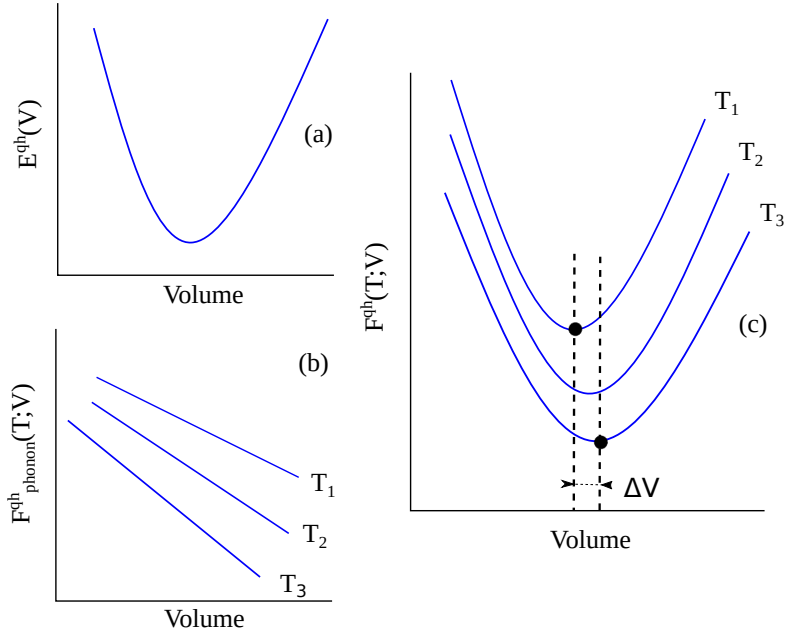


Figure 2.8: Schematic representation of (a) the internal energy $E^{\text{qh}}(V)$ together with (b) the volume dependence of the phonon contribution to the Helmholtz free energy $F^{\text{qh}}_{\text{phonon}}(T;V)$ as well as (c) the total Helmholtz free energy $F^{\text{qh}}(T;V) = E^{\text{qh}}(V) + F^{\text{qh}}_{\text{phonon}}(T;V)$ according to the quasi-harmonic approximation. $F^{\text{qh}}_{\text{phonon}}(T;V)$ and $F^{\text{qh}}(T;V)$ are shown for three different temperatures $T_3 > T_2 > T_1$. $\Delta V = V_0(T_3) - V_0(T_1)$ denotes the volume expansion as further detailed in the text.

lattice vectors \mathbf{R}^{eq} by general lattice vectors $\mathbf{R} = (\mathbf{a}, \mathbf{b}, \mathbf{c})$ in Eq. (2.65) leads to lattice-vector-dependent force constants $\Phi_{n,i,\alpha}^{n',i',\alpha'}(\mathbf{u} = \mathbf{0}; \mathbf{R})$. Consequently, the internal energy E^{harm} can be written as a function of the unit cell volume $V(\mathbf{R}) = \mathbf{a} \cdot (\mathbf{b} \times \mathbf{c})$

$$E^{\text{qh}}(\mathbf{u}; V(\mathbf{R})) = E^{\text{harm}}(\mathbf{u}; \mathbf{R}) \quad (2.77)$$

such that

$$\min_V E^{\text{qh}}(\mathbf{u} = \mathbf{0}; V(\mathbf{R})) = E^{\text{harm}}(\mathbf{u} = \mathbf{0}; V^{\text{eq}}) = E^{\text{eq}} \quad , \quad (2.78)$$

with $V^{\text{eq}} = V(\mathbf{R}^{\text{eq}})$. This is called quasi-harmonic approximation (QHA). $E^{\text{qh}}(V)$ is schematically depicted in Fig. 2.8 (a).⁹ Obviously, $E^{\text{qh}}(V)$ alone still does not describe any thermal expansion.

Together with the force constants also the dynamical matrix and thus the solutions of the lattice dynamical equations (see Section 2.4.2) depend on V , i.e., in particular $\omega = \omega(\mathbf{q}; V)$. Substitution into the expressions introduced in Section 2.4.3 results in a volume dependent phonon contribution to the Helmholtz free energy $F_{\text{phonon}}^{\text{qh}}(T; V)$, which is shown schematically in Fig. 2.8 (b) for three different temperatures. Accounting for the internal and phonon contributions according to the QHA, the total Helmholtz free energy becomes

$$F^{\text{qh}}(T; V) = E^{\text{qh}}(V) + F_{\text{phonon}}^{\text{qh}}(T; V) \quad , \quad (2.79)$$

which is depicted in panel (c) of Fig. 2.8. $F_{\text{phonon}}^{\text{qh}}(T; V)$ leads to a temperature-dependent shift of the minimum of $E^{\text{qh}}(V)$. The equilibrium volume is obtained from $\min_V F^{\text{qh}}(T; V) = F(T; V_0(T))$ and changes according to $\Delta V^{\text{eq}}(T) = V_0(T) - V^{\text{eq}}$ compared to the $T = 0$ K. This means that the canonical ensemble given by the QHA can effectively describe volume expansion due to increasing temperature.

2.4.5 Computational Aspects

The essential computational challenge for phonon calculations is to obtain the force constants elements $\Phi_{n,i,\alpha}^{n',i',\alpha'}$ (see Eq. (2.65)), because this defines the computationally

⁹Assuming that for a given set of lattice vectors \mathbf{R} only relaxed atomic coordinates are being considered (i.e., $\mathbf{u} = \mathbf{0}$), the dependence on the displacements and lattice vectors are no longer explicitly denoted here and in the following.

rather simple eigenvalue given in Eq. (2.71) the solution of which then yields phonon frequencies and displacements vectors and thus all thermodynamic properties describe in Section 2.4.3. Unfortunately, in particular for electronic structure calculations in periodic boundary conditions, second derivatives of the total internal energy with respect to atomic (displacement) coordinates are usually not as “easily” available as the corresponding first derivatives (forces). Density-functional perturbation theory (DFPT) [97] has been formulated for that reason, but (obviously) cannot be combined with force fields. To treat both DFT and force fields at equal footing, all phonon calculations in this thesis are based on the so-called finite displacement technique [98, 99]. The only systematic drawback of this technique is that it cannot account for the splitting of longitudinal and transversal optical phonon modes at the Γ -point (known as LO-TO splitting), which however is negligible for properties that are integrated over the entire Brillouin zone.

The basic idea behind the finite-displacement technique is to evaluate the elements of the force constants matrix by using finite differences of the respective force components

$$\Phi_{n,i,\alpha}^{n',i',\alpha'} \approx \frac{F_{n',i',\alpha'}(+u_{n,i,\alpha}) - F_{n',i',\alpha'}(-u_{n,i,\alpha})}{2\Delta}. \quad (2.80)$$

Here $F_{n',i',\alpha'}(\pm u_{n,i,\alpha})$ is the force component α' acting on atom i' in unit cell n' of the crystal after only the single atom i in unit cell n has been displaced by $\pm u_{n,i,\alpha} = \pm\Delta$ along the Cartesian direction α while all other atoms remain in their equilibrium positions.¹⁰ Of course, the latter is problematic when forces are calculated within periodic boundary conditions, because this always results in the displacement of infinitely many atoms. Using a supercell of the primitive unit cell allows to displace at least a certain amount of atom pairs $((n', i'), (n, i))$ with $(n', i') \neq (n, i)$ independently from each other. These pairs can be up to a certain maximum distance apart, which is inherent to the chosen supercell. Assuming that $\Phi_{n,i,\alpha}^{n',i',\alpha'} = 0$ for atom pairs at even larger distances then allows to obtain a reasonable approximation for the force constant matrix if the supercell is indeed large enough. This can and needs to be tested in practice by

¹⁰For a given set of lattice vectors.

checking the convergence of calculated phononic properties with respect to the supercell. The dynamical matrix resulting from the former is then exact for phonons with wavevectors \mathbf{q} that are commensurate with the supercell, and Eq. (2.69) describes a Fourier interpolation for all other wave vectors. Consequently, for a given force constant matrix, phonons can be calculated with very modest computational effort throughout the entire Brillouin zone, and convergence of phononic properties with respect to the \mathbf{q} -grid used for the Brillouin zone sampling can be easily checked.

In principal, the central difference approximation used in Eq. (2.80) could also be replaced by forward or backward differencing, which both reduce the amount of force evaluations because only $F_{n',i',\alpha'}(+u_{n,i,\alpha})$ or $F_{n',i',\alpha'}(-u_{n,i,\alpha})$ would be required, respectively. At the same time, however, this results in a numerical truncation error for $\Phi_{n,i,\alpha}^{n',i',\alpha'}$ of order Δ , while it is of order Δ^2 with the central difference approximation. This is of particular importance since the displacement size Δ cannot be chosen arbitrarily small due to

1. limitations of floating point arithmetics when evaluating Eq. (2.80) and
2. numerical noise making it exceedingly difficult to accurately obtain “small” non-analytically defined forces (usually the case in electronic structure calculations).

The quasi-harmonic approximation (see Section 2.4.4) relies on solving lattice dynamics for harmonic Hamiltonians according to Eq. (2.71), but now for a different one for each different volume. Depending on the volume range to be covered, this comes at only moderately increased computational costs – in particular when considering alternatives as, e.g., a fully dynamical description. Furthermore, computer codes for lattice dynamics often already include the QHA or can be rather easily extended otherwise.

In this thesis, the PHONOPY package [100] is employed for all phonon calculations. Most important for this thesis is that it can be easily coupled to external codes that perform the force evaluations thanks to the well-structured and documented PYTHON code base. PHONOPY implements the finite displacement method originally introduced by Parlinski *et al.* [99], including an automatic recognition and exploitation of symme-

try to (potentially) significantly reduce the amount of $2 \times 3 \times N_{\text{cell}}$ force evaluations that are required when symmetry is not considered (or not present in the structure). Furthermore, it has been extended to enable calculations within the QHA. In the first step, a set of symmetry-reduced atomic displacements in the requested supercell are generated. After calculating forces for these structures with the external code (DFT or force fields in this work), PHONOPY is again invoked to generate the force constant matrix in Eq. (2.80) and solve the phonon eigenvalue problem (see Eq. (2.71)). In the QHA these steps need to be repeated for a set of different primitive cells each with a different cell volume. In the last step, e.g. phonon DOSs (Eq. (2.72)) or vibrational free energy (and entropy) contributions can then be calculated.

2.5 References

1. M. Born, R. Oppenheimer, *Annalen der physik* **389**, 457–484 (1927).
2. P. Hohenberg, W. Kohn, *Phys. Rev.* **136**, B864 (1964).
3. J. P. Perdew, A. Ruzsinszky, J. Tao, V. N. Staroverov, G. E. Scuseria, *et al.*, *J. Chem. Phys.* **123**, 062201 (2005).
4. D. M. Ceperley, B. J. Alder, *Phys. Rev. Lett.* **45**, 566–569 (1980).
5. M. Gell-Mann, K. A. Brueckner, *Phys. Rev.* **106**, 364 (1957).
6. S. H. Vosko, L. Wilk, M. Nusair, *Canadian J. Phys.* **58**, 1200–1211 (1980).
7. J. P. Perdew, A. Zunger, *Phys. Rev. B* **23**, 5048–5079 (1981).
8. J. P. Perdew, Y. Wang, *Phys. Rev. B* **45**, 13244–13249 (1992).
9. O. Gunnarsson, B. I. Lundqvist, *Phys. Rev. B* **13**, 4274 (1976).
10. K. Burke, J. P. Perdew, M. Ernzerhof, *J. Chem. Phys.* **109**, 3760–3771 (1998).
11. C. Lee, D. Vanderbilt, K. Laasonen, R. Car, M. Parrinello, *Phys. Rev. B* **47**, 4863 (1993).
12. D. Hamann, *Phys. Rev. B* **55**, R10157 (1997).
13. P. J. Feibelman, *Physical Chemistry Chemical Physics* **10**, 4688–4691 (2008).
14. C. Lee, W. Yang, R. G. Parr, *Phys. Rev. B* **37**, 785–789 (1988).
15. J. P. Perdew, P. Ziesche, H. Eschrig, *Electronic structure of solids’ 91*, 1991.
16. J. P. Perdew, K. Burke, M. Ernzerhof, *Phys. Rev. Lett.* **77**, 3865–3868 (1996).
17. J. Tao, J. P. Perdew, V. N. Staroverov, G. E. Scuseria, *Phys. Rev. Lett.* **91**, 146401 (2003).
18. J. Sun, A. Ruzsinszky, J. P. Perdew, *Phys. Rev. Lett.* **115**, 036402 (2015).
19. V. N. Staroverov, G. E. Scuseria, J. Tao, J. P. Perdew, *J. Chem. Phys.* **119**, 12129–12137 (2003).
20. Y. Zhao, D. G. Truhlar, *J. Phys. Chem. A* **109**, 5656–5667 (2005).
21. J. Sun, R. C. Remsing, Y. Zhang, Z. Sun, A. Ruzsinszky, *et al.*, *Nature chemistry* **8**, 831 (2016).
22. Y. Zhang, J. Sun, J. P. Perdew, X. Wu, *Phys. Rev. B* **96**, 035143 (2017).
23. E. R. Johnson, I. D. Mackie, G. A. DiLabio, *J. Phys. Org. Chem.* **22**, 1127–1135 (2009).
24. S. Grimme, L. Goerigk, R. Fink, *Rev.: Comput. Mol. Sci* **1**, 211 (2011).
25. A. Tkatchenko, L. Romaner, O. T. Hofmann, E. Zojer, C. Ambrosch-Draxl, *et al.*, *MRS bulletin* **35**, 435–442 (2010).
26. J. Klimeš, A. Michaelides, *J. Chem. Phys.* **137**, 120901 (2012).
27. F. London, *Transactions of the Faraday Society* **33**, 8b–26 (1937).
28. H. B. Casimir, D. Polder, *Phys. Rev.* **73**, 360 (1948).
29. H. Sutter, R. Cole, *J. Chem. Phys.* **52**, 132–139 (1970).
30. V. A. Maltsev, O. A. Nerushev, S. A. Novopashin, B. A. Selivanov, *Chemical physics letters* **212**, 480–482 (1993).
31. A. Salop, E. Pollack, B. Bederson, *Phys. Rev.* **124**, 1431 (1961).

32. A. Tkatchenko, M. Scheffler, *Phys. Rev. Lett.* **102**, 073005 (2009).
33. X. Chu, A. Dalgarno, *J. Chem. Phys.* **121**, 4083–4088 (2004).
34. F. L. Hirshfeld, *Theoretica chimica acta* **44**, 129–138 (1977).
35. P. Jurečka, J. Černý, P. Hobza, D. R. Salahub, *J. Comp. Chem.* **28**, 555–569 (2007).
36. A. Tkatchenko, R. A. DiStasio, R. Car, M. Scheffler, *Phys. Rev. Lett.* **108**, 236402 (2012).
37. D. C. Langreth, M. Mehl, *Phys. Rev. Lett.* **47**, 446 (1981).
38. M. Dion, H. Rydberg, E. Schröder, D. C. Langreth, B. I. Lundqvist, *Phys. Rev. Lett.* **92**, 246401 (2004).
39. K. Lee, É. D. Murray, L. Kong, B. I. Lundqvist, D. C. Langreth, *Phys. Rev. B* **82**, 081101 (2010).
40. O. A. Vydrov, T. Van Voorhis, *Phys. Rev. Lett.* **103**, 063004 (2009).
41. O. A. Vydrov, T. Van Voorhis, *J. Chem. Phys.* **133**, 244103 (2010).
42. J. Wang, G. Román-Pérez, J. M. Soler, E. Artacho, M.-V. Fernández-Serra, *J. Chem. Phys.* **134**, 024516 (2011).
43. É. D. Murray, G. Galli, *Phys. Rev. Lett.* **108**, 105502 (2012).
44. G. Román-Pérez, J. M. Soler, *Phys. Rev. Lett.* **103**, 096102 (2009).
45. V. Blum, R. Gehrke, F. Hanke, P. Havu, V. Havu, *et al.*, *Comp. Phys. Comm.* **180**, 2175–2196 (2009).
46. H. J. Monkhorst, J. D. Pack, *Phys. Rev. B* **13**, 5188 (1976).
47. H. Berendsen, J. Grigera, T. Straatsma, *J. Phys. Chem.* **91**, 6269–6271 (1987).
48. W. L. Jorgensen, J. Chandrasekhar, J. D. Madura, R. W. Impey, M. L. Klein, *J. Chem. Phys.* **79**, 926–935 (1983).
49. J. L. Abascal, C. Vega, *J. Chem. Phys.* **123**, 234505 (2005).
50. J. L. F. Abascal, E. Sanz, R. García Fernández, C. Vega, *J. Chem. Phys.* **122**, 234511 (2005).
51. S. Habershon, T. E. Markland, D. E. Manolopoulos, *J. Chem. Phys.* **131**, 024501 (2009).
52. P. Ren, J. W. Ponder, *J. Phys. Chem. B* **107**, 5933–5947 (2003).
53. J. W. Ponder *et al.*, *Washington University School of Medicine, Saint Louis, MO* **3** (2004).
54. V. Babin, C. Leforestier, F. Paesani, *J. Chem. Theory Comput.* **9**, 5395–5403 (2013).
55. V. Babin, G. R. Medders, F. Paesani, *J. Chem. Theory Comput.* **10**, 1599–1607 (2014).
56. K. T. Wikfeldt, E. Batista, F. Vila, H. Jónsson, *Physical Chemistry Chemical Physics* **15**, 16542–16556 (2013).
57. E. Lambros, F. Paesani, *The Journal of Chemical Physics* **153**, 060901 (2020).
58. R. A. Gilmore, M. T. Dove, A. J. Misquitta, *Journal of chemical theory and computation* **16**, 224–242 (2019).

-
59. G. A. Cisneros, K. T. Wikfeldt, L. Ojamäe, J. Lu, Y. Xu, *et al.*, *Chemical reviews* **116**, 7501–7528 (2016).
60. H. J. Berendsen, J. P. Postma, W. F. van Gunsteren, J. Hermans, in *Intermolecular forces* (Springer, 1981), pp. 331–342.
61. F. Paesani, W. Zhang, D. A. Case, T. E. Cheatham III, G. A. Voth, *J. Chem. Phys* **125**, 184507 (2006).
62. C. Burnham, D. Anick, P. Mankoo, G. Reiter, *J. Chem. Phys* **128**, 154519 (2008).
63. P. E. Lopes, B. Roux, A. D. MacKerell, *Theoretical Chemistry Accounts* **124**, 11–28 (2009).
64. J. Applequist, J. R. Carl, K.-K. Fung, *J. Am. Chem. Soc.* **94**, 2952–2960 (1972).
65. B. T. Thole, *Chemical Physics* **59**, 341–350 (1981).
66. G. S. Fanourgakis, S. S. Xantheas, *J. Chem. Phys* **128**, 074506 (2008).
67. R. Kumar, F.-F. Wang, G. R. Jenness, K. D. Jordan, *J. Chem. Phys* **132**, 014309 (2010).
68. R. Bukowski, K. Szalewicz, G. C. Groenenboom, A. van der Avoird, *J. Chem. Phys* **128**, 094314 (2008).
69. R. Bukowski, K. Szalewicz, G. C. Groenenboom, A. van der Avoird, *J. Chem. Phys* **128**, 094313 (2008).
70. Y. Wang, X. Huang, B. C. Shepler, B. J. Braams, J. M. Bowman, *J. Chem. Phys* **134**, 094509 (2011).
71. Y. Wang, V. Babin, J. M. Bowman, F. Paesani, *J. Am. Chem. Soc.* **134**, 11116–11119 (2012).
72. J. D. Bernal, R. H. Fowler, *J. Chem. Phys* **1**, 515–548 (1933).
73. D. Frenkel, B. Smit, *Understanding Molecular Simulation – From Algorithms to Applications* (Academic Press, San Diego, 2002), vol. 1.
74. K. Toukan, A. Rahman, *Phys. Rev. B* **31**, 2643 (1985).
75. D. M. Carey, G. M. Korenowski, *J. Chem. Phys.* **108**, 2669–2675 (1998).
76. S. Plimpton, *J. Comput. Phys.* **117**, 1–19 (1995).
77. M. L. Laury, L.-P. Wang, V. S. Pande, T. Head-Gordon, J. W. Ponder, *J. Phys. Chem. B* **119**, 9423–9437 (2015).
78. A. Stone, *The Theory of Intermolecular Forces* (OUP Oxford, 2013).
79. P. T. Van Duijnen, M. Swart, *J. Phys. Chem. A* **102**, 2399–2407 (1998).
80. T. A. Halgren, *J. Am. Chem. Soc.* **114**, 7827–7843 (1992).
81. M. J. Dudek, J. W. Ponder, *J. Comp. Chem.* **16**, 791–816 (1995).
82. J. W. Ponder *et al.*, *AMOEBA-WATER-2014 parameters*.
83. T. R. Dyke, J. Muentner, *J. Chem. Phys* **59**, 3125–3127 (1973).
84. J. Verhoeven, A. Dymanus, *J. Chem. Phys* **52**, 3222–3233 (1970).
85. E. R. Batista, S. S. Xantheas, H. Jónsson, *J. Chem. Phys* **109**, 4546–4551 (1998).
86. K. Tang, J. P. Toennies, *J. Chem. Phys* **80**, 3726–3741 (1984).
87. G. R. Medders, V. Babin, F. Paesani, *J. Chem. Theory Comput.* **10**, 2906–2910 (2014).

- 88. V. Babin, G. R. Medders, F. Paesani, *J. Phys. Chem. Lett.* **3**, 3765–3769 (2012).
- 89. G. R. Medders, V. Babin, F. Paesani, *J. Chem. Theory Comput.* **9**, 1103–1114 (2013).
- 90. S. S. Xantheas, *Chemical Physics* **258**, 225–231 (2000).
- 91. M. P. Hodges, A. J. Stone, S. S. Xantheas, *J. Phys. Chem. A* **101**, 9163–9168 (1997).
- 92. A. Hermann, R. P. Krawczyk, M. Lein, P. Schwerdtfeger, I. P. Hamilton, *et al.*, *Phys. Rev. A* **76**, 013202 (2007).
- 93. J. Cui, H. Liu, K. D. Jordan, *J. Phys. Chem. B* **110**, 18872–18878 (2006).
- 94. H. Partridge, D. W. Schwenke, *The Journal of Chemical Physics* **106**, 4618–4639 (1997).
- 95. C. J. Burnham, J. Li, S. S. Xantheas, M. Leslie, *J. Chem. Phys.* **110**, 4566–4581 (1999).
- 96. C. J. Burnham, S. S. Xantheas, *J. Chem. Phys.* **116**, 1479–1492 (2002).
- 97. S. Baroni, S. De Gironcoli, A. Dal Corso, P. Giannozzi, *Reviews of modern Physics* **73**, 515 (2001).
- 98. W. Frank, C. Elsässer, M. Fähnle, *Phys. Rev. Lett.* **74**, 1791 (1995).
- 99. K. Parlinski, Z. Li, Y. Kawazoe, *Phys. Rev. Lett.* **78**, 4063 (1997).
- 100. A. Togo, I. Tanaka, *Scripta Mater.* **108**, 1–5 (2015).

CHAPTER 3

Importance of Zero-point Energy for Crystalline Ice Phases

This chapter is based on:

S. Rasti and J. Meyer, Importance of zero-point energy for crystalline ice phases: A comparison of force fields and density functional theory, *J. Chem. Phys.* **150**, 234504 (2019).

Abstract

Density functional theory (DFT) including van der Waals (vdW) interactions and accounting for zero-point energy (ZPE) is believed to provide a good description of crystalline ice phases [B. Pamuk *et al.*, Phys. Rev. Lett. **108**, 193003 (2012)]. Given the computational cost of DFT, it is not surprising that extensive phonon calculations, which yield the ZPE, have only been done for a limited amount of ice structures. Computationally convenient force fields on the other hand are the method of choice for large systems and/or dynamical simulations e.g. of supercooled water. Here I present a systematic comparison for seven hydrogen-ordered crystalline ice phases (Ih, IX, II, XIII, XIV, XV, VIII) between many commonly-used non-polarizable force fields and density functionals, including some recently developed meta-GGA functionals and accounting for vdW interactions. Starting from the experimentally determined crystal structures, I perform space-group-constrained structural relaxations. These provide the starting point for highly-accurate phonon calculations that yield effectively volume-dependent ZPEs within the quasi-harmonic approximation. In particular when including ZPE, the force fields show a remarkably good performance for equilibrium volumes and cohesive energies superior to many density functionals. A decomposition of the cohesive energies into intramolecular deformation, electrostatic and vdW contributions quantifies the differences between force fields and DFT. Results for the equilibrium volumes and phase transition pressures for all studied force fields are much more strongly affected by ZPE than all studied density functionals. I track this down to significantly smaller shifts of the O-H-stretch modes and compare with experimental data from Raman spectroscopy.

3.1 Introduction

Ice is a condensed phase of water which plays an important role in different fields including astrophysics and planetary sciences [1–4] as well as cryobiology [5]. It occurs in many different phases due to the large variety of forming different hydrogen bonds

between the individual H_2O molecules. With increasing pressure these ice phases get more close packed [6], which makes their phase diagram and their structures more unusual [7]. From the 17 known ice phases [8] seven are proton ordered and thus have a well-defined crystal structure. These ice phases (ice Ih, ice IX, ice II, ice XIII, ice XIV, ice XV, ice VIII) capture a wide range of local coordination and thus (hydrogen) bonding scenarios between individual H_2O molecules in solid water. They are listed together with their space groups and depicted in Table 3.1 and Fig. 3.1, respectively, ordered by increasing pressures at which they form. The geometric structure and relative stability of these different ice phases can be conveniently model using small unit cells and periodic boundary conditions in order to compare to available experimental data.

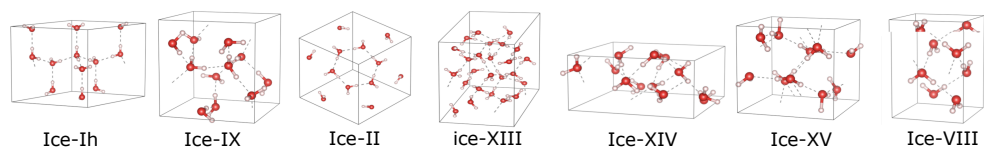


Figure 3.1: The unit cell of seven proton ordered ice structures. The oxygen and hydrogen atoms are shown in red and white colors, respectively.

Despite more than 30 years of computer simulations of water, chemical interaction models are still challenged to accurately describe the phase diagram of water [9–11] due to the complex interplay between hydrogen bonding [12, 13], van der Waals (vdW) [14–18] and other non-local exchange-correlation effects [10, 11, 19–21]. Density functional theory (DFT) can capture many of these contributions with varying accuracy for different exchange correlation functionals [10, 11, 16–19] and so can force fields depending on the sophistication of their parametrization [22]. Furthermore, vibrational properties can also play an important role, but this has so far been investigated only for a small amount of ice phases [17, 18, 23–26]. For example, zero-point energy associated with the lattice vibrations has been found to be responsible for the anomalous volume isotope effect (VIE) of ice Ih [18, 27] as well as isotope effects for phase transitions [28].

CHAPTER 3. IMPORTANCE OF ZERO-POINT ENERGY FOR CRYSTALLINE ICE PHASES

It is the goal of this study to provide an extensive comparison between off-the-shelve (non-polarizable) force fields, most of which have been fitted to experimental data for liquid water, and state-of-the-art density functionals for the aforementioned seven proton-ordered ice phases (Table 3.1 and Fig. 3.1). Given the computational efficiency and good performance in previous studies of ice Ih, II and III [18, 24, 28] compared to path integral molecular dynamics [23], lattice dynamics combined with the quasi harmonic approximation has been used to obtain the ZPE and account for its influence on equilibrium structures and cohesive energies. I find a large effect on structural properties in case of the force fields and almost none for DFT, which are related to a different description of the O-H-stretch frequency shifts upon compression and expansion. Likewise, I identify qualitatively different trends for the contributions to the cohesive energies.

Table 3.1: Bravais lattice, space group, number of water molecules N per unit cell and formation conditions (minimum and maximum pressures P_{\min} and P_{\max} , respectively) of the crystalline ice phases considered in this work.

Ice	Bravais Lattice	Space group	N	$P_{\min} \dots P_{\max}$ (GPa)
Ih	Hexagonal	$P6_3cm$ ^a	12	0.0 ... 0.2 ^b
IX	Tetragonal	$P4_12_12$ ^c	12	0.2 ... 0.4 ^{b,d}
II	Trigonal	$R\bar{3}$ ^e	12	0.3 ... 0.5 ^{b,f}
XIII	Monoclinic	$P2_1/a$ ^d	28	0.5 ... 1.1 ^b
XIV	Orthorombic	$P2_12_12_1$ ^d	12	1.1 ... 1.3 ^b
XV	Triclinic	$P\bar{1}$ ^f	10	1.2 ... 1.5 ^b
VIII	Tetragonal	$I4_1/amd$ ^g	8	1.5 ... 2.5 ^{b,h}

^aFrom Ref. [29] ^bFrom Ref. [30] ^cFrom Ref. [31] ^dFrom Ref. [32] ^eFrom Ref. [33]

^fFrom Ref. [34] ^gFrom Ref. [35] ^hFrom Ref. [36]

This chapter is structured as follows: In Section 3.2 the theoretical methods and computational details are briefly described. Subsequently, results for the relaxed structures (Section 3.3.1), the cohesive energies for these structures together with a decomposition into different bonding contributions (Section 3.3.2) and phase transition pressures

(Section 3.3.3) are presented. This is followed by a detailed analysis of the ZPE (Section 3.3.4). The chapter ends with conclusions and a short outlook on future work in Section 3.4.

3.2 Methodology

3.2.1 Total energy calculations

The LAMMPS code has been used [37] in order to calculate total energies, forces and stress tensors for the SPC/E [38], TIP3P [39], TIP4P/2005 [40], TIP4P/ice [41] and q-TIP4P/F [42] force fields (FF), that have been parametrized and are commonly used for simulations of water. Harmonic potentials were added to SPC/E, TIP3P, TIP4P/2005 and TIP4P/ice in order to enable intramolecular OH-bond stretching ($\omega_{\text{stretch}} = 3357 \text{ cm}^{-1}$) and HOH-angle bending ($\omega_{\text{bend}} = 1610 \text{ cm}^{-1}$) based on experimental data [43] for the corresponding vibrational modes of liquid water. q-TIP4P/F already describes flexible water molecules by construction [42]. The Lennard-Jones parts of these force fields have been truncated at a cut-off distance of 9 Å. Long-range Coulomb interactions are accounted for via Ewald summation [44].

DFT calculations at the LDA [45] and GGA [46] level have been carried out with the FHI-aims package [47, 48] using the standard tight settings. For the latter, pairwise dispersion interactions were added to the PBE exchange-correlation functional [46] using the Tkatchenko-Scheffler (PBE+TS) [49] as well as the many body dispersion correction (PBE+MBD) [50] methods. Calculations at meta-GGA level (and beyond) were performed with the VASP code [51, 52] using the hard projector-augmented-wave (PAW) potentials [53] for hydrogen and oxygen included with VASP [54] together with a plane-wave cut-off energy of 900 eV. The SCAN [55] and SCAN+rVV10 [56] exchange-correlations functionals have been used, where the latter includes the non-local rVV10 van der Waals functional [57, 58] on top of the SCAN meta-GGA. In all cases a $4 \times 4 \times 4$ Monkhorst-Pack grid [59] is used for Brillouin zone sampling.

CHAPTER 3. IMPORTANCE OF ZERO-POINT ENERGY FOR CRYSTALLINE ICE PHASES

For the force fields the total energy E_{FF} can be decomposed according to

$$E_{\text{FF}} = E_{\text{mol}} + E_{\text{elec}} + \underbrace{E_{\text{LJ-r}} + E_{\text{LJ-a}}}_{E_{\text{LJ}}} , \quad (3.1)$$

where E_{mol} is the sum of all intramolecular (stretching and bending) contributions and E_{elec} is the electrostatic (Coulomb) energy. $E_{\text{LJ-r}}$ denote the repulsive and $E_{\text{LJ-a}}$ the attractive part of the Lennard-Jones potential (E_{LJ}), that is employed in all of the force fields used in this study in order to account for intermolecular Pauli-repulsion and van der Waals (vdW) interactions, respectively. Likewise, for the DFT calculations, it is straightforward to decompose the total energy $E_{\text{DFT(+vdW)}}$ into

$$E_{\text{DFT(+vdW)}} = E_{\text{kin+XC}} + E_{\text{elec}} (+E_{\text{vdW}}) . \quad (3.2)$$

Here $E_{\text{kin+XC}}$ is the sum exchange-correlation and kinetic, E_{elec} is the Hartree and E_{vdW} the vdW energy.

Data obtained from neutron diffraction experiments [31–35, 60] has been used in order to generate the initial structures of proton ordered ice phases compiled in Fig. 3.1 and Table 3.1. As originally suggested by Hamann [29], ice Ih has been modeled with a unit cell containing 12 molecules. In order to simultaneously relax the lattice vectors and the internal coordinates of each ice structure while constraining its space group, the algorithm suggested by Pfrommer *et al.* [61] has been implemented into the Atomic Simulation Environment [62]. Using this implementation with the stress tensor and forces obtained from the FF and DFT calculations, space-group constrained equilibrium structures with equilibrium unit cell volume V_0 could be obtained. A tight (generalized) maximum force threshold of 10^{-4} eV/Å has been used as convergence criterion for the geometry optimizations. This ensures (*vide infra*) high-quality phonon calculations. In order to obtain bulk moduli B_0 , energy-volume curves $E(V)$ are fitted to 13 structures within $\pm 4\%$ of the isotropically contracted and expanded V_0 using the Rose-Vinet [63] equation of state (EOS), performing geometry optimizations of the internal coordinates for each of them. Based on the optimized structures, cohesive energies are obtained according to

$$E_{\text{coh}} = E_{\text{mol}} - \frac{1}{N_{\text{ice}}} E_{\text{ice}} \quad (3.3)$$

in the usual way, where E_{mol} is the total energy of an isolated H_2O molecule, E_{ice} is the total energy of the optimized unit cell of the ice phase with N_{ice} water molecules therein.

3.2.2 Inclusion of Zero-Point Energy Effects

The quasi-harmonic approximation (QHA) has been used in order to evaluate the Helmholtz free energy

$$F(V, T) = E(V) + F_{\text{phonon}}(V, T) \quad (3.4)$$

with

$$F_{\text{phonon}}(V, T) = \underbrace{\frac{1}{2} \sum_{\mathbf{q}, b} \hbar \omega_{\mathbf{q}, b}(V)}_{E_{\text{ZPE}}} + k_{\text{B}} T \sum_{\mathbf{q}, b} \ln \left[1 - \exp \left(\frac{-\hbar \omega_{\mathbf{q}, b}(V)}{k_{\text{B}} T} \right) \right] \quad (3.5)$$

Here k_{B} is the Boltzmann constant and $\omega_{\mathbf{q}, b}$ is the phonon frequency at wavevector \mathbf{q} for band b . The zero-point energy (ZPE) is (equivalently) given by the first moment of the phonon density of states (DOS) n_{phonon}

$$E^{\text{ZPE}} = F_{\text{phonon}}(V, T = 0) = \frac{\hbar}{2} \int_0^\infty d\omega \omega n_{\text{phonon}}(\omega) \quad (3.6)$$

where $n_{\text{phonon}}(\omega) = \sum_{\mathbf{q}, b} \delta(\omega - \omega_{\mathbf{q}, b})$. Because of the volume dependence of the phonon frequencies and the ZPE the minimum of $F_{\text{phonon}}(V, T)$ with respect to V can be shifted compared $E(V)$, resulting in equilibrium volumes V_0^{ZPE} , bulk moduli B_0^{ZPE} and cohesive energies $E_{\text{coh}}^{\text{ZPE}}$ that account for ZPE effects. These are obtained by calculating phonons for the same 13 structures that have been used for the $E(V)$ curves before. The Parlinski-Li-Kawazoe finite-displacement method [64] has been employed for the phonon calculations (with displacement of 0.001 Å), and $F(V, T = 0)$ -curves fitted employing the Rose-Vinet [63] EOS, both as implemented in the PHONOPY package [65]. Exploiting symmetry, the Brillouin zone has been sampled by $30 \times 30 \times 30$ grids for those calculations, which is equal to at least 1456 irreducible \mathbf{q} -points for each structure.

3.2.3 Determination of Phase-Transition Pressures

Transition pressures $P_{A \rightarrow B}$, at which an ice phase A goes over into a phase B, are obtained at $T = 0$ using three different approximations:

1. The Δ -approximation yields the transition pressure as the negative slope of the common tangent between the $E(V)$ -

$$P_{A \rightarrow B}^{\Delta} = -\frac{\Delta E}{\Delta V_0} = -\frac{E_B - E_A}{V_B - V_A} \quad (3.7)$$

or the $F(V, T = 0)$ -curves

$$P_{A \rightarrow B}^{\Delta, \text{ZPE}} = -\frac{\Delta F_0}{\Delta V_0^{\text{ZPE}}} = -\left. \frac{F(V_{0,B}^{\text{ZPE}}, T) - F(V_{0,A}^{\text{ZPE}}, T)}{V_{0,B}^{\text{ZPE}} - V_{0,A}^{\text{ZPE}}} \right|_{T=0} \quad (3.8)$$

of the two ice phases A and B. Obviously, the latter includes ZPE effects.

2. The effect of contraction and expansion can also be included directly in the thermodynamic description by adding the PV to $E(V)$ and minimizing the resulting enthalpy with respect to the volume

$$H(P) = \min_V [E(V) + PV] . \quad (3.9)$$

The crossing point of $H(P)$ for two ice phases A and B then defines the corresponding transition pressure $P_{A \rightarrow B}^H$

$$H_A(P_{A \rightarrow B}^H) = H_B(P_{A \rightarrow B}^H) . \quad (3.10)$$

3. Also accounting for the phonon contributions within the QHA, the Gibbs free energy

$$G(T, P) = \min_V [E(V) + F_{\text{phonon}}(V, T) + PV] \quad (3.11)$$

is calculated in the same fashion $H(P)$ above. The zero-temperature transition pressure $P_{A \rightarrow B}^G$ is then defined as the pressure where the Gibbs free energies of two ice phases A and B are equal

$$G_A(P_{A \rightarrow B}^G, T)|_{T=0} = G_B(P_{A \rightarrow B}^G, T)|_{T=0} . \quad (3.12)$$

3.3 Results and Discussions

3.3.1 Equilibrium Structures

The detailed results from the structural optimization with all interaction models are provided in the Section 3.A. Figure 3.2 highlights the relative differences of the calculated equilibrium volumes with respect to measured data. Without considering ZPE (Fig. 3.2 (a)), q-TIP4P/F shows the best agreement with experiments for all ice phases among the force fields. It yields the smallest average deviation of about 3%, which increases in the order q-TIP4P/F < TIP4P/ice < TIP4P/2005 < TIP3P < SPC/E to almost 8%.

As expected from previous studies for selected ice phases, LDA shows the worst performance among all DFT methods [11]. The PBE-based results are in good agreement with results from previous calculations [19]. PBE shows an overall good performance, while including the TS and MBD corrections to account for vdW-interactions improve the PBE structures for high-pressure ice phases. On the other hand, the equilibrium volumes of the low-pressure ice phases (ice Ih in particular) are better described by TIP3P and q-TIP4P/F. The more compact forms of the high-pressure ice phases thus pose a much bigger challenge to the force fields to properly account for molecular deformation, vdW interactions hydrogen bonding networks. On average though, the deviation of the equilibrium volumes for all PBE-based methods is comparable to the TIP4P-family FFs. Quite in contrast, SCAN and (even worse) SCAN+RVV10 show significantly larger deviations from the experimentally determined structures than all force fields.

Figure 3.2 (b) shows the results for the equilibrium volumes including ZPE. Apart from PBE, the volumes for all DFT methods increase very little towards the corresponding experimental data. ZPE-corrected PBE also yields enlarged unit cells, but these now become too large. The ZPE-corrected equilibrium volumes for all FFs increase much more and become significantly closer to the experimental data. Consequently, the average deviations for the latter become less than 3% and thus outperform all DFT

methods. The importance of individual phonon modes for this result will be analyzed in more detail in Section 3.3.4.

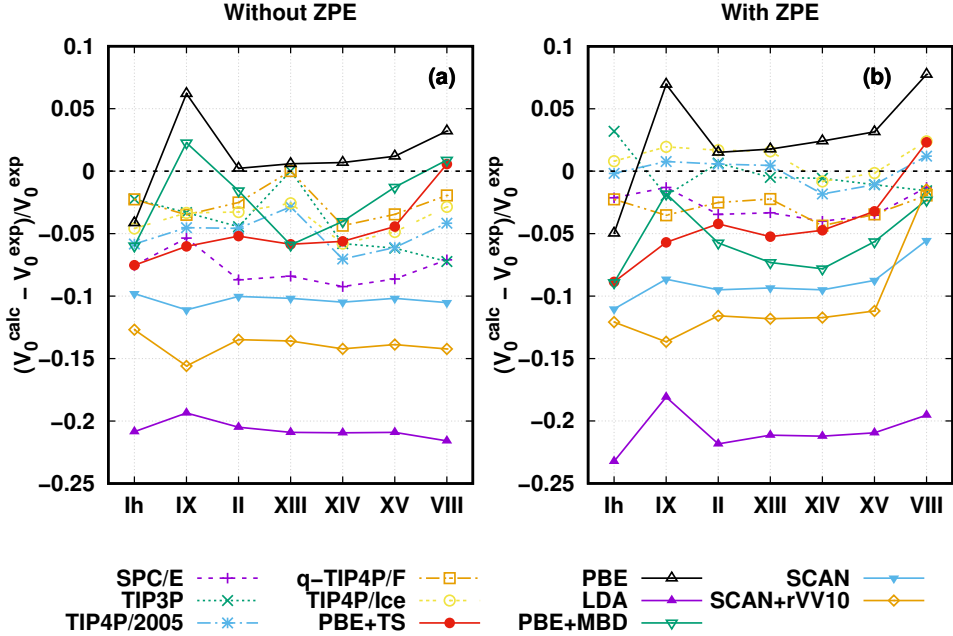


Figure 3.2: Relative differences of calculated V_0 (a) and V_0^{ZPE} (b) from experimental data (black dashed line at 0) for the unit cell volumes of the various ice phases. Lines are meant to guide the eye only, with differently colored dashed (solid) lines marking force fields (density functionals).

3.3.2 Cohesive Energies

The cohesive energy per H_2O molecule allows to characterize the relative stability of the different ice phases. Experimental data is available ice Ih, IX, II and VIII from Whalley [66] without and with ZPE. ZPE is excluded from the latter in a linear fashion, and ice IX, II, VIII are less stable than ice Ih by 5, 1 and 33 meV/ H_2O , respectively. This data is shown together with the results of the calculations from this work without (with) ZPE in Fig. 3.3 (a)(Fig. 3.3 (b)). The sequence of increasingly compressed ice structures listed in Table 3.1 is therefore expected to decrease in stability and thus

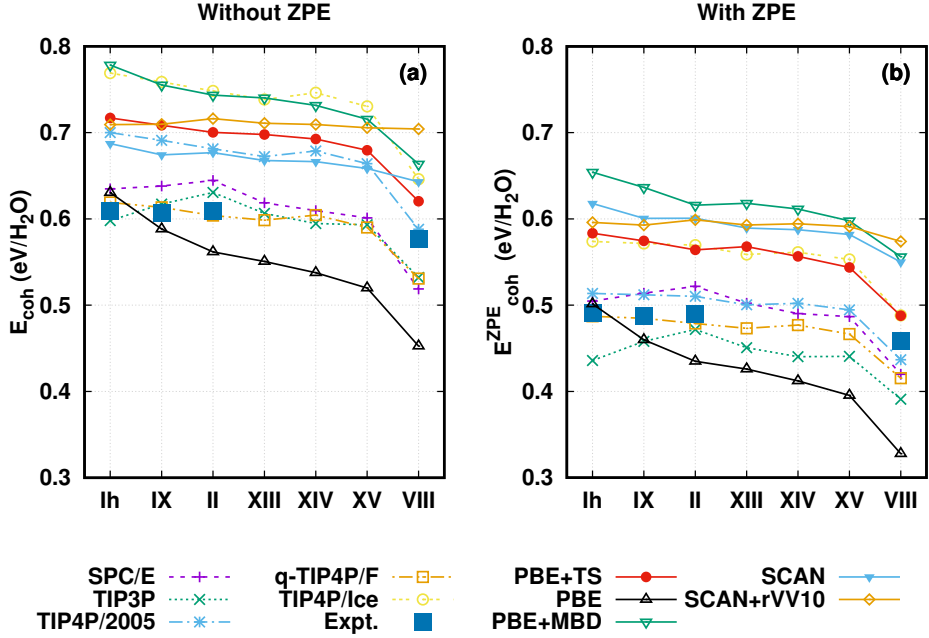


Figure 3.3: Cohesive energies per water molecule for the various ice phases without (a) and with (b) account for ZPE. Lines are meant to guide the eye only, with differently colored dashed (solid) lines marking force fields (density functionals). Experimental data from Whalley [66] is shown by blue squares, without (a) and with (b) ZPE correction suggested as part of that work. Due to the strong overbinding of LDA relative to the experimental reference, results are not shown here, but provided in the supplementary material together with all other numerical values.

yield decreasing cohesive energies.

Without ZPE (see Fig. 3.3 (a)) all methods correctly predict ice Ih (ice VIII) to be most (least) stable. Only the SCAN functional yields the relative cohesive energies in outstanding quantitative agreement with experiments. It is therefore the only method that is able to predict that ice II is more stable than ice IX, as has been observed before by Sun *et al.* [21]. In addition to SCAN, the near degeneracy between ice Ih and ice II is only captured correctly with DFT functionals that explicitly account for vdW interactions (PBE+TS, PBE+MBD, SCAN+rVV10). Still, all DFT methods

CHAPTER 3. IMPORTANCE OF ZERO-POINT ENERGY FOR CRYSTALLINE ICE PHASES

functionals overbind the structures by more than 50 meV per water molecule with LDA being significantly further away. Absolute cohesive energies are on average much better described by all the FFs, except for TIP4P/ice, which surprisingly shows the largest offset with respect to the experimental data. The relative stability can be problematic (in particular for TIP3P). Like for the equilibrium volumes q-TIP4P/F performs best overall by predicting even the absolute cohesive energies very accurately.

Including ZPE reduces the cohesive energy in all calculations (see Fig. 3.3 (b)) as expected according to the ZPE correction employed by Whalley [66]. Consequently, the superiority of the FFs for the prediction of the absolute cohesive energies does not change. q-TIP4P/F remains the best choice among the FFs and TIP4P/ice remains the worst. The prediction of relative stability does not improve or even gets worse for TIP3P. For the DFT methods LDA gains the biggest improvements due to ZPE but still shows the worst description. The cohesive energies of PBE and PBE+TS improve slightly for ice VIII. For the SCAN functional on the other hand, the inclusion of ZPE very slightly worsens the predicted relative stability of the ice phases.

In order to analyze where the differences of the cohesive energies come from, Fig. 3.4 shows a decomposition into the total-energy contributions described in Section 3.2.1. As shown by the negative sign of $E_{\text{coh}}^{\text{mol}} + E_{\text{coh}}^{\text{LJ-r}}$ for the FFs (Fig. 3.4 (a)) and $E_{\text{coh}}^{\text{kin+xc}}$ for almost all DFT methods (Fig. 3.4 (d)) these contributions decrease the absolute cohesive energy of each ice phase due to structural deformation in the crystal compared to the gas phase. LDA as well as SCAN for ice VIII and PBE+TS are noteworthy exceptions to this trend by yielding positive $E_{\text{coh}}^{\text{kin+xc}}$. Overall, for both DFT and FFs, the destabilization decreases for the more compact ice phases with increasing pressure.

In contrast, the electrostatic contributions $E_{\text{coh}}^{\text{coul}}$ shown in Fig. 3.4 (b) and Fig. 3.4 (e) for FFs and DFT, respectively, stabilize each ice phase, and the stabilization reduces from ice Ih to ice VIII. For LDA, the magnitude of the stabilization can be up to two times larger than for TIP4P/ice, which has the largest $E_{\text{coh}}^{\text{coul}}$ among the force fields.

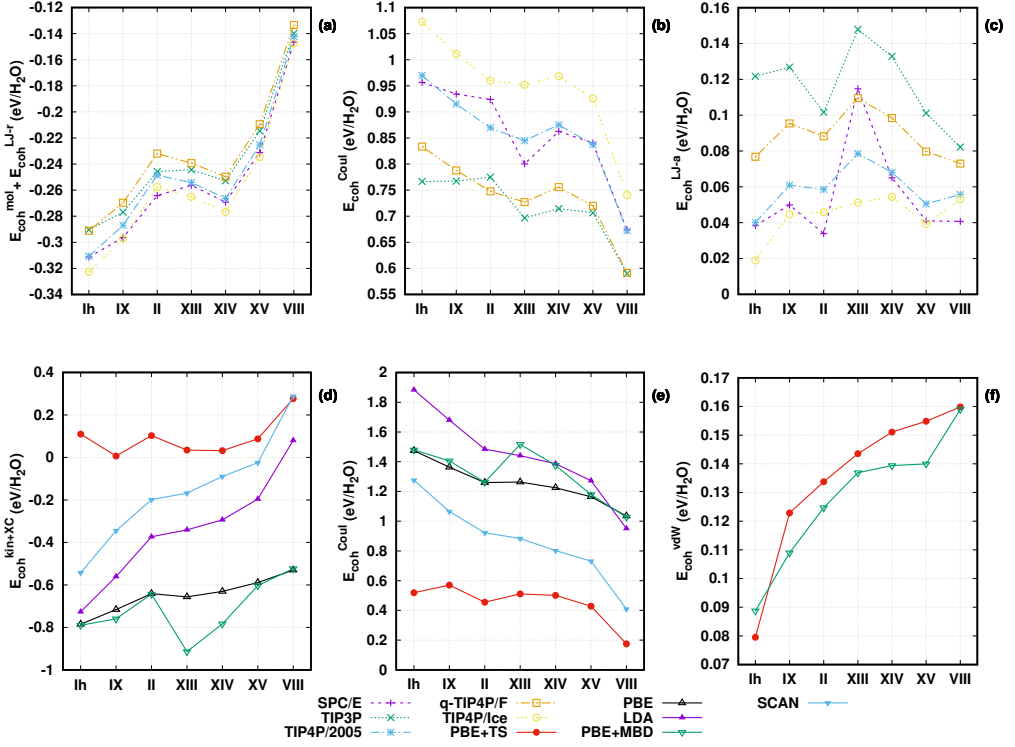


Figure 3.4: Decomposition of cohesive energy without ZPE for the various ice phases (see 3.3 (a)) into contributions to the total energies for FFs ((a)-(c), see Eq. (3.1)) and DFT ((d)-(f), see Eq. (3.2)). Lines are meant to guide the eye only, with differently colored dashed (solid) lines marking force fields (density functionals).

Naturally, the contributions to the cohesive energies related to the attractive part of the Lennard-Jones potential $E_{\text{coh}}^{\text{LJ-a}}$ in case of the FFs (Fig. 3.4 (c)) and van der Waals energies $E_{\text{coh}}^{\text{vdW}}$ for PBE+TS and PBE+MBD (Fig. 3.4 (f)), stabilize each ice phase. The latter two DFT methods, which explicitly separate E_{vdW} , show a monotonously increasing stabilization from ice Ih to ice VIII. In particular, as already discussed by Santra *et al.* [16], the $E_{\text{coh}}^{\text{vdW}}$ for PBE+TS stabilizes ice VIII about two times more than ice Ih. Figure 3.4 (f) shows that PBE+MBD yields almost the same result. $E_{\text{coh}}^{\text{LJ-a}}$ for the FFs is of very similar magnitude, but, quite in contrast, this does not show such a monotonous trend. This is mirrored by the fact that the Pauli repulsion, which

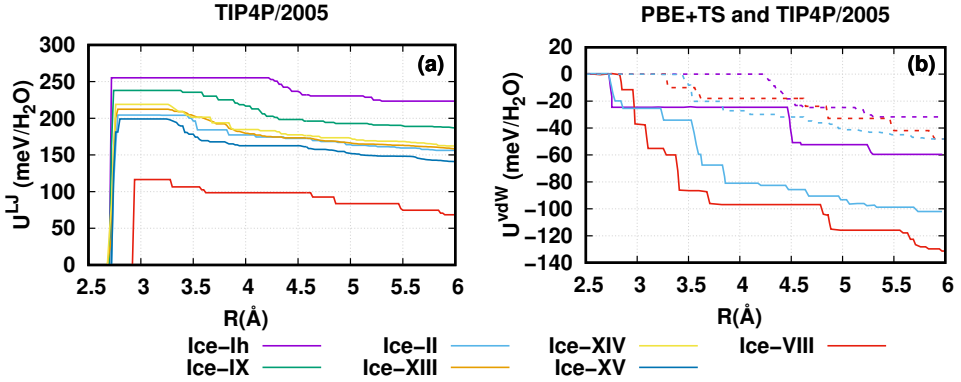


Figure 3.5: The solid lines show the accumulated the Lennard-Jones potential E_{LJ} for TIP4P/2005 (this work, (a)) and van der Waals energies E_{vdW} for PBE+TS (data from Santra *et al.* [16], (b)), when more and more pairs contribute with increasing oxygen-oxygen distance R . Different ice phases are shown by the differently colored lines. In panel (b), the attractive part of the Lennard-Jones potential E_{LJ-a} for TIP4P/2005 is indicated by dashed lines for comparison.

is described by the repulsive part of the Lennard-Jones potential, does not decrease monotonously when going from ice Ih to ice VIII as shown in Fig. 3.5 for TIP4P/2005 as representative example. Inspired by the analysis of Santra *et al.* [16], Fig. 3.5 (a) shows E_{LJ} as a function of contributing pairs in growing neighbor shells that can be characterized by maximum oxygen-oxygen distances R . For TIP4P/2005 and equivalently for all the other FFs, the first neighbor shell at $\leq 3\text{\AA}$ is in the repulsive regime of the Lennard-Jones potentials used for the FFs (e.g. $\sigma = 3.1668\text{\AA}$ for TIP4P/2005 [41]). Only subsequent neighbor shells then accumulate attractive contributions E_{LJ-a} to E_{LJ} . Compared to PBE+TS (Fig. 3.5 (b)) (for which all neighbors yield attractive contributions to E_{vdW} by construction), the E_{LJ-a} contributions to TIP4P/2005 are much smaller at comparable distances. Altogether, since the parameters of E_{LJ} of the FFs have been fitted without separating E_{LJ-r} and E_{LJ-a} , it is not surprising that E_{coh}^{LJ-a} and E_{coh}^{vdW} show different trends.

3.3.3 Phase Transition Pressures

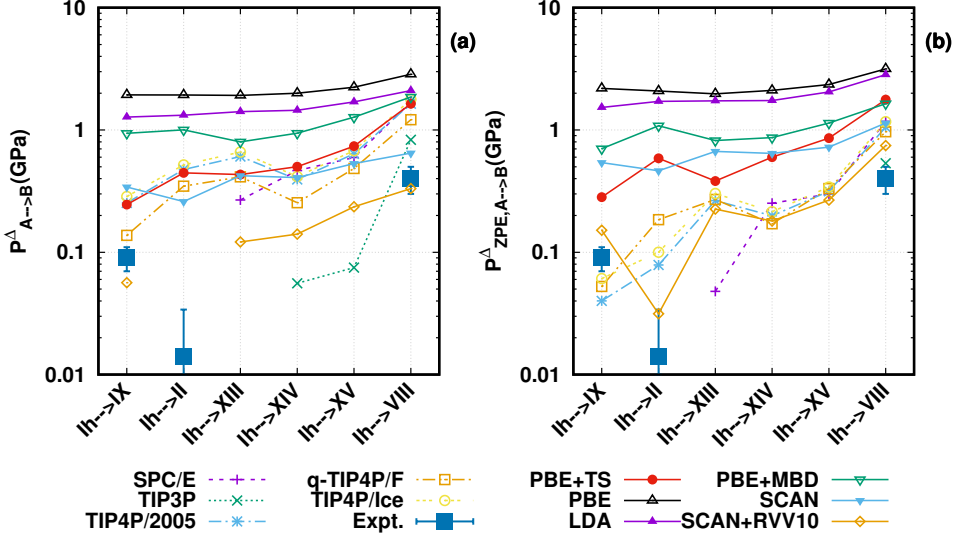


Figure 3.6: Phase transition pressures at which ice Ih goes over into the other six ice phases (IX, II, XIII, XIV, VIII) considered in this work as obtained by the Δ -approximation (a) without and (b) ZPE (see Eq. (3.7) and Eq. (3.8) in Section 3.2.3, respectively). Lines are meant to guide the eye only, with differently colored dashed (solid) lines marking force fields (density functionals). The blue filled squares show experimental data extrapolated to the zero temperature including error bars where available as given by Whalley [66].

Since phase transition pressures for two ice phases A and B are generally influenced both by structural and energetic effects, it is interesting to calculate the latter using the different techniques described in Section 3.2.3 and compare with experimental reference values [30, 32, 34, 36]. Figure 3.6 shows the results for the Δ -approximation. No values are shown when the transition pressure turn out to be negative. As observed by Santra *et al.* [19] before, without taking ZPE into account (Fig. 3.6 (a)) PBE largely overestimates $P^{\Delta}_{A \rightarrow B}$, but can be significantly improved by accounting for vdW interactions in PBE+MBD and (even more) PBE+TS. LDA benefits from error canceling for both the equilibrium volumes and cohesive energies and does slightly better than PBE, but

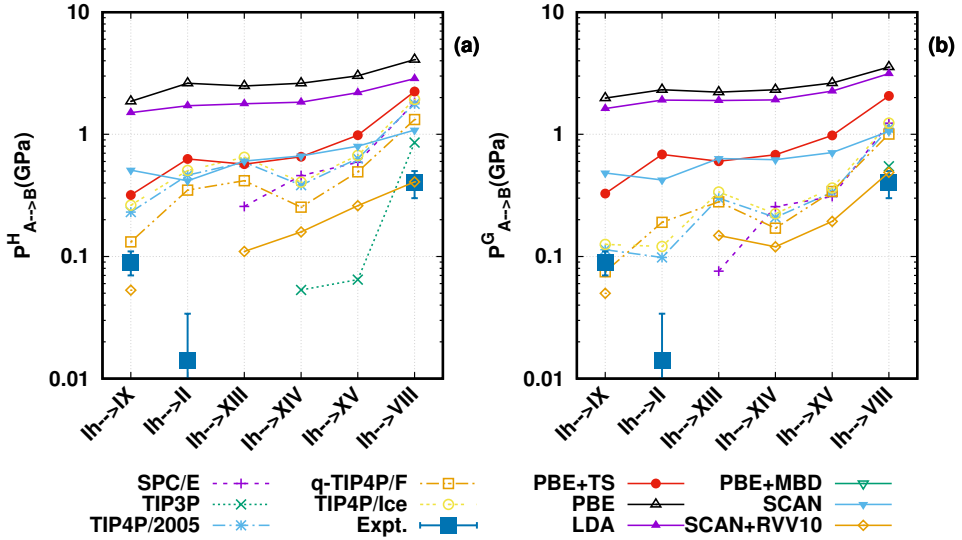


Figure 3.7: Same as 3.6, but for phase transition pressures obtained from (a) enthalpy and (b) Gibbs free energy (see Eq. (3.10) and Eq. (3.12) in Section 3.2.3, respectively).

not as good PBE+MBD. The SCAN functional performs even better than PBE+TS, and SCAN+rVV10 (likewise with account for vdW) yields the best results. Due to the problems with the relative stability of the ice phases discussed in Section 3.3.2, only q-TIP4P/F, again the best among the FFs, yielding meaningful results for all transitions which are comparable to PBE+TS. Including ZPE (Fig. 3.6 (b)) does not change most of the DFT results except for SCAN+rVV10, which now yields positive $P_{A \rightarrow B}^{\Delta, \text{ZPE}}$ for all transitions. The same happens for all force fields apart from SPC/E. Their agreement with the available experimental data is not as good as for SCAN+rVV10, but still much better than LDA, SCAN and all PBE-based methods.

Transition pressures obtained based on the enthalpy and Gibbs free energy, $P_{A \rightarrow B}^H$ and $P_{A \rightarrow B}^G$ shown in Fig. 3.7 (a) and Fig. 3.7 (b), respectively, which the latter includes ZPE, follow the same qualitative trends. However, in case of $P_{A \rightarrow B}^H$ more DFT methods and FFs than for $P_{A \rightarrow B}^{\Delta, \text{ZPE}}$ failed to predict a positive values or simply yield results that are out of the range plotted in Fig. 3.7 (a). Results based on the Gibbs free energy on the other hand are comparable to the ZPE-corrected Δ -approximation. Furthermore,

those results for $P_{A \rightarrow B}^G$ shown in Fig. 3.7 (b) are only mildly affected by temperature, i.e. the change in the worst case by about 0.08 GPa at $T = 200$ K.

3.3.4 Analysis of Zero-Point Energy Effects

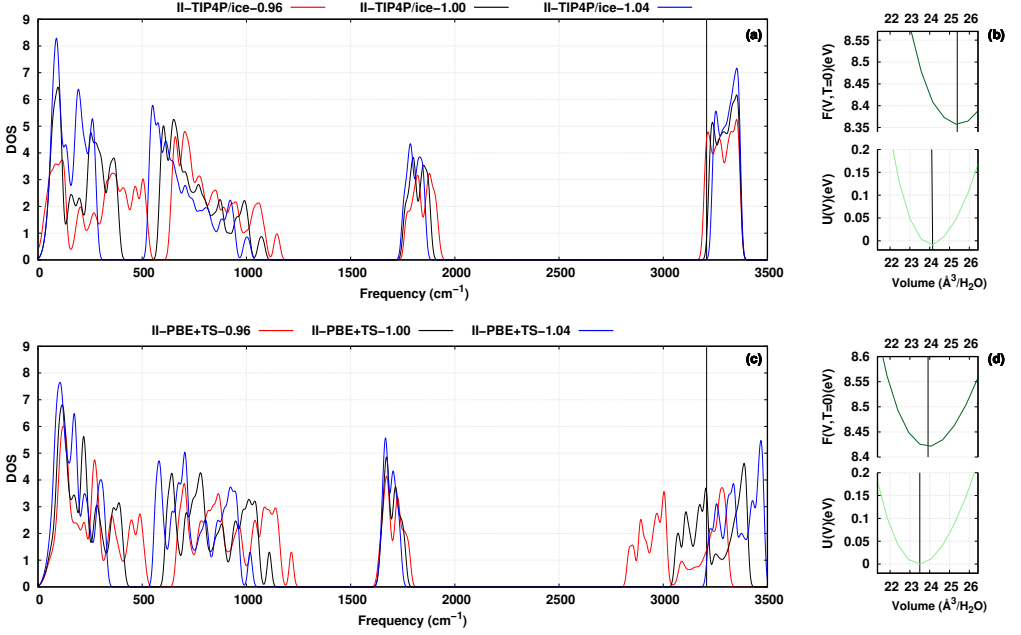


Figure 3.8: Phonon densities of states for ice II obtained with TIP4P/ice (a) and PBE + TS (c). Black, red and blue lines show the phonon DOSs at the corresponding equilibrium volumes (V_0) as well as isotropically compressed ($0.96 \cdot V_0$) and expanded ($1.04 \cdot V_0$) structures, respectively. Experimental data for the stretching frequencies is indicated by the black vertical lines. Internal energy $E(V)$ (dark green) and Helmholtz free energy $F(V, T = 0)$ (light green) are plotted for TIP4P/ice (b) and PBE + TS (d) using $E(V_{0,\text{TIP4P/ice}})$ and $E(V_{0,\text{PBE+TS}})$ as energy zeros, respectively. $V_{0,\text{TIP4P/ice}}$ ($V_{0,\text{TIP4P/ice}}^{\text{ZPE}}$) and $V_{0,\text{PBE+TS}}$ ($V_{0,\text{PBE+TS}}^{\text{ZPE}}$) are the corresponding equilibrium volumes without (with) taking ZPE into account, which are indicated by black vertical lines.

As observed in Sections 3.3.1 to 3.3.3, ZPE has much more pronounced effects on the results of FF compared to DFT calculations. These effects originate from the influence

CHAPTER 3. IMPORTANCE OF ZERO-POINT ENERGY FOR CRYSTALLINE ICE PHASES

of the QHA (see Section 3.2.2) on the equation of state for the different ice phases, i.e. phonon frequencies must change significantly differently for these two families of interaction potentials when compressing or expanding the unit cell. Focusing on ice II, Fig. 3.8 illustrates the reason for these differences by taking TIP4P/ice and PBE+TS as representative examples for the respective families. The other family members show the same qualitative trend for ice II and also the other ice structures.

In ascending order, the phonon frequencies can be grouped into crystal modes (0 to 500 cm^{-1} , a.k.a. hydrogen-bond bending and stretching), librational modes (500 to 1500 cm^{-1}) and finally intramolecular bending (1500 to 2000 cm^{-1} as well as stretching (2000 to 4000 cm^{-1}) modes.¹ Upon compression, the phonon DOS for TIP4P/ice (Fig. 3.8 (a)) shows strong shifts towards higher frequencies for the crystal and librational. The intramolecular bending and stretching modes on the other hand are hardly affected. Consequently, the first moment of the phonon DOSs (i.e. $E_{\text{ZP,TIP4P/ice}}(V)$, see Eq. (3.6)) is monotonously increasing for $V < V_0$, and thus the minimum of $F_{\text{TIP4P/ice}}(V, T = 0)$ (see 3.5) shifts to the right as shown in Fig. 3.8 (b). This is in good agreement with the microscopic Grüneisen parameters ($\gamma_i = -\frac{V}{\omega_i} \frac{\partial \omega_i}{\partial V}$) that Ramírez *et al.* [24] have calculated for ice II using the q-TIP4P/F model.

For PBE+TS these upwards shifts of the crystal and librational modes due to compression are almost the same as for TIP4P/ice (Fig. 3.8 (c)). However, only the bending modes remain unaffected, whereas the stretching modes shift in the exact opposite way. This almost compensates the effect of the low-frequency modes on the first moment of the phonon DOS, so that $E_{\text{ZP,PBE+TS}}(V)$ is almost constant and the minima of $E_{\text{PBE+TS}}(V)$ and $F_{\text{PBE+TS}}(V, T = 0)$, $V_{0,\text{PBE+TS}}$ and $(V_{0,\text{PBE+TS}}^{\text{ZPE}})$, practically coincide as shown in Fig. 3.8 (d).

According to the Raman spectra measured by Minceva-Sukarova *et al.* [67] the change of O-H stretch frequencies with pressure $\frac{\partial \nu}{\partial P}$ is about $80\text{ cm}^{-1}/\text{GPa}$ for most crystalline ice phases for a wide range of temperatures between 250 and 0 K. Given a bulk modulus B_0 between 12 and 16.5 GPa in this temperature range for ice II [68], this allows us to

¹See also Fig. 2.7 in Section 2.4.2 for ice Ih.

estimate the expected frequency change $\Delta\nu \approx \frac{-B_0}{V_0} \frac{\partial\nu}{\partial P} \Delta V_0 \approx \pm 38$ to 53cm^{-1} for the volume change $\Delta V_0 = \pm 0.04 \cdot V_0$ considered in Fig. 3.8. The average frequency shifts according to the data presented in that figure are 10 cm^{-1} and 116 cm^{-1} for TIP4P/ice and PBE + TS, respectively, thus revealing slightly larger relative errors for the FF considering the fact that the simulations have been carried out for 0 K. The better description of the equilibrium volumes by the FFs thus appears to be fortuitous error canceling. This is consistent with the failure of q-TIP4P/F to describe the anomalous volume isotope effect for ice Ih [18] as well as isotope dependence of the ice XI-ice Ih phase transition temperature [28], which, however, is also quite challenging to be modeled correctly by first-principles-based techniques [27].

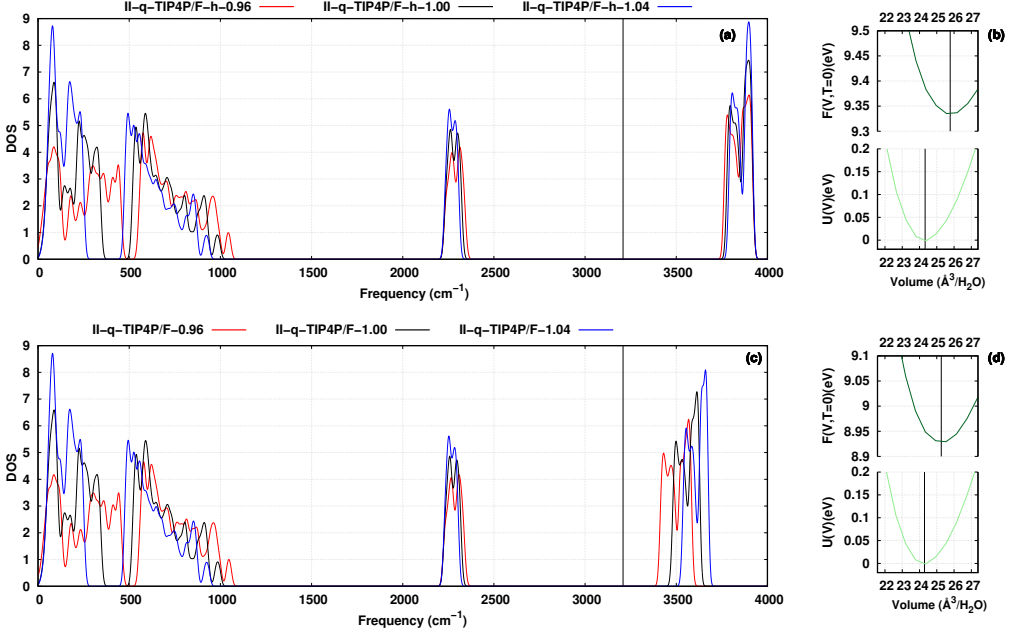


Figure 3.9: Same as Fig. 3.8, but for q-TIP4P/F-h ((a) and (b)) and q-TIP4P/F ((c) and (d)). In q-TIP4P/F-h the Morse potential describing the intramolecular OH bond has been replaced by the harmonic potential that is identical to the Morse potential up to second order.

In order to analyze how much harmonic potential used together with TIP4P/ice for

the intramolecular O-H-bond (see Section 3.2.1) affects the results shown in Fig. 3.8, I turn to q-TIP4P/F, where these bonds are described by a Morse potential. Approximating the latter by a second-order Taylor expansion and keeping all other parameters unchanged (force field labeled q-TIP4P/F-h), I have recalculated the phonon DOS for ice II. The results are shown in Fig. 3.9 (a) in comparison to conventional q-TIP4P/F shown in Fig. 3.9 (b). As expected by construction, only the O-H stretching modes in the phonon DOS are different. The harmonic potential in q-TIP4P/F-h yields much more rigid O-H bonds than the Morse potential in q-TIP4P/F, as evidenced by their position and much smaller shift upon compression and expansion. In fact, for q-TIP4P/F the corresponding average frequency shifts of 87 cm^{-1} (53 cm^{-1}) for 4% compression (4% expansion) fit very nicely to the aforementioned values suggested by the Raman experiments. The strong influence of the Morse potential can be understood by considering its second derivative with respect to the O-H bond distance r^{OH}

$$\frac{\partial^2 V^{\text{Morse}}}{\partial r_{\text{OH}}^2} = 2D\alpha^2 e^{-\alpha\Delta r^{\text{OH}}} \left(2e^{-\alpha\Delta r^{\text{OH}}} - 1 \right) \quad , \quad (3.13)$$

where D is the well depth, α is the width and $\Delta r^{\text{OH}} = r^{\text{OH}} - r_0^{\text{OH}}$ is the deviation from the equilibrium O-H bond length r_0^{OH} for a single H_2O molecule. Despite the small changes of the latter in the ice crystal (i.e. $0 < \Delta r^{\text{OH}} \ll 1$), the exponential terms in Eq. (3.13) show that vibrational frequencies are very sensitive to Δr^{OH} . Quite in contrast, the second derivative of the harmonic potential is constant, i.e. completely unaffected by Δr^{OH} .

3.4 Conclusion

I have performed a comprehensive study on seven crystalline (proton-ordered) ice phases with a wide range of DFT functional, including the recently developed meta-GGAs SCAN and SCAN+RVV10, and commonly-used off-the-shelf (non-polarizable) water force fields. A particular focus has been on accurate phonon calculations within the quasi-harmonic approximation, which has been found to be very successful for ice structures [23, 24], in order to account for zero-point energy effects. Looking at

equilibrium volumes, cohesive energies and phase transition pressure, the force fields show an overall good or even better performance than DFT. q-TIP4P/F is the clear winner among the FFs considered in this study with 5 % error in equilibrium volume and quite accurate cohesive energy and transition pressures in particular when ZPE is taken into account. Quite in contrast, the DFT results are much less affected by ZPE. The DFT functionals struggle much more with a simultaneously good description for all these properties as already discussed in earlier studies: PBE+MBD deviates from the cohesive energy by more than 100 meV/H₂O, but shows the best agreement with the experimental volumes [19]. The SCAN functional underestimates the equilibrium volume by 10 % and overestimates the absolute cohesive energy by 60 meV/H₂O, but yields relative cohesive energies and relative equilibrium volumes that are in remarkable agreement with experiment [55].

Our decomposition of the cohesive energies reveals that intramolecular deformation is over-compensated by electrostatics and the attractive part of the Lennard-Jones potentials in case of the FFs. The electrostatics are also the dominant and typically even larger bonding contribution for the DFT methods. In case of PBE+TS and PBE+vdW van der Waals interactions stabilize the crystals additionally. While the latter monotonously increase from ice Ih to ice VIII this is not the case for the attractive part of the Lennard-Jones potentials. Our analysis of phonon DOSs has revealed that the smaller redshift (blueshift) of the O-H stretch vibrations upon compression (expansion) of the crystal (i.e. the corresponding Grüneisen parameters) obtained with all FFs compared to all DFT functionals considered here is responsible for the larger effect of ZPE for the FFs. This is in line with previous work for a few ice structures [18, 24]. Comparison to Raman spectra measured as function of pressure [67] indicates that neither shifts are accurate when the intramolecular O-H stretching is described with a harmonic potential in case of the FFs. I have clearly identified the Morse potential in q-TIP4P/F to yield a significant improvement. Future work with state-of-the polarizable force fields [22] could provide valuable insights for both the bonding contributions and the vibrational frequency shifts.

3.A Appendix

3.A.1 Data for Equilibrium Ice Structures

Tables 3.2 to 3.8 list the optimum lattice parameters for the seven proton-ordered ice phases (see Table 3.1 and Fig. 3.1) as obtained using different force fields (SPC/E [38], TIP3P [39], TIP4P/2005 [40], TIP4P/ice [41] and q-TIP4P/F [42]) and exchange-correlation functionals (LDA [45], PBE [46], PBE+TS [49], PBE+MBD [50], SCAN [55], SCAN+rVV10 [56]). Corresponding volumes per water molecule V_0 (V_0^{ZPE}), bulk moduli B_0 (B_0^{ZPE}) and cohesive energies E_{coh} ($E_{\text{coh}}^{\text{ZPE}}$) without (with) zero-point energy taken into account are given as well. Experimental data is included for comparison.

Table 3.2: Data for ice Ih.

	SPC/E	TIP3P	TIP4P /2005	q-TIP4P /F	TIP4P /ice	LDA	PBE	PBE +TS	PBE +MBD	SCAN	SCAN +rVV10	Exp.
Ice Ih, $P6_3cm$												
a (Å)	7.60	7.78	7.67	7.74	7.71	7.19	7.67	7.58	7.63	7.51	7.42	7.78 ^a
c (Å)	7.10	7.17	7.10	7.24	7.12	6.80	7.24	7.15	7.18	7.11	7.04	7.33 ^a
V_0 (Å ³)	29.63	31.33	30.16	31.33	30.58	25.37	30.72	29.64	30.13	28.91	27.98	
V_0^{ZPE} (Å ³)	31.37	33.07	31.99	32.44	32.31	24.57	30.46	29.21	29.19	28.51	28.18	32.05 ^a
B_0 (GPa)	20.53	18.61	19.36	17.76	21.03	29.05	14.54	16.48	16.55	17.26	18.28	
B_0^{ZPE} (GPa)	14.95	13.42	14.99	14.20	16.52	24.63	12.53	14.08	14.20	18.23	20.58	9.2 ^b
E_{coh} (eV)	0.635	0.598	0.700	0.619	0.769	1.168	0.630	0.717	0.778	0.687	0.709	0.609 ^c
$E_{\text{coh}}^{\text{ZPE}}$ (eV)	0.505	0.436	0.514	0.487	0.574	1.059	0.501	0.583	0.654	0.618	0.596	0.491 ^c

^a10 K, from Ref. [69]. ^b248 K, from Ref. [70].

^c0 K, from Ref. [66].

Table 3.3: Data for ice IX.

	SPC/E	TIP3P	TIP4P	q-TIP4P	TIP4P	LDA	PBE	PBE	PBE	SCAN	SCAN	Exp.
			/2005	/F	/ice			+TS	+MBD		+rVV10	
Ice IX, $P4_12_12$												
a (Å)	6.68	6.91	6.57	6.59	6.60	6.18	6.60	6.49	6.56	6.46	6.39	6.72 ^a
c (Å)	6.43	6.22	6.79	6.84	6.83	6.49	7.50	6.80	7.31	6.55	6.36	6.79 ^a
V_0 (Å ³)	23.92	24.78	24.42	24.74	24.77	20.67	27.22	23.88	26.21	22.79	21.63	
V_0^{ZPE} (Å ³)	25.30	26.10	25.83	25.59	26.13	20.42	27.41	24.17	25.17	23.41	22.13	25.63 ^a
B_0 (GPa)	14.97	15.51	13.83	12.24	14.83	21.53	11.77	15.68	11.88	14.30	17.28	
B_0^{ZPE} (GPa)	9.74	10.27	8.60	9.84	9.82	22.06	10.29	13.92	12.87	14.71	14.11	7.55 ^b
E_{coh} (eV)	0.638	0.617	0.691	0.613	0.759	1.131	0.588	0.708	0.755	0.674	0.710	0.607 ^c
$E_{\text{coh}}^{\text{ZPE}}$ (eV)	0.514	0.458	0.512	0.485	0.572	1.020	0.460	0.575	0.636	0.601	0.593	0.487 ^c

^a30 K, from Ref. [31].^b253 K, for ice III (i.e. proton-disordered ice IX), Ref. [71].^c0 K, from Ref. [66].

Table 3.4: Data for ice II.

	SPC/E	TIP3P	TIP4P	q-TIP4P	TIP4P	LDA	PBE	PBE	PBE	SCAN	SCAN	Exp.
			/2005	/F	/ice			+TS	+MBD		+rVV10	
Ice II, $R\bar{3}$												
a (Å)	7.49	7.62	7.63	7.68	7.67	7.14	7.70	7.57	7.66	7.47	7.39	7.78 ^a
α (°)	112.98	113.10	113.17	113.15	113.17	112.92	112.81	113.02	112.87	113.08	113.17	113.10 ^a
V_0 (Å ³)	22.80	23.86	23.79	24.34	24.15	19.85	25.03	23.50	24.58	22.47	21.60	
V_0^{ZPE} (Å ³)	24.11	25.13	25.11	25.26	25.39	19.74	25.35	23.92	23.54	22.60	22.08	24.97 ^b
B_0 (GPa)	25.40	25.18	24.46	20.69	26.69	35.73	15.83	20.66	20.03	22.19	24.03	
B_0^{ZPE} (GPa)	19.60	19.67	19.10	16.85	20.75	32.73	13.34	17.22	11.45	17.66	24.29	16.18 ^c
E_{coh} (eV)	0.645	0.631	0.681	0.604	0.748	1.123	0.562	0.700	0.743	0.677	0.716	0.609 ^d
$E_{\text{coh}}^{\text{ZPE}}$ (eV)	0.522	0.472	0.510	0.479	0.570	1.007	0.435	0.564	0.616	0.601	0.599	0.490 ^d

^a200 K, from Ref. [33]. ^b0 K, from Ref. [66].^c0 K, from Ref. [68]. ^d0 K, from Ref. [66].

CHAPTER 3. IMPORTANCE OF ZERO-POINT ENERGY FOR CRYSTALLINE ICE PHASES

Table 3.5: Data for ice XIII.

	SPC/E	TIP3P	TIP4P	q-TIP4P	TIP4P	LDA	PBE	PBE	PBE	SCAN	SCAN	Exp.
			/2005	/F	/ice			+TS	+MBD		+rVV10	
Ice XIII, P_{21}/a												
a (Å)	9.22	9.43	9.24	9.35	9.28	8.51	9.22	8.94	8.96	8.88	8.74	9.24 ^a
b (Å)	7.05	6.99	7.32	7.37	7.36	6.94	7.52	7.39	7.41	7.25	7.17	7.47 ^a
c (Å)	9.93	10.10	10.04	10.13	10.09	9.54	10.30	10.01	10.04	9.91	9.77	10.29 ^a
β (°)	108.01	107.82	109.77	110.38	109.83	109.97	109.25	109.04	109.06	109.53	109.28	109.70 ^a
V_0 (Å ³)	21.92	22.63	22.79	23.37	23.13	18.91	24.05	22.30	22.50	21.48	20.65	
V_0^{ZPE} (Å ³)	23.11	23.79	24.02	24.24	24.29	18.85	24.33	22.66	22.16	21.67	21.09	23.91 ^a
B_0 (GPa)	23.61	21.03	22.60	20.05	24.53	34.42	15.11	21.66	20.10	21.53	23.62	
B_0^{ZPE} (GPa)	18.16	16.22	18.62	17.19	20.63	31.82	12.94	18.06	21.93	17.71	21.76	13.2 ^b
E_{coh} (eV)	0.619	0.606	0.672	0.598	0.738	1.111	0.551	0.698	0.740	0.668	0.711	
$E_{\text{coh}}^{\text{ZPE}}$ (eV)	0.502	0.451	0.500	0.473	0.559	0.997	0.426	0.568	0.618	0.589	0.593	

^a80 K, from Ref. [32].

^b248 K, for ice V (i.e. proton-disordered ice XIII), Ref. [70].

Table 3.6: Data for ice XIV.

	SPC/E	TIP3P	TIP4P	q-TIP4P	TIP4P	LDA	PBE	PBE	PBE	SCAN	SCAN	Exp.
			/2005	/F	/ice			+TS	+MBD		+rVV10	
Ice XIV, $P_{21}2_12_1$												
a (Å)	7.83	7.84	8.05	8.17	8.09	7.74	8.45	8.25	8.33	8.07	7.94	8.35 ^a
b (Å)	8.35	8.61	8.31	8.28	8.35	7.60	8.22	8.01	8.09	7.80	7.67	8.14 ^a
c (Å)	3.85	3.87	3.85	3.92	3.87	3.73	4.02	3.93	3.96	3.94	3.91	4.08 ^a
V_0 (Å ³)	20.98	21.78	21.47	22.11	21.78	18.28	23.28	21.61	22.23	20.70	19.83	
V_0^{ZPE} (Å ³)	22.19	22.99	22.70	22.94	22.93	18.22	23.68	22.03	21.31	20.92	20.41	23.12 ^a
B_0 (GPa)	27.14	25.29	27.34	24.31	30.02	38.91	15.82	21.92	21.85	23.49	25.87	
B_0^{ZPE} (GPa)	20.52	19.06	20.57	20.07	23.22	35.46	13.51	18.31	32.68	21.05	22.91	
E_{coh} (eV)	0.610	0.595	0.679	0.604	0.746	1.104	0.538	0.692	0.732	0.666	0.709	
$E_{\text{coh}}^{\text{ZPE}}$ (eV)	0.490	0.440	0.502	0.477	0.561	0.990	0.412	0.557	0.612	0.587	0.594	

^a80 K, from Ref. [32].

Table 3.7: Data for ice XV.

	SPC/E	TIP3P	TIP4P /2005	q-TIP4P /F	TIP4P /ice	LDA	PBE	PBE +TS	PBE +MBD	SCAN	SCAN +rVV10	Exp.
Ice XV, $P\bar{1}$												
a (Å)	6.00	6.01	6.14	6.21	6.17	5.76	6.24	6.13	6.20	6.01	5.94	6.23 ^a
b (Å)	5.99	6.00	6.12	6.20	6.15	5.78	6.24	6.13	6.21	6.00	5.92	6.24 ^a
c (Å)	55.74	5.91	5.63	5.65	5.65	5.35	5.85	5.69	5.77	5.62	5.52	5.79 ^a
α (°)	87.93	85.95	89.63	90.22	89.65	89.93	90.09	90.30	90.24	90.08	89.98	90.10 ^a
β (°)	86.57	84.60	88.49	88.84	88.53	89.90	89.57	89.83	89.79	89.85	89.94	89.90 ^a
γ (°)	87.97	86.54	89.27	89.72	89.31	90.52	90.61	90.50	90.50	90.70	90.731	89.90 ^a
V_0 (Å ³)	20.58	21.14	21.13	21.75	21.43	17.82	22.80	21.33	22.24	20.24	19.40	
V_0^{ZPE} (Å ³)	21.74	22.29	22.29	22.53	22.50	17.81	23.24	21.80	21.26	20.56	20.01	22.53 ^a
B_0 (GPa)	27.71	26.75	27.52	24.49	30.46	40.27	16.26	22.09	21.22	24.29	26.74	
B_0^{ZPE} (GPa)	20.87	20.35	21.03	20.27	23.80	36.89	13.68	18.40	22.64	19.58	24.53	13.08 ^b
E_{coh} (eV)	0.601	0.593	0.664	0.590	0.730	1.088	0.520	0.680	0.715	0.658	0.706	
$E_{\text{coh}}^{\text{ZPE}}$ (eV)	0.487	0.441	0.495	0.467	0.553	0.973	0.395	0.544	0.598	0.582	0.591	

^a80 K, from Ref. [34].^b253 K, for ice VI (i.e. proton-disordered ice XV), Ref. [71].

Table 3.8: Data for ice VIII.

	SPC/E	TIP3P	TIP4P /2005	q-TIP4P /F	TIP4P /ice	LDA	PBE	PBE +TS	PBE +MBD	SCAN	SCAN +rVV10	Exp.
Ice VIII, $I4_1/amd$												
a (Å)	4.48	4.38	4.63	4.74	4.65	4.44	4.86	4.79	4.81	4.63	4.57	4.57 ^a
c (Å)	7.44	7.76	7.17	7.01	7.20	6.38	7.03	6.96	7.00	6.70	6.60	6.77 ^a
V_0 (Å ³)	18.66	18.64	19.22	19.70	19.52	15.75	20.73	19.93	20.27	17.98	17.23	
V_0^{ZPE} (Å ³)	19.83	19.78	20.33	20.57	20.57	16.17	21.65	20.55	19.63	18.97	19.80	20.09 ^b
B_0 (GPa)	29.00	28.31	29.37	26.05	31.63	46.01	15.61	18.11	22.60	28.23	31.23	
B_0^{ZPE} (GPa)	21.19	19.49	21.68	20.97	23.33	41.56	11.73	16.24	85.57	48.04	6.92	24.3 ^c
E_{coh} (eV)	0.519	0.532	0.588	0.531	0.646	1.042	0.453	0.620	0.663	0.643	0.704	0.577 ^d
$E_{\text{coh}}^{\text{ZPE}}$ (eV)	0.420	0.391	0.437	0.415	0.488	0.910	0.328	0.488	0.556	0.550	0.574	0.458 ^d

^a10 K, from Ref. [35]. ^b0 K, from Ref. [66].^c87 K, from Ref. [72]. ^d0 K, from Ref. [66].

3.5 References

1. J. Poirier, *Nature* **299**, 683 (1982).
2. P. Jenniskens, D. Blake, *Science* **265**, 753–756 (1994).
3. P. Jenniskens, D. Blake, M. Wilson, A. Pohorille, *Astrophys. J.* **455**, 389 (1995).
4. B. J. Murray, D. A. Knopf, A. K. Bertram, *Nature* **434**, 202–205 (2005).
5. P. Mehl, P. Boutron, *Le Journal de Physique Colloques* **48**, C1–449 (1987).
6. C. Lee, D. Vanderbilt, K. Laasonen, R. Car, M. Parrinello, *Phys. Rev. Lett.* **69**, 462–465 (1992).
7. N. H. Fletcher, *Rep. Prog. Phys.* **34**, 913–994–2 (1971).
8. T. L. Malkin, B. J. Murray, C. G. Salzmann, V. Molinero, S. J. Pickering, *et al.*, *Phys. Chem. Chem. Phys.* **17**, 60–76 (2015).
9. E. Sanz, C. Vega, J. L. F. Abascal, L. G. MacDowell, *Phys. Rev. Lett.* **92**, 255701 (2004).
10. Y. Fang, B. Xiao, J. Tao, J. Sun, J. P. Perdew, *Phys. Rev. B* **87**, 214101 (2013).
11. M. J. Gillan, D. Alfè, A. Michaelides, *J. Chem. Phys.* **144**, 130901 (2016).
12. J. Li, D. K. Ross, *Nature* **365**, 327–329 (1993).
13. S. J. Singer, J.-L. Kuo, T. K. Hirsch, C. Knight, L. Ojamäe, *et al.*, *Phys. Rev. Lett.* **94**, 135701 (2005).
14. I. Hamada, *J. Chem. Phys.* **133**, 214503 (2010).
15. B. Kolb, T. Thonhauser, *Phys. Rev. B* **84**, 045116 (2011).
16. B. Santra, J. Klimeš, D. Alfè, A. Tkatchenko, B. Slater, *et al.*, *Phys. Rev. Lett.* **107**, 185701 (2011).
17. É. D. Murray, G. Galli, *Phys. Rev. Lett.* **108**, 105502 (2012).
18. B. Pamuk, J. M. Soler, R. Ramírez, C. P. Herrero, P. W. Stephens, *et al.*, *Phys. Rev. Lett.* **108**, 193003 (2012).
19. B. Santra, J. Klimeš, A. Tkatchenko, D. Alfè, B. Slater, *et al.*, *J. Chem. Phys.* **139**, 154702 (2013).
20. A. M. Reilly, A. Tkatchenko, *J. Chem. Phys.* **139**, 024705 (2013).
21. J. Sun, R. C. Remsing, Y. Zhang, Z. Sun, A. Ruzsinszky, *et al.*, *Nat. Chem.* **8**, 831–836 (2016).
22. G. A. Cisneros, K. T. Wikfeldt, L. Ojamäe, J. Lu, Y. Xu, *et al.*, *Chem. Rev.* **116**, 7501–7528 (2016).
23. C. P. Herrero, R. Ramírez, *J. Chem. Phys.* **134**, 094510 (2011).
24. R. Ramírez, N. Neuerburg, M.-V. Fernández-Serra, C. P. Herrero, *J. Chem. Phys.* **137**, 044502 (2012).
25. E. A. Engel, B. Monserrat, R. J. Needs, *J. Chem. Phys.* **143**, 244708 (2015).
26. E. A. Engel, B. Monserrat, R. J. Needs, *Phys. Rev. X* **5**, 021033 (2015).
27. M. A. Salim, S. Y. Willow, S. Hirata, *J. Chem. Phys.* **144**, 204503 (2016).
28. B. Pamuk, P. B. Allen, M.-V. Fernández-Serra, *Phys. Rev. B* **92**, 134105 (2015).
29. D. R. Hamann, *Phys. Rev. B* **55**, R10157–R10160 (1997).

-
30. C. G. Salzmann, P. G. Radaelli, B. Slater, J. L. Finney, *Phys. Chem. Chem. Phys.* **13**, 18468–18480 (2011).
 31. J. D. Londono, W. F. Kuhs, J. L. Finney, *J. Chem. Phys.* **98**, 4878–4888 (1993).
 32. C. G. Salzmann, P. G. Radaelli, A. Hallbrucker, E. Mayer, J. L. Finney, *Science* **311**, 1758–1761 (2006).
 33. C. Lobban, J. L. Finney, W. F. Kuhs, *J. Chem. Phys.* **117**, 3928–3934 (2002).
 34. C. G. Salzmann, P. G. Radaelli, E. Mayer, J. L. Finney, *Phys. Rev. Lett.* **103**, 105701 (2009).
 35. W. F. Kuhs, J. L. Finney, C. Vettier, D. V. Bliss, *J. Chem. Phys.* **81**, 3612–3623 (1984).
 36. G. S. Kell, E. Whalley, *J. Chem. Phys.* **48**, 2359–2361 (1968).
 37. S. Plimpton, *J. Comput. Phys.* **117**, 1–19 (1995).
 38. H. J. C. Berendsen, J. R. Grigera, T. P. Straatsma, *J. Phys. Chem.* **91**, 6269–6271 (1987).
 39. W. L. Jorgensen, J. Chandrasekhar, J. D. Madura, R. W. Impey, M. L. Klein, *J. Chem. Phys.* **79**, 926–935 (1983).
 40. J. L. F. Abascal, C. Vega, *J. Chem. Phys.* **123**, 234505 (2005).
 41. J. L. F. Abascal, E. Sanz, R. García Fernández, C. Vega, *J. Chem. Phys.* **122**, 234511 (2005).
 42. S. Habershon, T. E. Markland, D. E. Manolopoulos, *J. Chem. Phys.* **131**, 024501 (2009).
 43. D. M. Carey, G. M. Korenowski, *J. Chem. Phys.* **108**, 2669–2675 (1998).
 44. D. Frenkel, B. Smit, *Understanding Molecular Simulation – From Algorithms to Applications* (Academic Press, San Diego, 2002), vol. 1.
 45. J. P. Perdew, A. Zunger, *Phys. Rev. B* **23**, 5048–5079 (1981).
 46. J. P. Perdew, K. Burke, M. Ernzerhof, *Phys. Rev. Lett.* **77**, 3865–3868 (1996).
 47. V. Blum, R. Gehrke, F. Hanke, P. Havu, V. Havu, *et al.*, *Comp. Phys. Comm.* **180**, 2175–2196 (2009).
 48. V. Havu, V. Blum, P. Havu, M. Scheffler, *J. Comput. Phys.* **228**, 8367–8379 (2009).
 49. A. Tkatchenko, M. Scheffler, *Phys. Rev. Lett.* **102**, 073005 (2009).
 50. A. Tkatchenko, R. A. DiStasio, R. Car, M. Scheffler, *Phys. Rev. Lett.* **108**, 236402 (2012).
 51. G. Kresse, J. Hafner, *Phys. Rev. B* **47**, 558–561 (1993).
 52. G. Kresse, J. Furthmüller, *Phys. Rev. B* **54**, 11169–11186 (1996).
 53. P. E. Blöchl, *Phys. Rev. B* **50**, 17953–17979 (1994).
 54. G. Kresse, D. Joubert, *Phys. Rev. B* **59**, 1758–1775 (1999).
 55. J. Sun, A. Ruzsinszky, J. P. Perdew, *Phys. Rev. Lett.* **115**, 036402 (2015).
 56. H. Peng, Z.-H. Yang, J. P. Perdew, J. Sun, *Phys. Rev. X* **6**, 041005 (2016).
 57. O. A. Vydrov, T. Van Voorhis, *J. Chem. Phys.* **133**, 244103 (2010).
 58. R. Sabatini, T. Gorni, S. de Gironcoli, *Phys. Rev. B* **87**, 041108 (2013).

59. H. J. Monkhorst, J. D. Pack, *Phys. Rev. B* **13**, 5188–5192 (1976).
60. C. M. B. Line, R. W. Whitworth, *J. Chem. Phys.* **104**, 10008–10013 (1996).
61. B. G. Pfrommer, M. Côté, S. G. Louie, M. L. Cohen, *J. Comput. Phys.* **131**, 233–240 (1997).
62. A. H. Larsen, J. J. Mortensen, J. Blomqvist, I. E. Castelli, R. Christensen, *et al.*, *J. Phys.: Condens. Matter* **29**, 273002 (2017).
63. P. Vinet, J. R. Smith, J. Ferrante, J. H. Rose, *Phys. Rev. B* **35**, 1945–1953 (1987).
64. K. Parlinski, Z. Q. Li, Y. Kawazoe, *Phys. Rev. Lett.* **78**, 4063–4066 (1997).
65. A. Togo, I. Tanaka, *Scripta Mater.* **108**, 1–5 (2015).
66. E. Whalley, *J. Chem. Phys.* **81**, 4087–4092 (1984).
67. B. Minceva-Sukarova, W. F. Sherman, G. R. Wilkinson, *J. Phys. C: Solid State Phys.* **17**, 5833–5850 (1984).
68. A. D. Fortes, I. G. Wood, J. P. Brodholt, L. Vočadlo, *J. Chem. Phys.* **119**, 4567–4572 (2003).
69. K. Röttger, A. Endriss, J. Ihringer, S. Doyle, W. F. Kuhs, *Acta Cryst. B* **50**, 644–648 (1994).
70. G. H. Shaw, *J. Chem. Phys.* **84**, 5862–5868 (1986).
71. C. A. Tulk, R. E. Gagnon, H. Kiefte, M. J. Clouter, *J. Chem. Phys.* **107**, 10684–10690 (1997).
72. H. Yamawaki, H. Fujihisa, M. Sakashita, A. Nakayama, K. Aoki, *Physica B* **344**, 260–264 (2004).

CHAPTER 4

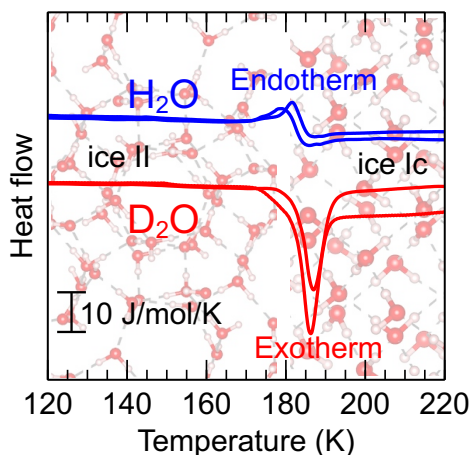
Calorimetric Signature of Deuterated Ice II

This chapter is based on:

V. Fuentes-Landete, S. Rasti, R. Schlögl, J. Meyer and T. Loerting, Calorimetric Signature of Deuterated Ice II: Turning an Endotherm to an Exotherm, *J. Phys. Chem. Lett.* **11**, 8268 (2020).

Abstract

Calorimetric studies on ice II reveal a surprising $\text{H}_2\text{O}/\text{D}_2\text{O}$ isotope effect. While the ice II to ice Ic transition is endothermic for H_2O , it is exothermic for D_2O samples. The transition enthalpies are $+40 \text{ J mol}^{-1}$ and -140 J mol^{-1} , respectively, where such a sign change upon isotope substitution is unprecedented in ice research. In order to understand the observations, force field calculations are employed using two water models known to perform well for H_2O ice phases and their vibrational properties. These simulations reveal that the isotope effect can be traced back to zero-point energy. q-TIP4P/F fares better and is able to account for about 3/4 of the isotope effect, while MB-pol only catches about 1/3. Phonon and configurational entropy contributions are necessary to predict reasonable transition enthalpies, but do not have an impact on the isotope effect. This study suggests to use these calorimetric isotope data as benchmark for water model.



4.1 Introduction

The first high-pressure form of ice, ice II, was discovered in 1900 by Tammann [1]. In the 1960s the structure of ice II has been determined to be hydrogen-ordered [2–

5]. Within the framework of the Bernal-Fowler rules [6] ice II is a phase of zero configurational entropy, where configurational entropy is solely based on the number of microstates differing in terms of H-atom positions. By contrast, hexagonal ice (ice Ih) is geometrically frustrated, showing a disordered network of H atoms. Ice Ih is hence a phase of non-zero configurational entropy. In fact, ice II is thermodynamically more stable than hexagonal ice even at ambient pressure because the entropy of ice Ih is smaller at low temperatures. The idea that the high-pressure phase ice II is the ground state at 0 K and ambient pressure had to be abandoned years later, after the discovery of the hydrogen-ordered counterpart of hexagonal ice, ice XI [7]. In 1963 Bertie, Calvert and Whalley examined the transformations that occur when heating high-pressure ices from liquid nitrogen temperatures at ambient pressure [8]. The thermal analysis was made by using a small silvered-glass vacuum flask as a calorimeter. The heating curve of ice II shows a small break in the heat capacity around 170 to 175 K. Two possible interpretations consistent with the observations were given: (i) A first-order phase transition involving an undetectably small heat, but associated with a large decrease of heat capacity, and (ii) a continuous transition involving decrease in heat capacity. 25 years later, in 1988, Handa and Klug [9] demonstrated that actually interpretation (i) is correct, by detecting the heat involved in the transition to cubic ice (ice Ic). They reported a weak endotherm when heating ice II in their Tian-Calvet calorimeter at 10 K h^{-1} with an onset temperature at 161 K and enthalpy of transformation (ΔH) of $+54 \pm 5 \text{ J mol}^{-1}$ [9]. That makes ice II the only example of a high-pressure ice converting endothermically to ice Ic at 1 bar. For comparison other high-pressure ice phases such as ice V, ice VI or ice XII show pronounced exotherms of $-926 \pm 20 \text{ J mol}^{-1}$ [10], $-1523 \pm 16 \text{ J mol}^{-1}$ [11] and $-1233 \pm 23 \text{ J mol}^{-1}$ [12], respectively.

This is explained by taking into account that the heat of transformation is composed of two contributions. The first contribution is an enthalpic term arising from the transformation from high density (ice II) to low density (ice Ic). The restructuring from ice II to ice Ic involves a density change from 1.21 g/cm^3 to 0.94 g/cm^3 [13]. In spite of this 22 % density decrease, the structural motif of hexagonal channels is conserved. Up to 7/12 of all hydrogen bonds are retained at the irreversible cooperative $\text{II} \rightarrow \text{Ic}$

transition [14]. Just like for all other high-pressure ice phases this enthalpic term is exothermic [9]. The second contribution is an entropic term arising from the transformation of hydrogen-ordered (ice II) to hydrogen-disordered (ice Ic). This change in the H-atom subnetwork is also responsible for the increase in heat capacity observed in the calorimetry scans - the number of degrees of freedom and hence heat capacity is smaller in an H-ordered ice. This entropic term is endothermic, just like for all disordering transformations, e.g., melting. In sum the two contributions result in a very weak overall endotherm associated with the ice II \rightarrow ice Ic transformation at 1 bar. By contrast, ices V, VI and XII are all hydrogen-disordered. On their phase transitions to hydrogen-disordered ice Ic only the enthalpic term plays a role, but not the entropic term. The presence of both terms makes the ice II \rightarrow ice Ic transition a particularly challenging case, also of great interest for simulations and benchmarking water models. Studies with deuterated samples are of high importance since these are required to deduce the crystal structure from neutron diffraction data. The thermal behavior of several deuterated ice samples has been investigated by differential scanning calorimetry [11, 12, 15–17]. Deuteration usually translates into a more exothermic transformation to ice Ic. Specifically, the exotherm increases by 107 and 175 J mol⁻¹ after deuteration of ices VI and XII, respectively [11, 12]. Although ice II was discovered more than a century ago, no calorimetric data for D₂O ice II have been available up to now. This chapter reports the thermal behavior of recovered D₂O ice II and compare it with the one for H₂O. Our study reveals an exothermic ice II to ice Ic transition for D₂O, contrary to the endothermic nature for H₂O. This represents the first example in which the calorimetric signature changes from endothermic to exothermic upon deuteration. To rationalize these findings the transition is analyzed based on lattice energy and phonon calculations.

4.2 Methods

4.2.1 Experimental Methods

The ice II samples were prepared in the piston-cylinder apparatus by using a computerized universal testing machine (Zwick, model BZ100/TL3S). This study used 600 μL of H_2O or D_2O , which were pipetted into an indium container inside the high-pressure apparatus for compression. Indium containers were employed to avoid unwanted pressure drops during experiments [18]. Two different protocols were followed for the preparation of ice II samples. The first protocol is taken from Bauer *et al.* [19] and consists of the direct polymorphic transformation of ice Ih to ice II by slow compression to 0.40 GPa at 198 K. The rather low compression rate of 10 MPa min^{-1} between 0.20 to 0.40 GPa ensures that no parallel polymorphic transformation takes place [19]. The second protocol used to produce ice II is adapted from the work of Salzmann *et al.* [20]. By heating ice Ih at 0.50 GPa, a chain of polymorphic transformations to ice III, ice II and ice V takes place up to $\sim 250 \text{ K}$. By isobaric heating of Ih at 0.50 GPa to $\sim 200 \text{ K}$ ice II is obtained.

In both routes the pressurized ice II sample is then quenched in liquid nitrogen, and the pressure released to recover ice II at ambient pressure. No transformations take place upon quench-recovery. In spite of hexagonal ice being the stable phase at 77 K, no transformation back to hexagonal ice takes place while storing the sample at ambient pressure and 77 K. At 77 K the kinetics of O-atom restructuring is immeasurably slow. The restructuring of the network of O atoms only proceeds at measurable rates above about 150 K.

Typically, a mass of 10 to 20 mg was cut from the cylindrical ice II sample of 600 mg in total. The grains of ice II were then transferred under liquid nitrogen into an aluminum crucible and covered with a lid. These crucibles were cold loaded into our differential scanning calorimeter (DSC 8000 Perkin Elmer) and subsequently heated two times at 30 K min^{-1} . The first scan, heated to 253 K, shows the polymorphic transitions first to ice Ic and ultimately yielding hexagonal ice Ih. The second one, to 313 K, shows

the endotherm due to the melting of hexagonal ice Ih. From the melting peak the mass of the sample have been calculated based on the known heat of fusion of D_2O , 6280 J mol^{-1} [21] (or 6012 J mol^{-1} in case of H_2O). All calorimetry scans were recorded at ambient pressure. This procedure is identical to the established procedure reported in earlier work from Gasser *et al.* [22] and Fuentes-Landete *et al.* [23, 24]

4.2.2 Computational Details

The computational setup is almost identical to the one used in Chapter 3. Briefly, the q-TIP4P/F water model [25] has been evaluated using the Atomic Simulation Environment (ASE) [26] with the LAMMPS code [27] via the available calculator, whereas a new calculator has been implemented in order to interface with the MB-pol model¹ as developed and implemented by the Paesani group [28–30]. Data obtained from neutron diffraction experiments [31, 32] has been used with the GENICE package [33] in order to generate the initial structures of ice II and I.

ASE is employed for all geometry optimizations² with a tight maximum force threshold of $10^{-4} \text{ eV } \text{\AA}^{-1}$. Vibrational properties have been calculated for the different ice phases based on the Parlinski-Li-Kawazoe finite-displacement method [35] (using displacements of 10^{-3} \AA) as implemented in the PHONOPY package [36]. Very tight $30 \times 30 \times 30$ reciprocal space grids have been used for the evaluation of Eq. (4.5), resulting in at

¹MB-pol calculations are based on an in-house ASE-calculator building on the MB-pol plugin for OpenMM (Release 1.1.2), available from the Paesani group (<https://github.com/paesani-lab/mbpol-openmm-plugin>). This implementation can only handle periodic boundary conditions for orthogonal cells of a certain minimum size. For this reason, a $3 \times 3 \times 3$ ($3 \times 2 \times 7$) supercell of ice Ih (ice II) has been constructed internally in our ASE-MB-pol calculator.

²The calculations reported here are based on structure optimizations that do not constrain the space group. The structure optimizations have also been repeated for ice Ih using the in-house space-group constraint (SPGC) discussed in more details in Chapter 3. Briefly, in order to simultaneously relax the lattice vectors and the internal coordinates of each ice structure while constraining its space group, the algorithm suggested by Pfrommer *et al.* [34] has been implemented into the Atomic Simulation Environment (ASE) [26]. At Tables 4.5 and 4.6, the results were compared from these calculations to the corresponding ones in Tables 4.2 and 4.3

least 1456 points in the irreducible wedge of the Brillouin zone for which vibrational frequencies have been calculated. In these calculations, ice Ih has been used in place of ice Ic since these two ice phases are energetically almost degenerate, with hexagonal ice being more stable by a margin close to zero, even difficult to measure in calorimetry scans. Fig. 4.1 shows a very small baseline change near 210 K that corresponds to the ice Ic to ice Ih transition - this exotherm is smaller than 10 J/mol and negligible in the present context. Engel *et al.* [37] have suggested that the proper energetic ordering of ices Ih and Ic can only be described by taking anharmonic effects into account, which is beyond the scope of the present work. Furthermore, ice Ic and ice Ih have almost indistinguishable spectral properties from the microwave to the ultraviolet. For this reason they are commonly both denoted as ice I, where the difference between ice Ic and ice Ih is the stacking-sequence. Specifically, all vibrational transitions have long been thought to be identical for ice Ic and ice Ih [38]. Also the intermolecular phonon modes in the far-infrared spectral range barely reveal any difference. [39, 40] Subtle differences based on different polytypes of ice Ih containing different hexagonal and cubic stacking sequences have only been noted recently by Carr *et al.* [41]. In a very recent work the transition from a pure cubic stacking sequence to a pure hexagonal stacking sequence was identified, where only very small shifts, e.g., of about 2 cm^{-1} in the translational band mark the transition [42].

4.3 Results and Discussion

4.3.1 Experiments

Figure 4.1 shows the representative scans of ice II for H_2O and D_2O . For each isotopologue two different scans are reported which correspond to the two distinct routes followed for preparation of the ice II samples (for details see “Computational details” above). The H_2O calorimetric signature represented here in blue agrees well with the one published by Handa and Klug [9]. Table 4.1 shows the enthalpy and onset values for the ice II to ice Ic transition calculated in this study. Note that the heating rate

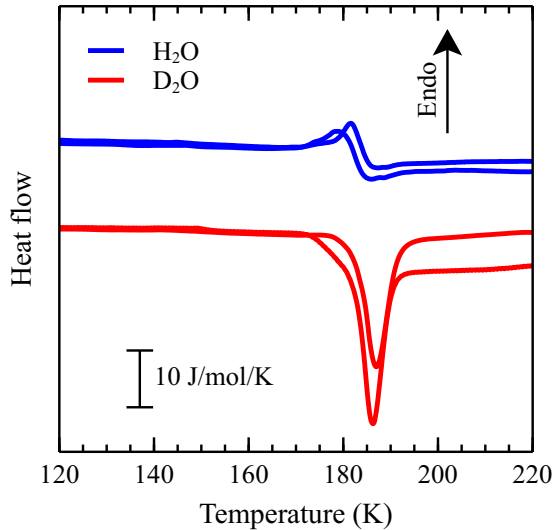


Figure 4.1: DSC heating scans recorded at 30 K min^{-1} and ambient pressure for H_2O (blue) and D_2O (red) ice II. The signal is normalized to 1 mol.

employed by Handa and Klug [9] is 10 K h^{-1} while here 30 K min^{-1} is employed, thus explaining the onset temperature shift of about $\sim 10 \text{ K}$. The D_2O scans in Fig. 4.1 in red represent the first measurements for deuterated ice II shown in literature. The exothermic nature of this transition can be easily recognized. Whereas the transition is endothermic for the two preparation protocols for H_2O ($+33 \pm 11 \text{ J mol}^{-1}$ and $+48 \pm 9 \text{ J mol}^{-1}$, respectively), it is exothermic for D_2O ice II ($-132 \pm 36 \text{ J mol}^{-1}$ and $-149 \pm 50 \text{ J mol}^{-1}$, respectively) [19, 20]. That is, the ice II \rightarrow ice Ic transition is more exothermic by about $180 \pm 20 \text{ J mol}^{-1}$ in D_2O than in H_2O . In the present work, the enthalpy values are averages of at least ten different scans for each preparation route. In Fig. 4.1, only one representative DSC scan is shown. This isotope effect on the enthalpy difference to ice Ic is not unusual. Similar differences were found for other high-pressure polymorphs, too. As mentioned above, the transition from ice XII to Ic is about 175 J mol^{-1} more exothermic for D_2O than for H_2O [12].

In addition, the onset temperatures for the transition in hydrogenated and deuterated

samples are shown in Table 4.1. The difference in onsets is 7 to 10 K. This is substantially more than the usual difference between structural transitions in H_2O and D_2O . For instance, all the triple points in the phase diagram are higher in D_2O than in H_2O by between 2.2 K (for the liquid-ice V-ice VI triple point) and 3.8 K (for the liquid-ice Ih-gas triple point) [43, 44]. By contrast, dynamic transitions have larger isotope effects. D_2O – H_2O isotope effects of 6 to 8 K were found for the orientational glass transitions in the H-subnetwork of ices IV, V, VI and XII [24]. This suggests that dynamics plays a crucial role for the ice II \rightarrow ice Ic transition as well. While it is H-atom dynamics in case of the orientational glass transitions, this study here measures the isotope effect on the O-atom restructuring. This restructuring takes place in an out-of-equilibrium situation, since ice II is kinetically stable at 77 K and 1 bar, but not thermodynamically. Similarly, also for the case of the ice XII \rightarrow ice Ic and ice IV \rightarrow ice Ic transitions the isotope effect on the onset temperature amounts to 7 ± 1 K at heating rates of 30 K min^{-1} [12]. Reducing the heating rate to 5 K min^{-1} the isotope effect is reduced to 4 ± 1 K [12]. That is, the onset temperature of the transition is kinetically controlled.

4.3.2 Calculations

In order to better understand the observed isotope effect on the transition enthalpy, calculations with two different water models have been performed, q-TIP4P/F [25] and MB-pol [28–30]. Both of them involve flexible water molecules, which allow to calculate vibrational properties including all inter- and intramolecular contributions. It is found in previous work that including zero-point energy (ZPE) with q-TIP4P/F provides a very good description of experimental data for a plethora of different crystalline ice phases – outperforming several density functionals despite its simplicity [45]. This study has also included the state-of-the-art polarizable many-body force field MB-pol given its excellent description of vibrational properties of ice [46, 47].

Periodic boundary conditions have been used in order to model the different ice phases and relax the structures while constraining the space group symmetry as suggested

by Pfrommer *et al.* [34]. Absolute lattice energies E_{lat} are calculated as differences of total energies between the ice phase with N_{ice} molecules in the unit cell after relaxation (E_{ice}) and the corresponding constituent molecules at infinite separation (E_{mol})

$$E_{\text{lat}} = \frac{1}{N_{\text{ice}}} E_{\text{ice}} - E_{\text{mol}} . \quad (4.1)$$

Calculating vibrational frequencies then allows to include the missing ZPE effects according to

$$E_{\text{lat}}^{\text{ZPE}} = \frac{1}{N_{\text{ice}}} (E_{\text{ice}} + E_{\text{ice}}^{\text{ZPE}}) - (E_{\text{mol}} + E_{\text{mol}}^{\text{ZPE}}) \quad (4.2)$$

In order to compare with the measured enthalpies for the ice II \rightarrow Ic transition and analyze the isotope effect, the following (free) energy differences has been considered, decreasing the number of approximations in each step:

1. Our starting point is the lattice energy difference

$$\Delta E_{\text{lat}} = E_{\text{lat}}(\text{I}) - E_{\text{lat}}(\text{II}) , \quad (4.3)$$

which is of course identical for H_2O and D_2O .

2. Isotope effects at $T = 0$ K are accounted for when including the (slightly) different ZPE corrections to the lattice energies for each ice phase

$$\Delta E_{\text{lat}}^{\text{ZPE}} = E_{\text{lat}}^{\text{ZPE}}(\text{I}) - E_{\text{lat}}^{\text{ZPE}}(\text{II}) . \quad (4.4)$$

3. Since the ice II \rightarrow ice Ic transformation occurs at ambient pressure in the experiments, the contribution of the pV -term in the Gibbs free energy related to the density decrease during the transformation is negligible. On the other hand, $T \gg 0$ K and so the temperature dependence of the vibrational contribution to the Gibbs free energy cannot *a priori* be neglected:

$$F_{\text{phonon}}(V, T) = \underbrace{\frac{1}{2} \sum_{\mathbf{q}, b} \hbar \omega_{\mathbf{q}, b}(V)}_{E_{\text{ZPE}}} + k_{\text{B}} T \sum_{\mathbf{q}, b} \ln \left[1 - \exp \left(\frac{-\hbar \omega_{\mathbf{q}, b}(V)}{k_{\text{B}} T} \right) \right] \quad (4.5)$$

Here k_{B} is the Boltzmann constant and $\omega_{\mathbf{q}, b}$ is the phonon frequency at wavevector \mathbf{q} for band b . This results in

$$\Delta \tilde{H}(T) = \Delta E_{\text{lat}} + F_{\text{phonon}}(T; \text{I}) - F_{\text{phonon}}(T; \text{II}) , \quad (4.6)$$

4. Finally, the configurational entropy S_{conf} has been also accounted for that results from the number of possible microstates in the H-subnetwork of the ice. This also includes the temperature dependence to the enthalpies according to

$$\Delta H(T) = \Delta \tilde{H}(T) + TS_{\text{conf}}. \quad (4.7)$$

The expression $R \ln(\frac{3}{2}) = 3.37 \text{ J mol}^{-1} \text{ K}$ for S_{conf} is used as given by Pauling [48] throughout in this work. This expression is based on the number of microstates allowed according to the Bernal-Fowler ice rules [6], where only one central water molecule and four tetrahedrally connected water molecules are considered. Considering the actual structure of ice Ih and using a more rigorous approach, the Pauling expression has been corrected to $R \ln(1.507) = 3.40 \text{ J mol}^{-1} \text{ K}$ [49–52]. In spite of neglecting long-range effects such as ring closures, the Pauling approach is accurate to better than 1% for all ice structures. This accuracy is much better than chemical accuracy aimed for here.

It is noted that $\Delta H(T = 0 \text{ K}) = \Delta \tilde{H}(T = 0 \text{ K}) = \Delta E_{\text{lat}}^{\text{ZPE}}$, i.e. Eqs. (4.4), (4.6) and (4.7) are identical at $T = 0 \text{ K}$. Furthermore, Eqs. (4.2), (4.4), (4.6) and (4.7)) has been evaluated based on the quasi-harmonic approximation (QHA). For $T \gg 0 \text{ K}$ this study thus accounts for the thermal expansion due to the dependence of ω_i on the unit cell volume. The QHA has been very successful to account for nuclear quantum effects in different ice phases [53, 54] and found to be very accurate for $T \leq 200 \text{ K}$ for ice Ih and ice II [55].

Lattice energies without and with ZPE for ice Ih and ice II are listed in Table 4.2. E_{lat} is identical for H_2O and D_2O , whereas $E_{\text{lat}}^{\text{ZPE}}$ differs for both isotopologues. Within the experimental uncertainties both models reproduce the available data for E_{lat} and $E_{\text{lat}}^{\text{ZPE}}$ within 1.5 kJ mol^{-1} , which is much better than chemical accuracy (4.2 kJ mol^{-1}).

Table 4.3 compiles the transition enthalpies for the ice II \rightarrow ice Ih transition. Based on E_{lat} alone (given in the first column) the transition is calculated to be strongly exothermic, where q-TIP4P/F predicts a much stronger exothermicity than MB-pol (-1466 vs. -801 J mol^{-1}). This alone does not match the experiments, which are weakly en-

Table 4.1: Summary of the onset temperatures T_o and enthalpies ΔH for H_2O and D_2O samples obtained from DSC measurements for the ice II \rightarrow ice Ic transition following different preparation routes.

Preparation method	Ice II	T_o (K)	ΔH (J mol^{-1})	Isotope effect on	
				T_o (K)	ΔH (J mol^{-1})
Bauer <i>et al.</i> [19]	H_2O	172 ± 1	$+33 \pm 11$	7.0 ± 1.4	-165 ± 38
	D_2O	179 ± 1	-132 ± 36		
Salzmann <i>et al.</i> [20]	H_2O	170 ± 2	$+48 \pm 9$	10.0 ± 2.2	-197 ± 51
	D_2O	180 ± 1	-149 ± 50		

dothemic in the H_2O case and weakly exothermic in the D_2O case (see Table 4.1). The exothermicity is significantly reduced when including the ZPE in $\Delta E_{\text{lat}}^{\text{ZPE}}$ (second column in Table 4.3). Yet, even after consideration of ZPE the transitions are still clearly exothermic for both models and both isotopes (between -561 and -732 J mol^{-1}). q-TIP4P/F predicts a somewhat stronger influence of ZPE than MB-pol does. Also when including the vibrational correction in $\Delta \tilde{H}$ this picture does not change very much (third column in Table 4.3). In fact, the vibrational correction at 150 K is almost identical for both H_2O and D_2O . It amounts to about 2 J mol^{-1} for the MB-pol model, and about 30 J mol^{-1} for q-TIP4P/F. The closest match with experiment is reached when also including the Pauling correction for the configurational entropy in ΔH (last column in Table 4.3). After this correction the ice II \rightarrow Ic transition is exothermic by -105 J mol^{-1} for the D_2O case and the MB-pol model. This is very close to the experimental value given in Table 4.1. However, the switch from endothermic to exothermic cannot be accounted for. Both models show the ice II \rightarrow Ic transition to be slightly exothermic for the H_2O case, by -57 J mol^{-1} for the MB-pol model. This transition enthalpy is very close to zero, just like the experimental value, but on the exothermic side. Considering the accuracy with which both water models reproduce the lattice energies in Table 4.2, it is not surprising that they fail to predict the absolute transition enthalpies correctly. On the other hand, the difference that quantifies the isotope effect on the ice II \rightarrow Ic transition introduces some cancellation of errors, which leads to a

Table 4.2: Lattice energies for ice Ih and ice II in kJ mol^{-1} as defined in Eqs. (4.1) and (4.2). Experimental values have been obtained by extrapolating experimental values for the vibrational frequencies back to 0 K and calculating the zero-point energy therefrom [56, 57].

	E_{lat}	$E_{\text{lat}}^{\text{ZPE}}$	
		H ₂ O	D ₂ O
ice Ih			
q-TIP4P/F	−59.782	−47.216	−49.885
MB-pol	−59.464	−46.756	−49.552
experiments	−58.82 ^a	−47.341(15) ^{a, b}	−48.611(615) ^b
ice II			
q-TIP4P/F	−58.316	−46.621	−49.153
MB-pol	−58.663	−46.195	−48.975
experiments	−58.88(10) ^a	−47.400(100) ^a	

^aref. [57]; ^bref. [56].

better agreement with the experimental value of $-180 \pm 20 \text{ J mol}^{-1}$. The q-TIP4P/F model fares somewhat better, predicting an isotope effect of -135 J mol^{-1} as opposed to -48 J mol^{-1} in case of MB-pol. Since the configurational entropy is exactly the same and the vibrational correction is almost identical for H_2O and D_2O , they cancel each other when considering the differences of $\Delta\tilde{H}$ and ΔH , which thus yield essentially the same result as $\Delta E_{\text{lat}}^{\text{ZPE}}$. That is, the main reason for the isotope effect noticed in this work is ZPE.

4.4 Conclusions

In summary, this study reports calorimetry scans for the high-pressure phase ice II at ambient pressure. These scans feature (i) the transition to cubic ice (ice Ic) at $170 \pm 2 \text{ K}$, (ii) the very subtle transition from ice Ic to hexagonal (ice Ih) near 210 K

Table 4.3: Energy differences for the ice II \rightarrow ice Ih transition in J mol^{-1} as defined by Eqs. (4.3), (4.4), (4.6) and (4.7).

	ΔE_{lat}	$\Delta E_{\text{lat}}^{\text{ZPE}}$		$\Delta \tilde{H}(T = 150 \text{ K})$		$\Delta H(T = 150 \text{ K})$	
		H_2O	D_2O	H_2O	D_2O	H_2O	D_2O
q-TIP4P/F	-1466	-595	-732	-627	-762	-121	-256
Isotope effect		-137		-135		-135	
MB-pol	-801	-561	-612	-563	-611	-57	-105
Isotope effect		-51		-48		-48	

and (iii) melting of ice Ih at 273 K (not shown in Fig. 4.1). Upon deuteration the onset temperature of the ice II \rightarrow ice Ic transition shifts to $180 \pm 1 \text{ K}$. This shift of about 10 K is clearly a kinetic effect and reflects the fact that the transition is from kinetically stable ice II to metastable ice Ic at ambient pressure. The enthalpy associated with the transition changes sign upon isotope substitution, from an endotherm of $+40 \text{ J mol}^{-1}$ in case of H_2O to an exotherm of -140 J mol^{-1} in case of D_2O . This represents, to the best of our knowledge, the first observation of sign change upon isotope substitution, at least in the thermal study of ice phases. That is, our findings show how isotope effects may change stability and how a metastable material may become stable upon isotope exchange.

Lattice energy calculations based on two flexible water models (q-TIP4P/F and MB-pol) were carried out to explain this finding. The observed isotope effect on the enthalpy can be traced back to the difference of lattice energies including ZPE. ZPE alone results in a difference of 137 J mol^{-1} for the ice II \rightarrow ice Ih transition for q-TIP4P/F, which is close to the experimental value of 180 J mol^{-1} . By contrast, MB-pol shows a difference of only 50 J mol^{-1} , clearly underestimating the ZPE. The vibrational contribution has been also considered at 150 K and the configurational entropy contribution related to the H-order in ice II and H-disorder in ice Ic. Both of these are important for obtaining good values on the absolute transition enthalpy for the ice II \rightarrow ice Ic transition in H_2O . However, these effects are similar for D_2O and H_2O , and accordingly not of relevance

in explaining the isotope effect. Future water models are challenged to reproduce the experimentally observed sign change of the ice II \rightarrow ice Ic transition enthalpy. It might be necessary to include zero-point energies of different ice phases directly in the construction of these models. This study suggests the isotope effects on the melting transition of ice Ih (6012 vs 6280 J mol⁻¹) and the isotope effects on the transformation from high-pressure ices II (see Table 4.1), VI [11] and XII [12] to ice Ic as benchmark data, for which reliable calorimetric studies are available for both D₂O and H₂O. The ice II \rightarrow ice Ic transition is particularly challenging because this polymorphic transition involves both entropy and enthalpy changes. They are both of similar size but opposed sign, and so it is highly challenging to reproduce whether an endotherm or an exotherm results in sum.

4.A Appendix

Table 4.4: Thermal expansion at $T = 150$ K relative to $T = 0$ K in percent as calculated according to the quasi-harmonic approximation (QHA). See main text and [45] for details.

	H ₂ O	D ₂ O
ice Ih		
q-TIP4P/F	0.05	0.08
MB-pol	0.24	0.31
ice II		
q-TIP4P/F	0.82	0.85
MB-pol	1.16	1.25

Table 4.5: Lattice energies for ice Ih in kJ mol^{-1} as defined in Eqs. (4.3) and (4.4). Experimental values have been obtained by extrapolating experimental values for the vibrational frequencies back to 0 K and calculating the zero-point energy therefrom [56, 57].

	E_{lat}	$E_{\text{lat}}^{\text{ZPE}}$	
		H_2O	D_2O
ice Ih			
q-TIP4P/F	−59.782	−47.216	−49.885
q-TIP4P/F (SPGC)	−59.645	−46.911	−49.600
MB-pol	−59.464	−46.756	−49.552
MB-pol (SPGC)	−59.390	−46.817	−49.609
experiments	−58.82 ^a	−47.341(15) ^{a,b}	−48.611(615) ^b

^aref. [57]; ^bref. [56].

Table 4.6: Energy differences for the ice II \rightarrow ice Ih transition in J mol^{-1} as defined by Eqs. (4.3), (4.4), (4.6) and (4.7)

	ΔE_{lat}	$\Delta E_{\text{lat}}^{\text{ZPE}}$		$\Delta \tilde{H}(T = 150 \text{ K})$		$\Delta H(T = 150 \text{ K})$	
		H_2O	D_2O	H_2O	D_2O	H_2O	D_2O
q-TIP4P/F	−1466	−595	−732	−627	−762	−121	−256
Isotope effect		−137		−135		−135	
q-TIP4P/F (SPGC)	−1379	−290	−477	−662	−809	−156	−303
Isotope effect		−187		−147		−147	
MB-pol	−801	−561	−612	−563	−611	−57	−105
Isotope effect		−51		−48		−48	
MB-pol (SPGC)	−875	−622	−669	−673	−715	−167	−209
Isotope effect		−47		−42		−42	

4.5 References

1. G. Tammann, *Ann. Phys.* **308**, 161–194 (1900).
2. G. J. Wilson, R. K. Chan, D. W. Davidson, E. Whalley, *J. Chem. Phys.* **43**, 2384–2391 (1965).
3. J. E. Bertie, E. Whalley, *J. Chem. Phys.* **40**, 1646–1659 (1964).
4. E. D. Finch, S. W. Rabideau, R. G. Wenzel, N. G. Nereson, *J. Chem. Phys.* **49**, 4361–4365 (1968).
5. B. Kamb, W. C. Hamilton, S. J. LaPlaca, A. Prakash, *J. Chem. Phys.* **55**, 1934–1945 (1971).
6. J. D. Bernal, R. H. Fowler, *J. Chem. Phys.* **1**, 515–548 (1933).
7. S. Kawada, *J. Phys. Soc. Jpn.* **32**, 1442–1442 (1972).
8. J. E. Bertie, L. D. Calvert, E. Whalley, *J. Chem. Phys.* **38**, 840–846 (1963).
9. Y. P. Handa, D. D. Klug, *J. Phys. Chem.* **92**, 3323–3325 (1988).
10. C. G. Salzmann, I. Kohl, T. Loerting, E. Mayer, A. Hallbrucker, *Phys. Chem. Chem. Phys.* **5**, 3507–3517 (2003).
11. J. J. Shephard, C. G. Salzmann, *Chem. Phys. Lett.* **637**, 63–66 (2015).
12. C. G. Salzmann, E. Mayer, A. Hallbrucker, *Phys. Chem. Chem. Phys.* **6**, 1269–1276 (2004).
13. T. Loerting, M. Bauer, I. Kohl, K. Watschinger, K. Winkel, *et al.*, *J. Phys. Chem. B* **115**, 14167–14175 (2011).
14. E. A. Zheligovskaya, *Crystallogr. Rep.* **60**, 714–720 (2015).
15. J. J. Shephard, C. G. Salzmann, *J. Phys. Chem. Lett.* **7**, 2281–2285 (2016).
16. M. S. Elsaesser, K. Winkel, E. Mayer, T. Loerting, *Phys. Chem. Chem. Phys.* **12**, 708–712 (2010).
17. G. P. Johari, A. Hallbrucker, E. Mayer, *Nature* **330**, 552 (1987).
18. O. Mishima, L. Calvert, E. Whalley, *Nature* **310**, 393 (1984).
19. M. Bauer, M. S. Elsaesser, K. Winkel, E. Mayer, T. Loerting, *Phys. Rev. B* **77**, 220105 (2008).
20. C. G. Salzmann, P. G. Radaelli, J. L. Finney, E. Mayer, *Phys. Chem. Chem. Phys.* **10**, 6313–6324 (2008).
21. E. Long, J. Kemp, *J. Am. Chem. Soc.* **58**, 1829–1834 (1936).
22. T. M. Gasser, A. V. Thoeny, L. J. Plaga, K. W. Köster, M. Etter, *et al.*, *Chem. Sci.* **9**, 4224–4234 (2018).
23. V. Fuentes-Landete, K. W. Köster, R. Böhmer, T. Loerting, *Phys. Chem. Chem. Phys.* **20**, 21607–21616 (2018).
24. V. Fuentes-Landete, L. J. Plaga, M. Keppler, R. Böhmer, T. Loerting, *Phys. Rev. X* **9**, 011015 (2019).
25. S. Habershon, T. E. Markland, D. E. Manolopoulos, *J. Chem. Phys.* **131**, 024501 (2009).

-
26. A. H. Larsen, J. J. Mortensen, J. Blomqvist, I. E. Castelli, R. Christensen, *et al.*, *J. Phys.: Condens. Matter* **29**, 273002 (2017).
 27. S. Plimpton, *J. Comput. Phys.* **117**, 1–19 (1995).
 28. V. Babin, C. Leforestier, F. Paesani, *J. Chem. Theory Comput.* **9**, 5395–5403 (2013).
 29. V. Babin, G. R. Medders, F. Paesani, *J. Chem. Theory Comput.* **10**, 1599–1607 (2014).
 30. G. R. Medders, V. Babin, F. Paesani, *J. Chem. Theory Comput.* **10**, 2906–2910 (2014).
 31. C. Lobban, J. L. Finney, W. F. Kuhs, *J. Chem. Phys.* **117**, 3928–3934 (2002).
 32. A. D. Fortes, *Acta Cryst. B* **74**, 196–216 (2018).
 33. M. Matsumoto, T. Yagasaki, H. Tanaka, *J. Comput. Chem.* **39**, 61–64 (2018).
 34. B. G. Pfrommer, M. Côté, S. G. Louie, M. L. Cohen, *J. Comput. Phys.* **131**, 233–240 (1997).
 35. K. Parlinski, Z. Q. Li, Y. Kawazoe, *Phys. Rev. Lett.* **78**, 4063–4066 (1997).
 36. A. Togo, I. Tanaka, *Scripta Mater.* **108**, 1–5 (2015).
 37. E. A. Engel, B. Monserrat, R. J. Needs, *Phys. Rev. X* **5**, 021033 (2015).
 38. M. Taylor, E. Whalley, *J. Chem. Phys.* **40**, 1660–1664 (1964).
 39. J. Li, *J. Chem. Phys.* **105**, 6733–6755 (1996).
 40. D. D. Klug, E. Whalley, E. C. Svensson, J. H. Root, V. F. Sears, *Phys. Rev. B* **44**, 841–844 (1991).
 41. T. H. G. Carr, J. J. Shephard, C. G. Salzmann, *J. Phys. Chem. Lett.* **5**, 2469–2473 (2014).
 42. M. Celli, L. Ulivi, L. del Rosso, *J. Phys. Chem. C* **124**, 17135–17140 (2020).
 43. M. Chaplin, *Water Phase Diagram - Triple Points*, Accessed on July 31st, 2020.
 44. International Association for the Properties of Water and Steam, “Revised Release on the Pressure along the Melting and Sublimation Curves of Ordinary Water Substance,” tech. rep.
 45. S. Rasti, J. Meyer, *J. Chem. Phys.* **150**, 234504 (2019).
 46. D. R. Moberg, S. C. Straight, C. Knight, F. Paesani, *J. Phys. Chem. Lett.* **8**, 2579–2583 (2017).
 47. D. R. Moberg, P. J. Sharp, F. Paesani, *J. Phys. Chem. B* **122**, 10572–10581 (2018).
 48. L. Pauling, *J. Am. Chem. Soc.* **57**, 2680–2684 (1935).
 49. J. Nagle, *J. Math. Phys.* **7**, 1484–1491 (1966).
 50. B. A. Berg, C. Muguruma, Y. Okamoto, *Phys. Rev. B* **75**, 092202 (2007).
 51. C. P. Herrero, R. Ramírez, *J. Chem. Phys.* **140**, 234502 (2014).
 52. M. V. Ferreyra, S. A. Grigera, *Phys. Rev. E* **98**, 042146 (2018).
 53. B. Pamuk, J. M. Soler, R. Ramírez, C. P. Herrero, P. W. Stephens, *et al.*, *Phys. Rev. Lett.* **108**, 193003 (2012).

54. K. Umemoto, E. Sugimura, S. de Gironcoli, Y. Nakajima, K. Hirose, *et al.*, *Phys. Rev. Lett.* **115**, 173005 (2015).
55. R. Ramírez, N. Neuerburg, M.-V. Fernández-Serra, C. P. Herrero, *J. Chem. Phys.* **137**, 044502 (2012).
56. E. Whalley, *Trans. Faraday Soc.* **53**, 1578 (1957).
57. E. Whalley, *J. Chem. Phys.* **81**, 4087–4092 (1984).

CHAPTER 5

Transferable Potential Function for Flexible H₂O

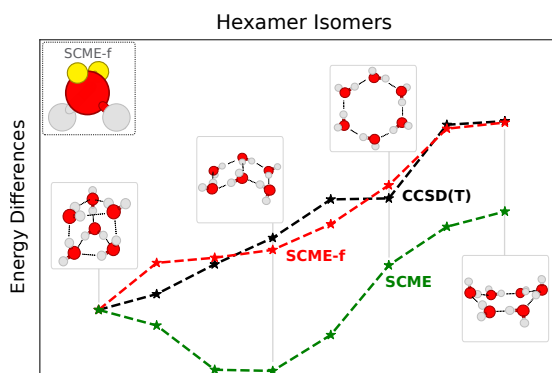
This chapter is based on:

E. Ö. Jónsson, S. Rasti, M. Galynska, J. Meyer and H. Jónsson, Transferable Potential Function for Flexible H₂O Molecules Based on the Single Center Multipole Expansion, *submitted to the Journal of Chemical Theory and Computation (JCTC)*

The submitted version of is available at [arXiv:2007.06090v2](https://arxiv.org/abs/2007.06090v2) [physics.comp-ph].

Abstract

A potential function is presented for describing a system of flexible H₂O molecules based on the single center multipole expansion (SCME) of the electrostatic interaction. The model, referred to as SCME/f, includes the variation of the molecular quadrupole moment as well as the dipole moment with changes in bond length and angle so as to reproduce results of high level electronic structure calculations. The multipole expansion also includes fixed octupole and hexadecapole moments, as well as anisotropic dipole-dipole, dipole-quadrupole and quadrupole-quadrupole polarizability tensors. The model contains five adjustable parameters related to the repulsive interaction and damping functions in the electrostatic and dispersion interactions. Their values are adjusted to reproduce the lowest energy isomers of small clusters, (H₂O)_n with $n = 2 - 6$, as well as measured properties of the ice Ih crystal. Subsequent calculations of the energy difference between the various isomer configurations of the clusters show that SCME/f gives good agreement with results of electronic structure calculations and represents a significant improvement over the previously presented rigid SCME potential function. Analysis of the vibrational frequencies of the clusters and structural properties of ice Ih crystal show the importance of accurately describing the variation of the quadrupole moment with molecular structure.



5.1 Introduction

The most commonly used potential energy functions for describing water molecules and their interaction are based on simple pairwise additive functions with fixed point charges [1–4], such as the well known TIPnP and SPC force fields. Extensions of these potential functions to describe flexible molecules have been developed, such as aSPC/Fw [5] and q-TIP4P/F [6], and they offer, for example, the possibility to include the effect of zero point energy. The point charge potential functions are typically parameterized in such a way as to reproduce a few thermally averaged properties of liquid water. The properties of water molecules are, however, strongly environment dependent as illustrated by the molecular dipole moment, which is 1.8 D in the gas phase and 3.1 D in ice Ih [7]. This large environment dependence needs to be modeled accurately in order to develop a transferable potential function applicable, for example, to small clusters and crystal structures as well as liquid water.

Such environment dependence is best described using well established physical laws, since empirical fitting to some limited set of data is likely not going to work well when the potential function is applied to configurations that are significantly different from the ones used in the fitting process. A systematic multipole expansion up to and including the hexadecapole, with dipole and quadrupole polarizability, has been shown to reproduce well the electrostatics in water clusters and ice [8]. A potential function based on this approach has been presented for rigid molecules and is referred to as the single center multipole expansion (SCME) potential function [9, 10]. In the present work, this approach is extended to flexible molecules.

By expanding the electrostatics around a single center on each molecule, the introduction of point charges is avoided and the correct long range distance dependence of the Coulomb potential built in naturally. The leading term, the dipole potential, decays as $1/R^3$, and combined with the polarization response of the molecules this makes it possible to use a long range cut-off for the electrostatic interaction between molecules in typical condensed matter simulations. [7]

Hybrid simulation schemes, where part of the system is simulated using a potential function while another part is described using electronic structure calculations, the so-called quantum mechanics / molecular mechanics (QM/MM) simulations, have been used in important simulation studies in various fields such as biochemistry [11–15], medicine [16], photochemistry [17] and solvation dynamics [18–21], nanostructures [22], and materials science [23]. In most cases, such simulations make use of fixed point charge models [24–27], thereby neglecting the mutual polarization of the charges in the MM subsystem by the QM subsystem – an effect that was, however, included in the inceptive work initiating the QM/MM approach [28]. The use of fixed point charge models to represent water molecules in the MM region results in errors that limit the applicability of the QM/MM method.

Several H₂O potential functions that include some level of polarizability exist [29–31]. These include the Thole-type multipole models such as the TTMn series [32–35], and HBB2-pol [36, 37]. The MB-pol [38–40] potential function has arguably reached the highest precision as it includes an explicit treatment of two-body and three-body interactions through an intricate permutationally invariant polynomial fit to data bases constructed with high level quantum chemistry calculations. However, inclusion of such explicit many body terms makes the interfacing with a QM region more challenging. Instead, simpler polarizable MM potential functions based on pair-wise potentials to describe the short-range interactions are used in so-called polarizable embedding QM/MM (PE-QM/MM) approach [26, 41–71]. The PE-QM/MM approach can be used to study the effects of solvation and solvent response to excitations and charge transfer in solvated species. However, such simulations have typically included only the molecular dipole-dipole response and make use of atomic point charges.

Here, an extension of the single-center multipole expansion [9, 10] (SCME) potential function is described, which has recently been integrated in a PE-QM/MM scheme [72, 73]. The extended potential function, SCME/f, includes flexibility of the internal geometry of the water molecules while still maintaining the single center description of the electrostatic interaction in terms of molecular moment tensors. The SCME/f model in-

cludes variable dipole and quadrupole moment tensors that depend on the geometry of the H_2O molecule. The dipole is described by the well established Partridge-Schwenke model, [74] but a new, geometrical model based on four sites is presented here for the quadrupole moment. It reproduces results of high-level multireference electronic structure calculations of the quadrupole moment to within 1.6% RMS over a broad range in its magnitude. This model for the quadrupole moment is found to provide better description than the so-called M-site models that have been used previously. [2, 32–40, 75–78]

There are five adjustable parameters in the description of the intermolecular interaction. They include parameters relating to the pair-wise repulsive interaction as well as damping parameter in the dispersion interaction and a screening parameter for the electrostatic interaction tensors. These parameters are optimized in such a way that the SCME/f reproduces the binding energy and intermolecular distance of the dimer, the interaction energy of the lowest energy conformation of water clusters $(\text{H}_2\text{O})_n$ with n ranging from 3 to 6, calculated at the level of RI-MP2 with CCSD(T) corrections [79] and full CCSD(T) at the complete basis set limit [80] as well as measured properties of crystalline ice Ih taking into account the zero-point energy. The resulting parametrization of the model reproduces nicely trends in the relative energy of the conformers of the hexamer obtained from high level quantum chemistry calculations. Some discrepancies, however, exist in the series of pentamer isomers. An analysis of the frequency of vibrational modes of the various clusters and the structure of ice Ih crystal highlights the importance of an accurate model for the molecular quadrupole moment.

The article is organized as follows: The SCME/f potential function is described in Section 5.2. The dipole and quadrupole surfaces are presented in Section 5.3 and the calculation of atomic forces is described in Section 5.4. The fitting of the five adjustable parameters is described in Section 5.5 and comparison with *ab initio* data on the cluster conformer energy and vibrational frequencies of small clusters is described in Section 5.6. Discussion and conclusions are in Section 5.7.

5.2 Flexible SCME Model

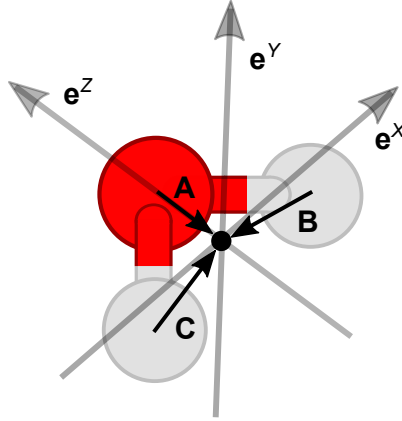


Figure 5.1: The definition of the principal vectors and local reference frame for the water molecule used in the SCME/f model. The black circle denotes the expansion center, chosen here to be at the center of mass. Black arrows show the three principal vectors **A**, **B** and **C** pointing *from* the oxygen and the hydrogen atoms *to* the expansion center. The gray opaque arrows show the local reference frame basis vectors $\{e^x, e^y, e^z\}$. The principal vectors **B** and **C** define a local-to-global reference frame rotation matrix. Due to symmetry specific indexing of the atoms is omitted, and positions and scales are exaggerated for clarity.

Fig. 5.1 shows the principal vectors which define both the position of the expansion center and the local-to-global reference frame rotation matrix for the flexible water molecule. The local frame origin is placed at the center of mass (COM). In SCME/f each water molecule is ascribed a molecular dipole and quadrupole moments in terms of variable partial charges based on the internal geometry, $\mu_\alpha^i(\{\mathbf{r}^{ia}\})$ and $\theta_{\alpha\beta}^i(\{\mathbf{r}^{ia}\})$, respectively, where $\{\mathbf{r}^{ia}\} = \{\mathbf{r}^{iO}, \mathbf{r}^{iH_1}, \mathbf{r}^{iH_2}\}$, and is the set of position vectors for atoms a in molecule i in the global reference frame. The details of the dipole moment and quadrupole moment surfaces are described in Section 5.3. The index i is used to denote both the specific water molecule, as well as the corresponding COM site. Furthermore, each water molecule is ascribed, in the local reference frame, a fixed octupole, $\Omega_{\alpha\beta\gamma}^{i'}$, and

hexadecapole, $\Phi_{\alpha\beta\gamma\delta}^{i'}$, moment tensors, as well as polarizability tensors including dipole-dipole, $\alpha_{\alpha\beta}^{i'}$, dipole-quadrupole, $A_{\alpha\beta\gamma}^{i'}$, and quadrupole-quadrupole, $C_{\alpha\beta\gamma\delta}^{i'}$, induction terms.

Lipparini *et al.* [81] describe commonly used local reference frames and associated rotation matrices. The derivation here follows closely their work, with some obvious sign changes. The expansion center is placed at the COM

$$\mathbf{r}^i = \sum_a^{n_i} \mathbf{r}^{ia} \frac{M^a}{M^i} \quad (5.1)$$

where n_i denotes the atomic sites $\{\text{O}, \text{H}_1, \text{H}_2\}$ of molecule i , and M^a and M^i is the mass of the atom and molecule, respectively. The principal vectors used to define the rotation are

$$\mathbf{B}^i = \mathbf{r}^i - \mathbf{r}^{i\text{H}_1}, \quad \mathbf{C}^i = \mathbf{r}^i - \mathbf{r}^{i\text{H}_2} \quad , \quad (5.2)$$

where in general, i.e. for a flexible H_2O molecule, $B^i \neq C^i$. Unit basis vectors are in terms of the principal vectors given by

$$\begin{aligned} \mathbf{e}^{iZ} &= \frac{B^i \mathbf{C}^i + C^i \mathbf{B}^i}{|B^i \mathbf{C}^i + C^i \mathbf{B}^i|} \\ \mathbf{e}^{iX} &= \frac{\mathbf{B}^i - (\mathbf{B}^i \cdot \mathbf{e}^{iZ}) \mathbf{e}^{iZ}}{|\mathbf{B}^i - (\mathbf{B}^i \cdot \mathbf{e}^{iZ}) \mathbf{e}^{iZ}|} \\ \mathbf{e}^{iY} &= \mathbf{e}^{iZ} \times \mathbf{e}^{iX} \end{aligned} \quad (5.3)$$

where \mathbf{e}^{iZ} is, as defined above, the bisector between the two oxygen-hydrogen bonds. In terms of the unit basis vectors a unitary local-to-global reference frame rotation matrix is

$$\mathbf{R}^i = \begin{bmatrix} e_x^{iX} & e_y^{iX} & e_z^{iX} \\ e_x^{iY} & e_y^{iY} & e_z^{iY} \\ e_x^{iZ} & e_y^{iZ} & e_z^{iZ} \end{bmatrix} \quad (5.4)$$

Given the rotation matrix for each molecule the fixed moment and polarizability matrices are rotated into the global reference frame for each COM site i^1

¹Throughout this work Einstein notation was used, i.e. Cartesian vector spaces are indexed with Greek letters, $\alpha = \beta = \dots = \nu \in \{x, y, z\}$, and repeated Greek indices are to be summed over.

$$M_{\alpha\dots\delta}^i = R_{\eta\alpha}^i \dots R_{\sigma\delta}^i M_{\eta\dots\sigma}^{i'} \quad (5.5)$$

where $M_{\alpha\dots\delta}^i$ is a generalized tensor of order t , requiring t rotation operations (e.g. $\alpha_{\alpha\beta}^i = R_{\eta\alpha}^i R_{\tau\beta}^i \alpha_{\eta\tau}^{i'}$). With the definitions above atomic forces are derived (see the Supplementary Information) from the contribution of the fixed moments and polarizabilities to the electrostatic interactions involving the single expansion center on each molecule.

General formulation, and notation, of the perturbative expansion of the electrostatic intermolecular interaction – resulting in the multipole moment model – can be found elsewhere [82]. Here only the main expressions are presented which are used to arrive at a self-consistent solution to polarized molecular moments at sites i in response to the external field due to all other neighboring molecules $j (\neq i)$.

Given the external field, V_α^i (negative of the electric field), and the field gradient, $V_{\alpha\beta}^i$, at the COM of i , the molecules are polarized resulting in induced dipole and quadrupole moments

$$\Delta\mu_\alpha^i = -\alpha_{\alpha\beta}^i V_\beta^i - \frac{1}{3} A_{\alpha\beta\gamma}^i V_{\beta\gamma}^i \quad (5.6)$$

$$\Delta\theta_{\alpha\beta}^i = -A_{\gamma\alpha\beta}^i V_\gamma^i - C_{\gamma\delta\alpha\beta}^i V_{\gamma\delta}^i \quad (5.7)$$

where the external field is given by

$$V_\alpha^i = \sum_{j \neq i}^n V_\alpha^{ij} \quad (5.8)$$

and the contribution to the external field at site i due to site j is given by

$$\begin{aligned} V_\alpha^{ij} = & -T_{\alpha\beta}^{ij}(\mu_\beta^j(\{\mathbf{r}^{jb}\}) + \Delta\mu_\beta^j) + \frac{1}{3}T_{\alpha\beta\gamma}^{ij}(\theta_{\beta\gamma}^j(\{\mathbf{r}^{jb}\}) + \Delta\theta_{\beta\gamma}^j) \\ & - \frac{1}{15}T_{\alpha\beta\gamma\delta}^{ij}\Omega_{\beta\gamma\delta}^j + \frac{1}{105}T_{\alpha\beta\gamma\delta\epsilon}^{ij}\Phi_{\beta\gamma\delta\epsilon}^j \end{aligned} \quad (5.9)$$

The field gradient – and higher order gradients – are given by the subsequent use of the gradient operator, $\nabla_\beta V_\alpha^i = V_{\alpha\beta}^i$, $\nabla_\gamma V_{\alpha\beta}^i = V_{\alpha\beta\gamma}^i$.

At the start the external field and field gradient due to the intrinsic moments is evaluated at each site. This results in an induced dipole and quadrupole moment, which

in turn results in a change in the external field and field gradient. A self-consistent solution to the non-linear relation between Eq. (5.6)–Eq. (5.9) is achieved with an iterative procedure and a suitable convergence threshold of the induced moments to achieve energy-force consistency (see the Supplementary Information).

As the point moments come close the multipole moment expansion breaks down – resulting in the so-called polarization catastrophe. [83] In order to avoid this screened interaction tensors are introduced [83–88] which effectively smear out the point moments. To zeroth order the Coulomb interaction tensors in Eq. (5.9) are defined as

$$T^{ij} = \frac{1}{|\mathbf{r}^j - \mathbf{r}^i|} \lambda_0(r) = \frac{1}{r} \lambda_0(r) \quad (5.10)$$

where $\lambda_0(r)$ is a short-range electrostatic interaction screening function. The gradient operators act to increase the order of the screened interaction tensors, for example

$$\nabla_\alpha T^{ij} = T_\alpha^{ij} \equiv -\frac{r_\alpha}{r^3} \lambda_1(r) \quad (5.11)$$

$$\nabla_\beta T_\alpha^{ij} = T_{\alpha\beta}^{ij} \equiv 3\frac{r_\alpha r_\beta}{r^5} \lambda_2(r) - \frac{\delta_{\alpha\beta}}{r^3} \lambda_1(r) \quad (5.12)$$

where $r_\alpha = (\mathbf{r}^j - \mathbf{r}^i)_\alpha$.

Most commonly used interaction tensor screening functions in the context of polarizable force fields are based on exponential decay of the point charges resulting in the Thole-type damped tensors. [83] Here we make use of screening functions derived from considering the overlap and resulting Coulomb electrostatic screening of Gaussian charge densities and multipoles. [87] In the equations above they are

$$\lambda_1(r) = \text{erf}(S) - \frac{2}{\sqrt{\pi}} S e^{-S^2} \quad (5.13)$$

$$\lambda_2(r) = \text{erf}(S) - \frac{2}{\sqrt{\pi}} \left(S + \frac{2}{3} S^3 \right) e^{-S^2} \quad (5.14)$$

where S is the screened distance, $S = r/g$, and g is the screening length – describing the spatial extent of the Gaussian functions.

In the SCME/f model the total energy is a functional of the external field, V_α^i , at each

molecular COM site i and is given by

$$E_{\text{tot}}[\{V_{\alpha}^i\}] = E_{\text{elst}}[\{V_{\alpha}^i\}] + E_{\text{non-elst}} + E_{\text{mon}} \quad (5.15)$$

where the terms on the right hand side are, $E_{\text{elst}}[\{V_{\alpha}^i\}]$, the total electrostatic energy functional, the non-electrostatic terms, $E_{\text{non-elst}}$, which includes a pair-wise repulsive and a dispersion potential, and E_{mon} , which is a sum of the internal energies described by the Partridge-Schwenke potential energy surface (PS-PES) of the water monomer. [74]

More explicitly the first term on the right hand side of Eq. (5.15) can be further separated into three terms describing the inter- and intramolecular contributions to the total electrostatic energy of the system, namely

$$E_{\text{elst}}[\{V_{\alpha}^i\}] = E_{\text{in}}[\{V_{\alpha}^i\}] + E_{\text{pol}}[\{V_{\alpha}^i\}] + E_{\text{self}}[\{V_{\alpha}^i\}] \quad (5.16)$$

where $E_{\text{in}}[\{V_{\alpha}^i\}]$ is the electrostatic interaction between the intrinsic molecular moments and $E_{\text{pol}}[\{V_{\alpha}^i\}]$ is the field-induced polarization energy. At self-consistency these terms combine to give

$$\begin{aligned} E_{\text{in+pol}}[\{V_{\alpha}^i\}] = & \frac{1}{2} \sum_i^n \left((\mu_{\alpha}^i(\{\mathbf{r}^{ia}\}) + \Delta\mu_{\alpha}^i) V_{\alpha}^i + \frac{1}{3} (\theta_{\alpha\beta}^i(\{\mathbf{r}^{ia}\}) + \Delta\theta_{\alpha\beta}^i) V_{\alpha\beta}^i \right. \\ & \left. + \frac{1}{15} \Omega_{\alpha\beta\gamma}^i V_{\alpha\beta\gamma}^i + \frac{1}{105} \Phi_{\alpha\beta\gamma\delta}^i V_{\alpha\beta\gamma\delta}^i \right) \end{aligned} \quad (5.17)$$

E_{self} is the on-site self-energy, given by

$$E_{\text{self}}[\{V_{\alpha}^i\}] = -\frac{1}{2} \sum_i^n \left(\Delta\mu_{\alpha}^i V_{\alpha}^i + \frac{1}{3} \Delta\theta_{\alpha\beta}^i V_{\alpha\beta}^i \right) \quad (5.18)$$

and accounts for the change in internal energy required to polarize the molecules.

The non-electrostatic term is composed of two intermolecular pair-wise potentials centered on the oxygen atom

$$E_{\text{non-elst}} = E_{\text{rep}} + E_{\text{disp}} \quad (5.19)$$

describing repulsion, E_{rep} , and dispersion E_{disp} . In the following expressions for the potentials the distance r refers to the oxygen-oxygen distance between pair i and j , or $r = |\mathbf{r}^{j\text{O}} - \mathbf{r}^{i\text{O}}|$.

Making use of the same dispersion coefficients as in the original SCME model [89]. The dispersion energy is

$$E_{\text{disp}} = - \sum_i^n \sum_{j < i}^n \left(\frac{C_6}{r^6} t_6(r) + \frac{C_8}{r^8} t_8(r) + \frac{C_{10}}{r^{10}} t_{10}(r) \right) \quad (5.20)$$

with isotropic coefficients up to tenth order from Wormer and Hettema [90]. At short range the interaction is smoothly switched off with a Tang-Toennies damping function [91]

$$t_m(r) = 1 - e^{-\tau_d r} \sum_{k=0}^m \frac{(\tau_d r)^k}{k!} \quad (5.21)$$

where the parameter τ_d represents the inverse decay length of the charge density.

In the rigid SCME [89] model a modified Born-Mayer potential is used, which includes a term which scales the magnitude of the repulsion depending on the local environment around the repulsion center – a molecular density dependent term. With the introduction of the Gaussian type interaction tensor screening function we find the molecular density dependence unnecessary and revert back to the basic Born-Mayer type potential. The pair-wise repulsion is

$$E_{\text{rep}} = \sum_i^n \sum_{j < i}^n A_{\text{rep}} r^{-k} e^{-hr} \quad (5.22)$$

The parameters of the non-electrostatic terms, τ_d , A_{rep} , k and h , are optimized to work with the new SCME/f model. The optimization also includes the screening length parameter g of Eq. (5.14). The fitting is described in Section 5.5.

5.3 The Dipole and Quadrupole Moment Surfaces

The internal energy as described by the PS-PES includes analytical atomic force components, [74] as well as an accurate mapping of the dipole moment surface (DMS) for an isolated water molecular as a function of the internal geometry. The DMS is given by

$$\mu_{\alpha}^i(\mathbf{r}^{i\text{O}}, \mathbf{r}^{i\text{H}_1}, \mathbf{r}^{i\text{H}_2}) = q^{i\text{H}_1} r_{\alpha}^{i\text{H}_1} + q^{i\text{H}_2} r_{\alpha}^{i\text{H}_2} + q^{i\text{O}} r_{\alpha}^{i\text{O}} \quad (5.23)$$

where $q^{iO} = -(q^{iH_1} + q^{iH_2})$ and the partial charges of the two hydrogens are in turn a function of the internal geometry, fitted to recreate the calculated DMS. For example $q^{iH_1} = q^{iH_1}(r^{OH_1}, r^{OH_2}, \cos(\theta_{HOH}))$, where r^{OH_1} and r^{OH_2} are the internal bond lengths between the oxygen and the two hydrogens, and θ_{HOH} the HOH angle. This mapping is used, and it was left unchanged.

The DMS partial charges are not suitable to describe a quadrupole moment surface (QMS) without modification. Instead the charge site associated with the oxygen is split up into two components and placed within a plane perpendicular to the symmetry plane of the hydrogens and oxygens. The sites are denoted L₁ and L₂, where the site positions are directly related to the length of the hydrogen bond lengths indexed H₁ and H₂, and the HOH angle. See Fig. 5.2. The QMS is written as

$$\theta_{\alpha\beta}^i(\mathbf{r}^{iO}, \mathbf{r}^{iH_1}, \mathbf{r}^{iH_2}) = \sum_a^{n'_i} \frac{3}{2} \left\{ q^{ia} \left((\mathbf{r}^{ia} - \mathbf{r}^i)_\alpha (\mathbf{r}^{ia} - \mathbf{r}^i)_\beta - \frac{\delta_{\alpha\beta}}{3} \|\mathbf{r}^{ia} - \mathbf{r}^i\| \right) \right\} \quad (5.24)$$

where n'_i denotes the sites $\{H'_1, H'_2, L_1, L_2\}$ associated with molecule i . The apostrophe on the hydrogen is used to discern their role in the QMS from their role in the DMS since the charges $q^{iH_l'}$ are different from the DMS charges, and are

$$q^{iH_l'} = Aq^{iH_l} + Bq_{eq}^H \quad (5.25)$$

and for the L-sites they are

$$q^{iL_l} = Cq^{iH_l} + Dq_{eq}^H \quad (5.26)$$

where q_{eq}^H is the DMS charge of the hydrogen in the equilibrium monomer configuration.

The position of the L₁ and L₂ charge sites is related to the atomic positions of each water molecule through a rotation operator times a scaling factor which controls the length of the rotated vector. A translation operator translates the vector to the COM position of molecular site i for completeness. Explicitly this operation is

$$r_\alpha^{iL_l} = R_{\eta\alpha}^{iL_l} e_\eta^{iZ} f(\mathbf{r}^{iH_l}) + r_\alpha^i \quad (5.27)$$

We make use of the unit basis vectors previously used to define the local-to-global rotation matrices in Eq. (5.1)–Eq. (5.3). The rotation matrices for the L₁ and L₂ sites

are

$$\mathbf{R}^{iL_1} = \left(\cos(f(\theta))\mathbf{I} - \sin(f(\theta)) [\mathbf{e}^{iX}]_{\times} \right) \quad (5.28)$$

$$\mathbf{R}^{iL_2} = \left(\cos(f(\theta))\mathbf{I} + \sin(f(\theta)) [\mathbf{e}^{iX}]_{\times} \right) \quad (5.29)$$

and is a simplification of the general Rodrigues' rotation operator [92] in terms of the local orthonormal basis vectors (shown in Fig. 5.1).

In order to allow for flexibility of the L-sites and correlate their positions to the change in the positions of the hydrogens, both the angle factor and length scale factor are defined in terms of the OH bond lengths and HOH angle through

$$f(\mathbf{r}^{H_l}) = a + b(|\mathbf{r}^{iO} - \mathbf{r}^{iH_l}| - r_{eq}) + c(|\mathbf{r}^{iO} - \mathbf{r}^{iH_l}| - r_{eq})^2 \quad (5.30)$$

$$f(\theta) = d + e(\theta - \theta_{eq}) \quad (5.31)$$

where r_{eq} and θ_{eq} are the equilibrium hydrogen to oxygen bond length and HOH angle of the isolated PS-PES water molecule, respectively, see Fig. 5.2. It is found that a second order polynomial in terms of the change in bond length, and a linear term for the change in bond angles is adequate to capture the QMS with good accuracy. The charge scaling parameters A, B, C and D, and the geometric parameters a, b, c, d, e are fitted parameters, described below.

5.3.1 Ab initio QMS Calculations and Fit

The dipole and quadrupole moment is mapped using the ab initio quantum chemistry software ORCA [93, 94]. An iterative-configuration expansion configuration interaction (ICE-CI) method is used, with the aug-cc-pvqz basis set and the energy convergence threshold is set to $10^{-8} E_h$. Eight correlated electrons are included and the active orbitals were chosen by including MP2 orbitals of natural orbital occupation numbers ranging between 1.99999 and 0.00001. The ICE-CI method is related to the CIPSI technique [95]. Note that this level of theory is necessary to accurately determine the dipole and quadrupole moment using their well defined charge density based operators, instead of resorting to energy based schemes to estimate these quantities. For example, it is found that coupled-cluster at the CCSD(T)/aug-cc-pvqz level of theory and

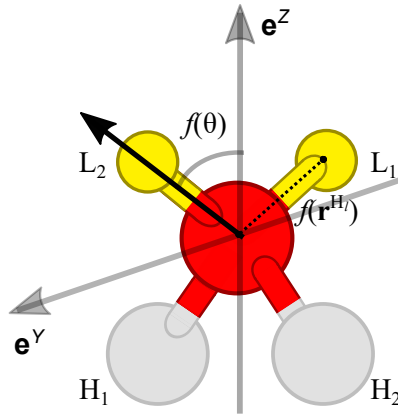


Figure 5.2: L-site placement (yellow) in the water monomer structure. The relationship of the angle to the unit basis vectors which describe the local reference frame is shown, Eq. (5.31) and eqs Eq. (5.28)–Eq. (5.29). For example, operating with the rotation vector corresponding to hydrogen indexed 1 on e_{α}^{iZ} results in $(\cos(f(\theta))e_{\alpha}^{iZ} - \sin(f(\theta))e_{\alpha}^{iY})$. Due to symmetry specific indexing of the atoms is completely interchangeable, and either pair of H and L in the Figure above can serve as pair 1 or 2. The distance from the oxygen to a L-site, controlled with $f(\mathbf{r}^{H_i})$ is a second order polynomial function depending on the position of one of the hydrogens (while the position of the other L-site depends on the other hydrogen), Eq. (5.30). Positions and scales are exaggerated for clarity.

orbital optimized coupled-cluster theory OOCSD(T)/aug-cc-pvdz, did not provide a satisfactory agreement with the DMS of the PS-PES, when using the dipole moment operator $\mu_{\alpha} = \int \rho(\mathbf{r})r_{\alpha}d\mathbf{r}$. See the Supporting Information for more details.

Starting from the ground state geometry in the local-frame as shown in Fig. 5.1 the internal bond lengths and HOH angle are systematically changed and range from 0.7 to 1.3 Å, and 60 to 175°, respectively. These intervals broadly represent the variation in the bond lengths and the angle of the water molecule in the liquid phase at ambient conditions. Fig. 5.3 shows a comparison between the internal energy change of each configuration as calculated by the ICE-CI method compared to the PS-PES. The

agreement is excellent, and justifies the use of the ab initio data to fit the QMS while retaining the original PS-PES energy mapping to describe the internal energy change and resulting atomic forces in our model. Fig. 5.4, left, presents a comparison between the ICE-CI DMS and the PS-PES DMS, again in an excellent agreement.

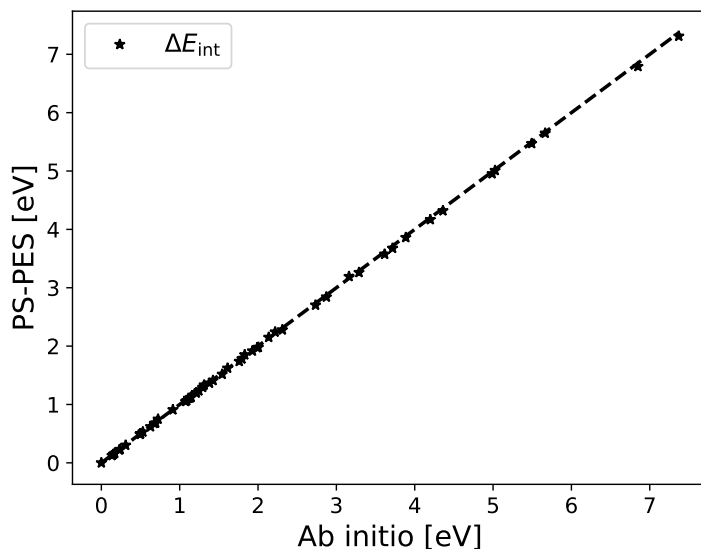


Figure 5.3: The relative internal energy difference between the different monomer configurations used in the QMS fit, compared between the ab initio results and the PS-PES. The good agreement between the two methods implies that the use of the ICE-CI data to fit the QMS justifies the use of the original PS-PES to represent internal energy changes and resulting atomic forces, as both potential energy surfaces are close with RMSD of 0.022 eV, within chemical accuracy (~ 0.51 kcal/mol).

The QMS model parameters associated with the charges in eqs Eq. (5.25)–Eq. (5.26), A, B, C and D, as well as the geometric parameters of eqs Eq. (5.30)–Eq. (5.31), a, b, c, d and e, are fitted to best reproduce the principal quadrupole moment component. Considering the water molecule in the ground state configuration the symmetric

quadrupole moment tensor can be written as

$$\theta = \begin{bmatrix} \theta_T - \Delta & 0 & 0 \\ 0 & -\theta_T - \Delta & 0 \\ 0 & 0 & 2\Delta \end{bmatrix} \quad (5.32)$$

where $\theta_T = (\theta_{xx} - \theta_{yy})/2$.

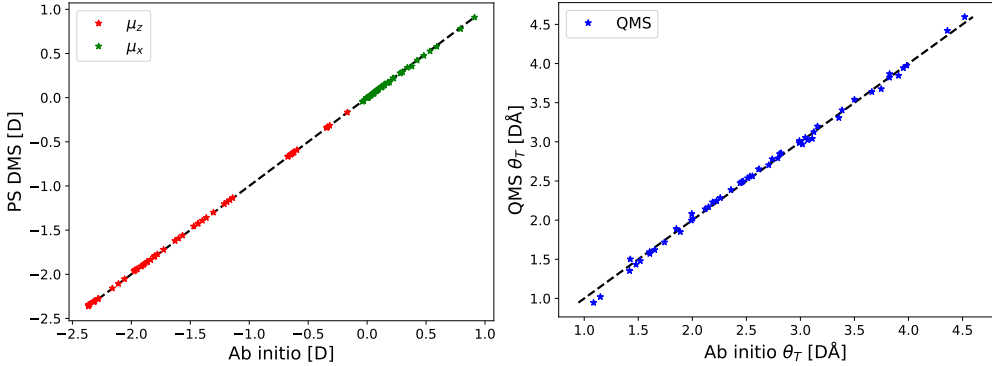


Figure 5.4: Left: comparison of the dipole z- and x-components, μ_z and μ_x respectively, as predicted by the DMS, Eq. (5.23) and compared to the ICE-CI μ_z and μ_x . Note that due to a choice of local reference frame the μ_y component is always numerically zero. The DMS of the PS-PES and ICE-CI are in an excellent agreement, with a RMSD of 0.004 D and within 0.5% on average. Right: comparison of the θ_T component mapped by the QMS, Eq. (5.24), with the ab initio ICE-CI data. The geometric QMS model of this work, which is fitted to best reproduce the ab initio results, captures the results to a good degree with low scatter, a mean absolute error of 0.04 DÅ, and an average RMS difference of around 1.6% (see Supplementary Information for the RMSD analysis).

The values of the QMS parameters are determined by carrying out a least-squares optimization, using a module freely available in the scientific computing package SciPy. [96] Table 5.1 presents the numerical values and units of the resulting best fit parameters, and Fig. 5.4, right, shows the resulting fit of the θ_T components, compared between the QMS fit and ab initio ICE-CI values. The overall fit is in good agreement with the ab initio values over a broad range of θ_T values, with very low scatter. The largest

deviation is found where θ_T is lowest, i.e. where the quadrupole moment interaction strength is the weakest.

Table 5.1: Numerical values and units of the quadrupole moment surface function, Eq. (5.24).

Geometry		Charges	
a [Å]	0.5149	A	0.9763
b	-1.1271	B	0.6418
c [Å ⁻¹]	0.5146	C	0.7251
d [rad]	3.5908	D	-1.0603
e	-0.1081	q_{eq}^{H}	0.3310
r_{eq} [Å]	0.9578		
θ_{eq} [rad]	1.8240		

5.4 Forces

With the various expressions given in the preceding section analytical atomic force components can be obtained and are derived from the negative gradient of the total energy expression, Eq. (5.15), with respect to the position of atom a in molecule i , or

$$\begin{aligned}
 F_{\alpha}^{ia} &= - \frac{dE_{\text{tot}}}{dr_{\alpha}^{ia}} \\
 &= - \frac{\partial E_{\text{elst}}}{\partial r_{\alpha}^{ia}} - \frac{\partial E_{\text{non-elst}}}{\partial r_{\alpha}^{ia}} - \frac{\partial E_{\text{mon}}}{\partial r_{\alpha}^{ia}}
 \end{aligned} \tag{5.33}$$

The first term on the right hand side result in several contributing factors to the atomic forces due to the definition of the principal axes, choice of expansion center and the DMS and QMS. The atomic forces resulting from the simple pair-wise potentials describing the non-electrostatic terms are omitted for the sake of brevity, and the atomic forces due to the monomer energy expression – the PS-PES – are accounted for in their original work. [74]

The first term on the right hand side of Eq. (5.33), the total intermolecular electrostatic interaction, can be further divided into four contributions

$$\begin{aligned}
 -\frac{\partial E_{\text{elst}}}{\partial r_{\alpha}^{ia}} = & -\frac{\partial E_{\text{elst}}}{\partial \mu_{\beta}^j(\{\mathbf{r}^{jb}\})} \frac{\partial \mu_{\beta}^j(\{\mathbf{r}^{jb}\})}{\partial r_{\alpha}^{ia}} - \frac{\partial E_{\text{elst}}}{\partial \theta_{\beta\gamma}^j(\{\mathbf{r}^{jb}\})} \frac{\partial \theta_{\beta\gamma}^j(\{\mathbf{r}^{jb}\})}{\partial r_{\alpha}^{ia}} \\
 & - \frac{\partial E_{\text{elst}}}{\partial V_{\beta\gamma\delta\epsilon\ldots\eta}^j} \frac{\partial V_{\beta\gamma\delta\epsilon\ldots\eta}^j}{\partial r_{\alpha}^{ia}} - \frac{\partial E_{\text{elst}}}{\partial R_{\eta\beta}^j} \frac{\partial R_{\eta\beta}^j}{\partial r_{\alpha}^{ia}}
 \end{aligned} \quad (5.34)$$

which are, in order, the partial derivative of the DMS and QMS, partial derivative of the external field and gradients thereof, and partial derivatives of the local-to-global rotation matrices as defined in Eq. (5.1)–Eq. (5.4).

At self-consistency of the iterative process which minimizes the energy in terms of the polarized moments the following conditions apply

$$\frac{\partial E_{\text{elst}}}{\partial \Delta \mu_{\alpha}^i} = \frac{\partial E_{\text{elst}}}{\partial \Delta \theta_{\alpha\beta}^i} = \frac{\partial E_{\text{self}}}{\partial \Delta \mu_{\alpha}^i} = \frac{\partial E_{\text{self}}}{\partial \Delta \theta_{\alpha\beta}^i} = 0$$

There are no explicit force contributions from the self-energy terms due to the on-site external field as the self-energy can be written solely in terms of the on-site induced moments (see the Supplementary Information). This results in a non-trivial additional condition

$$\frac{\partial E_{\text{self}}}{\partial V_{\beta\gamma\delta\epsilon\ldots\eta}^j} = 0 \quad (5.35)$$

Due to these conditions of the self-energy a single force contribution arises and is due to the local-to-global transformation of the fixed polarizability tensors

$$-\frac{\partial E_{\text{self}}}{\partial r_{\alpha}^{ia}} = -\frac{\partial E_{\text{self}}}{\partial R_{\eta\beta}^j} \frac{\partial R_{\eta\beta}^j}{\partial r_{\alpha}^{ia}} \quad (5.36)$$

The total force contribution due to the intermolecular electrostatic interaction and intramolecular self-energy is then

$$\begin{aligned}
 -\left(\frac{\partial E_{\text{in+pol}}}{\partial r_{\alpha}^{ia}} + \frac{\partial E_{\text{self}}}{\partial r_{\alpha}^{ia}} \right) = & -\frac{\partial E_{\text{in+pol}}}{\partial \mu_{\beta}^j(\{\mathbf{r}^{jb}\})} \frac{\partial \mu_{\beta}^j(\{\mathbf{r}^{jb}\})}{\partial r_{\alpha}^{ia}} - \frac{\partial E_{\text{in+pol}}}{\partial \theta_{\beta\gamma}^j(\{\mathbf{r}^{jb}\})} \frac{\partial \theta_{\beta\gamma}^j(\{\mathbf{r}^{jb}\})}{\partial r_{\alpha}^{ia}} \\
 & - \frac{\partial E_{\text{in+pol}}}{\partial V_{\beta\gamma\delta\epsilon\ldots\eta}^j} \frac{\partial V_{\beta\gamma\delta\epsilon\ldots\eta}^j}{\partial r_{\alpha}^{ia}} - \left(\frac{\partial E_{\text{in+pol}}}{\partial R_{\eta\beta}^i} + \frac{\partial E_{\text{self}}}{\partial R_{\eta\beta}^i} \right) \frac{\partial R_{\eta\beta}^i}{\partial r_{\alpha}^{ia}}
 \end{aligned} \quad (5.37)$$

The terms in the expression above are given explicitly in the Supporting Information. It is noted that in order to evaluate the first term on the right hand side, explicit partial charge derivatives with respect to atomic positions of the DMS are required, which were not included in the original work on the PS-PES. [74] These are provided by Burnham and Xantheas, first used in the development of a flexible Thole-type multipole moment expansion potential. [32]

5.5 Flexible Model Fit

With the introduction of the DMS and QMS, the Gaussian type interaction tensor screening functions, as well as the changes to the pair-wise repulsion function, all of the five model parameters which affect the intermolecular interactions g , τ_d , A_{ref} , k and h are re-fitted. The fitting is performed with the same least-squares optimization module used for the QMS fit. The same numerical values are used for the fixed octupole and hexadecapole, as well as the dipole-dipole, dipole-quadrupole and quadrupole-quadrupole polarizability as in the original SCME model. [89] The Fortran based SCME/f code is freely available online [97], and includes an interface to the Python based Atomic Simulation Environment [98, 99] library. The data set used for the fitting

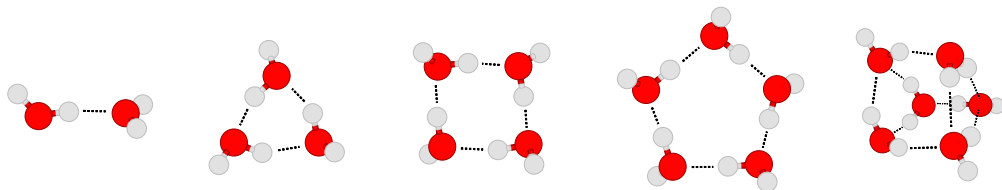


Figure 5.5: The lowest lying water cluster $(\text{H}_2\text{O})_n$ isomers for $n=2-6$ used in the fitting procedure for the model parameters. From left to right; dimer (Cs), trimer (UUD), quadrumer (S4), pentamer (cyclic, CYC) and hexamer (prism, PRI).

includes several points around the minimum of the dimer binding curve with the energy minimum and oxygen-oxygen distance corresponding to CCSD(T) calculations. [80] A single interaction energy for the lowest lying trimer, tetramer, pentamer and hexamer

is included. Fig. 5.5 shows the geometry of the lowest-lying water clusters (H₂O)_n in the range $n = 2 - 6$. The reference calculations which are used here include the complete basis set limit CCSD(T) energies of the low-lying water hexamer structures by Bates and Tschumper. [79] For the other cluster sizes – trimers, tetramers and pentamers – complete basis set limit RI-MP2 calculations, with CCSD(T) corrections, are used. [80]

Table 5.2: Properties of crystal ice Ih evaluated with SCME [9, 10] and SCME/f, compared to experimental values. $\langle r_{\text{OO}} \rangle$ is the average oxygen-oxygen distance, a , b , c the lattice parameters for a dipole-free orthorhombic cell (containing eight molecules). V_0^{ZPE} (V_0) is the optimized cell volume, $E_{\text{lat}}^{\text{ZPE}}$ (E_{lat}) and B_0^{ZPE} (B_0) are the lattice energy and bulk modulus with (and without) zero-point energy correction, all expressed per molecule.

Property	SCME	SCME/f	Exp. ¹
$\langle r_{\text{OO}} \rangle$ [Å]	2.742	2.751	2.751
a [Å]	4.470	4.478	4.497
b [Å]	7.747	7.777	7.789
c [Å]	7.287	7.331	7.321
V_0 [Å ³]	31.55	30.38	
V_0^{ZPE} [Å ³]		31.98	32.05
E_{lat} [eV]	−0.611	−0.645	−0.611
$E_{\text{lat}}^{\text{ZPE}}$ [eV]		−0.489	−0.491
B_0 [GPa]	11.4	15.0	
B_0^{ZPE} [GPa]		12.2	10.9

¹ Experimental values: average oxygen-oxygen distance is from Bjerrum [100], lattice parameters from Röttger *et al.* [101] (and resulting V_0^{ZPE}), enthalpy of vaporization ($E_{\text{lat}}^{\text{ZPE}}$) and lattice energy (E_{lat}) from Whalley [102], and bulk modulus from Hobbs [103].

In addition to the clusters, properties of hexagonal ice (ice Ih) have been considered, which is the most common ice phase. There are no high-level first-principles calculations with sufficient accuracy to serve as reference values. Instead, experimental data

for lattice constants, unit cell volume, bulk modulus and lattice energies need to be used, which generally include zero-point energy (ZPE) effects – and these effects are quite sizeable. [102, 104–106] Consequently, I have performed phonon calculations with the SCME/f model for proton disordered units cells of ice Ih containing 96 water molecules using the Parlinski-Li-Kawazoe finite-displacement method [107] as implemented in the PHONOPY package [108] using $3 \times 3 \times 3$ supercells and a displacement of 0.01 Å. For a unit cell with fixed cell vectors a geometry relaxation has been performed, which employs the analytical SCME/f forces with a force threshold of 10^{-3} eV/Å. Then, using a $10 \times 10 \times 10$ q-point sampling for the Brillouin zone integration, A numerically converged phonon density of states $g(\omega)$ has been obtained, the first moment of which provides the ZPE

$$E_{\text{ZPE}} = \frac{\hbar}{2} \int_0^\infty \omega g(\omega) d\omega \quad . \quad (5.38)$$

Considering the dependence of the phonon frequencies on the unit cell volume $\omega = \omega(V)$ within the so-called quasi-harmonic approximation yields a ZPE-corrected energy-volume curve

$$E_{\text{tot+ZPE}}(V) = E_{\text{tot}}(V) + E_{\text{ZPE}}(V) \quad , \quad (5.39)$$

where the energy zero is such that it describes infinitely separated (non-bound) individual water molecules. By fitting the Rose-Vinet equation of state [109] the minimum $E_{\text{lat}}^{\text{ZPE}} = E_{\text{tot+ZPE}}(V_0^{\text{ZPE}})$ of that curve together with the ZPE-corrected bulk modulus B_0^{ZPE} has been obtained (see supporting information for more details), which can be compared against accurate experimental data. [101–103] In order to include this data in the fitting process, an initial $E_{\text{tot+ZPE}}(V)$ was calculated based on the SCME/f parameters first determined by fitting the data set derived from the water clusters. Then, $E_{\text{tot}}(V)$ was improved by further parameter adjustments such that the expected ZPE correction would bring it close to the experimental values.

This trial and error scheme was found necessary since the phonon calculations are significantly more expensive than the calculation of the cluster properties. The end results based on a new set of phonon calculations is presented in Table 5.2 and shows good agreement with the experimental target properties. (The concomitant energy-volume

Table 5.3: Intermolecular interaction model parameters, numerical values and units.

Damping		Repulsion	
τ_d [\AA^{-1}]	7.5548	A_{rep} [eV]	8149.63
g [\AA]	1.1045	k	0.5515
		h [\AA^{-1}]	3.4695

curves are shown in the supporting information.) Table 5.3 compiles the concomitant final optimized parameters of the SCME/f model.

Table 5.4 shows the resulting interaction energy and relative interaction energy versus the reference CCSD(T) calculations of the lowest lying isomers used in the fit. This includes a structural analysis comparing the relaxed SCME/f structure to the CCSD(T) reference structures, where the RMS deviation of nearest neighbor oxygen-oxygen distances, $\langle d_{\text{r}_{\text{OO}}} \rangle$, intramolecular oxygen-hydrogen bond lengths of the donor hydrogens, $\langle d_{\text{r}_{\text{OH}}} \rangle$, hydrogen bonding (H-bond) bond lengths, $\langle d_{\text{r}_{\text{O} \dots \text{H}}} \rangle$, and angles between oxygen-hydrogen-oxygen in H-bonds, $\langle d\angle \text{OHO} \rangle$, are presented. The overall RMSD of the atomic positions is also presented, $\langle d\mathbf{r}^a \rangle$, and is evaluated with the Kabsch algorithm [110]. The interaction energies for the different cluster sizes are reproduced to a reasonable degree, with sub kcal/mol difference compared to the CCSD(T) results, except for the prism isomer of the hexamer where the interaction energy is overestimated by $1.18 \text{ kcal mol}^{-1}$. The resulting relaxed structures are in an overall very good agreement with the reference structures, with small variations in the second decimal in terms of atomic distances. Similarly, the angles between OHO in H-bonds are in a good agreement with the reference. The largest deviation is found in the angle between the donor-acceptor in the dimer.

5.6 Model Validation

For further validation of the new model the interaction energies and relative energy differences of all higher lying isomers of the pentamers and hexamers are calculated, which are not included in the fitting data set, and compared to the relative energies from

Table 5.4: Interaction energy (kcal/mol) and distances (\AA) between atoms in the most stable configuration of clusters $(\text{H}_2\text{O})_n$ with $n=2, \dots, 6$. E_{int} is the SCME/f calculated interaction energy of the clusters and ΔE_{int} (kcal/mol) the difference with respect to the CCSD(T) values. $\langle d\mathbf{r}_{\text{OO}} \rangle$, $\langle d\mathbf{r}_{\text{OH}} \rangle$ and $\langle d\mathbf{r}_{\text{O}\dots\text{H}} \rangle$ are the RMSD of the oxygen-oxygen neighbour distances, intramolecular oxygen-hydrogen bond lengths of the donor-hydrogen and bonding oxygen \cdots hydrogen bond length distances, respectively, compared to the CCSD(T) obtained structures. [79, 80] $\langle d\mathbf{r}^a \rangle$ is the overall RMSD of the relaxed SCME/f structure evaluated using the Kabsch algorithm [110]. $\langle d\angle\text{OHO} \rangle$ is the RMSD of the angle (in degrees) between the oxygen-hydrogen-oxygen in hydrogen bonds.

$(\text{H}_2\text{O})_n$	E_{int}	ΔE_{int}	$\langle d\mathbf{r}_{\text{OO}} \rangle$	$\langle d\mathbf{r}_{\text{OH}} \rangle$	$\langle d\mathbf{r}_{\text{O}\dots\text{H}} \rangle$	$\langle d\mathbf{r}^a \rangle$	$\langle d\angle\text{OHO} \rangle$
2-Cs	-4.85	+0.18	0.011	0.000	0.017	0.017	5.923
3-UUD	-15.16	+0.54	0.035	0.010	0.037	0.037	2.489
4-S4	-27.51	-0.11	0.005	0.014	0.006	0.045	1.382
5-CYC	-36.72	-0.71	0.014	0.015	0.003	0.046	0.369
6-PRI	-47.10	-1.18	0.017	0.012	0.035	0.033	4.564

the quantum chemistry references. [79, 80] The trends are shown in Figs. 5.6 and 5.7, and the trend predicted with the rigid SCME is shown for comparison. All structures are relaxed with a force tolerance of $10^{-4} \text{ eV } \text{\AA}^{-1}$, and results collected in Table 5.5, which also presents the RMS difference between the relaxed SCME/f structures and the quantum chemistry reference structures.

For the pentamers, Fig. 5.6, most of the relative energy difference trend is captured with the exception of isomer FRA, whose relative stability is underestimated. Another key difference between SCME/f and the reference calculations is the series of CAA-CAB isomers, which have a cagelike structure. In particular the cage structure of isomers CAA and CAB are not stable and rearrange to isomers which are more akin to the fused ring structures of the FRA-FRC isomers. The resulting SCME/f structures of CAA and CAB are near identical, with an interaction energy difference of only 0.01

Table 5.5: Energies and relative energy and structural properties of the pentamer and hexamer isomers. See the caption of Table 5.4 for the definition of the table entries.

$(\text{H}_2\text{O})_n$	E_{int}	ΔE_{int}	$\langle d\mathbf{r}_{\text{OO}} \rangle$	$\langle d\mathbf{r}_{\text{OH}} \rangle$	$\langle d\mathbf{r}_{\text{O}\cdots\text{H}} \rangle$	$\langle d\mathbf{r}^a \rangle$	$\langle d\angle\text{OHO} \rangle$
5-FRB	-35.60	-0.72	0.026	0.012	0.041	0.036	4.008
5-CAC	-35.50	-0.81	0.053	0.012	0.089	0.136	8.548
5-CAA	-35.07	-0.53	0.060	0.012	0.053	0.254	9.281
5-CAB	-35.06	-1.23	0.065	0.011	0.080	0.237	6.107
5-FRC	-33.56	-1.12	0.025	0.013	0.026	0.043	1.859
5-FRA	-32.91	0.22	0.025	0.013	0.032	0.059	1.731
6-CAG	-46.44	-0.74	0.013	0.017	0.019	0.054	1.607
6-BK1	-46.37	-1.09	0.014	0.015	0.009	0.033	2.346
6-BK2	-46.26	-1.35	0.014	0.016	0.008	0.038	3.433
6-BAG	-45.90	-1.52	0.015	0.017	0.012	0.065	3.826
6-CYR	-45.36	-1.00	0.012	0.015	0.006	0.018	3.913
6-CB1	-44.57	-1.23	0.013	0.015	0.003	0.031	2.924
6-CB2	-44.49	-1.20	0.013	0.015	0.005	0.025	2.284

1 Pentamers; fused-ring-B (FRB), cage-C (CAC), cage-A (CAA), cage-B (CAB), fused-ring-C (FAC) and fused-ring-A (FRA); and the hexamers; cage (CAG), book-1 (BK1), book-2 (BK2), bag (BAG), cyclic-ring (CYR), cyclic-boat-1 (CB1) and cyclic-boat-2 (CB2).

kcal/mol. Only the CAC isomer keeps its cagelike structure, but one of the H-bonds is not stable (between a donor acceptor oxygen with distance greater than 3.0 Å), resulting in a rotation of one of the water monomers. Compared to the rigid SCME predecessor this represents an improvement, in particular for the FRB, CAC and CAA isomers, whose stability is greatly underestimated relative to the CYC isomer.

For the hexamers, Fig. 5.7, the overall trend in the relative interaction energies is captured to a good degree compared to the CCSD(T) reference, and is a substantial improvement over the rigid SCME model, which greatly underestimates the stability of the prism isomer relative to all other isomers. The bond lengths and angles of

the hexamer isomers are all in very good agreement with the reference structures, with small differences in the second or third decimal in terms of the bond lengths, and the H-bonded OHO angles deviate by only 2-4°. Tables 5.6 and 5.7 presents vibrational frequency analysis of the lowest lying isomers, including the cyclic ring isomer of the hexamer. The RMS deviation from near-CBS CCSD(T) calculations [111, 112] are presented for the different classes of modes. These are intermolecular low-energy vibrational modes (10-1000 cm^{-1}), intramonomer bending modes (1600-1800 cm^{-1}) and H-bonded and non-bonded OH stretching modes (ca. 3200-3900 cm^{-1}). For comparison, the same analysis is performed for the SCME/f model, but with the quadrupole moment fixed and corresponding to the numerical value of the quadrupole moment for the ground state monomer configuration.

With the inclusion of the QMS (left column Tables 5.6 and 5.7) the low-energy vibrational modes and, in particular, the bending modes are in a good agreement with the reference calculations. The RMS deviation ranges from 18 to 23 cm^{-1} and 7 to 14 cm^{-1} for the two classes of modes, respectively. The maximum difference in the bending modes does not exceed 20 cm^{-1} for any of the clusters analyzed. The red shift of the H-bonded OH stretches is, however, not captured by our model, resulting in an overestimation of these modes, which becomes systematically larger with cluster size. This is due to the underlying monomer potential energy surface, whose limit in terms of hydrogen dissociation is $\text{OH}^\cdot + \text{H}^\cdot$ whereas should be in the condensed phase $\text{OH}^- + \text{H}^+$. The model potential does not describe this important change, and the resulting weakening of oxygen-hydrogen bonds in H-bonding OH. The high-frequency modes for the dimer are though in a reasonable agreement with the reference calculations.

A comparison to the same vibrational frequency analysis is performed with the quadrupole moment fixed (right column, Tables 5.6 and 5.7). Fixing the quadrupole moment results in a drastic change in the difference between all of the types of modes and for all cluster sizes, with for example a RMS deviation of up to three times greater for the bending modes. The overall agreement with the reference calculations of all modes is consistently worse, in particular for the larger cluster, $n=4-6$. Only the low-frequency

Table 5.6: Relative vibrational properties of three lowest lying water clusters (H₂O)_n with $n=2,3,4$ (Cs, UUD, S4). The entries for each system correspond from top to bottom, the low-frequency intermolecular vibrational modes (l, 10 to 1000 cm⁻¹), intramonomer bending (b, 1600 to 1800 cm⁻¹) and high frequency stretching of H-bond OH and non-bonded OH bonds (h, 3200 to 3900 cm⁻¹). $\langle \Delta \text{cm}^{-1} \rangle$ is the RMSD between the frequencies in the low, medium and high range, as predicted with SCME/f compared to near-CBS CCSD(T) reference calculations. [111, 112] The last entry is RMSD for the total frequency range (**t**), where the value in the parenthesis excludes the overestimated H-bond OH stretches. $\max |\Delta \text{cm}^{-1}|$ is the maximum absolute difference for each entry. The two columns on the right are for the SCME/f model potential with the quadrupole moment set to a fixed value corresponding to the ground state water monomer configuration.

(H ₂ O) _n		quadrupole moment surface		fixed quadrupole moment	
		$\langle \Delta \text{cm}^{-1} \rangle$	$\max \Delta \text{cm}^{-1} $	$\langle \Delta \text{cm}^{-1} \rangle$	$\max \Delta \text{cm}^{-1} $
2-Cs	l	17.52	41.50	15.33	23.10
	b	6.71	9.10	9.18	12.70
	h	28.55	36.10	50.41	70.30
	t	17.23		23.56	
3-UUD	l	23.03	49.20	34.43	71.70
	b	7.75	12.20	18.41	23.90
	h	68.09	89.30	153.65	190.40
	t	31.20	(24.98)	64.02	(29.19)
4-S4	l	20.87	44.40	29.43	58.10
	b	10.74	12.80	25.69	29.40
	h	155.58	200.20	266.11	334.10
	t	59.19	(21.06)	100.25	(26.49)

Table 5.7: Same as Table 5.6, but for different water clusters $(\text{H}_2\text{O})_n$ with $n=5,6$ (CYC, CYR, PRI).

$(\text{H}_2\text{O})_n$		quadrupole moment surface		fixed quadrupole moment	
		$\langle \Delta \text{cm}^{-1} \rangle$	$\max \Delta \text{cm}^{-1} $	$\langle \Delta \text{cm}^{-1} \rangle$	$\max \Delta \text{cm}^{-1} $
5-CYC	l	18.47	35.20	35.08	65.30
	b	14.22	19.60	26.44	34.40
	h	179.34	229.60	282.41	358.10
	t	66.02	(20.13)	105.22	(31.38)
6-CYR	l	21.10	44.30	35.16	75.40
	b	11.55	13.10	32.53	40.00
	h	185.38	239.30	280.06	356.30
	t	67.75	(23.24)	103.48	(32.56)
6-PRI	l	21.70	87.60	27.74	56.20
	b	9.86	18.30	35.16	45.80
	h	208.58	408.60	313.99	571.80
	t	75.79	(24.60)	113.85	(36.40)

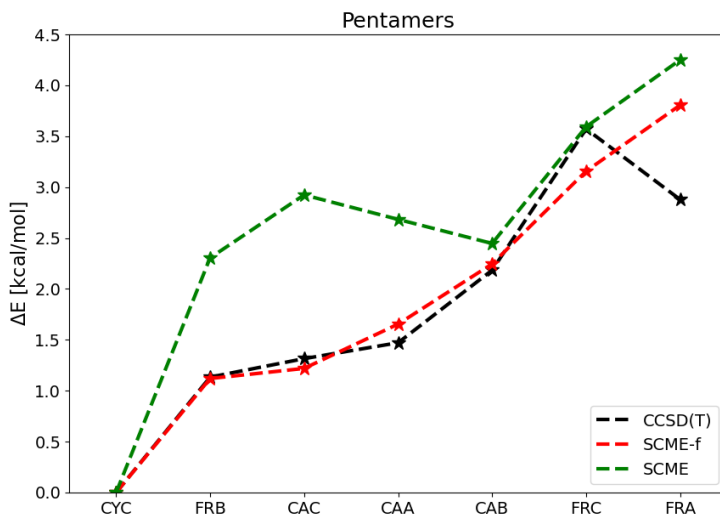


Figure 5.6: Relative energy difference for the lowest lying pentamers water cluster isomers. The results for the rigid version of SCME [9, 89] and SCME/f are compared. Relative energy differences from high level quantum chemistry calculations are also shown. RI-MP2 energies at the complete basis set limit with CCSD(T) corrections [80] (MP2/CBS+ Δ CCSD(T)). The acronyms from left to right are the different isomers: Cyclic (CYC), fused-ring-B (FRB), cage-C (CAC), cage-A (CAA), cage-B (CAB), fused-ring-C (FAC) and fused-ring-A (FRA).

modes of the Cs dimer seem improved by fixing the quadrupole moment. While the parametrization of the intermolecular interaction parameters is with the QMS included, the structural properties and interaction energy of the small clusters are not drastically changed with the quadrupole moment fixed (see Supplementary Information).

It is also of interest to analyze the structure of the monomers in crystal ice Ih with or without the QMS included. Table 5.8 presents the average internal HOH angle of each water monomer in the crystal lattice, extracted at volume V_0^{ZPE} , and compares to the experimental value of the angle for the isolated monomer and in crystal ice Ih. The

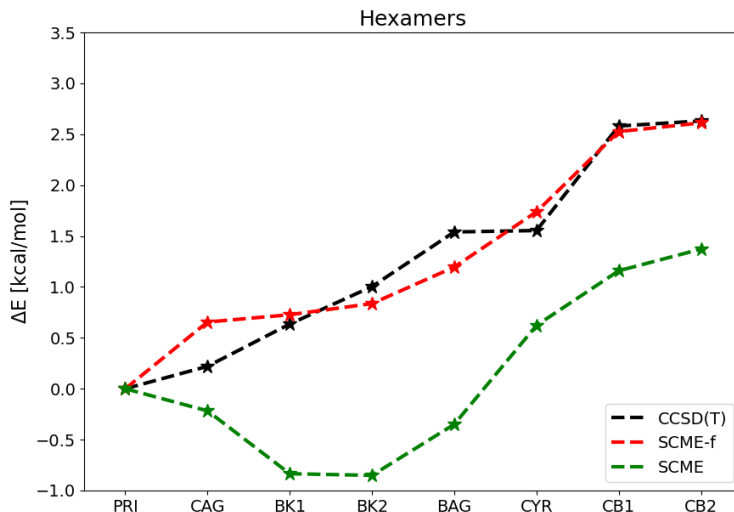


Figure 5.7: The same as Fig. 5.6 but for hexamer water cluster isomers. CCSD(T) energies at the complete basis set limit (CCSD(T)/CBS) [79]. The acronyms from left to right are the different isomers: Prism (PRI), cage (CAG), book-1 (BK1), book-2 (BK2), bag (BAG), cyclic-ring (CYR), cyclic-boat-1 (CB1) and cyclic-boat-2 (CB2).

experiments show a clear widening of the monomer HOH angle by about 3.5 degrees (104.5° – 108.1°) going from the gas to crystal phase. Without the QMS the trend is opposite, with the angle favoring lower values by about 4.5 degrees (104.5° – 99.95°), where the dipole moment is high. The correct trend is captured again with the inclusion of the QMS, with the angle widening by about 2 degrees (104.5° – 106.51°). The QMS correctly balances the magnitude of the dipole moment and principal quadrupole moment in the lattice, and in such a way that a widening of the angle is favoured.

5.7 Discussion and Conclusions

An extension of the SCME potential function has been presented for water molecules to allow for distortion of the molecular structure. In addition to the dipole moment

Table 5.8: Average intramolecular HOH angles (in degrees) for the SCME/f model with and without the QMS. Experimental angles for the isolate water molecule (gas) and in crystal ice Ih (Ih) are presented for comparison.

	Exp (gas)	Exp (Ih)	SCME/f	SCME/f no QMS
$\langle \angle \text{HOH} \rangle$	104.5	108.1	106.51	99.95

surface, this flexible potential function, SCME/f, includes a mapping of the quadrupole moment surface which has not been previously included at this level of detail to our knowledge. A simpler model for the quadrupole moment that has been used in both rigid and flexible point charge based potential functions [2, 75–78], as well as more sophisticated polarizable models [32–40], make use of the so-called M-site. We now digress in a brief comparison between the QMS model described in this work and the M-site model.

In the M-site model the partial charge associated with the oxygen is moved off the atomic center to a position behind the oxygen and on to the bisector defined by the two OH bond vectors. The position of the M-site in the global coordinate frame is written as [113–115]

$$\mathbf{r}_M = (1 - \gamma)\mathbf{r}_O + \frac{\gamma}{2}(\mathbf{r}_{H_1} + \mathbf{r}_{H_2}) \quad (5.40)$$

where $0 < \gamma \leq 1$. For any finite value of γ the partial charges are re-scaled according to

$$q^{H_i^\gamma} = \frac{q^{H_i}}{1 - \gamma}, \quad q^M = -q^{H_1^\gamma} - q^{H_2^\gamma} \quad (5.41)$$

such that the dipole moment remains unchanged in the M-site frame, and a single set of three partial charges describes both the dipole and quadrupole moment.

More importantly, a value of γ can be derived such that the Δ component in Eq. (5.32) vanishes, resulting in the compactly written moment tensor

$$\theta = \begin{bmatrix} \theta_T & 0 & 0 \\ 0 & -\theta_T & 0 \\ 0 & 0 & 0. \end{bmatrix} \quad (5.42)$$

This illustrates that the principal quadrupole moment component θ_T is origin independent, and is the rational for placing the partial charge on the M-site and not on the oxygen center. The strength of the quadrupole moment interaction is determined by θ_T . For the ground state PE-PES water monomer configuration used in this work a $\gamma = 0.4071$ results in a compact tensor of the form in Eq. (5.42) (see the Supplementary Information). Similar values for γ are reported in potential functions based on the M-site. While such a three site partial charge model can capture both the dipole and principal quadrupole moment for a fixed ground state monomer configuration, the question is how the model holds up in the case of a flexible water monomer.

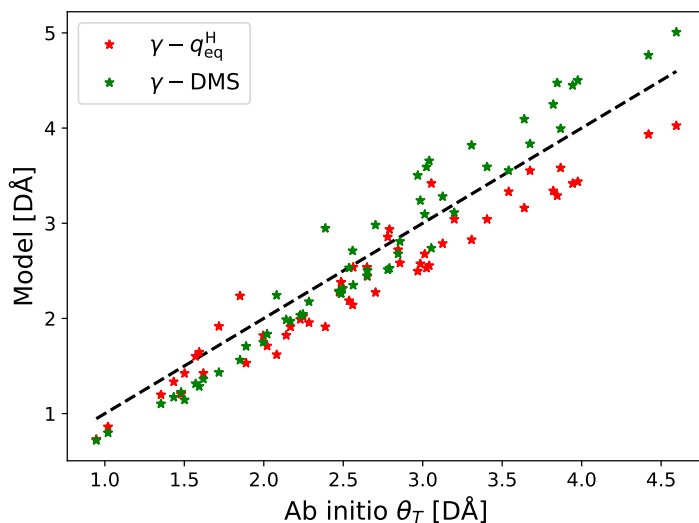


Figure 5.8: M-site model making use of a fixed charge ($\gamma - q_{\text{eq}}^{\text{H}}$, red) in the ground state monomer configuration or the DMS charges ($\gamma - \text{DMS}$, green). The fixed point charge model (red) tends to underestimate the strength of the quadrupole moment over the whole range, whereas when based on the DMS charges (green) the quadrupole moment is underestimated in the lower region and overestimated in the higher region ($> 3.0 \text{ DÅ}$).

Using the ab initio ICE-CI quadrupole moment data four M-site models are considered and compared, and are representative of M-site models encountered in the literature.

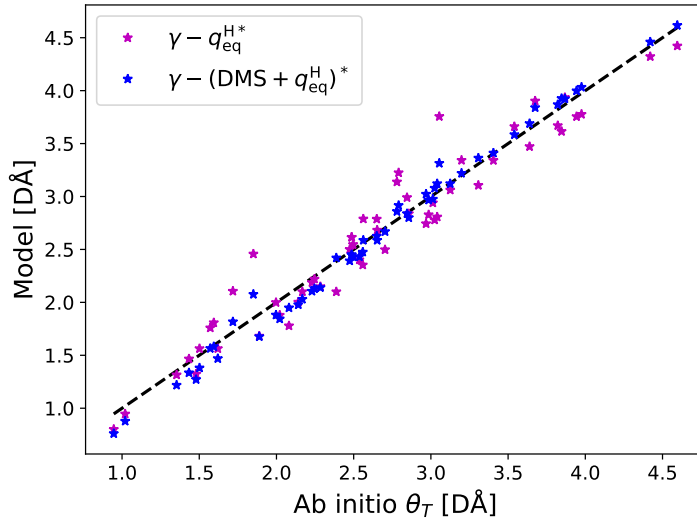


Figure 5.9: M-site model making use of scaled charge ($\gamma - q_{\text{eq}}^{\text{H}*}$, magenta) and a combination of scaled DMS and fixed charges as in Eq. (5.25) ($\gamma - (\text{DMS} + q_{\text{eq}}^{\text{H}})^*$, blue). The overall trend is better captured in Figs. 5.8 and 5.9, but the scatter is still substantial for the scaled fixed charge model (magenta). The agreement is improved substantially with the mixture of fixed charges and variable DMS charges (blue) compared to the other models, and the scatter is more concentrated in the region of low θ_T . See the Supplementary Information for details on the M-site models.

The details of the models and parameters are presented in the Supplementary Information. The first two models, Fig. 5.10 left, make use of $\gamma = 0.4071$ and a set of fixed partial charges ($\gamma - q_{\text{eq}}^{\text{H}}$) – corresponding to the partial charges of the ground state monomer configuration – or scaled ground state charges ($\gamma - q_{\text{eq}}^{\text{H}*}$). The scaling parameter is fit such that the model best captures θ_T over the whole range. The fixed point charge model tends to underestimate the strength of the quadrupole moment over the whole range, whereas the scaling of the charge results in a change in the slope and overall better agreement. However, in both cases the scatter is substantial and the RMS difference between the trace components of the quadrupole moment versus the ab initio values is $> 10\%$ on average (see the Supplementary Information).

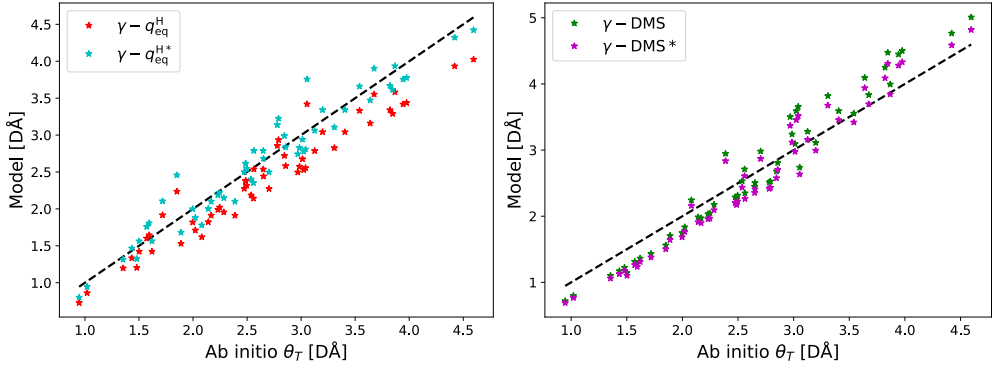


Figure 5.10: M-site models. See the Supplementary Information for details on the individual models. Left: M-site models making use of a fixed charge ($\gamma - q_{eq}^H$, red) corresponding to the ground state monomer configuration or scaled charge ($\gamma - q_{eq}^{H,*}$, cyan). The fixed point charge model (red) tends to underestimate the strength of the quadrupole moment over the whole range, whereas the scaling results in a change in the slope and an overall better agreement. Right: M-site models making use of variable DMS charges ($\gamma - \text{DMS}$, green) and scaled DMS charges ($\gamma - \text{DMS}^*$, magenta). Both model tend to underestimate the strength of the quadrupole moment in region of low strength, whereas overestimate in the region of large strength. The agreement is only slightly improved with the scaled DMS model, corresponding to a shift of the M-site to $\gamma = 0.3838$.

In the third and fourth model, Fig. 5.10 right, the charge are described with the DMS charge. In the third model the optimal γ value is used ($\gamma - \text{DMS}$) and in the fourth model the DMS charges are scaled ($\gamma - \text{DMS}^*$) to best capture θ_T over the whole range. The qualitative trend is the same in both cases, with the strength of the quadrupole moment underestimated in the region of low strength, and overestimated in the region of large strength, and the overall agreement is only slightly improved with a change in the slope. Similar to the fixed charge models the scatter is substantial, and the RMS difference is found to be $\approx 10\%$, on average.

While the simple M-site models capture the overall qualitative trend in the change of the principal quadrupole moment over a broad range of configurations, an analysis of the RMS difference of the quadrupole moment components shows that they deviate significantly for monomer configurations different than the ground state configuration. Neither the fixed charge or DMS charge M-site models (scaled or not) seem to better capture the principal quadrupole component over the other, and in all cases the RMS difference is around 10% or greater. This illustrates that a three site model based on the M-site principle is not able to capture the variation of the quadrupole moment in a flexible water potential model to a good degree. The four site QMS model developed in this work, which captures the principal quadrupole moment with a mean absolute error of 0.04 DÅ, similarly has low scatter throughout the range with an average RMS difference of 1.6%, with greatest discrepancy in the region where the quadrupole moment interaction is the weakest.

Furthermore, the intermolecular interactions of the SCME/f model only depend on five parameters. The parameters have been fitted to reproduce high level quantum chemistry calculations for the water dimer energy surface near the equilibrium geometry and interaction energy of the lowest-lying water clusters up to and including the hexamer, as well as the properties of the Ih ice crystal – and in such a way that experimental values are reproduced to a good degree after including zero point energy corrections.

The simple parameterization of the flexible model and the use of a single center for

the electrostatic interactions allows for the seamless integration into our recently implemented PE-QM/MM interface [72, 73].

The calculated energy of the higher lying energy isomers of hexamer water cluster are found to be in a reasonable agreement with the results of CCSD(T) calculations in the complete basis set limit. [79] The relative trend in the energy differences between the isomers, as well as the overall structures are captured to a good degree. This represents a significant improvement over the rigid SCME potential function and is on par with the trend predicted with the HBB2-pol [36, 37] potential function, which explicitly models the N-body expansion up to the three-body terms in the interaction energy and is the predecessor of the MB-pol potential function. [38–40] However, discrepancies are present in the series of pentamer isomers, in particular the cage-like isomers. H-bonds in bonds where the distance is greater than 3 Å are found to be unstable, leading to a rearrangement of some of the SCME/f structures compared to the reference structures.

Analysis of the vibrational modes of the small water clusters reveal a substantial improvement with the QMS mapping included (as opposed to a fixed value). In particular are the intramolecular bending modes in the range 1600 to 1800 cm^{-1} , with maximum absolute deviation consistently less than 20 cm^{-1} with the QMS included, compared to near-CBS CCSD(T) calculations. [111, 112] Importantly, including the DMS only results in the opposite trend of the intramolecular angle widening in crystal ice Ih compared to the gas phase. The inclusion of the QMS recovers the correct trend due to the balance between the magnitude of the dipole and principal quadrupole moment which are functions of the internal geometry and strongly dependent on this angle.

While the results presented here represent an important step forward in the development of a single center multipole expansion model for water, there is room for improvement, and this will be addressed in future work. A natural next step to the mapping of the dipole and the quadrupole is to incorporate a mapping of the polarizability tensors. Work is ongoing to incorporate the intramolecular geometry dependent mapping of the dipole-dipole, dipole-quadrupole and quadrupole-quadrupole polarizability tensors by

Loboda *et al.* [116]. It has been suggested that a critical part of the H-bond OH softening lies in the correct mapping of the polarizability surface of the individual monomers. [35]

In particular, and in order to further address the overestimated H-bonded OH stretches, an improvement of the underlying water monomer potential energy surface – whose limit in terms of hydrogen dissociation is $\text{OH}^\cdot + \text{H}^\cdot$ – must be made when there are neighboring water molecules such that it approaches to some degree the dissociation limit in a condensed phase which is $\text{OH}^- + \text{H}^+$. In order to capture this one could modify the DMS and QMS charges to better represent this limit, and in a way which depends on the environment. Modifying the charge of the DMS has, for example, previously been considered in water potentials in order to capture the charge delocalization and resulting softening of the H-bond, such as in the TTM3-F model. [34] Further improvements to this flexible SCME model that are being pursued include a more elaborate repulsive part including deviations from spherical symmetry.

5.A Appendix

The supporting information includes a detailed derivation of the atomic forces corresponding to contributions presented in Eq. (5.37), as well as a comparison between the numerical and analytical forces as the convergence criteria of the induced moments is varied. The parameters used for the model M-site description of the principal quadrupole moment are presented, followed by an analysis of the RMSD between ab initio versus the QMS quadrupole as well as model M-site quadrupoles with respect to geometrical variation of the monomer. Binding energies and relative structural properties of the lowest-lying water clusters are given for the case where the quadrupole moment is set to a fixed value corresponding to the ground state monomer configuration. Finally, the evaluation of the bulk properties from fitting the energy-volume relation – with and without zero-point energy corrections – is described.

5.A.1 Analytical Forces

We further apply the chain rule considering the main electrostatic plus induction force expression in the main text

$$\begin{aligned}
 - \left(\frac{\partial E_{\text{ele+ind}}}{\partial r_{\alpha}^{ia}} + \frac{\partial E_{\text{self}}}{\partial r_{\alpha}^{ia}} \right) = & - \frac{\partial E_{\text{ele+ind}}}{\partial \mu_{\beta}^j(\{\mathbf{r}^{jb}\})} \frac{\partial \mu_{\beta}^j(\{\mathbf{r}^{jb}\})}{\partial r_{\alpha}^{ia}} - \frac{\partial E_{\text{ele+ind}}}{\partial \theta_{\beta\gamma}^j(\{\mathbf{r}^{jb}\})} \frac{\partial \theta_{\beta\gamma}^j(\{\mathbf{r}^{jb}\})}{\partial r_{\alpha}^{ia}} \\
 & - \frac{\partial E_{\text{ele+ind}}}{\partial V_{\beta\gamma\delta\epsilon\dots\eta}^j} \frac{\partial V_{\beta\gamma\delta\epsilon\dots\eta}^j}{\partial r_{\alpha}^{ia}} - \left(\frac{\partial E_{\text{ele+ind}}}{\partial R_{\nu o}^j} + \frac{\partial E_{\text{self}}}{\partial R_{\nu o}^j} \right) \frac{\partial R_{\nu o}^j}{\partial r_{\alpha}^{ia}}
 \end{aligned} \tag{5.43}$$

The last term on the right hand side describes the force contribution due to the definition of the local-to-global reference frame transformation, and is the only term which includes an explicit contribution to the atomic forces due to the self-energies. To see this we first write the MM induced dipoles and quadrupoles as

$$\Delta\mu_{\alpha}^i = -\alpha_{\alpha\beta}V_{\beta}^i - \frac{1}{3}A_{\alpha,\beta\gamma}V_{\beta\gamma}^i = \Delta\mu_{\alpha}^i(\alpha) + \Delta\mu_{\alpha}^i(A) \tag{5.44}$$

$$\Delta\theta_{\alpha\beta}^i = -A_{\gamma,\alpha\beta}V_{\gamma}^i - C_{\gamma\delta,\alpha\beta}V_{\gamma\delta}^i = \Delta\theta_{\alpha\beta}^i(A) + \Delta\theta_{\alpha\beta}^i(C) \tag{5.45}$$

where on the right hand side of the second equality the contribution from the external field and field gradient due to the on-site potential is split up. With these definitions it is easy to relate the external field and field gradient at site i to the self-consistent moments of molecule i

$$V_{\beta}^i = - \frac{\Delta\mu_{\alpha}^i(\alpha)}{\alpha_{\alpha\beta}} \quad (5.46)$$

$$V_{\gamma}^i = - \frac{\Delta\theta_{\alpha\beta}^i(A)}{A_{\gamma,\alpha\beta}} \quad (5.47)$$

and

$$V_{\gamma\delta}^i = - \frac{\Delta\theta_{\alpha\beta}^i(C)}{C_{\gamma\delta,\alpha\beta}} \quad (5.48)$$

$$V_{\beta\gamma}^i = - \frac{\Delta\mu_{\alpha}^i(A)}{A_{\alpha,\beta\gamma}}. \quad (5.49)$$

The self-energy of an induced dipole in linear response theory is

$$E_{\text{self}}^{\mu} = - \int_0^{\Delta\mu^i} V_{\beta}^i d\Delta\mu^i. \quad (5.50)$$

It gives the energy cost of inducing a first order moment in the potential field at site i . By inserting the relation in Eq. (5.46) into the equation above, and by considering only (for the moment) the induced dipole in response to an external field gives

$$E_{\text{self}}^{\mu} = \int_0^{\Delta\mu^i(\alpha)} \frac{\Delta\mu_{\alpha}^i(\alpha)}{\alpha_{\alpha\beta}} d\Delta\mu^i = \frac{1}{2} \frac{\Delta\mu_{\alpha}^i(\alpha)\Delta\mu_{\beta}^i(\alpha)}{\alpha_{\alpha\beta}}. \quad (5.51)$$

For isotropic atomic polarization this becomes

$$E_{\text{self}}^{\text{iso}} = \frac{1}{2} \frac{(\Delta\mu^i)^2}{\alpha}. \quad (5.52)$$

This form is most frequently encountered in MM work based on isotropic atomic polarization and induced dipole in response to an external field. Similarly for the induced quadrupole

$$E_{\text{self}}^{\theta} = -\frac{1}{3} \int_0^{\Delta\theta^i} V_{\beta\gamma}^i d\Delta\theta^i \quad (5.53)$$

which expresses the energy cost of inducing a second order moment in the field gradient at site i . The factor of 1/3 follows from the definition of the traceless Cartesian moments

[82] used in SCME. The total self-energy for a single site i in SCME is then

$$\begin{aligned}
E_{\text{self}} &= E_{\text{self}}^{\mu} + E_{\text{self}}^{\theta} \\
&= \int_0^{\Delta\mu^i} \frac{\Delta\mu_{\alpha}^i(\alpha)}{\alpha_{\alpha\beta}} d\Delta\mu^i + \frac{1}{3} \int_0^{\Delta\theta^i} \frac{\Delta\theta_{\alpha\beta}^i(C)}{C_{\gamma\delta,\alpha\beta}} d\Delta\theta^i \\
&= \frac{1}{2} \frac{\Delta\mu_{\alpha}^i(\alpha)}{\alpha_{\alpha\beta}} \left(\Delta\mu_{\beta}^i(\alpha) + \frac{1}{3} \Delta\mu_{\beta}^i(A) \right) + \frac{1}{6} \frac{\Delta\theta_{\alpha\beta}^i(C)}{C_{\gamma\delta,\alpha\beta}} (\Delta\theta_{\gamma\delta}^i(C) + \Delta\theta_{\gamma\delta}^i(A)) \\
&= \frac{1}{2} \frac{\Delta\mu_{\alpha}^i(\alpha) \Delta\mu_{\beta}^i(\alpha)}{\alpha_{\alpha\beta}} + \frac{1}{3} \frac{\Delta\mu_{\alpha}^i(\alpha) \Delta\theta_{\beta\gamma}^i(C)}{k_{\alpha,\beta\gamma}} + \frac{1}{6} \frac{\Delta\theta_{\alpha\beta}^i(C) \Delta\theta_{\gamma\delta}^i(C)}{C_{\gamma\delta,\alpha\beta}} \quad (5.54)
\end{aligned}$$

where the relations in Eqs. (5.46) and (5.49) are used. The matrix k is given by

$$k = \frac{\alpha C}{A} \quad (5.55)$$

This expression for the self-energies is very useful at self-consistency (SCF). First and foremost it shows that there are no force contributions arising from partial derivatives of the on-site potential field and field gradients when considering the self-energy terms, since at SCF we have

$$\frac{\partial E_{\text{tot}}^{\text{sys}}}{\partial \Delta\mu_{\alpha}^i} = \frac{\partial E_{\text{tot}}^{\text{sys}}}{\partial \Delta\theta_{\alpha}^i} = 0, \quad (5.56)$$

which implies

$$\frac{\partial E_{\text{self}}}{\partial V_{\beta\gamma\delta\epsilon\dots\eta}^{jb}} = 0 \quad (5.57)$$

Contributions arise from the static octupole and static hexadecapole, as well as the dipole-dipole, dipole-quadrupole quadrupole-quadrupole polarizability matrices. The general contributions are of the following form

$$\frac{\partial E}{\partial R_{\nu o}^j} \frac{\partial R_{\nu o}^j}{\partial r_{\alpha}^{ia}} \rightarrow \delta_{ij} \delta_{\nu o, \beta\gamma} \quad (5.58)$$

resulting in for the static moments

$$\begin{aligned}
\frac{\partial E_{\text{ele+ind}}}{\partial R_{\nu o}^j} \frac{\partial R_{\nu o}^j}{\partial r_{\alpha}^{ia}} &= \frac{1}{15} \left(\frac{\partial R_{\eta\beta}^i}{\partial r_{\alpha}^{ia}} R_{\tau\gamma}^i R_{\kappa\delta}^i + R_{\eta\beta}^i \frac{\partial R_{\tau\gamma}^i}{\partial r_{\alpha}^{ia}} R_{\kappa\delta}^i + R_{\eta\beta}^i R_{\tau\gamma}^i \frac{\partial R_{\kappa\delta}^i}{\partial r_{\alpha}^{ia}} \right) \Omega_{\eta\tau\kappa}^{i'} V_{\beta\gamma\delta}^i \\
&+ \frac{1}{105} \left(\frac{\partial R_{\eta\beta}^i}{\partial r_{\alpha}^{ia}} R_{\tau\gamma}^i R_{\kappa\delta}^i R_{\sigma\eta}^i + R_{\eta\beta}^i \frac{\partial R_{\tau\gamma}^i}{\partial r_{\alpha}^{ia}} R_{\kappa\delta}^i R_{\sigma\eta}^i \right. \\
&\left. + R_{\eta\beta}^i R_{\tau\gamma}^i \frac{\partial R_{\kappa\delta}^i}{\partial r_{\alpha}^{ia}} R_{\sigma\eta}^i + R_{\eta\beta}^i R_{\tau\gamma}^i R_{\kappa\delta}^i \frac{\partial R_{\sigma\eta}^i}{\partial r_{\alpha}^{ia}} \right) \Phi_{\eta\tau\kappa\sigma}^{i'} V_{\beta\gamma\delta\epsilon}^i \quad (5.59)
\end{aligned}$$

and for the polarizability matrices the contributions are

$$\begin{aligned}
 & \left(\frac{\partial E_{\text{ele+ind}}}{\partial R_{\nu o}^j} + \frac{\partial E_{\text{self}}}{\partial R_{\nu o}^j} \right) \frac{\partial R_{\nu o}^j}{\partial r_{\alpha}^{ia}} = -\frac{1}{2} \left(\frac{\partial R_{\eta\beta}^i}{\partial r_{\alpha}^i} R_{\tau\gamma}^i + R_{\eta\beta}^i \frac{\partial R_{\tau\gamma}^i}{\partial r_{\alpha}^i} \right) \alpha_{\eta\tau}^{i'} V_{\beta}^i V_{\gamma}^i \\
 & - \frac{1}{3} \left(\frac{\partial R_{\eta\beta}^i}{\partial r_{\alpha}^i} R_{\tau\gamma}^i R_{\kappa\delta}^i + R_{\eta\beta}^i \frac{\partial R_{\tau\gamma}^i}{\partial r_{\alpha}^i} R_{\kappa\delta}^i + R_{\eta\beta}^i R_{\tau\gamma}^i \frac{\partial R_{\kappa\delta}^i}{\partial r_{\alpha}^i} \right) A_{\eta\tau\kappa}^{i'} V_{\beta}^i V_{\gamma\delta}^i \\
 & - \frac{1}{6} \left(\frac{\partial R_{\eta\beta}^i}{\partial r_{\alpha}^i} R_{\tau\gamma}^i R_{\kappa\delta}^i R_{\sigma\eta}^i + R_{\eta\beta}^i \frac{\partial R_{\tau\gamma}^i}{\partial r_{\alpha}^i} R_{\kappa\delta}^i R_{\sigma\eta}^i \right. \\
 & \quad \left. + R_{\eta\beta}^i R_{\tau\gamma}^i \frac{\partial R_{\kappa\delta}^i}{\partial r_{\alpha}^i} R_{\sigma\eta}^i + R_{\eta\beta}^i R_{\tau\gamma}^i R_{\kappa\delta}^i \frac{\partial R_{\sigma\eta}^i}{\partial r_{\alpha}^i} \right) C_{\eta\tau\kappa\sigma}^{i'} V_{\beta}^i V_{\delta\eta}^i
 \end{aligned} \tag{5.60}$$

where the factors 1/2, 1/3 and 1/6 are due to the self-energy terms – i.e. the contribution from the electrostatic plus induction interaction is reduced exactly by one-half due to net cancellation by the self-energy terms.

Different choices of local frames and principal vectors, as well as atomic force contributions, are detailed in the work of Lipparini *et al.* [81] The specific choices in this work which define the rotation matrix $R_{\Lambda\lambda}^i$ result in obvious sign changes compared to their work, so the atomic contributions are detailed below in compact form. We require the derivatives of the rotation matrix with respect to the atomic coordinates which can be written as

$$\frac{\partial R_{\Lambda\lambda}^i}{\partial r_{\alpha}^{ia}} = \begin{bmatrix} \frac{\partial e_{\nu}^{iX}}{\partial r_{\alpha}^{ia}} & \frac{\partial e_{\nu}^{iY}}{\partial r_{\alpha}^{ia}} & \frac{\partial e_{\nu}^{iZ}}{\partial r_{\alpha}^{ia}} \\ \frac{\partial e_{\gamma}^{iX}}{\partial r_{\alpha}^{ia}} & \frac{\partial e_{\gamma}^{iY}}{\partial r_{\alpha}^{ia}} & \frac{\partial e_{\gamma}^{iZ}}{\partial r_{\alpha}^{ia}} \\ \frac{\partial e_{\delta}^{iX}}{\partial r_{\alpha}^{ia}} & \frac{\partial e_{\delta}^{iY}}{\partial r_{\alpha}^{ia}} & \frac{\partial e_{\delta}^{iZ}}{\partial r_{\alpha}^{ia}} \end{bmatrix} \tag{5.61}$$

The COM and principal vectors used to define the rotation are

$$\mathbf{r}^i = \sum_{a \in i} \mathbf{r}^{ia} \frac{M^a}{M^i}, \quad \mathbf{B}^i = \mathbf{r}^i - \mathbf{r}^{iH_1}, \quad \mathbf{C}^i = \mathbf{r}^i - \mathbf{r}^{iH_2} \tag{5.62}$$

Defining

$$\mathbf{D}^i = \mathbf{B}^i \mathbf{C}^i + \mathbf{C}^i \mathbf{B}^i \tag{5.63}$$

such that

$$\mathbf{e}^{iZ} = \frac{\mathbf{D}^i}{D^i} \tag{5.64}$$

where B^i, C^i and D^i are the euclidean norms of the vectors, the terms in the derivative of the rotation matrix, Eq. (5.61), are then

$$\frac{\partial e_\lambda^{iZ}}{\partial r_\alpha^{ia}} = \frac{\partial e_\lambda^{iZ}}{\partial D^i} \left(\frac{\partial D_\beta^i}{\partial r_\gamma^i} \frac{\partial r_\gamma^i}{\partial r_\alpha^{ia}} + \frac{\partial D_\beta^i}{\partial r_\alpha^{ia}} \right) \quad (5.65)$$

$$\frac{\partial e_\lambda^{iX}}{\partial r_\alpha^{ia}} = \frac{\partial e_\lambda^{iX}}{\partial B_\beta^i} \left(\frac{\partial B_\beta^i}{\partial r_\gamma^i} \frac{\partial r_\gamma^i}{\partial r_\alpha^{ia}} + \frac{\partial B_\beta^i}{\partial r_\alpha^{ia}} \right) + \frac{\partial e_\lambda^{iX}}{\partial e_\beta^{iZ}} \frac{\partial e_\beta^{iZ}}{\partial r_\alpha^{ia}} \quad (5.66)$$

$$\frac{\partial e_\lambda^{iY}}{\partial r_\alpha^{ia}} = \frac{\partial e_\lambda^{iY}}{\partial e_\beta^{iX}} \frac{\partial e_\beta^{iX}}{\partial r_\alpha^{ia}} + \frac{\partial e_\lambda^{iY}}{\partial e_\beta^{iZ}} \frac{\partial e_\beta^{iZ}}{\partial r_\alpha^{ia}} \quad (5.67)$$

where the leading terms are as follows

$$\frac{\partial e_\lambda^{iZ}}{\partial D^i} = \left(\frac{\mathbf{I}}{D^i} - \frac{\mathbf{D}^i \otimes \mathbf{D}^i}{(D^i)^3} \right)_{\lambda\beta} \quad (5.68)$$

$$\frac{\partial e_\lambda^{iX}}{\partial B_\beta^i} = \left(\frac{\mathbf{I} - \mathbf{e}^{iZ} \otimes \mathbf{e}^{iZ} - \mathbf{e}^{iX} \otimes \mathbf{e}^{iX}}{|\mathbf{B}^i - (\mathbf{B}^i \cdot \mathbf{e}^{iZ})\mathbf{B}^i|} \right)_{\lambda\beta} \quad (5.69)$$

$$\frac{\partial e_\lambda^{iX}}{\partial e_\beta^{iZ}} = \left(\frac{(\mathbf{B}^i \cdot \mathbf{e}^{iZ})\mathbf{e}^{iX} \otimes \mathbf{B}^i}{|\mathbf{B}^i - (\mathbf{B}^i \cdot \mathbf{e}^{iZ})\mathbf{B}^i|^2} - \frac{(\mathbf{B}^i \cdot \mathbf{e}^{iZ})\mathbf{I} + \mathbf{e}^{iZ} \otimes \mathbf{B}^i}{|\mathbf{B}^i - (\mathbf{B}^i \cdot \mathbf{e}^{iZ})\mathbf{B}^i|} \right)_{\lambda\beta} \quad (5.70)$$

$$\frac{\partial e_\lambda^{iY}}{\partial e_\beta^{iZ}} = \epsilon_{\lambda\sigma\tau} \delta_{\beta\sigma} e_\tau^{iX} \quad (5.71)$$

$$\frac{\partial e_\lambda^{iY}}{\partial e_\beta^{iX}} = \epsilon_{\lambda\sigma\tau} e_\sigma^{iZ} \delta_{\beta\tau} \quad (5.72)$$

where \mathbf{I} is the 3×3 identity matrix and $\epsilon_{\alpha\beta\gamma}$ the Levi-Civita symbols. The latter terms are

$$\frac{\partial D_\beta^i}{\partial r_\gamma^i} \frac{\partial r_\gamma^i}{\partial r_\alpha^{ia}} = \left((B^i + C^i)\mathbf{I} + \frac{\mathbf{B}^i \otimes \mathbf{C}^i}{C^i} + \frac{\mathbf{C}^i \otimes \mathbf{B}^i}{B^i} \right)_{\beta\gamma} \delta_{\gamma\alpha} \frac{M^a}{M^i} \quad (5.73)$$

$$\frac{\partial D_\beta^i}{\partial r_\alpha^{iH_1}} = - \left(B^i \mathbf{I} + \frac{\mathbf{B}^i \otimes \mathbf{C}^i}{C^i} \right)_{\beta\alpha} \quad (5.74)$$

$$\frac{\partial D_\beta^i}{\partial r_\alpha^{iH_2}} = - \left(C^i \mathbf{I} + \frac{\mathbf{C}^i \otimes \mathbf{B}^i}{B^i} \right)_{\beta\alpha} \quad (5.75)$$

$$\frac{\partial B_\beta^i}{\partial r_\gamma^i} \frac{\partial r_\gamma^i}{\partial r_\alpha^{ia}} = \delta_{\beta\gamma} \delta_{\gamma\alpha} \frac{M^a}{M^i} \quad (5.76)$$

$$\frac{\partial B_\beta^i}{\partial r_\alpha^{iH_1}} = - \delta_{\beta\alpha} \quad (5.77)$$

For the DMS (see the main text) the first term on the right hand side is

$$\frac{\partial E_{\text{ele+ind}}}{\partial \mu_{\beta}^j(\{\mathbf{r}^{jb}\})} = \left(\frac{\partial E_{\text{ele+ind}}}{\partial \mu_{\beta}^j(\{\mathbf{r}^{jb}\})} + \frac{\partial E_{\text{ele+ind}}}{\partial V_{\gamma\delta\ldots\eta}^k} \frac{\partial V_{\gamma\delta\ldots\eta}^k}{\partial \mu_{\beta}^j(\{\mathbf{r}^{jb}\})} \right) = \frac{1}{2} V_{\beta}^j + \frac{1}{2} \sum_k^n \delta_{jk} V_{\beta}^k \quad (5.78)$$

$$\frac{\partial \mu_{\beta}^j(\{\mathbf{r}^{jb}\})}{\partial r_{\alpha}^{ia}} = \left(\frac{\partial q^{jb}}{\partial r_{\alpha}^{ia}} + \frac{\partial r^{jb}}{\partial r_{\alpha}^{ia}} \right) = \delta_{ji} \left(\sum_b^{n_i} \frac{\partial q^{jb}}{\partial r_{\alpha}^{ia}} r_{\beta}^{jb} + \delta_{ba} q^{jb} \delta_{\beta\alpha} \right) \quad (5.79)$$

$$\frac{\partial E_{\text{ele+ind}}}{\partial \mu_{\beta}^j(\{\mathbf{r}^{jb}\})} \frac{\partial \mu_{\beta}^j(\{\mathbf{r}^{jb}\})}{\partial r_{\alpha}^{ia}} = q^{ia} V_{\alpha}^i + \sum_b^{n_i} \frac{\partial q^{ib}}{\partial r_{\alpha}^{ia}} r_{\beta}^{ib} V_{\beta}^i \quad (5.80)$$

The derivatives of the DMS, $\frac{\partial q^{ib}}{\partial r_{\beta}^{ia}}$, with respect to the atomic positions are derived by Burnham and Xantheas [32] and are available in open source repositories.

For the force contribution due to the QMS we first rewrite the following expression

$$\theta_{\alpha\beta}^i(\mathbf{r}^{iO}, \mathbf{r}^{iH_1}, \mathbf{r}^{iH_2}) = \sum_a^{H'_1, H'_2, L_1, L_2} \frac{3}{2} \left\{ q^{ia} \left((\mathbf{r}^{ia} - \mathbf{r}^i)_{\alpha} (\mathbf{r}^{ia} - \mathbf{r}^i)_{\beta} - \frac{\delta_{\alpha\beta}}{3} \|\mathbf{r}^{ia} - \mathbf{r}^i\| \right) \right\} \quad (5.81)$$

noting that the position of the L-sites in the global frame are

$$r_{\alpha}^{iL_l} = R_{\eta\alpha}^{iH_l} e_{\eta}^{iZ} f(\mathbf{r}^{H_l}) + r_{\alpha}^i \quad (5.82)$$

we remove redundant terms and the expression for the QMS becomes

$$\begin{aligned} \theta_{\alpha\beta}^i(\mathbf{r}^{iO}, \mathbf{r}^{iH_1}, \mathbf{r}^{iH_2}) = & \frac{3}{2} \left\{ \sum_a^{H'_1, H'_2} q^{ia} \left((\mathbf{r}^{ia} - \mathbf{r}^i)_{\alpha} (\mathbf{r}^{ia} - \mathbf{r}^i)_{\beta} - \frac{\delta_{\alpha\beta}}{3} \|\mathbf{r}^{ia} - \mathbf{r}^i\| \right) \right. \\ & \left. + \sum_l^{1,2} q^{iL_l} \left(dr_{\alpha}^{iL_l} dr_{\beta}^{iL_l} - \frac{\delta_{\alpha\beta}}{3} \|dr^{iL_l}\| \right) \right\} \end{aligned} \quad (5.83)$$

where

$$dr_{\alpha}^{iL_l} = R_{\eta\alpha}^{iH_l} e_{\eta}^{iZ} f(\mathbf{r}^{H_l}) \quad (5.84)$$

Similar to the DMS we have

$$\frac{\partial E_{\text{ele+ind}}}{\partial \theta_{\beta\gamma}^j(\{\mathbf{r}^{jb}\})} = \left(\frac{\partial E_{\text{ele+ind}}}{\partial \theta_{\beta\gamma}^j(\{\mathbf{r}^{jb}\})} + \frac{\partial E_{\text{ele+ind}}}{\partial V_{\delta\kappa\dots\eta}^k} \frac{\partial V_{\delta\kappa\dots\eta}^k}{\partial \theta_{\beta\gamma}^j(\{\mathbf{r}^{jb}\})} \right) = \frac{1}{6} V_{\beta\gamma}^j + \frac{1}{6} \sum_k^n \delta_{jk} V_{\beta\gamma}^k \quad (5.85)$$

$$\begin{aligned} \frac{\partial \theta_{\beta\gamma}^j(\{\mathbf{r}^{jb}\})}{\partial r_{\alpha}^{ia}} = & \frac{3}{2} \delta_{ji} \left\{ \sum_b^{H'_1, H'_2} \frac{\partial q^{jb}}{\partial r_{\alpha}^{ia}} \left((\mathbf{r}^{jb} - \mathbf{r}^j)_{\beta} (\mathbf{r}^{jb} - \mathbf{r}^j)_{\gamma} - \frac{\delta_{\beta\gamma}}{3} \|\mathbf{r}^{jb} - \mathbf{r}^j\| \right) \right. \\ & + \sum_l^{1,2} \frac{\partial q^{jL_l}}{\partial r_{\alpha}^{ia}} \left(dr_{\beta}^{jL_l} dr_{\gamma}^{jL_l} - \frac{\delta_{\beta\gamma}}{3} \|dr^{jL_l}\| \right) \\ & + \sum_b^{H'_1, H'_2} q^{jb} \left(\delta_{\beta\alpha} \left(\delta_{ba} - \sum_c^{n_j} \delta_{ca} \frac{M^c}{M^j} \right) (\mathbf{r}^{jb} - \mathbf{r}^j)_{\gamma} \right. \\ & \quad + (\mathbf{r}^{jb} - \mathbf{r}^j)_{\beta} \delta_{\gamma\alpha} \left(\delta_{ba} - \sum_c^{n_j} \delta_{ca} \frac{M^c}{M^j} \right) \\ & \quad \left. + \delta_{\beta\gamma} \frac{2}{3} \left(\delta_{ba} - \sum_c^{n_j} \delta_{ca} \frac{M^c}{M^j} \right) \delta_{\alpha\delta} (\mathbf{r}^{jb} - \mathbf{r}^j)_{\delta} \right) \\ & + \sum_l^{1,2} q^{jL_l} \left(\delta_{\beta\alpha} \frac{\partial dr_{\beta}^{jL_l}}{\partial r_{\alpha}^{ia}} dr_{\gamma}^{jL_l} + dr_{\beta}^{jL_l} \delta_{\gamma\alpha} \frac{\partial dr_{\gamma}^{jL_l}}{\partial r_{\alpha}^{ia}} \right. \\ & \quad \left. + \delta_{\beta\gamma} \frac{2}{3} \frac{\partial r_{\delta}^{jL_l}}{\partial r_{\alpha}^{ia}} dr_{\delta}^{jL_l} \right) \left. \right\} \quad (5.86) \end{aligned}$$

The terms involving the partial derivative of the charges for each site are readily available since through the definition of the QMS charges we have

$$q^{iH'_l} = Aq^{iH_l} + Bq_{\text{eq}}^{iH_l} \quad (5.87)$$

$$q^{iL_l} = Cq^{iH_l} + Dq_{\text{eq}}^{iH_l} \quad (5.88)$$

and hence the expression reduces to

$$\begin{aligned}
 \frac{\partial E_{\text{ele+ind}}}{\partial \theta_{\beta\gamma}^j(\{\mathbf{r}^{jb}\})} \frac{\partial \theta_{\beta\gamma}^j(\{\mathbf{r}^{jb}\})}{\partial r_{\alpha}^{ia}} = & \frac{1}{2} \sum_l^{1,2} \left\{ \frac{\partial q^{iH_l}}{\partial r_{\alpha}^{ia}} \left(A \left(dr_{\beta}^{iH_l} dr_{\gamma}^{iH_l} - \frac{\delta_{\beta\gamma}}{3} \|dr^{iH_l}\| \right) \right. \right. \\
 & + C \left(dr_{\beta}^{iL_l} dr_{\gamma}^{iL_l} - \frac{\delta_{\beta\gamma}}{3} \|dr^{iL_l}\| \right) \Bigg) \\
 & + q^{iH_l'} \left(2 \left(\delta_{ba} - \sum_c^{n_i} \delta_{ca} \frac{M^c}{M^i} \right) dr_{\gamma}^{iH_l} \delta_{\beta\alpha} \right. \\
 & \quad \left. - \frac{2}{3} \left(\delta_{ba} - \sum_c^{n_i} \delta_{ca} \frac{M^c}{M^i} \right) dr_{\alpha}^{iH_l} \delta_{\beta\gamma} \right) \\
 & \left. + q^{iL_l} \left(2 \frac{\partial dr_{\beta}^{iL_l}}{\partial r_{\alpha}^{ia}} dr_{\gamma}^{iL_l} - \frac{2}{3} \frac{\partial dr_{\delta}^{iL_l}}{\partial r_{\alpha}^{ia}} dr_{\delta}^{iL_l} \delta_{\beta\gamma} \right) \right\} V_{\beta\gamma}^i \quad (5.89)
 \end{aligned}$$

where

$$dr_{\alpha}^{iH_l} = (\mathbf{r}^{iH_l} - \mathbf{r}^i)_{\alpha} \quad (5.90)$$

The only unknowns are the derivatives of the position of the L-sites in the local frame reference. Applying the rotation operators

$$\mathbf{R}^{iL_1} = \left(\cos(\theta') \mathbf{I} - \sin(\theta') [\mathbf{e}^{iX}]_{\times} \right) \quad (5.91)$$

$$\mathbf{R}^{iL_2} = \left(\cos(\theta') \mathbf{I} + \sin(\theta') [\mathbf{e}^{iX}]_{\times} \right) \quad (5.92)$$

on \mathbf{e}^{iZ} in the case of L₁ and L₂ the expression for the local frame vectors becomes

$$dr_{\alpha}^{iL_1} = (\cos(\theta') e_{\alpha}^{iZ} - \sin(\theta') e_{\alpha}^{iY}) f(\mathbf{r}^{iH_1}) \quad (5.93)$$

$$dr_{\alpha}^{iL_2} = (\cos(\theta') e_{\alpha}^{iZ} + \sin(\theta') e_{\alpha}^{iY}) f(\mathbf{r}^{iH_2}) \quad (5.94)$$

Derivatives of the expressions above are of the form

$$\begin{aligned}
 \frac{\partial dr_{\beta}^{iL_l}}{\partial r_{\alpha}^{ia}} = & \frac{\partial dr_{\beta}^{iL_l}}{\partial e_{\gamma}^{iZ}} \frac{\partial e_{\gamma}^{iZ}}{\partial r_{\alpha}^{ia}} + \frac{\partial dr_{\beta}^{iL_l}}{\partial e_{\gamma}^{iY}} \frac{\partial e_{\gamma}^{iY}}{\partial r_{\alpha}^{ia}} + \frac{\partial dr_{\beta}^{iL_l}}{\partial f(\mathbf{r}^{iH_l})} \frac{\partial f(\mathbf{r}^{iH_l})}{\partial r_{\alpha}^{ia}} \\
 & + \left(\frac{\partial dr_{\beta}^{iL_l}}{\partial \cos(\theta')} \frac{\partial \cos(\theta')}{\partial \theta'} + \frac{\partial dr_{\beta}^{iL_l}}{\partial \sin(\theta')} \frac{\partial \sin(\theta')}{\partial \theta'} \right) \frac{\partial \theta'}{\partial r_{\alpha}^{ia}} \quad (5.95)
 \end{aligned}$$

For $l = 1$ as an example the leading terms are

$$\frac{\partial dr_{\beta}^{iL_l}}{\partial e_{\gamma}^{iZ}} = \cos(\theta') f(\mathbf{r}^{iH_1}) \delta_{\beta\gamma} \quad (5.96)$$

$$\frac{\partial dr_{\beta}^{iL_l}}{\partial e_{\gamma}^{iY}} = -\sin(\theta') f(\mathbf{r}^{iH_1}) \delta_{\beta\gamma} \quad (5.97)$$

$$\frac{\partial dr_{\beta}^{iL_1}}{\partial f(\mathbf{r}^{H_1})} = (\cos(\theta') e_{\beta}^{iZ} - \sin(\theta') e_{\beta}^{iY}) \quad (5.98)$$

$$\frac{\partial dr_{\beta}^{iL_l}}{\partial \cos(\theta')} \frac{\partial \cos(\theta')}{\partial \theta'} = e_{\beta}^{iZ} (\sin(\theta')) f(\mathbf{r}^{iH_1}) \quad (5.99)$$

$$\frac{\partial dr_{\beta}^{iL_l}}{\partial \sin(\theta')} \frac{\partial \sin(\theta')}{\partial \theta'} = e_{\beta}^{iY} (-\cos(\theta')) f(\mathbf{r}^{iH_1}) \quad (5.100)$$

and the two remaining latter terms are

$$\frac{\partial f(\mathbf{r}^{H_1})}{\partial r_{\alpha}^{iH_1}} = -b \frac{(\mathbf{r}^O - \mathbf{r}^{H_1})_{\alpha}}{|\mathbf{r}^O - \mathbf{r}^{H_1}|} - 2cf(\mathbf{r}^{H_1}) \frac{(\mathbf{r}^O - \mathbf{r}^{H_1})_{\alpha}}{|\mathbf{r}^O - \mathbf{r}^{H_1}|} \quad (5.101)$$

$$\frac{\partial \theta'}{\partial r_{\alpha}^{iH_1}} = \frac{1}{\sqrt{1-x^2}} \left(-\frac{(\mathbf{r}^O - \mathbf{r}^{H_2})_{\alpha}}{|\mathbf{r}^O - \mathbf{r}^{H_1}| |\mathbf{r}^O - \mathbf{r}^{H_2}|} + x \frac{(\mathbf{r}^O - \mathbf{r}^{H_1})_{\alpha}}{|\mathbf{r}^O - \mathbf{r}^{H_1}|^2} \right) \quad (5.102)$$

where

$$x = \frac{(\mathbf{r}^O - \mathbf{r}^{H_1}) \cdot (\mathbf{r}^O - \mathbf{r}^{H_2})}{|\mathbf{r}^O - \mathbf{r}^{H_1}| |\mathbf{r}^O - \mathbf{r}^{H_2}|}$$

and

$$\theta' = \arccos(x) \quad (5.103)$$

Finally, the third term on the right hand side in the force expression of equation 5.43 is the partial derivatives of the external field at each site with respect to the atomic positions. It is of the general form

$$\frac{\partial E_{\text{ele+ind}}}{\partial V_{\beta\gamma\delta\epsilon\ldots\eta}^j} \frac{\partial V_{\beta\gamma\delta\epsilon\ldots\eta}^j}{\partial r_{\delta}^k} \frac{\partial r_{\delta}^k}{\partial r_{\alpha}^{ia}} \rightarrow O_{\beta\gamma\delta\epsilon\ldots\eta}^i V_{\alpha\beta\gamma\delta\epsilon\ldots\eta}^i \frac{M^a}{M^i} \quad (5.104)$$

where $O_{\beta\gamma\delta\epsilon\ldots\eta}^i$ is the $(n-1)$ th ranked moment tensor (static plus induced) and $V_{\alpha\beta\gamma\delta\epsilon\ldots\eta}^i$ the corresponding n th ranked external potential gradient. Considering the electrostatic plus induction interaction expression (see the main text), this leads to

$$\begin{aligned} \frac{\partial E_{\text{ele+ind}}}{\partial V_{\beta\gamma\delta\epsilon\ldots\eta}^j} \frac{\partial V_{\beta\gamma\delta\epsilon\ldots\eta}^j}{\partial r_{\delta}^k} \frac{\partial r_{\delta}^k}{\partial r_{\alpha}^{ia}} = & \left((\mu_{\beta}^i(\{\mathbf{r}^{ia}\}) + \Delta\mu_{\beta}^i) V_{\alpha\beta}^i + \frac{1}{3} (\theta_{\beta\gamma}^i(\{\mathbf{r}^{ia}\}) + \Delta\theta_{\beta\gamma}^i) V_{\alpha\beta\gamma}^i \right. \\ & \left. + \frac{1}{15} \Omega_{\beta\gamma\delta}^i V_{\alpha\beta\gamma\delta}^i + \frac{1}{105} \Phi_{\beta\gamma\delta\epsilon}^i V_{\alpha\beta\gamma\delta\epsilon}^i \right) \frac{M^a}{M^i} \quad (5.105) \end{aligned}$$

The energy-force consistency of the formulation is checked against numerical forces, and at different convergence criteria of the induced moments, see figure 5.11.

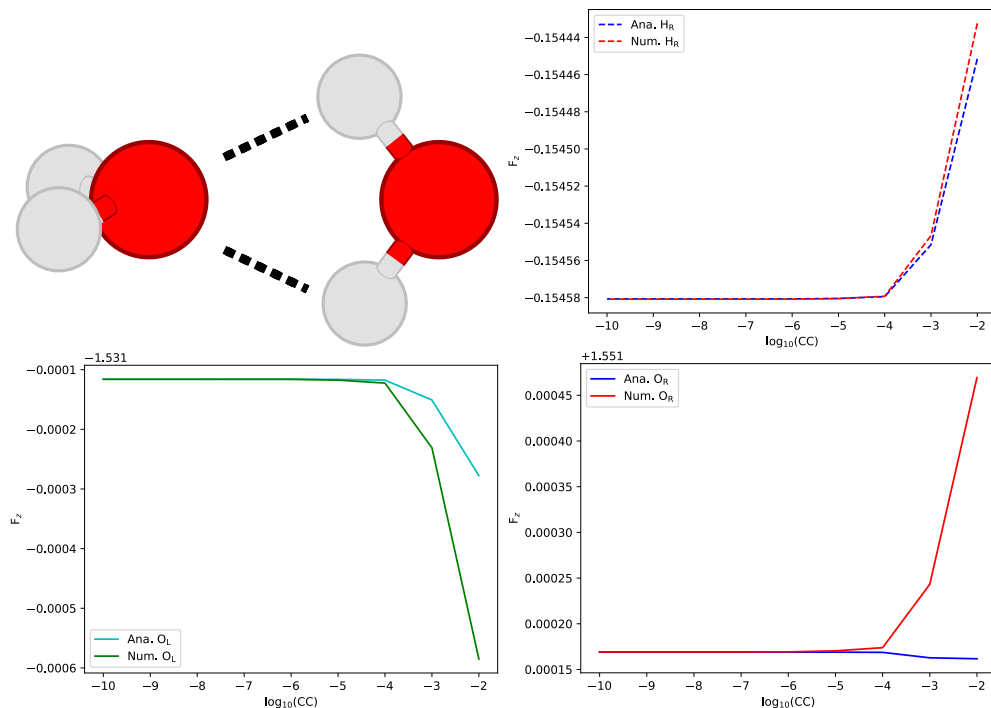


Figure 5.11: C_{2v} isomer configuration for the water dimer (top left), used for the numerical versus analytical forces at different convergence criteria ranges for one of the right hydrogens, H_R (top right), as well as the left and right oxygen, O_L (bottom left) and O_R (bottom right). The convergence of the force components is shown versus the magnitude of the convergence criteria, CC, which is defined as $\sum_i |\Delta\mu_{n+1}^i - \Delta\mu_n^i| \leq \text{CC}$, and similarly for the induced quadrupole moment. Good energy-force consistency is reached reliably at a criteria of $1\text{e-}6$ D for the dipole (or $\text{D}\text{\AA}$ for the quadrupole).

5.A.2 Deviation of M-site Models

The general expression for the %RMS difference is given by

$$\%RMS = \sqrt{\frac{\sum_i^{x,y,z} (\theta_{ii} - \theta_{ii}^{\text{ab initio}})^2}{\sum_i^{x,y,z} (\theta_{ii}^{\text{ab initio}})^2}} \times 100\% \quad (5.106)$$

and reveals if there is a large deviation from the individual components of the quadrupole moment along the trace, $\{\theta_{xx}, \theta_{yy}, \theta_{zz}\}$, relative to the trace norm. While a quadrupole model may capture the principal quadrupole component θ_T , such as the M-site based $\gamma - (\text{DMS} - q_{\text{eq}}^{\text{H}})^*$ model, to a reasonable degree this can simply be due to a net cancellation of errors in the individual components. The QMS model captures both the θ_T and the Δ component on average at around 1.6% evaluated over the whole range. There is no systematic correlation in the deviation of the quadrupole components of the QMS models and the RMSD of the monomer geometry from the equilibrium geometry. The RMSD of the geometry is evaluated with the Kabsch algorithm [110].

To solve for the γ factor and hence the position of the M-site such that Δ vanishes (see main text), one considers the water monomer in the equilibrium configuration with the oxygen placed at the origin. In this configuration and frame of reference the quadrupole moment tensor only has components along the trace $\{\theta_{xx}, \theta_{yy}, \theta_{zz}\}$, where $\theta_{zz} = 2\Delta$. This component, in terms of the charges and positions of the hydrogens and the M-site, is given by [117]

$$\theta_{zz} = q^{\text{H}}(-(r_x^{\text{H}})^2 + 2(r_z^{\text{H}})^2 - 2(r_z^{\text{M}})^2) \quad (5.107)$$

which is trivial to solve in order for Δ to vanish, by using the generalization of this expression in the global coordinate frame [113–115]

$$\mathbf{r}_{\text{M}} = (1 - \gamma)\mathbf{r}_{\text{O}} + \frac{\gamma}{2}(\mathbf{r}_{\text{H}_1} + \mathbf{r}_{\text{H}_2}) \quad (5.108)$$

5.A.3 Energy-Volume Curves for Ice Ih

Fig. 5.13 shows energy-volume curves without ($E_{\text{tot}}(V)$, blue) and with zero-point-energy correction according to the quasi-harmonic approximation ($E_{\text{tot}+\text{ZPE}}(V)$, red).

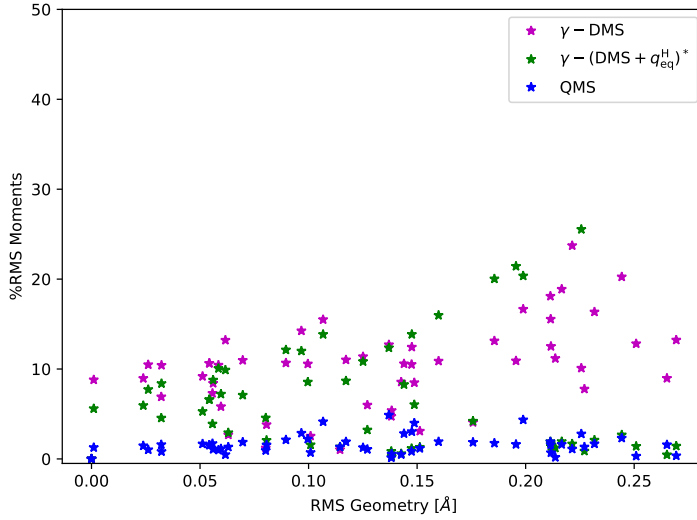


Figure 5.12: Root-mean-square percentage difference between the three diagonal components of the quadrupole moment tensors of two M-site models and the QMS model versus the ab initio (ICE-CI) quadrupole moment tensor respectively. The ab initio and the average RMS percentage QMS difference is around 1.6%. The largest deviation corresponds to the numerically lowest θ_T . There is no correlation between the magnitude of the relative geometrical change relative to the ground state monomer geometry and the deviation of the quadrupole moment.

The indicated 6 data points are the direct results from the calculations with the optimized (final) parameters for SCME/f described in the main article around the equilibrium volume. The lines are the results of least-square fits to the Rose-Vinet equation of state

$$E(\eta) = E_0 + \frac{2B_0V_0}{(B'-1)^2} \cdot \left[2 - (5 + 3B'(\eta - 1) - 3\eta) \cdot \exp\left(-\frac{3}{2}(B' - 1)(\eta - 1)\right) \right] \quad (5.109)$$

as implemented in the PHONOPY package [108], where $\eta = \frac{V}{V_0}$ and $E_0 = -E_{\text{lat}}$. The corresponding fit parameters compiled in Table 5.9. We have verified that adding more points does not yield significant changes for the fit parameters, in particular those that are directly compared against experimental data (E_0 , V_0 and B_0).

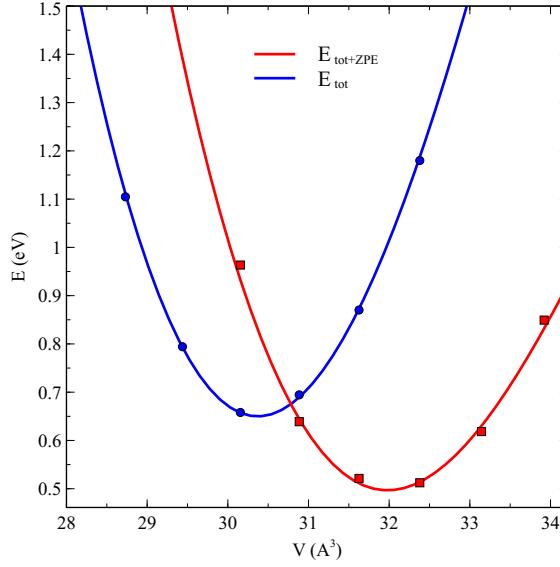


Figure 5.13: Energy-volume curves without ($E_{\text{tot}}(V)$, blue) and with zero-point-energy correction ($E_{\text{tot}+\text{ZPE}}(V)$, red) obtained with the optimized (final) parameters for SCME/f. Energies and volumes are per water molecule.

	E_0 (eV)	V_0 (\AA^3)	B_0 (eV/ \AA^3)	B_0 (GPa)	B'
E_{tot}	0.645	30.38	0.094	15.0	5.39
$E_{\text{tot}+\text{ZPE}}$	0.489	31.98	0.076	12.2	5.68

Table 5.9: Fit parameters for the Rose-Vinet equation (Eq. (5.109)) for the fits to $E_{\text{tot}}(V)$ and $E_{\text{tot}+\text{ZPE}}(V)$ shown in Fig. 5.13. All quantities are given per water molecule.

5.8 References

1. W. L. Jorgensen, J. Chandrasekhar, J. D. Madura, R. W. Impey, M. L. Klein, *J. Chem. Phys.* **79**, 926–935 (1983).
2. W. L. Jorgensen, *J. Am. Chem. Soc.* **103**, 335–340 (1981).
3. H. W. Horn, W. C. Swope, J. W. Pitera, J. D. Madura, T. J. Dick, *et al.*, *J. Chem. Phys.* **120**, 9665 (2004).
4. J. Zielkiewicz, *J. Chem. Phys.* **123**, 104501 (2005).
5. K. Park, W. Lin, F. Paesani, *J. Phys. Chem. B* **116**, 343–352 (2012).
6. S. Habershon, T. E. Markland, D. E. Manolopoulos, *J. Chem. Phys.* **131**, 024501 (2009).
7. E. R. Batista, S. S. Xantheas, H. Jónsson, *J. Chem. Phys.* **109**, 4546 (1998).
8. E. R. Batista, S. S. Xantheas, H. Jónsson, *J. Chem. Phys.* **112**, 3285 (2000).
9. E. Batista, *Development of a New Water-Water Interaction Potential and Applications to Molecular Processes in Ice* (University of Washington, 1999).
10. K. T. Wikfeldt, E. R. Batista, F. D. Vila, H. Jónsson, *Phys. Chem. Chem. Phys.* **15**, 16542 (2013).
11. I. V. Smirnov, A. V. Golovin, S. D. Chatziefthimiou, A. V. Stepanova, Y. Peng, *et al.*, *Sci. Adv.* **2**, e1501695 (2016).
12. T. R. M. Barends, L. Foucar, A. Ardevol, K. Nass, A. Aquila, *et al.*, *Science* **350**, 445–450 (2015).
13. H. M. Senn, W. Thiel, *Angew. Chem. Int. Ed. (English)* **48**, 1198–1229 (2009).
14. K. Senthilkumar, J. I. Mujika, K. E. Ranaghan, F. R. Manby, A. J. Mulholland, *et al.*, *J. Royal Soc. Interface* **5**, 207–216 (2008).
15. A. Warshel, P. K. Sharma, M. Kato, Y. Xiang, H. Liu, *et al.*, *Chem. Rev.* **106**, 3210–3235 (2006).
16. F. Zheng, L. Xue, S. Hou, J. Liu, M. Zhan, *et al.*, *Nat. Commun.* **5**, 3457 (2014).
17. J. Knorr, P. Sokkar, S. Schott, P. Costa, W. Thiel, *et al.*, *Nat. Commun.* **7**, 12968 (2016).
18. V.-T. Pham, T. J. Penfold, R. M. van der Veen, F. Lima, A. E. Nahhas, *et al.*, *J. Am. Chem. Soc.* **133**, 12740–12748 (2011).
19. A. O. Dohn, E. O. Jónsson, K. S. Kjær, T. B. van Driel, M. M. Nielsen, *et al.*, *J. Phys. Chem. Lett.* **5**, 2414–2418 (2014).
20. A. O. Dohn, K. S. Kjær, T. B. Harlang, S. E. Canton, M. M. Nielsen, *et al.*, *Inorg. Chem.* **55**, 10637–10644 (2016).
21. G. Levi, M. Pápai, N. E. Henriksen, A. O. Dohn, K. B. Møller, *J. Chem. Phys. C* **122**, 7100–7119 (2018).
22. A. O. Dohn, D. Selli, G. Fazio, L. Ferraro, J. Mortensen, *et al.*, *Molecules* **23**, 2958 (2018).
23. Y.-J. Zhang, A. Khorshidi, G. Kastlunger, A. A. Peterson, *J. Chem. Phys.* **148**, 241740 (2018).

-
24. H. Lin, D. G. Truhlar, *Theor. Chem. Acc.* **117**, 185 (2006).
 25. S. Pezeshki, H. Lin, *Mol. Sim.* **41**, 168–189 (2015).
 26. K. Snedkov, T. Schwabe, O. Christiansen, J. Kongsted, *Phys. Chem. Chem. Phys.* **13**, 18551–18560 (2011).
 27. U. N. Morzan, D. J. A. de Armiño, N. O. Foglia, F. Ramírez, M. C. G. Lebrero, *et al.*, *Chem. Rev.* **118**, 4071–4113 (2018).
 28. A. Warshel, M. Levitt, *J. Mol. Biol.* **103**, 227–249 (1976).
 29. G. A. Cisneros, K. T. Wikfeldt, L. Ojamäe, J. Lu, Y. Xu, *et al.*, *Chem. Rev.* **116**, 7501–7528 (2016).
 30. H. Yu, W. F. Van Gunsteren, *Comput. Phys. Commun.* **172**, 69–85 (2005).
 31. P. E. Lopes, B. Roux, A. D. MacKerell, *Theoretical Chemistry Accounts* **124**, 11–28 (2009).
 32. C. J. Burnham, S. S. Xantheas, *J. Chem. Phys.* **116**, 1479–1492 (2002).
 33. G. S. Fanourgakis, S. S. Xantheas, *J. Phys. Chem. A* **110**, 4100–4106 (2006).
 34. G. S. Fanourgakis, S. S. Xantheas, *J. Chem. Phys.* **128**, 074506 (2008).
 35. C. Burnham, D. Anick, P. Mankoo, G. Reiter, *J. Chem. Phys.* **128**, 154519 (2008).
 36. G. R. Medders, V. Babin, F. Paesani, *J. Chem. Theory Comput.* **9**, 1103–1114 (2013).
 37. V. Babin, G. R. Medders, F. Paesani, *J. Phys. Chem. Lett.* **3**, 3765–3769 (2012).
 38. V. Babin, C. Leforestier, F. Paesani, *J. Chem. Theory Comput.* **9**, 5395–5403 (2013).
 39. V. Babin, G. R. Medders, F. Paesani, *J. Chem. Theory Comput.* **10**, 1599–1607 (2014).
 40. G. R. Medders, V. Babin, F. Paesani, *J. Chem. Theory Comput.* **10**, 2906–2910 (2014).
 41. M. A. Thompson, G. K. Schenter, *J. Phys. Chem.* **99**, 6374–6386 (1995).
 42. M. A. Thompson, *J. Phys. Chem.* **100**, 14492–14507 (1996).
 43. R. A. Bryce, R. Buesnel, I. H. Hillier, N. A. Burton, *Chem. Phys. Lett.* **279**, 367–371 (1997).
 44. F. Lipparini, V. Barone, *J. Chem. Theory Comput.* **7**, 3711–3724 (2011).
 45. E. Boulanger, W. Thiel, *J. Chem. Theory Comput.* **8**, 4527–4538 (2012).
 46. Z. Lu, Y. Zhang, *J. Chem. Theory Comput.* **4**, 1237–1248 (2008).
 47. N. M. Thellamurege, D. Si, F. Cui, H. Zhu, R. Lai, *et al.*, *J. Comput. Chem.* **34**, 2816–2833 (2013).
 48. E. G. Kratz, A. R. Walker, L. Lagardère, F. Lipparini, J.-P. Piquemal, *et al.*, *J. Comput. Chem.* **37**, 1019–1029 (2016).
 49. J. Dziedzic, Y. Mao, Y. Shao, J. Ponder, T. Head-Gordon, *et al.*, *J. Chem. Phys.* **145**, 124106 (2016).
 50. A. S. P. Gomes, C. R. Jacob, *Ann. Rep. Prog. Chem., Sect. C: Phys. Chem.* **108**, 222–277 (2012).

51. P. Söderhjelm, C. Husberg, A. Strambi, M. Olivucci, U. Ryde, *J. Chem. Theory Comput.* **5**, 649–658 (2009).
52. K. Snedkov, T. Schwabe, J. Kongsted, O. Christiansen, *J. Chem. Phys.* **134**, 03B608 (2011).
53. S. Caprasecca, S. Jurinovich, L. Viani, C. Curutchet, B. Mennucci, *J. Chem. Theory Comput.* **10**, 1588–1598 (2014).
54. J. Kongsted, A. Osted, K. V. Mikkelsen, O. Christiansen, *Mol. Phys.* **100**, 1813–1828 (2002).
55. Q. Zeng, W. Liang, *J. Chem. Phys.* **143**, 134104 (2015).
56. D. Loco, É. Polack, S. Caprasecca, L. Lagardère, F. Lipparini, *et al.*, *J. Chem. Theor. Comput.* **12**, 3654–3661 (2016).
57. D. Loco, L. Lagardère, S. Caprasecca, F. Lipparini, B. Mennucci, *et al.*, *J. Chem. Theory Comput.* **13**, 4025–4033 (2017).
58. L. Jensen, P. T. van Duijnen, J. G. Snijders, *J. Chem. Phys.* **119**, 3800–3809 (2003).
59. A. H. Steindal, K. Ruud, L. Frediani, K. Aidas, J. Kongsted, *J. Phys. Chem. B* **115**, 3027–3037 (2011).
60. C. B. Nielsen, O. Christiansen, K. V. Mikkelsen, J. Kongsted, *J. Chem. Phys.* **126**, 154112 (2007).
61. J. M. Olsen, K. Aidas, J. Kongsted, *J. Chem. Theory Comput.* **6**, 3721–3734 (2010).
62. F. Lipparini, C. Cappelli, V. Barone, *J. Chem. Theory Comput.* **8**, 4153–4165 (2012).
63. C. Curutchet, A. Muñoz-Losa, S. Monti, J. Kongsted, G. D. Scholes, *et al.*, *J. Chem. Theory Comput.* **5**, 1838–1848 (2009).
64. N. H. List, J. M. H. Olsen, J. Kongsted, *Phys. Chem. Chem. Phys.* **18**, 20234–20250 (2016).
65. M. Schwörer, B. Breitenfeld, P. Tröster, S. Bauer, K. Lorenzen, *et al.*, *J. Chem. Phys.* **138**, 244103 (2013).
66. C. Curutchet, A. Muñoz-Losa, S. Monti, J. Kongsted, G. D. Scholes, *et al.*, *J. Chem. Theory Comput.* **5**, 1838–1848 (2009).
67. K. Visscher, W. Swope, D. Geerke, *Molecules* **23**, 3131 (2018).
68. D. Hršak, J. M. H. Olsen, J. Kongsted, *J. Chem. Theory Comput.*, [acs.jctc.7b01153](#) (2018).
69. M. F. S. J. Menger, S. Caprasecca, B. Mennucci, *J. Chem. Theory Comput.* **13**, 3778–3786 (2017).
70. Y. Mao, Y. Shao, J. Dziedzic, C.-K. Skylaris, T. Head-Gordon, *et al.*, *J. Chem. Theory Comput.* **13**, 1963–1979 (2017).
71. J. Dziedzic, T. Head-Gordon, M. Head-Gordon, C.-K. Skylaris, *J. Chem. Phys.* **150**, 074103 (2019).

-
72. E. O. Jónsson, A. O. Dohn, H. Jónsson, *J. Chem. Theory Comput.* **15**, 6562–6577 (2019).
 73. A. O. Dohn, E. O. Jónsson, H. Jónsson, *J. Chem. Theory Comput.* **15**, 6578–6587 (2019).
 74. H. Partridge, D. W. Schwenke, *J. Chem. Phys.* **106**, 4618–4639 (1997).
 75. S. Habershon, T. E. Markland, D. E. Manolopoulos, *J. Chem. Phys.* **131**, 024501 (2009).
 76. H. W. Horn, W. C. Swope, J. W. Pitera, J. D. Madura, T. J. Dick, *et al.*, *J. Chem. Phys.* **120**, 9665–9678 (2004).
 77. J. Abascal, E. Sanz, R. García Fernández, C. Vega, *J. Chem. Phys.* **122**, 234511 (2005).
 78. J. L. Abascal, C. Vega, *J. Chem. Phys.* **123**, 234505 (2005).
 79. D. M. Bates, G. S. Tschumper, *J. Phys. Chem. A* **113**, 3555–3559 (2009).
 80. B. Temelso, K. A. Archer, G. C. Shields, *J. Phys. Chem. A* **115**, 12034–12046 (2011).
 81. F. Lipparini, L. Lagardère, B. Stamm, E. Cancès, M. Schnieders, *et al.*, *J. Chem. Theory Comput.* **10**, 1638–1651 (2014).
 82. A. Stone, *The Theory of Intermolecular Forces* (OUP Oxford, 2013).
 83. B. Thole, *Chem. Phys.* **59**, 341–350 (1981).
 84. M. Masia, M. Probst, R. Rey, *J. Chem. Phys.* **123**, 164505 (2005).
 85. M. Masia, M. Probst, R. Rey, *Chem. Phys. Lett.* **420**, 267–270 (2006).
 86. C. J. Burnham, J. Li, S. S. Xantheas, M. Leslie, *J. Chem. Phys.* **110**, 4566–4581 (1999).
 87. A. J. Stone, *J. Phys. Chem. A* **115**, 7017–7027 (2011).
 88. J. Sala, E. Guàrdia, M. Masia, *J. Chem. Phys.* **133**, 234101 (2010).
 89. K. T. Wikfeldt, E. R. Batista, F. D. Vila, H. Jónsson, *Phys. Chem. Chem. Phys.* **15**, 16542 (2013).
 90. P. E. Wormer, H. Hettema, *J. Chem. Phys.* **97**, 5592–5606 (1992).
 91. K. Tang, J. P. Toennies, *J. Chem. Phys.* **80**, 3726–3741 (1984).
 92. O. Rodrigues, *J. Math. Pures Appl.* **5**, 380–440 (1840).
 93. F. Neese, *WIREs Computational Molecular Science* **2**, 73–78 (2012).
 94. F. Neese, *WIREs Computational Molecular Science* **8**, e1327 (2018).
 95. B. Huron, J. Malrieu, P. Rancurel, *J. Chem. Phys.* **58**, 5745–5759 (1973).
 96. P. Virtanen, R. Gommers, T. E. Oliphant, M. Haberland, T. Reddy, *et al.*, *Nat. Meth.* **17**, 261–272 (2020).
 97. *Unified SCME*, 2020.
 98. S. R. Bahn, K. W. Jacobsen, *Comput. Sci. Eng.* **4**, 55 (2002).
 99. A. H. Larsen, J. J. Mortensen, J. Blomqvist, I. E. Castelli, R. Christensen, *et al.*, *J. Phys. Condens. Matter* **29**, 273002 (2017).
 100. N. Bjerrum, *Science* **115**, 385–390 (1952).

101. K. Röttger, A. Endriss, J. Ihringer, S. Doyle, W. F. Kuhs, *Acta Cryst. Sec. B* **50**, 644–648 (1994).
102. E. Whalley, *Trans. Faraday Soc.* **53**, 1578 (1957).
103. P. V. Hobbs, *Ice physics* (Oxford university press, 2010).
104. E. Whalley, "Trans. Faraday Soc." **54**, 1613 (1958).
105. E. Whalley, *J. Chem. Phys.* **81**, 4087–4092 (1984).
106. S. Rasti, J. Meyer, *J. Chem. Phys.* **150**, 234504 (2019).
107. K. Parlinski, Z. Q. Li, Y. Kawazoe, *Phys. Rev. Lett.* **78**, 4063–4066 (1997).
108. A. Togo, I. Tanaka, *Scripta Mater.* **108**, 1–5 (2015).
109. P. Vinet, J. R. Smith, J. Ferrante, J. H. Rose, *Phys. Rev. B* **35**, 1945–1953 (1987).
110. W. Kabsch, *Acta Cryst. Sec. A* **32**, 922–923 (1976).
111. J. C. Howard, J. L. Gray, A. J. Hardwick, L. T. Nguyen, G. S. Tschumper, *J. Chem. Theory Comput.* **10**, 5426–5435 (2014).
112. J. C. Howard, G. S. Tschumper, *J. Chem. Theory Comput.* **11**, 2126–2136 (2015).
113. J. Reimers, R. Watts, M. Klein, *Chem. Phys.* **64**, 95–114 (1982).
114. J. Reimers, R. Watts, *Chem. Phys.* **85**, 83–112 (1984).
115. M. A. Suhm, R. O. Watts, *Mol. Phys.* **73**, 463–469 (1991).
116. O. Loboda, F. Ingrosso, M. F. Ruiz-López, H. Reis, C. Millot, *J. Comp. Chem.* **37**, 2125–2132 (2016).
117. J. L. Abascal, C. Vega, *J. Phys. Chem. C* **111**, 15811–15822 (2007).

CHAPTER 6

Volume Isotope Effect of Ice Ih

This chapter is based on:

S. Rasti, E. Ö. Jónsson, H. Jónsson and J. Meyer, New Insights into the Volume Isotope Effect of Ice Ih from polarizable many-body Potentials, *to be submitted*

Abstract

The volume-isotope effect (VIE) of ice Ih is studied computationally. Nuclear quantum effects in the Helmholtz free energy are accounted for based on the quasi-harmonic approximation and evaluated by extensive phonon calculations. Focusing on recently developed polarizable many-body potentials as interaction models, one of them (MB-pol) is found to yield the anomalous VIE in very good agreement with the most recent high-resolution neutron diffraction measurements – much better than DFT calculations with the PBE functional. Using the MB-pol energy partitioning, a surprisingly large influence of the cooperative interaction between three water molecules for the VIE and its temperature dependence up to 200 K is being revealed. The interaction models are further scrutinized by decomposing the zero-point pressure into contributions from different vibrational mode groups. MB-pol’s remarkable performance is confirmed by comparing to a hitherto unconsidered benchmark value for the intramolecular stretching modes of H₂O ice Ih obtained from Raman spectroscopy data. This unveils the delicate competition between the librational and intramolecular stretching modes upon substitution of hydrogen by deuterium as the driving force behind the VIE – mitigated by three-body effects.

6.1 Introduction

Nuclear quantum effects can manifest themselves quite prominently in macroscopic thermodynamic properties, like for example phase transition enthalpies [1], negative thermal expansion (NTE) or density change at low temperatures upon substitution of a light by a heavier isotope [2]. The latter is called the volume isotope effect (VIE) and originates from the zero-point energy of the lattice vibrations (phonons). Most materials show a normal VIE, which means substitution with heavier isotopes results in a smaller volume per unit cell at temperatures approaching the absolute zero. A hand-waving rationalization in a classical picture is that the larger vibrational amplitude and concomitant volume ascribed to a lighter isotope compared to heavier isotope, which

both experience the same chemical interaction potential at the same temperature. In ice Ih, the most common form of solid water on earth, the VIE is anomalous, resulting in a smaller unit cell volume of the H_2O compared to the D_2O isotopologue (about 0.1 % up to 200 K [3, 4]). Despite its small magnitude, the effect has been very well quantified experimentally. Only recently, high-resolution neutron diffraction measurements [4] have reduced the uncertainties for the unit cell volumes of ice Ih compared to earlier work [3] over a wide temperature range and thus provide an excellent benchmark for atomistic interaction models that can be employed in computational studies.

Computational modeling of the VIE is very challenging. So far, water force fields ranging from simple fixed point charge up to sophisticated polarizable models have all predicted a normal VIE for ice Ih [5–7]. Density functional theory on the other hand is able to model the VIE of different ice phases [7–9]. However, even a qualitatively correct description depends very strongly on the computational settings, in particular the choice of the exchange-correlation functional [7]. Quantification of the VIE using embedded-fragment ab initio second-order many-body perturbation (MP2) theory has been faring somewhat better [10]. But also here, the results are very sensitive to computational details like the basis set size and the embedding field. This also holds for the individual contributions of the different groups of phonon modes to the zero-point pressure, which are ultimately responsible for the VIE [8, 10]. These contributions are commonly expressed in form of the mode-specific Grüneisen parameters and have not been benchmarked against experimental data. Consequently, a detailed understanding of the VIE’s origin in terms of the competition of different contributions to the chemical interaction potential has been elusive so far.

In this work, that understanding is provided based on recently developed polarizable many-body potentials as interaction models. Building on recent studies (see Chapters 3 and 5), the quasi-harmonic approximation is employed to account for nuclear quantum effects in the Helmholtz free energy by means of extensive phonon calculations. The MB-pol interaction model, whose short-range part is rooted in coupled-cluster calculations, yields the anomalous VIE of ice Ih in better agreement with the experimental

reference value than DFT calculations with the PBE functional. A decomposition of the zero-point pressure into contributions from different vibrational mode groups together with a hitherto unconsidered benchmark value obtained from Raman spectroscopy [11] allows to scrutinize this further. According to the MB-pol total energy partitioning, the delicate competition between the librational and intramolecular stretching modes driven by a surprisingly large influence of three-body effects is responsible for the anomalous VIE of ice Ih.

6.2 Methods

For the quantification of the VIE, this work employs the quasi-harmonic approximation (QHA), which has been used successfully for the same purpose in the past [7–10, 12]. According to the QHA, the Helmholtz free energy of the ice crystal is given by

$$F(V, T) = U(V) + \underbrace{\frac{1}{2} \sum_i \hbar \omega_i(V)}_{E_{\text{zp}}(V)} + k_{\text{B}} T \sum_i \ln \left(1 - \exp \left(\frac{-\hbar \omega_i(V)}{k_{\text{B}} T} \right) \right) \quad (6.1)$$

and is conveniently evaluated per molecule. U is the internal energy that describes the interaction between molecules in the crystal. ω_i are the vibrational modes, which determine the second (zero-point energy E_{zp}) and temperature-dependent third term of F . For the sake of simplicity, they are denoted by a collective index i that stands for both wave-vector and band indices of the corresponding phonon modes (see Section 2.4 for more details). The internal energy U and the vibrational modes ω_i depend on the unit cell volume V , so that the minimum of F with respect to V at a given temperature is generally different for H_2O and D_2O isotopologues. The corresponding volumes are labeled $V_{\text{H}_2\text{O}}(T)$ and $V_{\text{D}_2\text{O}}(T)$ in the following. V_0 minimizes $U(V)$, with the zero-reference of the latter defined such that the lattice energy $E_{\text{lat}} = U(V_0)$.

In this work, calculations with different interaction models are performed¹, employing and extending the Atomic Simulation Environment (ASE) [13] for interfacing

¹More details about these models are given in Sections 2.2 and 2.3 of this thesis.

their respective implementations. This includes the fixed-point-charges-based force fields q-TIP4P/F [14, 15] (as available in LAMMPS [16]), the polarizable force fields AMOEBA14 [17, 18] (as implemented in TINKER [19]), SCME/f [20] (and Chapter 5) and MB-pol (as implemented in the MBX package) [21–23]. All-electron density functional theory (DFT) calculations with the PBE exchange-correlation functional [24] are carried out with FHI-aims code [25, 26], using the same high-accuracy settings thoroughly verified [27] and employed [28, 29] for ice Ih in previous work (see Section 6.A.1 for details). The DFT calculations mimic proton disorder with a simulation cell containing 12 molecules [30]. A 96 molecule cell or supercells of this cell have been used for the force field interaction models to ensure the same level of convergence for V_0 ($\pm 0.01 \text{ \AA}^3$ per molecule [27]). For all interaction models, V_0 is calculated with ASE as in our earlier work by a combined optimization of the cell vectors and the molecular degrees of freedom preserving the space group [29] with a maximum force threshold of $1.0 \times 10^{-3} \text{ eV \AA}^{-1}$.

A continuous representation of $U(V)$ is obtained by least-square fitting to the Rose-Vinet [31] equation of state. Isotropic contraction and expansion of V_0 by $\pm 4\%$ yields 11 structures for each interaction model, for which again all molecular degrees of freedoms have been relaxed. Phonon calculations have been carried out for all of these structures with the PHONOPY code [32], using a finite displacement [33] of 0.02 \AA in $3 \times 3 \times 3$ supercells of the original simulation cell. The Brillouin zone has been sampled by $30 \times 30 \times 30$ and $10 \times 10 \times 10$ grids of phonon wave vectors in the 12 molecule and 96 molecule simulation cells, respectively. The implementation of the QHA in PHONOPY then yields a continuous representation of the volume-dependent second and third terms in Eq. (6.1) and thus $V_{\text{H}_2\text{O}}(T)$, $V_{\text{D}_2\text{O}}(T)$, $\text{VIE}(T) = \frac{V_{\text{D}_2\text{O}}}{V_{\text{H}_2\text{O}}} - 1^2$ and the phonon mode-dependent Grüneisen parameters γ_i . Convergence checks for the VIE can be

²This work uses the same convention as in the recent work Fortes [4] to quantify the volume isotope effect, i.e., $\text{VIE} = \frac{V_{\text{D}_2\text{O}} - V_{\text{H}_2\text{O}}}{V_{\text{H}_2\text{O}}}$, whereas others have used $\text{VIE}' = \frac{V_{\text{H}_2\text{O}} - V_{\text{D}_2\text{O}}}{V_{\text{D}_2\text{O}}}$, which leads to almost the same absolute numbers but flips the sign. Both expressions are related according to $\text{VIE} = -\frac{\text{VIE}'}{1+\text{VIE}'}$ and $\text{VIE}' = -\frac{\text{VIE}}{1+\text{VIE}}$, respectively. For the sake of brevity, the temperature dependence has been omitted.

found in Section 6.A.2.

6.3 Results and Discussion

Table 6.1 compiles experimental data and results from calculations for V_0 , $V_{\text{H}_2\text{O}}$, $V_{\text{D}_2\text{O}}$ and the VIE for ice Ih. A positive (negative) value corresponds to an anomalous (normal) VIE. The most recent results from the high-resolution neutron diffraction measurements by Fortes [4] yield an even smaller and more accurately determined anomalous VIE ($+0.050 \pm 0.002\%$) than the earlier data from the work of Röttger *et al.* [3] ($+0.090 \pm 0.015\%$). In both studies, the lowest temperature at which measurements have been performed is 10 K. For that reason, we have calculated $V_{\text{H}_2\text{O}}$ and $V_{\text{D}_2\text{O}}$ at both 0 and 10 K to confirm that this has no effect on any of the numbers presented in Table 6.1. As demonstrated only recently, errors related to the treatment of core and valence electrons in different DFT codes can be sizeable for the calculation of energy-volume curves $U(V)$ [34] and could thus significantly affect results for the VIE. This is the most likely reason for the difference of 0.07% between earlier DFT results obtained with the same exchange-correlation functional (PBE) [7, 12]. Our own PBE calculations eliminate this source of error and perfectly reproduce the value for V_0 obtained in earlier work [27, 28]. In combination with our meticulous convergence tests for the phonon calculations with respect to the VIE (see Section 6.A.2), we can therefore confirm without any further doubts the conclusions from earlier work [7, 12], namely that the PBE functional reproduces the experimentally observed anomalous VIE but overestimates it. Likewise, our computational setup also confirms that the q-TIP4P/F force field, which is based on fixed point charges (see Section 2.3.1) yields a normal VIE for ice Ih [7]. The same holds for the two polarizable force fields AMOEBA14 and the recently established SCME/f (see Chapter 5). The results for $V_{\text{H}_2\text{O}}$ and also for $V_{\text{D}_2\text{O}}$ obtained with SCME/f show the best agreement with the experimental values. SCME/f is followed by MB-pol, which also yields $V_{\text{H}_2\text{O}} < V_{\text{D}_2\text{O}}$ and consequently a correct description of the anomalous VIE. The absolute value of +0.14% is even in much better agreement with the experimental data than (our) PBE results. This re-

Table 6.1: Volumes V_0 , $V_{\text{H}_2\text{O}}$ and $V_{\text{D}_2\text{O}}$ for ice Ih (in \AA^3 per molecule, rounded to two decimals). The volume isotope effect is quantified by $\text{VIE} = \frac{V_{\text{D}_2\text{O}}}{V_{\text{H}_2\text{O}}} - 1$ (in percent, calculated using more decimals). The experimental data for $V_{\text{H}_2\text{O}}$, $V_{\text{D}_2\text{O}}$ and VIE have been measured at $T = 10\text{ K}$ [3, 4]. Calculations from this work with all interaction models at 0 and 10 K do not yield any differences in the second decimal.

	V_0	$V_{\text{H}_2\text{O}}$	$V_{\text{D}_2\text{O}}$	VIE
Experiments				
Fortes [4]		32.06	32.07	+0.05
Röttger <i>et al.</i> [3]		32.05	32.08	+0.09
Calculations – DFT with PBE functional ^a				
this work	30.78	31.03	31.14	+0.36
Pamuk <i>et al.</i> [7] ^b	29.98	30.09	30.19	+0.33
Murray and Galli [12]	30.50	30.57	30.67	+0.40
Calculations – polarizable force fields				
MB-pol	31.07	31.44	31.49	+0.14
MB-pol w/o 3B	29.14	30.18	30.06	−0.39
SCME/f	30.38	31.98	31.68	−0.90
AMOEBA14	31.82	33.35	33.12	−0.67
Calculations – fixed-charge force field				
q-TIP4P/F ^c	31.24	32.83	32.63	−0.61

^aSee Section 6.A.1 in the appendix to this chapter for a collection of other values for V_0 obtained with the PBE exchange-correlation functional in previous work.

^bValue obtained with the QHA and a k-mesh of 729 points, which is most comparable to the present work.

^cNote that these values differ slightly from the results obtained by Pamuk *et al.* [7] due to differences in the computational setups.

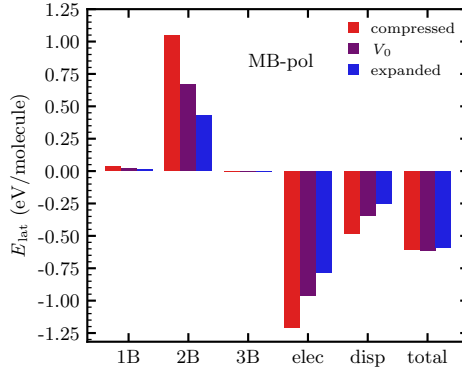


Figure 6.1: Lattice energy E_{lat} and its contributions according to the total energy decomposition of the MB-pol force field [21, 22, 35] (all in eV per molecule). The intramolecular (1B) as well as intermolecular short-range two-body (2B), three-body (3B) electrostatic (elec) and dispersion (disp) contributions add up to E_{lat} (total). Violet, red and blue bars depict equilibrium (V_0) and isotropically compressed ($0.96 \cdot V_0$) and expanded ($1.04 \cdot V_0$) lattice configurations, respectively, as encountered during the phonon calculations for the determination of the VIE according to the QHA.

markable result also bares the opportunity to better understand what contributions to the chemical bonding in the ice Ih crystal are responsible for the VIE. Among all the force fields considered here, MB-pol is the only one which explicitly accounts for short-range interactions involving triples of water molecules, which have been parameterized to quantum-chemical CCSD(T) calculations [21] (see also Section 2.3.4). Indeed, omitting these terms (MB-pol w/o 3B in Table 6.1) yields a normal VIE.

At first glance, the strong influence of these terms is surprising, because they do not constitute a large contribution to the cohesive (lattice) energy according to the decomposition of the internal energy at the equilibrium volume $U(V_0)$ in the MB-pol force field [36]. This does not change when moving away from V_0 as shown in Fig. 6.1. Compression of the ice Ih lattice leads to an increase of the repulsive short-range interactions between pairs of water molecules (two-body terms), which is almost compensated by the increase of the long-range electrostatic and dispersion contributions. The opposite

holds when expanding the volume. The one-body (i.e., deformation of individual water molecules) and three-body terms play hardly any role.³

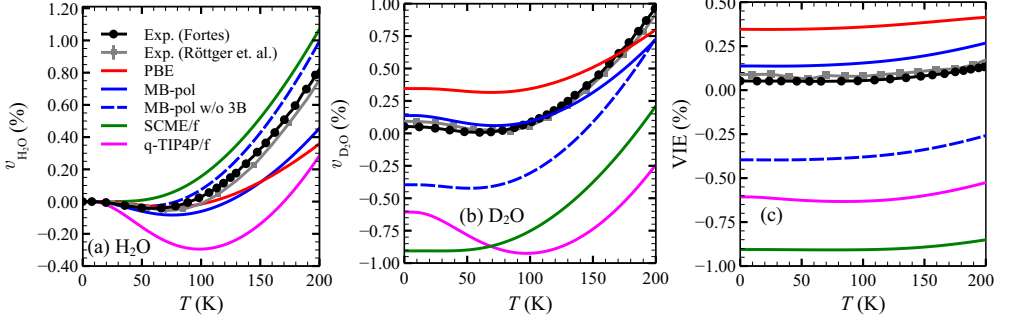


Figure 6.2: Relative volume changes (a) $v_{\text{H}_2\text{O}}(T) = \frac{V_{\text{H}_2\text{O}}(T)}{V_{\text{H}_2\text{O}}} - 1$ and (b) $v_{\text{D}_2\text{O}}(T) = \frac{V_{\text{D}_2\text{O}}(T)}{V_{\text{H}_2\text{O}}} - 1$ of ice Ih, both with respect to $V_{\text{H}_2\text{O}}$ from Table 6.1 for the same interaction models except AMOEBA14. (c) shows the resulting temperature dependence of the volume isotope effect $\text{VIE}(T) = \frac{V_{\text{D}_2\text{O}}(T)}{V_{\text{H}_2\text{O}}(T)} - 1 = \frac{v_{\text{D}_2\text{O}}(T)+1}{v_{\text{H}_2\text{O}}(T)+1} - 1$. Error indicators for the experimental data from Röttger *et al.* [3] (gray) are hardly visible, and even less so for the data from Fortes [4] (black), whereby lines are meant to guide the eye.

To investigate the importance of the three-body contributions (in MB-pol) for the VIE more closely, it is instructive to evaluate $V_{\text{H}_2\text{O}}$ and $V_{\text{D}_2\text{O}}$ over a wider range of temperatures, which has recently been remeasured with higher accuracy by Fortes [4] as well. This is illustrated in form of the relative volume changes $v_{\text{H}_2\text{O}}(T)$ and $v_{\text{D}_2\text{O}}(T)$ up to $T \leq 200$ K in Fig. 6.2(a) and Fig. 6.2(b), respectively. The experimental data for H_2O and D_2O ice Ih shows a negative slope for $T \leq 70$ K. This negative thermal expansion (NTE) has been modeled successfully before [10, 37] and is also reproduced by all methods considered here, except for SCME/f. This leads to a small offset in the relative volume change for H_2O between SCME/f and the experimental data at higher temperatures, which remains almost constant. Apart from that, SCME/f captures the shape of the experimental curve for $v_{\text{H}_2\text{O}}(T)$ very well, i.e. better than any other

³Because polarizability is accounted for in MB-pol, the electrostatics are long-range many-body interactions, see Section 2.3.4.

method considered here (except for MB-pol w/o 3B). MB-pol yields a slightly worse description of $v_{\text{H}_2\text{O}}(T)$ similar to PBE. For $v_{\text{D}_2\text{O}}(T)$ on the other hand, it provides by far the best possible description of the relative volume change (followed by PBE). Consequently, MB-pol also provides the best possible description of the VIE over the entire temperature range considered here. Not including the three-body effects in MB-pol improves the shape of $v_{\text{H}_2\text{O}}(T)$ but significantly worsens results for $\text{VIE}(T)$, resulting in the prediction of a normal volume isotope effect. Both SCME/f and q-TIP4P/f yield an even worse shape for $v_{\text{H}_2\text{O}}(T)$ compared to the experimental data. q-TIP4P/f describes a too strong NTE over a too large temperature interval ($T \leq 100 \text{ K}$) for both H_2O and D_2O , error canceling ultimately results in a better description of $\text{VIE}(T)$ compared to SCME/f.

According to the QHA (see Eq. (6.1)) the temperature dependence of the equilibrium volume is completely determined by the vibrational modes. As demonstrated in previous work [5, 7, 8, 10], their change upon compression and expansion can be analyzed in detail by means of the mode-dependent Grüneisen parameters $\gamma_i = -\frac{V}{\omega_i} \frac{\partial \omega_i}{\partial V}$, which define the zero-point pressure

$$P_{\text{ZP}} = -\frac{\partial E_{\text{ZP}}}{\partial V} = -\frac{\hbar}{2V} \sum_i \frac{\partial \omega_i}{\partial V} = \frac{\hbar}{2V} \sum_i \omega_i \gamma_i \quad . \quad (6.2)$$

Positive (negative) values for P_{ZP} yield expansion (contraction) of the volume due to zero-point energy effects.⁴ Figure 6.3(a) and (b) show that all methods yield a positive total zero-point pressure for both H_2O or D_2O , respectively, as to be expected according to the results compiled in Table 6.1. For an anomalous (normal) VIE (at 0 K), the total P_{ZP} needs to be smaller (larger) for H_2O than for D_2O . The corresponding differences are shown in Fig. 6.3(c), and indeed only for PBE and MB-pol comes out $P_{\text{ZP}}^{\text{H}_2\text{O}} - P_{\text{ZP}}^{\text{D}_2\text{O}} < 0$. Figure 6.3 also shows a decomposition of the zero-point pressure into contributions from the five different vibrational mode groups characterized by hydrogen-bond bending (HB) and stretching (HS), librations (L), intramolecular bending (B) and stretching (S). Unlike the differences of the total P_{ZP} , which unfor-

⁴ P_{ZP} is an intensive quantity. For its proper evaluation in practical calculations, $\frac{\partial E_{\text{ZP}}}{\partial V}$ must be evaluated for the same reference volume as $U(V)$, i.e., per molecule in this work.

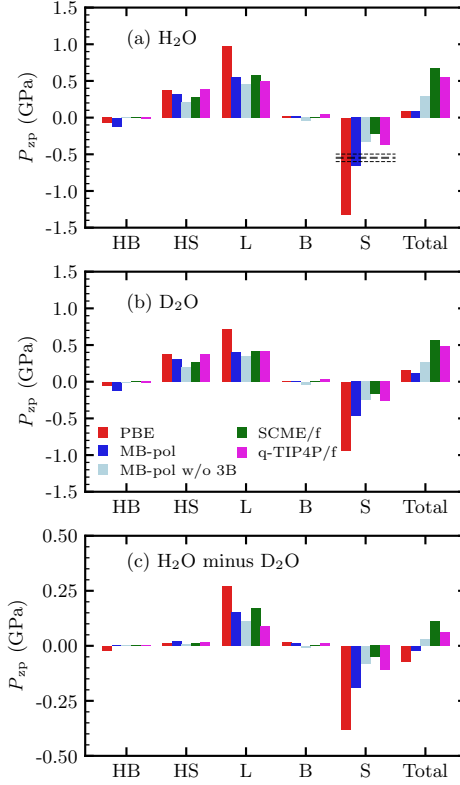


Figure 6.3: Total zero-point pressure P_{ZP} (rightmost bars) and its decomposition according to Eq. (6.2) into the vibrational mode groups comprised of hydrogen-bond bending (HB, 0 to 125 cm⁻¹), hydrogen-bond stretching (HS, 125 to 500 cm⁻¹), librations (L, 500 to 1500 cm⁻¹ (425 to 900 cm⁻¹) in H₂O (D₂O) ice Ih), intramolecular bending (B, 1500 to 2000 cm⁻¹ (900 to 1300 cm⁻¹) in H₂O (D₂O) ice Ih) and intramolecular stretching (S, 3000 to 4000 cm⁻¹ (2000 to 3000 cm⁻¹) in H₂O (D₂O) ice Ih) modes in (a) H₂O and (b) D₂O ice Ih. Results are shown using the same interaction models as in Fig. 6.2. Panel (c) illustrates the differences between (a) and (b) ($P_{ZP}(\text{H}_2\text{O}) - P_{ZP}(\text{D}_2\text{O})$). An estimate for P_{ZP}^S based on experimental data for H₂O ice Ih is indicated in panel (a) (see text and Section 6.A.3 for details).

Unfortunately cannot be measured directly, the differences between the contributions from the mode groups vary much more when considering different interaction models. The P_{ZP} contribution from the HB and HS groups is hardly affected by H-D substitution (see Fig. 6.3)(c)), which is not surprising because both of these mode groups involve the frustrated translation of entire H_2O and D_2O molecules. Likewise, all methods suggest that the B modes contribute very little to the VIE, and that it is the delicate balance between the expansive P_{ZP} of the L modes (frustrated rotations) and the contractive P_{ZP} of the S modes, which predominantly determine the sign of the zero-point pressures difference between both isotopologues.

Salim *et al.* [10] have already pointed that the subtle interplay of the P_{zp} contributions from different mode groups makes it additionally challenging to determine whether a particular interaction model captures the VIE correctly and for the right reason. We have already noted in our earlier work [29] that the measurements by Minceva-Sukarova *et al.* [11] of the pressure dependence of the Raman peak for the S mode group in H_2O ice Ih at 246 K play a key role in this context. As further detailed in Section 6.A.3, this allows us to obtain a good estimate for the contribution by the S mode group $P_{\text{zp}}^{\text{S}} \approx -0.548 \pm 0.051$ GPa, which is based on experimental data alone. Fig. 6.3(a) includes this value as black horizontal line. Considering that error estimates are lower bounds, MB-pol almost reproduces this value exactly (-0.66 GPa) and clearly comes much closer than PBE (-1.32 GPa) and MB-pol w/o 3B (-0.33 GPa). This confirms that three-body effects play indeed a very important role for the correct atomistic description of the VIE.

Unfortunately, Minceva-Sukarova *et al.* [11] have not measured the S mode group frequency shift for the D_2O isotopologue of ice Ih. Since all interaction models suggest a strongly localized character of the S modes, the outcome of such a measurement can be estimated based on the reduced masses associated with the O–H and O–D bonds as $0.728 \cdot P_{\text{zp}}^{\text{S}} \approx -0.399$ GPa (see Section 6.A.3), which is consequently again excellent agreement with the MB-pol value in Fig. 6.3(b) (-0.47 GPa). While it would be good to see this value confirmed in future experiments, the outstanding performance of MB-

pol and the concomitant understanding would be better scrutinized by experimental data for the L modes. Ideally, such data could also be measured at temperatures much lower than 246 K, to avoid systematic errors related to mode softening effects in future comparisons of experiments and theory.

6.4 Conclusion and Outlook

In summary, this study provides new insights into the volume isotope effect of ice Ih based on calculations within the quasi-harmonic approximation by employing a variety of different interaction models. All-electron DFT calculations with the PBE exchange-correlation functional provide a reference value and confirm that PBE yields an anomalous VIE but largely overestimates its magnitude. Among the three state-of-the-art polarizable force fields only MB-pol yields an anomalous VIE the magnitude of which is in significantly better agreement with the most recent experimental data than PBE. A detailed analysis based on the MB-pol energy partitioning reveals a surprisingly large influence of the cooperative interaction between three water molecules for the VIE and the temperature dependence of the volume of H₂O and D₂O ice Ih up to 200 K. Finally, the zero-point pressure is decomposed into contributions from different vibrational mode groups, and an estimate from experimental data for the contribution from the intramolecular stretching modes of H₂O ice Ih is extracted, which is completely independent from all measurements related to the VIE. Among all interaction models considered here, this is in best agreement with MB-pol – while being significantly overestimated by PBE and underestimated by all other force fields. This suggests that MB-pol yields the anomalous VIE of ice Ih for the right reason. It thus also enables unprecedented quantification and atomic-scale understanding of its driving force, namely the delicate competition between the expansive librational and contractive intramolecular stretching modes upon substitution of hydrogen by deuterium, mitigated by three-body effects. Future computational studies should investigate other ice polymorphs. However, before embarking on this endeavor, it would be highly desirable to have experimental benchmark data for contribution from other vibrational

mode groups to the zero-point pressure, ideally with smaller error bars and for both H_2O and D_2O isotopologues. This bares the exciting prospect of obtaining fundamental insights about volume isotope effects in those other polymorphs as well, and to establish a delicate benchmark that can be used for the further development of interaction models targeting condensed forms of water.

6.A Appendix

6.A.1 Comparison to Previous DFT Calculations

Table 6.2: Volumes V_0 for ice Ih (see main text for definition) as obtained “directly” from DFT calculations (i.e., without considering ZPE effects) with the PBE exchange-correlation functional. Results from this work, Pamuk *et al.* [7] and [12] are already given in Table 6.1. Equivalent results for ice VIII are shown to further illustrate difference between all-electron calculations and those which employ approximations for core and valence electrons. All values are in \AA^3 per molecule.

	$V_0(\text{ice Ih})$	$V_0(\text{ice VIII})$
<hr/>		
all-electron calculations		
this work	30.78	20.73
Santra <i>et al.</i> [27] and Sun <i>et al.</i> [28]	30.79	20.74
<hr/>		
calculations with approximations for core and valence electrons		
Pamuk <i>et al.</i> [7]	29.98	
Murray and Galli [12]	30.50	20.44
Umemoto and Wentzcovitch [38]		20.12
Feibelman [39]	30.65	
Brandenburg <i>et al.</i> [40]	30.15	20.36
Liu and Ojamäe [41]	30.3	20.5
<hr/>		

All DFT calculations in this work employ the PBE exchange-correlation functional [24]. They have been carried out the with the all-electron DFT code FHI-aims [25,

26], which employs numerically tabulated atom-centered orbitals as basis set. The standard tight settings and tier-2 and tier-3 basis sets for hydrogen and oxygen atoms, respectively. A $4 \times 4 \times 4$ Monkhorst-Pack grid [42] is employed for Brillouin zone sampling. These settings are the same as those established by Santra *et al.* [27], whose thorough convergence tests gave an estimate of $\pm 0.01 \text{ \AA}^3$ for the numerical accuracy of V_0 with respect to these settings. Sun *et al.* [28] have used the same settings afterwards, As to be expected and shown in Table 6.2, all three calculations agree perfectly within the aforementioned accuracy margin.

Table 6.2 also reveals that DFT-PBE calculations with approximations for the treatment of core and valence electrons (pseudopotentials) systematically underestimate V_0 for both ice Ih and ice VIII. A more detailed investigation of this interesting finding is outside the scope of this work.

6.A.2 Convergence Tests for the VIE Calculations

Three sets of convergence tests have been carried out, to scrutinize the accuracy of the results reported in Table 6.1 for $V_{\text{H}_2\text{O}}$ and $V_{\text{D}_2\text{O}}$ (and thus VIE) with respect to the following three parameters:

1. Accuracy of geometry optimization for the water molecules in the simulation cell. This is quantified by the force threshold F_{max} criterion that is used to stop the relaxation. Smaller values for F_{max} yield for accurate results.
2. Finite displacement in phonon calculations Δ_{disp} . For force fields where analytic formulations of forces are available, smaller values of Δ_{disp} reduce the error for the second derivatives in the phonon calculations. However, in DFT calculations, forces (usually) come with a numerical error, the reduction of which requires additional computational effort (i.e., increasing the accuracy of the self-consistent field cycle). Therefore, a small value that is as large as possible not to affect $V_{\text{H}_2\text{O}}$ and $V_{\text{D}_2\text{O}}$ (and thus VIE) is sought after here.
3. Range of isotropic contraction and expansion of V_0 used for the construction

of a continuous representation of the volume-dependent terms required for the quasi-harmonic approximation (QHA) given by Eq. (6.1). Different intervals $[(1 - s_{\max})V_0; (1 + s_{\max})V_0]$ have been considered, which are all discretized by 11 equidistant points. For too small intervals the numerical noise in the volumes gains a too large influence on the fit, while too large intervals leave the regime of validity for the QHA.

For reasons of computational convenience, all calculations for these convergence tests have been carried with the AMOEBA14 force field. All the results are compile in Table 6.3. Accurate results can be obtained with $F_{\max} = 10^{-3} \text{ eV } \text{\AA}^{-1}$, $\Delta_{\text{disp}} = 0.02 \text{ \AA}$ and $s_{\max} = 4\%$. As described in the main text, this is what has been used for all interaction models throughout this work.

6.A.3 Zero-point Pressures from Experimental Data

Using Raman spectroscopy Minceva-Sukarova *et al.* [11] measured the shift of the intramolecular stretching mode peak in the H_2O -isotopologue of ice Ih at 246 K when applying external pressure

$$\frac{\partial \nu_S}{\partial P} = -78.0 \pm 7.2 \text{ cm}^{-1} \text{ GPa}^{-1} \quad , \quad (6.3)$$

which yields

$$h \frac{\partial \nu_S}{\partial P} = 1.549 \pm 0.143 \times 10^{-21} \text{ J GPa}^{-1} \quad (6.4)$$

($1 \text{ h cm}^{-1} = 1.9863 \times 10^{-23} \text{ J}$). This allows us to obtain an estimate based on experimental data for the zero-point pressure of the intramolecular stretching mode group

$$P_{\text{zp}}^S \approx - \sum_{i \in S} \frac{\hbar}{2} \frac{\partial \omega_i}{\partial V} = \frac{1}{2} \frac{B_0}{V_0} h \sum_{i \in S} \frac{\partial \nu_i}{\partial P} \quad , \quad (6.5)$$

where $\frac{\partial \omega}{\partial V} = \frac{\partial P}{\partial V} \frac{\partial \omega}{\partial P} = -2\pi \frac{B_0}{V_0} \frac{\partial \nu}{\partial P}$. In the following, it is assumed that $\frac{\partial \nu_S}{\partial P}$ does not change significantly with temperature.

The highly accurate experimental values for the bulk modulus $B_0 = 11.33 \text{ GPa}$ (extrapolated to 0 K) [43] and the unit cell volume $V_0 = 32.05 \text{ \AA}^3$ per H_2O molecule [4]

Table 6.3: Results of convergence tests with respect to the three parameters F_{\max} , Δ_{disp} and s_{\max} as defined in the text. Note that the volumes $V_{\text{H}_2\text{O}}$ and $V_{\text{D}_2\text{O}}$ (for ice Ih) are rounded to two decimals, and that $\text{VIE} = \frac{V_{\text{D}_2\text{O}}}{V_{\text{H}_2\text{O}}} - 1$ is calculated using more decimals.

F_{\max} (eV Å ⁻¹)	Δ_{disp} (Å)	s_{\max} (%)	$V_{\text{H}_2\text{O}}$ (Å ³ /H ₂ O)	$V_{\text{D}_2\text{O}}$ (Å ³ /D ₂ O)	VIE (%)
Force threshold criterion for geometry optimizations					
1.0×10^{-4}	0.02	4.0	33.35	33.12	-0.67
1.0×10^{-3}	0.02	4.0	33.35	33.12	-0.67
2.5×10^{-3}	0.02	4.0	33.36	33.12	-0.69
5.0×10^{-3}	0.02	4.0	33.37	33.13	-0.69
Finite displacement for phonon calculations					
1.0×10^{-3}	0.01	4.0	33.35	33.12	-0.67
1.0×10^{-3}	0.02	4.0	33.35	33.12	-0.67
1.0×10^{-3}	0.03	4.0	33.36	33.12	-0.68
1.0×10^{-3}	0.06	4.0	33.37	33.13	-0.68
1.0×10^{-3}	0.08	4.0	33.38	33.14	-0.69
Maximum expansion and contraction of cell volume for the QHA					
1.0×10^{-3}	0.02	0.2	33.23	33.02	-0.60
1.0×10^{-3}	0.02	0.5	33.21	33.02	-0.56
1.0×10^{-3}	0.02	1.0	33.26	33.07	-0.54
1.0×10^{-3}	0.02	2.0	33.29	33.10	-0.60
1.0×10^{-3}	0.02	3.0	33.33	33.11	-0.68
1.0×10^{-3}	0.02	4.0	33.35	33.12	-0.67
1.0×10^{-3}	0.02	5.0	33.35	33.12	-0.67

(at 10 K), result in

$$\frac{1}{2} \frac{B_0}{V_0} = 0.177 \text{ GPa } \text{\AA}^{-3} \quad . \quad (6.6)$$

Assuming the same shift for both symmetric and antisymmetric stretching modes and neglecting dispersion ($\frac{\partial \nu_i}{\partial P} = \frac{\partial \nu_S}{\partial P}$), which is consistent with the Raman experiments of Minceva-Sukarova *et al.* [11]⁵, result in

$$h \sum_{i \in S} \frac{\partial \nu_i}{\partial P} \approx 2 \cdot h \frac{\partial \nu_S}{\partial P} \approx -3.099 \pm 0.286 \times 10^{-21} \text{ J GPa}^{-1} \quad (6.7)$$

where the factor of two comes from the summation over both stretching modes per molecule. This leads to the final value

$$P_{zp}^S \approx -0.548 \pm 0.051 \text{ GPa} \quad (6.8)$$

($1 \text{ J } \text{\AA}^{-3} = 10^{30} \text{ Pa}$). Due to aforementioned approximations, the indicated errors should be considered as lower bounds.

Unfortunately, Minceva-Sukarova *et al.* [11] do not report $\frac{\partial \nu_S}{\partial P}$ for D₂O ice Ih, and to the best of our knowledge no such measurement is available. Despite the relatively strong hydrogen bonding in ice Ih [44], the S modes are still largely dominated by the local intramolecular potential along a single O–H bond. This leads to a simple one-dimensional picture, where the relative shift of the corresponding O–D stretching mode is (approximately) given by

$$\alpha = \frac{\nu_S^{\text{D}_2\text{O}}}{\nu_S^{\text{H}_2\text{O}}} \approx \frac{\mu_{\text{O-H}}}{\mu_{\text{O-D}}} = \sqrt{\frac{m_{\text{H}}}{m_{\text{D}}} \frac{m_{\text{O}} + m_{\text{D}}}{m_{\text{O}} + m_{\text{H}}}} \approx 0.728 \quad , \quad (6.9)$$

where $\mu_{\text{O-X}} = \frac{m_{\text{X}} \cdot m_{\text{O}}}{m_{\text{X}} + m_{\text{O}}}$ ($X \in \{\text{H}, \text{D}\}$) is the reduced mass of the corresponding O–X bond with $m_{\text{H}} = 1.0078 \text{ u}$, $m_{\text{D}} = 2.0141 \text{ u}$, $m_{\text{O}} = 15.999 \text{ u}$. The calculations with all interaction models considered in this work leads to values between 0.726 and 0.730 for α , which confirms that deviations from this one-dimensional picture are very small. In fact, Minceva-Sukarova *et al.* [11] do provide the average stretching mode for both H₂O ($\nu_{\text{OH}(\text{H}_2\text{O})} = 3138 \text{ cm}^{-1}$) and D₂O ($\nu_{\text{OD}(\text{D}_2\text{O})} = 2316 \text{ cm}^{-1}$) ice Ih at 246 K, which yields $\alpha = 0.738$. Considering a Morse oscillator at this temperature, $\nu_S^{\text{H}_2\text{O}}$ should be

⁵These experiments only yield results for the Γ -point.

reduced more strongly compared to its value at 0 K than $\nu_{\text{S}}^{\text{D}_2\text{O}}$. Since temperature effects are neglected in Eq. (6.9), it is thus not surprising that the measured relative frequency shift is underestimated. On the other hand, measurements at 0 K should yield

$$\frac{\partial \nu_{\text{S}}^{\text{D}_2\text{O}}}{\partial P} \approx \frac{\partial(\alpha \nu_{\text{S}}^{\text{H}_2\text{O}})}{\partial P} \approx 0.728 \cdot \frac{\partial \nu_{\text{S}}^{\text{H}_2\text{O}}}{\partial P} \quad (6.10)$$

for the shift of the intramolecular stretching mode peak in the D_2O -isotopologue of ice Ih.

6.5 References

1. V. Fuentes-Landete, S. Rasti, R. Schlögl, J. Meyer, T. Loerting, *J. Phys. Chem. letters* **11**, 8268–8274 (2020).
2. E. R. Ponder, *The physics of ice* (Elsevier, 2013).
3. K. Röttger, A. Endriss, J. Ihringer, S. Doyle, W. F. Kuhs, *Acta Cryst. B* **50**, 644–648 (1994).
4. A. D. Fortes, *Acta Cryst. B* **74**, 196–216 (2018).
5. C. P. Herrero, R. Ramírez, *J. Chem. Phys.* **134**, 094510 (2011).
6. R. Ramírez, N. Neuerburg, M.-V. Fernández-Serra, C. P. Herrero, *J. Chem. Phys.* **137**, 044502 (2012).
7. B. Pamuk, J. M. Soler, R. Ramírez, C. P. Herrero, P. W. Stephens, *et al.*, *Phys. Rev. Lett.* **108**, 193003 (2012).
8. K. Umemoto, E. Sugimura, S. de Gironcoli, Y. Nakajima, K. Hirose, *et al.*, *Phys. Rev. Lett.* **115**, 173005 (2015).
9. K. Umemoto, R. M. Wentzcovitch, *Jpn. J. Appl. Phys.* **56**, 05FA03 (2017).
10. M. A. Salim, S. Y. Willow, S. Hirata, *J. Chem. Phys.* **144**, 204503 (2016).
11. B. Minceva-Sukarova, W. F. Sherman, G. R. Wilkinson, *J. Phys. C: Solid State Phys.* **17**, 5833–5850 (1984).
12. É. D. Murray, G. Galli, *Phys. Rev. Lett.* **108**, 105502 (2012).
13. A. H. Larsen, J. J. Mortensen, J. Blomqvist, I. E. Castelli, R. Christensen, *et al.*, *J. Phys.: Condens. Matter* **29**, 273002 (2017).
14. J. L. Abascal, C. Vega, *J. Chem. Phys.* **123**, 234505 (2005).
15. S. Habershon, T. E. Markland, D. E. Manolopoulos, *J. Chem. Phys.* **131**, 024501 (2009).
16. S. Plimpton, *J. Comput. Phys.* **117**, 1–19 (1995).
17. P. Ren, J. W. Ponder, *J. Phys. Chem. B* **107**, 5933–5947 (2003).
18. M. L. Laury, L.-P. Wang, V. S. Pande, T. Head-Gordon, J. W. Ponder, *J. Phys. Chem. B* **119**, 9423–9437 (2015).
19. J. W. Ponder *et al.*, *TINKER: Software tools for molecular design*, 2004.
20. K. T. Wikfeldt, E. R. Batista, F. D. Vila, H. Jónsson, *Phys. Chem. Chem. Phys.* **15**, 16542–16556 (2013).
21. V. Babin, G. R. Medders, F. Paesani, *J. Chem. Theory Comput.* **10**, 1599–1607 (2014).
22. V. Babin, C. Leforestier, F. Paesani, *J. Chem. Theory Comput.* **9**, 5395–5403 (2013).
23. G. R. Medders, V. Babin, F. Paesani, *J. Chem. Theory Comp.* **9**, 1103–1114 (2013).
24. J. P. Perdew, K. Burke, M. Ernzerhof, *Phys. Rev. Lett.* **77**, 3865–3868 (1996).
25. V. Blum, R. Gehrke, F. Hanke, P. Havu, V. Havu, *et al.*, *Comp. Phys. Comm.* **180**, 2175–2196 (2009).

-
26. V. Havu, V. Blum, P. Havu, M. Scheffler, *J. Comput. Phys.* **228**, 8367–8379 (2009).
 27. B. Santra, J. Klimeš, A. Tkatchenko, D. Alfè, B. Slater, *et al.*, *J. Chem. Phys.* **139**, 154702 (2013).
 28. J. Sun, R. C. Remsing, Y. Zhang, Z. Sun, A. Ruzsinszky, *et al.*, *Nat. Chem.* **8**, 831–836 (2016).
 29. S. Rasti, J. Meyer, *J. Chem. Phys.* **150**, 234504 (2019).
 30. D. R. Hamann, *Phys. Rev. B* **55**, R10157–R10160 (1997).
 31. P. Vinet, J. R. Smith, J. Ferrante, J. H. Rose, *Phys. Rev. B* **35**, 1945–1953 (1987).
 32. A. Togo, I. Tanaka, *Scripta Mater.* **108**, 1–5 (2015).
 33. K. Parlinski, Z. Q. Li, Y. Kawazoe, *Phys. Rev. Lett.* **78**, 4063–4066 (1997).
 34. K. Lejaeghere, G. Bihlmayer, T. Bjorkman, P. Blaha, S. Blugel, *et al.*, *Science* **351**, aad3000 (2016).
 35. G. R. Medders, V. Babin, F. Paesani, *J. Chem. Theory Comput.* **10**, 2906–2910 (2014).
 36. C. H. Pham, S. K. Reddy, K. Chen, C. Knight, F. Paesani, *J. Chem. Theory Comp.* **13**, 1778–1784 (2017).
 37. M. Gupta, R. Mittal, B. Singh, S. Mishra, D. Adroja, *et al.*, *Physical Review B* **98**, 104301 (2018).
 38. K. Umemoto, R. M. Wentzcovitch, *Phys. Rev. B* **69**, 180103 (2004).
 39. P. J. Feibelman, *Phys. Chem. Chem. Phys.* **10**, 4688–4691 (2008).
 40. J. G. Brandenburg, T. Maas, S. Grimme, *J. Chem. Phys.* **142**, 124104 (2015).
 41. Y. Liu, L. Ojamäe, *J. Phys. Chem. B* **120**, 11043–11051 (2016).
 42. H. J. Monkhorst, J. D. Pack, *Phys. Rev. B* **13**, 5188–5192 (1976).
 43. J. J. Neumeier, *J. Phys. Chem. Ref. Data* **47**, 033101 (2018).
 44. B. Santra, J. Klimeš, D. Alfè, A. Tkatchenko, B. Slater, *et al.*, *Phys. Rev. Lett.* **107**, 185701 (2011).

Samenvatting

IJs, de vaste vorm van water, speelt een belangrijke rol op onze planeet en in het hele universum. Ondanks het feit dat een individuele watermolecuul een zeer eenvoudige structuur heeft, kan de chemische binding van het molecuul in de vaste fase verrassend complex zijn. Tegenwoordig maken atomistische computermodellen het mogelijk deze eigenschappen te beschrijven en te begrijpen op een manier die lange tijd niet mogelijk was. Chemische interactiepotentialen vormen de kern van deze atomistische modellen. In oplopende volgorde van complexiteit zijn deze potentialen gebouwd op basis van eenvoudige paarpotentialen, polariseerbare krachtvelden, en berekeningen met dichtheidsfunctionaaltheorie (DFT). Het is een voortdurende wetenschappelijke uitdaging om deze potentialen verder te verbeteren en te testen. Dit proefschrift tracht een antwoord te geven op de volgende onderzoeksvragen: (i) Hoe belangrijk is de bijdrage van de nulpuntsvibratieënergie aan de thermodynamische eigenschappen van de fasen van ijs? (ii) Hoe nauwkeurig kunnen de beschikbare interactiepotentialen het (kleine) verschil in ijskristallen met betrekking tot nucleaire kwantumeffecten modelleren? (iii) Moeten interactiepotentialen worden verbeterd wanneer rekening wordt gehouden met nucleaire kwantumeffecten in ijs?

Hoofdstuk 3 presenteert een systematische vergelijking van veel gebruikte vaste-ladingpaarpotentialen en DFT op basis van van verschillende uitwisselingcorrelatiedichtheidsfunctionalen (UC-DF) voor zeven waterstof-geordende kristallijne ijsfasen (Ih, IX, II, XIII, XIV, XV, VIII). De UC-DF's omvatten de zogenaamde "local density approximation" (LDA-), "generalized gradient approximation" (GGA-) en meta-GGA-functionalen, alsmede verschillende uitbreidingen om rekening te houden met van der

Waals-interacties. Uitgaande van ruimte-groep-beperkte geoptimaliseerde structuren voor alle ijsfasen, worden zeer nauwkeurige fononberekeningen uitgevoerd in de quasi-harmonische benadering. De resulterende nulpuntsenergieën (NPE's) hebben een veel sterker effect op de cohesie-energieën en evenwichtsvolumes voor de krachtvelden dan voor DFT en resulteren in een betere overeenkomst met experimentele gegevens voor de eerstgenoemden. Wanneer NPE's worden meegenomen, leveren de krachtvelden evenwichtsvolumes en cohesie-energieën op die beter overeenkomen met experimentele gegevens dan de meeste dichtheidsfunctionalen. Om dit verder te analyseren is een decompositie van de cohesie-energieën in intramoleculaire deformatie-, elektrostatische en vdW-bijdragen uitgevoerd. Deze decompositie laat zien dat intramoleculaire deformatie wordt overgecompenseerd door elektrostatische en het attractieve deel van de Lennard-Jones potentialen in het geval van de krachtvelden. De elektrostatische is ook de dominante en typisch de grootste bindingsbijdrage voor de DFT-methoden. De bijdragen aan de nulpuntsenergie worden verder geanalyseerd door vergelijking van de frequentieverschuivingen in de OH-trillingen als gevolg van volumeveranderingen met beschikbare experimentele gegevens van Raman-spectroscopie. Alle krachtvelden geven een kleinere roodverschuiving van deze vibraties bij compressie dan alle hier beschouwde UC-DF's, en dit is verantwoordelijk voor het grotere effect van de NPE's op de energie-volume curves.

Zoals bediscussieerd in hoofdstuk 4 is de overgangsenthalpie van ijs II naar ijs Ic met behulp van calorimetrie gemeten als $+40 \text{ J mol}^{-1}$ voor H_2O en -140 J mol^{-1} voor D_2O , resulterend in een isotoopeffect van ongeveer 180 J mol^{-1} . Een hiërarchie van theoretische uitdrukkingen voor de overgangsenthalpie wordt gebruikt om rekening te houden met meer, en met subtielere bijdragen. Naast de nulpuntenergie wordt uiteindelijk ook rekening gehouden met de gewoonlijk verwaarloosde configuratiele entropie, omdat ijs II een waterstof-gordende fase en ijs Ic een waterstof-ongordende fase is. De uitdrukkingen worden rekenkundig geëvalueerd met behulp van twee krachtvelden, q-TIP4P/F en MB-pol, waarvan bekend is dat ze goed presteren voor de berekening van de cohesie-energie en de vibratie-eigenschappen van verschillende fasen van ijs. Daartoe worden zeer nauwkeurige fononberekeningen onder gebruik van de quasi-harmonische

benadering (QHB) uitgevoerd. Aangezien het feit dat de gemeten overgangsenthalpie één tot twee orden van grootte kleiner zijn dan wat gewoonlijk wordt beschouwd als chemische nauwkeurigheid (4 kJ) in computermodellen, is het niet verrassend dat de tekenverandering niet kan worden gereproduceerd. Beide krachtvelden geven echter het isotoopeffect als gevolg van voornamelijk de nulpuntenergieverschillen tussen de H_2O en overeenkomstige D_2O fasen van ijs, en wel in redelijke overeenstemming met de metingen: q-TIP4P/F kan ongeveer 3/4 van het isotoopeffect verklaren, terwijl MB-pol slechts ongeveer 1/3 er van beschrijft.

In hoofdstuk 5 wordt een potentiële energie-functie voor de beschrijving van een systeem van flexibele H_2O moleculen ontwikkeld op basis van de enkelvoudige centrum-multipoolexpansie van de elektrostatistische interactie (afkorting SCME in het Engels). Dit SCME/f genoemde model bevat de variatie van het moleculaire kwadрупoolmoment en het dipoolmoment met veranderingen in bindingslengte en -hoek om de resultaten van "high-level" elektronische structuurberekeningen te kunnen reproduceren. De multipooluitbreiding omvat ook vaste oktupool- en hexadecapoolmomenten, alsmede anisotrope dipool-dipool-, dipool-kwadрупool- en kwadрупool-quadрупool polarisatie tensoren. Het model bevat vijf aanpasbare parameters die betrekking hebben op de afstotende interactie en dempingsfuncties in de elektrostatistische en dispersie-interacties. Hun waarden worden aangepast om de laagste energie-isomeren van kleine clusters, $(\text{H}_2\text{O})_n$ met $n = 2 - 6$, te reproduceren, evenals gemeten eigenschappen van het Ih ijskristal. Berekeningen van het energieverschil tussen de verschillende isomeerconfiguraties van de clusters laten zien dat SCME/f goede overeenstemming geeft met resultaten van elektronische structuurberekeningen en een aanzienlijke verbetering betekent ten opzichte van de eerder gepresenteerde starre SCME-potentiaalfunctie. Analyse van de trillingsfrequenties van de clusters en de structurele eigenschappen van ijs Ih-kristal tonen het belang aan van een nauwkeurige beschrijving van de variatie van het kwadрупoolmoment met de moleculaire structuur.

In hoofdstuk 6 wordt het volume-isotoopeffect (VIE) van ijs Ih computationeel bestudeerd. Nucleaire kwantumeffecten in de Helmholtz-vrije energie worden meegenomen

op basis van de QHB en geëvalueerd via uitgebreide berekeningen aan de fononen. De nadruk ligt op de recent ontwikkelde polariseerbare "many body" potentialen als interactiemodellen. Een daarvan (MB-pol) blijkt de VIE van ijs Ih in zeer goede overeenstemming te beschrijven met de meest recente neutrondiffractiemetingen - veel beter dan DFT-berekeningen met het PBE-functionaal. Met behulp van de MB-pol energiede-compositie is een verrassend grote invloed van de coöperatieve interactie tussen drie watermoleculen op het VIE en de temperatuurafhankelijkheid daarvan gevonden. Een decompositie van de bijdragen tot de nulpuntsdruk samen met een tot nu toe niet meegenomen Raman spectroscopie meetwaarden betreffende OH-trillingen in H₂O-ijs Ih onthullen de drijvende kracht achter de VIE: de delicate competitie tussen OH-trillingen en de zogenaamde libratie modes.

Curriculum Vitae

Soroush Rasti was born on the 2nd of August 1991 in Isfahan (Iran). From 2003 to 2009, he followed his pre-university educations in his hometown. He received his B.Sc. degree in Physics in 2012 from the University of Tehran *cum laude* with the highest total GPA 18.37 among this classmates. In the last year of his bachelor studies, he participated in the National Physics Olympiad and obtained the 5th rank. After that in 2014, he entered Sharif University of Technology exceptionally without entrance exam as a brilliant young talented student. He received his Physics M.Sc. degree in 2015 *cum laude* again with the highest total GPA 19.37 among his classmates. After his master study, he did an internship in Japan in the molecular science department of the National Institute of Natural Science under the supervision of Prof. dr. K. Ohmori. This research was about developing a new type of Rydberg quantum simulators and computers. After that, Soroush joined the group of Dr. P. Kaghazchi at the Free University of Berlin as a visitor to perform research for the next generation of batteries focusing on the molecular level. In October 2016, Soroush started his PhD research under the supervision of Dr. Jörg Meyer at the in the theoretical chemistry group (headed by Prof. dr. Geert-Jan Kroes) of the Leiden Institute of Chemistry. His research was funded by the Netherlands Organisation for Scientific Research (NWO) and led to this thesis. From August 2021 onward, Soroush is working as a data science leader in a company focused on developing a new marketing model using artificial intelligence.

List of Publications

- S. Rasti and J. Meyer, Importance of zero-point energy for crystalline ice phases: A comparison of force fields and density functional theory, *J. Chem. Phys.* **150**, 234504 (2019).
- V. Fuentes-Landete, S. Rasti, R. Schlögl, J. Meyer and T. Loerting, Calorimetric Signature of Deuterated Ice II: Turning an Endotherm to an Exotherm, *J. Phys. Chem. Lett.* **11**, 8268 (2020).
- E. Ö. Jónsson, S. Rasti, M. Galynska, J. Meyer and H. Jónsson, Transferable Potential Function for Flexible H₂O Molecules Based on the Single Center Multipole Expansion, *submitted to the Journal of Chemical Theory and Computation (JCTC)*
- S. Rasti, E. Ö. Jónsson, H. Jónsson and J. Meyer, New Insights into the Volume Isotope Effect of Ice Ih from polarizable many-body Potentials, *to be submitted*

Afterword

Finally, my long academic journey as PhD student has been finished. It was full of all sorts of happiness, frustration, anxiety, hope and all other kinds of overwhelming emotions. I would like to thank the many people without whom I would not have finished this hard but enjoyable journey, and without whom I would not have been able to complete this research.

First, I would like to thank my PhD advisor **Jörg Meyer** for giving me the chance to pursue my PhD career at Leiden University and being patience and supportive during my doctoral research. His supportive approach and way of working helped me to develop some skills that allowed me to improve the quality of my work. In addition, I like to especially appreciate the tremendous time and effort he spent on proofreading the papers and this thesis: this thesis would not have been completed without your help and guidance. I am also thankful to my promotor **Geert-Jan Kroes** for generously sharing his priceless wisdom and experience with me.

I am very grateful to have been a part of the Leiden Theoretical Chemistry group, where I worked with many good colleagues. My special thanks to **Khosrow Shakouri** and **Hossein Tahmasbi** for helping me a lot in every moment of my PhD as a daily supervisor. I feel very lucky to have such exceptional friends. I never forget your encouragements and pleasing words about being perseverant and not to give up. I am thankful to **Thanja Lamberts** for teaching me how to supervise bachelor projects and being available for my questions. Thank you **Mark Somers** and **Marc van Hemert** for your advice about my presentations in the group. I also enjoyed being

together with other people in the group: **Paul Spiering, Sayan Seal, Elham Nour Ghassemi, Seenavasan Hariharan, Tim Jansen, Gernot Fücksel, Theophile Tchakoua, Andrew Powell, Guido Smeets, Nick Gerrtis, Francesco Nattino, Helen Chadwick and Katharina Doblhoff-Dier.**

I would like to thank all people from outside my academic environment, especially **Sobhan Niknam** and **Amin Tajik** for joyful gatherings in these years.

Last but not least, a big thanks to my beloved wife **Maryam**. You gave me a lot of motivations and energy and without your support, this PhD would not have been the same. During these hard time, you loved me unconditionally, sacrificed yourself to allow me to pursue my dreams. Words fail me but you didn't – thank you for all you've done. I wish I had the words to express my gratitude for all of your kindness. Thanks so much, **Maryam** for everything.